Technical Report Documentation Page

1. Report No. FHWA/NC/2006-48	2. Government Accession No.	3. Recipient's Catalog No.
4. Title and Subtitle Design Criteria for Post and Beam Bents with Drilled Shafts		5. Report Date December 2007
		6. Performing Organization Code
7. Author(s) Brent Robinson, Aidcer Vidot, Young Jin Park, Ben Possiel, Vinicio Suarez, Mervyn Kowalsky, and Mohammed Gabr		8. Performing Organization Report No.
9. Performing Organization Name and Address Department of Civil Engineering CB 7908, Mann Hall North Carolina State University Raleigh, NC 27695-7908		10. Work Unit No. (TRAIS)
		11. Contract or Grant No. 2006-15
12. Sponsoring Agency Name and Address North Carolina Department of Transportation Raleigh, NC 27611 Federal Highway Administration Raleigh, NC 27611		13. Type of Report and Period Covered Final Report July 2005-June 2007
		14. Sponsoring Agency Code
15. Supplementary Notes		

16. Abstract

The research work presented in the report addresses the potential areas of conservatism in the current practice related to bridge bents supported by drilled shafts and piles. The research encompasses modeling efforts and an experimental program. Modeling includes analysis of existing bridge case studies with drilled shaft foundations to characterize the impact of the current assumptions on sizing the various components of a bridge bent. An experimental program is performed to evaluate the connection stiffness, and to determine if a given connection has sufficient capacity to develop such stiffness and transfer moment The experimental program includes testing bearing pads in compression and shear to define their index properties. The bearing pads are then tested in a prototype bridge set up to measure their performance under simulated loading.

An improved set of design guidelines and recommendations regarding the superstructure-substructure connection's rotational stiffness, shaft/pile top boundary conditions, and resistance factors are proposed along with characterizing the impact of the current practice and various design assumptions on sizing components of bridge bents. Resistance factors are developed for drilled shafts, based on load test data from the state's geologic regions, for compatibility with LRFD implementation. Work in the report serves to provide a better understanding of the performance of bents supported by drilled shafts under AASHTO loading conditions. Such understanding serves as a tool that provides NCDOT engineers with the flexibility of specifying the level of conservatism to be built into a specific bridge bent design.

17. Key Words Analysis, Database, Design, LRFD, North Carolina, Drilled Shafts, Full Scale Testing, Elastomeric Bearing Pads, Reliability, Resistance Factors, Soil, Bridges	18. Distribution Statement		
19. Security Classif. (of this report) Unclassified	20. Security Classif. (of this page) Unclassified	21. No. of Pages 199	22. Price

Form DOT F 1700.7 (8-72) **Reproduction of completed page authorized**

DISCLAIMER

The contents of this report reflect the views of the authors, who are responsible for the fact and accuracy of the data presented herein. The contents do not necessarily reflect the official views or policies of the North Carolina Department of Transportation. This report does not constitute a standard, specification or regulation.

ACKNOWLEDGEMENTS

The authors would like to thank the members of the NCDOT Structures and Geotechnical divisions who served on the advisory panel for this project. These two divisions are led by Mr. Greg Perfetti, P.E., and Mr. Njoroge W. Wainaina, P.E, respectively. The time, expertise and assistance of NCDOT engineers were invaluable to this project, particularly Mr. Jeff Vones and Mr. Tom Koch, who were instrumental in facilitating the large scale testing. The authors also recognize the significant contributions of the staff and students of the Constructed Facilities Laboratory during the full scale tests, including Mr. Jerry Atkinson, Mr. Jonathan McEntire, Mr. Bill Dunleavy, Mr. Greg Lucier, Mr. Lee Nelson, and Ms. Amy Yonai. Luis Montejo's and Serena Hendrix's assistance with construction of the tests are also gratefully acknowledged. Full scale testing was also supported by S & G Precast who donated the AASHTO Type II girders and loaned lifting equipment. Bearing Pads were provided by Structural Materials, Inc.

\

EXECUTIVE SUMMARY

The geotechnical and structural design of bridge bents generally considers the substructure to be separated from the superstructure, with the superstructure idealized as a series of static loads and moments applied to the bearing locations on the bridge bent. The research work presented in this report aims at understanding and optimizing the design process of drilled shafts bents for safety and functionality. The work included the examination of the design process for drilled shaft bents and the approach used to estimate the shaft length and designate a corresponding point of fixity. Potential areas of conservatism in the current practice are studied through modeling and experimental investigation. Modeling included analysis of three existing bridge case studies with drilled shafts to characterize the impact of the current assumptions on sizing the various components of the bridge bent. Experimental studies included testing full scale connections between the sub- and super-structure including anchor bolts and bearing pads. In addition, resistance factors are developed for drilled shafts, based on load test data from the state's geologic regions, for compatibility with LRFD implementation.

Modeling of three bridge structures were performed within the framework of the computer softwrare MultiPier. SAP 2000 was also used and data indicated that MultiPier model results can be reproduced in the 3-D SAP program. SAP was also used to further verify the equivalent point of fixity method proposed in Robinson et al. (2006) for frame analysis. Analyses results indicated the feasibility of optimized design through reducing the number or size of the shafts while maintaining the same load cases. For example, in one of the bridge cases, seven 54 inch diameter drilled shafts were reduced to shafts of 36 inches while maintaining acceptable demand capacity ratios and lateral displacement.

Full scale testing was performed on a series of substructure-bearing pad connection-superstructure systems. This test included an inverted bent structure, with one 60 ft long deck/AASHTO Type II girder. Observations from the performance testing indicated the first yielding of the longitudinal steel bars in the square and circular piles occurred at approximately 3 in (76 mm) top deflection (at the point of load applicaiton.) The theoretically-estimated first yield displacement was 1 inch (25.4 mm) with the

assumption of a fixed base column. It seems that the test connection provided an additional ductility to the system.

The general trend observed during testing is an increase in the rotational stiffness of the anchor bolt-bearing pad connection with increasing axial load on the pads. As the lateral deformation of the foundation element increases, the overall rotational stiffness tends to decrease. The measured rotational stiffnesses were compared to rotational stiffness values expected based on a static equilibrium model; this model tends to overpredict the rotational stiffness compared to measured values. When the measured rotational stiffness values are implemented in the nonlinear bent models, the overall behavior of the bent depends on the relative ratio of the rotational stiffness of the connection to the stiffness of the individual foundation elements. If the foundation element is much stiffer than the connection, the bent behaves more like a free standing system without rotational restraint. If the connection is stiffer than the foundation element, the system behaves more like a bent with locations fixed against rotation.

The resistance factors for laterally and axially loaded drilled shaft are developed based on test data from sites in North Carolina. Based on Davisson's method of failure load interpretation, the resistance factor for the axial loading condition is estimated as 0.38 at a reliability index of 2.5. If the simulated loads are obtained from the Intermediate GeoMaterial model as well as using methods in the AASHTO bridge specifications, then the results, termed a "combined" approach, show a resistance factor that is equal to 0.57 for the same reliability index. On the other hand, the resistance factors under lateral loading based on 0.5 inches of lateral deflection at the top of the shaft (at the ground level) is estimated as 0.4 at a reliability index of 2.5.

TABLE OF CONTENTS

Table of Tables

Table of Figures

CHAPTER 1: INTRODUCTION

Bridge bents are often supported by shallow foundations, piles, drilled shafts, or a combination of these types of foundation. For example, the foundation for the New Bern Bridge consisted of more than 1000 piles and more than 800 drilled shafts. In general, and as described by NCDOT engineers, the design process for drilled shaft bents proceeds by conducting analysis using a computer program to estimate the load combinations on the bent under various AASHTO loading conditions. Geotechnical analyses of the laterally loaded single shaft are also conducted to estimate the shaft length and designate a corresponding point of fixity. The bent is then modeled using frame analyses to estimate bending moment and shear forces for structural design. For buckling analysis, an equivalent length K-factor of 1.9 to 2.1 is assumed in the longitudinal direction (assuming nearly free head conditions) while a K-factor of 1.2 is used in the transverse direction (assuming translation with no rotation).

Robinson et al (2006) proposed an approach for estimating the point of fixity based on matching the moment and pile top deflection from the geotechnical analysis with a statically equivalent system. Such an approach indirectly accounts for the presence of the soil around the pile, or shaft, from the point of fixity to the ground surface. Robinson et al (2006) also indicated the need for an accurate estimation of the rotational stiffness of typical NCDOT superstructure to substructure connections, as such stiffness affects the assumption of the boundary conditions at the pile, or shaft, top as well as the assumed value of the K-factor. The depth to fixity and effective length factors, as currently evaluated, may not be suitable for all conditions especially when the top boundary condition can be characterized as partially fixed. This can be the case if the bearing pads are capable of transferring moment between the superstructure and the cap beam. Estimation of the rotational stiffness is particularly important in the longitudinal direction for bridges with elastomeric bearings and diaphragms over the cap-beam connecting adjacent girders. In this case, NCDOT currently assumes that the K-factor for effective length is 2.1 (free head).

It seems that the consensus among NCDOT engineers is current bridge bent design can be optimized for cost-effectiveness. In several instances, it seems that the drilled shafts bent designs are overly conservative. Understanding and perhaps quantifying the level of conservatism will empower the NCDOT engineers with the tools to optimize the design process for safety and functionality.

Previous Research

Previous research by the project team on pile bent design criteria was reported by Robinson et al (2006) and achieved the following:

(i) Assessment of the approach used by NCDOT engineers in their design, including limits on deflection and strength as well as effective length factors;

(ii) Development of guidelines to systematically define the point of fixity for frame analysis,

(iii) Development of a proposed method by which uncertainties in effective length calculations and analysis assumptions are minimized through the use of commercial program applications such as MultiPier or SAP 2000; and,

(iv) Establishment of design limit states based on structural aspects and soil response.

Connection Stiffness and K-Factor

To illustrate the influence of connection stiffness on design assumptions, Figure 1 summarizes the relationship between the 'K' factor and ratio of the superstructure and connection stiffness to substructure stiffness (S_{ss}/S_{sub}). S_{ss} represents the combined stiffness of the superstructure (S_s) and the connection (S_c). Expressions for S_s, S_c, and S_{ss} are shown in Equations 1 through 4. An expression for 'K' value is shown in Equation 5.

Equation 1 $$S_s = \frac{3EI}{l}$$ when girders are pinned at end

Equation 2 $$S_s = \frac{4EI}{l}$$ when girders are fixed at end

Equation 3 $$S_c = \frac{d^2}{l\left(\frac{1}{EsAs} + \frac{1}{EpAp}\right)}$$

Equation 4 $$S_{ss} = \frac{1}{\frac{1}{S_s} + \frac{1}{S_c}}$$

Equation 5 $$K = \sqrt{\frac{\pi^2 EIc}{Pcr.lc^2}}$$

where:

E = Elastic modulus of the girder

I = Moment of inertia of the girder

l = Girder Length

E_s = Elastic modulus of steel anchor bolt

A_s = Area of steel anchor bolt

E_p = Elastic modulus of elastomeric bearing pad

A_p = Area of elastomeric bearing pad

P_{cr} = Critical Buckling load

d = Depth of bearing pads

l_c = Cross section moment of inertia of the column

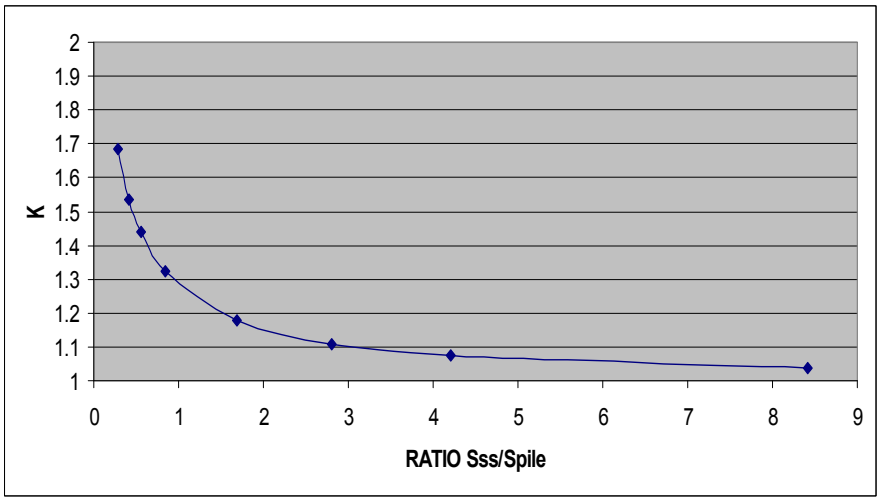

Figure 1. K vs. Stiffness Ratio

The estimation of the connection stiffness, shown in Equation 2, was derived for an elastomeric bearing pad with area (A_p), modulus (E_p) and distance (d) between bearings, as schematically shown in Figure 2. The data in Figure 1 were obtained by conducting an analysis of the system shown in Figure 3 with the following connection assumptions:

Es= 200000 MPa

Ep=300 MPa (AASHTO)

Ap= 0.229x0.559 m^2 (NCDOT E2 TYPE SREB)

As= 2x ø50mm anchor bolts

d= 0.64m (spacing between centerline of pads and center of bolts

h= 0.04m (height of elastomeric pad)

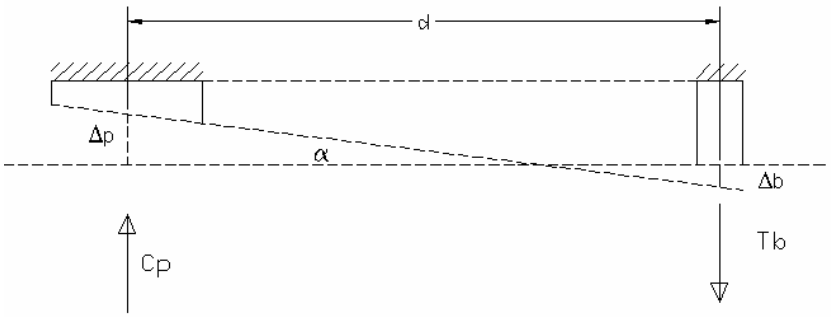

Figure 2. Elastomeric Bearing Pad Stiffness Calculation

Data in Figure 1 indicate that when a diaphragm is used to connect girders with elastomeric bearings pads, the potential exists for a reduced K factor depending on the relative superstructure, connection, and substructure stiffness. While there is high confidence in the analysis regarding the assumption of stiffness, the strength of the connection needs to be evaluated through experimental testing.

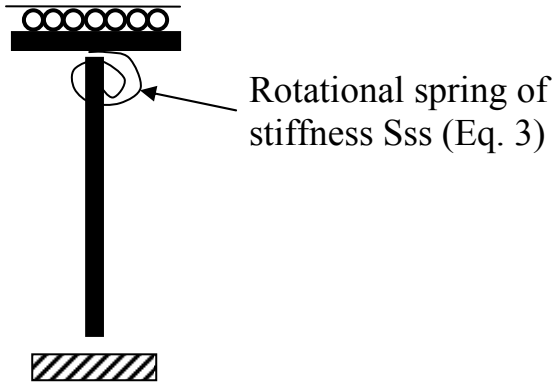

Figure 3. Model analyzed to obtain data shown in Figure 1

Objectives

The research work presented in the report addresses the potential areas of conservatism in the current practice related to bridge bents supported by drilled shafts and piles. An improved set of design guidelines and recommendations regarding super-sub structure rotational stiffness, shaft/pile top boundary conditions, and resistance factors are proposed along with characterizing the impact of the current practice and various design assumptions on sizing components of bridge bents. The research encompasses modeling efforts and an experimental program. Modeling includes analysis of existing bridge case studies with drilled shaft foundations to characterize the impact of the current assumptions on sizing the various components of the bridge bent. An experimental program is performed to evaluate the connection stiffness, and to determine if a given connection has sufficient moment capacity to develop such stiffness. The experimental program includes testing bearing pads in compression and shear to define their index properties. The bearing pads are then tested in a prototype bridge set up to measure their performance under simulated loading. Serviceability limit states are also presented and discussed.

Resistance factors are developed for drilled shafts, based on load test data from the state's geologic regions, for compatibility with LRFD implementation. Work in the report serves to provide a better understanding of the performance of bents supported by drilled shafts under AASHTO loading conditions. Such understanding serves as a tool that

provides NCDOT engineers with the flexibility of specifying the level of conservatism to be built into a specific bridge bent design.

Scope of Work

The work scope is accomplished through a combined structural and geotechnical effort as the issue of load transfer is related to the soil-structure interaction. The work scope includes detailed 3-D finite element analysis using FB MultiPier and SAP 2000, axial and lateral shaft analysis, probabilistic and reliability analyses for the development of resistance factors for drilled shafts, simplified frame analysis for assessment of design recommendations, and an experimental program for the testing of the bearing pads on pilot and prototype scales. Specifically, the report scope includes the following:

(1) **Review of current NCDOT design practices, and other state of the art approaches.** A series of three bridge structures are selected and analyzed to establish a base line description of the current state of practice and study the impace of various assumptions on the design configuration. The selected bridges' design files are reviewed and information is extracted for use in detailed 3-D numerical analyses.

(2) **Development of detailed 3D analysis models of drilled shaft bents: benchmark for comparison and development of design guidelines for current practice.** This task provides modeling of the bridge structure within the framework of MultiPier suite of programs for both structural and geotechnical analyses. A specific emphasis is placed on drilled shaft analysis and on automated generation and application of AASHTO load cases. In addition, modeling with SAP 2000 is performed to validate the results of MultiPier. Analytical modeling with both programs is performed and results are compared with those obtained from current practice to explain issues related to conservatism and impact of current design assumptions.

(3) **Experimental testing of Substructure to Superstructure Connection for Assessment of Rotational Stiffness Parameters**. This testing provides a measurement of the rotational stiffness of typical NCDOT superstructure to substructure connections.

As mentioned earlier, this directly impacts the assumption of the boundary conditions as well as the K-factor. If the connection can accommodate some level of moment transfer, then the current design assumptions are revisited. The experimental program includes compression and shear testing of bearing pads typically used by NCDOT in girder-cap beam arrangements. Prototype testing includes 42 tests on three different foundation configurations: (1) Pre-stressed concrete pile; (2) Steel tube pile; (3) H-pile. Each of these is tested with two different elastomeric bearing pads. These are Type V bearing pads for a steel superstructure, and Type VI pads for a concrete superstructure. The connection is tested simulating field conditions of NCDOT bridges. Two AASHTO Type II girders made continuous with a diaphragm are utilized in the testing program. The two different sets of bearing pads are used with the three different pile configurations. The axial load is varied in the bearing pads and test piles/shafts while lateral loading is applied in one-cycle increments of displacements.

It should be noted that, in the transverse direction, NCDOT currently assumes a K value of 1.4, which indicates the fixity of the connection. Such an assumption seems to be valid in that direction, and no investigation is focused on the behavior in the transverse direction. Furthermore, POT and TFE bearing pads are not included in this investigation as NCDOT does not use a diaphragm to connect adjacent girders with these types of bearings. Without a diaphragm, such connections will not transfer moment, and a K factor of 2.1 is deemed appropriate in the longitudinal direction.

(4) **LRFD Implementation.** Development of resistance factors based on drilled shaft testing data from North Carolina sites is performed. The factors are implemented using FB MultiPier. The results in terms of design length of the shafts are compared with current practice. Key differences are highlighted to assist in the transition of NCDOT engineers to AASHTO LRFD design approach.

(5) **Development of Limit States**. Currently, NCDOT practice utilizes a limit of one inch lateral displacement to assess shaft performance and decide upon the shaft length. Utilizing the analytical models developed in Task 2 and the results of the experimental

work defining the rotational stiffnesses, more rigorous serviceability limit state formulas are provided. These account for soil stiffness, pile/shaft to bent cap connection, bent cap stiffness, and superstructure details.

(6) **Development of Recommendations for rigorous analysis and design approaches** Improved design and analysis techniques are proposed. A series of conclusions and possible design procedures for current and future applications are suggested.

Report Layout

This report is organized as follows:

- Chapter 2 reviews appropriate studies from the literature and summarizes the results of the NCDOT pile bent project (Robinson et al., 2006).

- Chapter 3 presents the results of the nonlinear and frame analyses for the three drilled shaft bent bridge case studies provided by NCDOT.

- Chapters 4 and 5 present the experimental set-up and results for the index and performance testing of the elastomeric bearing pads and the connection tests for the superstructure-connection-substructure system.

- Chapter 6 reduces data and results from chapters 3 and 4 for application to NCDOT projects.

- Chapter 7 summarizes the method and data used to develop resistance factors for geotechnical drilled shaft design and provides recommendations for the values of such factors.

- Chapter 8 summarizes the report and provides recommendations, design guidance, and conclusions.

CHAPTER 2: LITERATURE REVIEW AND BACKGROUND

The design of drilled shaft bents should be viewed in the context of the larger bent-type substructural elements, in general. Similarly, the bent is a single element in the larger bridge system that includes the substructure elements, abutments, bearing pad connections, girders and a deck. This chapter will include a summary of previous work on the response of bridge bent foundations and point of fixity, as well as selected work performed by others on the subject.

Pile Bent Project

In 2006, a final report was issued for the NCDOT sponsored Project 2005-19, "Pile Bent Design Criteria." Some of the work performed for the current study builds off the results presented in the 2006 report. A brief review of the approach and significant findings are presented here; the interested reader is referred to the original report for further details.

Pile bents, like drilled shaft bents, are substructure units constructed by installing one or two rows of driven piles, then connecting them with a cast-in-place concrete bent cap. Once the abutments and bents are constructed, girders are placed to ultimately support the bridge deck. Most pile bents in North Carolina have elastomeric bearing pad placed at support points of the girders.

In general, NCDOT pile bent design is performed using frame analysis. In this case, the Geotechnical Unit estimates the foundation size from axial geotechnical analyses, as well as a "Point of Fixity" from single pile lateral analyses; buckling considerations are included using estimated lateral and axial loads. The point of fixity allows the designer to idealize the pile-soil system as a fixed base cantilever column without additional soil resistance. This cantilever column then forms the basis for elastic frame analyses, which in turn can be used to verify the size and reinforcement requirements for the bent cap given a superstructure design. The elastic frame also verifies if piles are sufficient from a structural standpoint.

The described frame analyses approach has been traditionally performed using the software program Georgia Pier (Georgia DOT, 1994). As discussed by Robinson et al. (2006), the approach implemented with the use of Georgia Pier has a few shortcomings. Figure 4 highlights three challenges when modeling is performed within Georgia Pier versus a more robust program such as SAP (Computers and Structures, Inc. 2004). An additional limitation with the use of Georgia Pier is the inability to perform LRFD analyses, given the recent federal requirement for LRFD design implementation. With those factors in mind, the Pile Bent Project looked at design details of four representative types of substructure elements: a steel H-Pile bent, a steel pipe pile bent and two prestressed concrete pile bents. These were originally designed by NCDOT using Georgia Pier and were then modeled using more rigorous finite element methods as implemented within the SAP and MultiPier (BSI, 2004) programs.

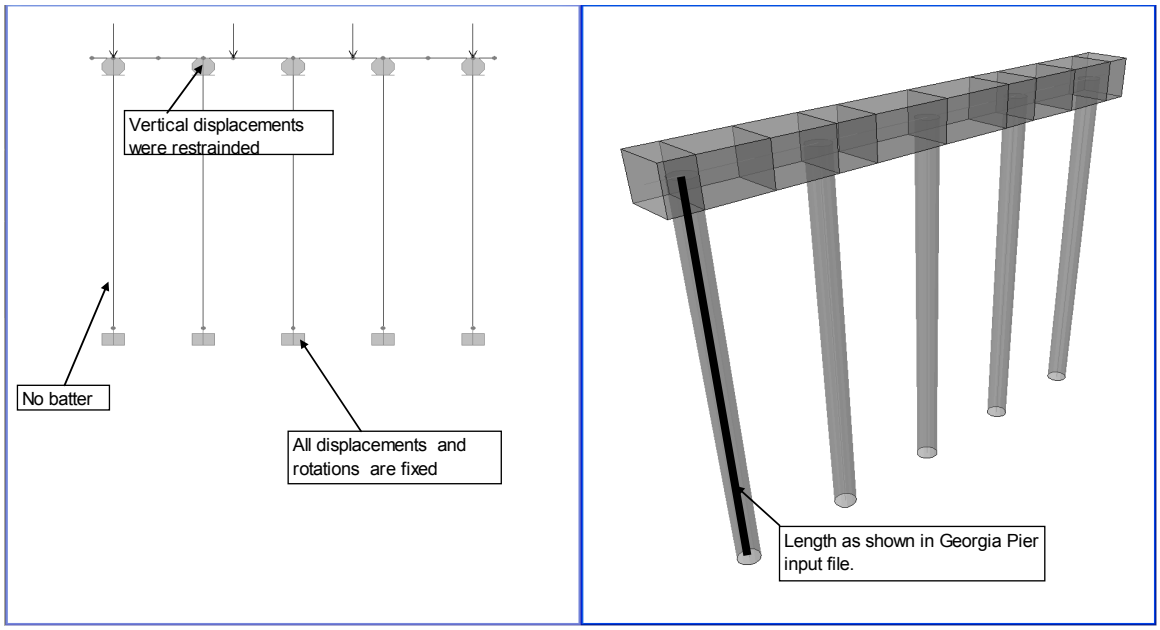

Figure 4. SAP Model to mimic Georgia Pier using NCDOT Point of Fixity, Robinson et al. (2006).

MultiPier, SAP, and Georgia Pier

Models of the four pile bents, from representative bridge projects, were built in two separate programs: MultiPier and SAP. MultiPier, a software package designed specifically for bridge substructure design, allows the user to model stand-alone pile bents or bridges connected by a superstructure with nonlinear material models for the

bent cap and the piles. The lateral and vertical resistance from the soil can be modeled using several non-linear relationships depending on the soil or rock type. Up to nine load cases can be input in each simulation, including the various load groups required by AASHTO. Figure 5 shows a sample MultiPier model for Robeson County Bridge as generated by the program.

On the other hand, SAP is a general purpose structural analysis program that also allows nonlinear material models for all structural elements. Unlike MultiPier, SAP requires direct numerical input of the P-y and t-z curves to model the pile-soil response. Figure 6 shows a representative SAP model.

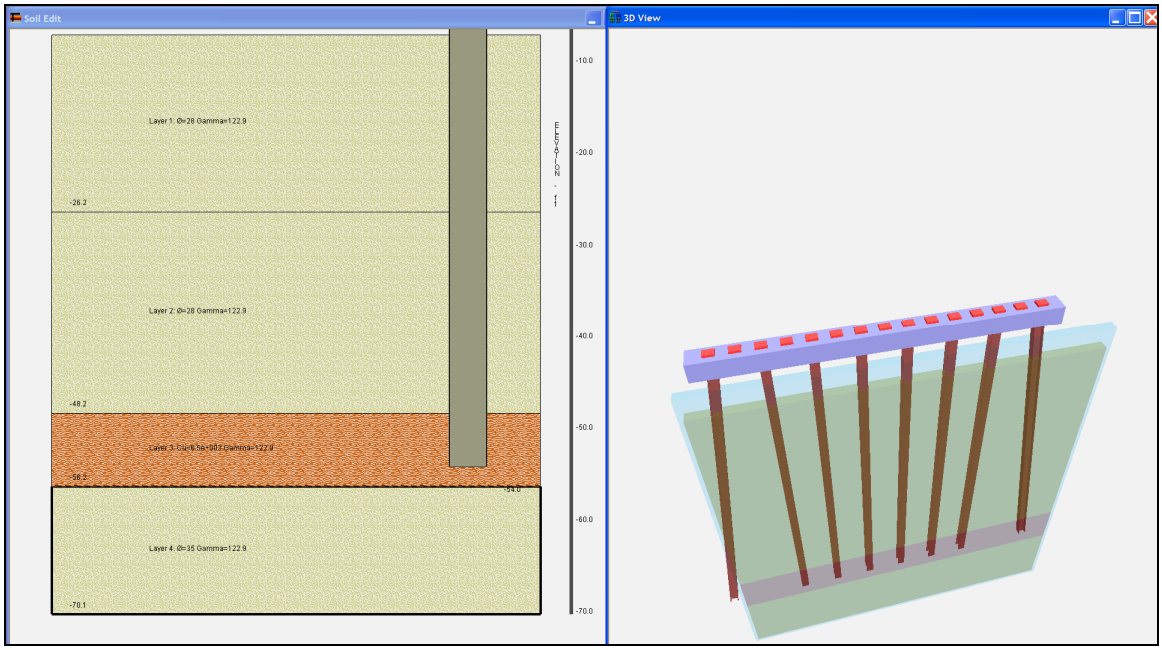

Figure 5. Robeson County Bridge MultiPier Model from Robinson et al. (2006)

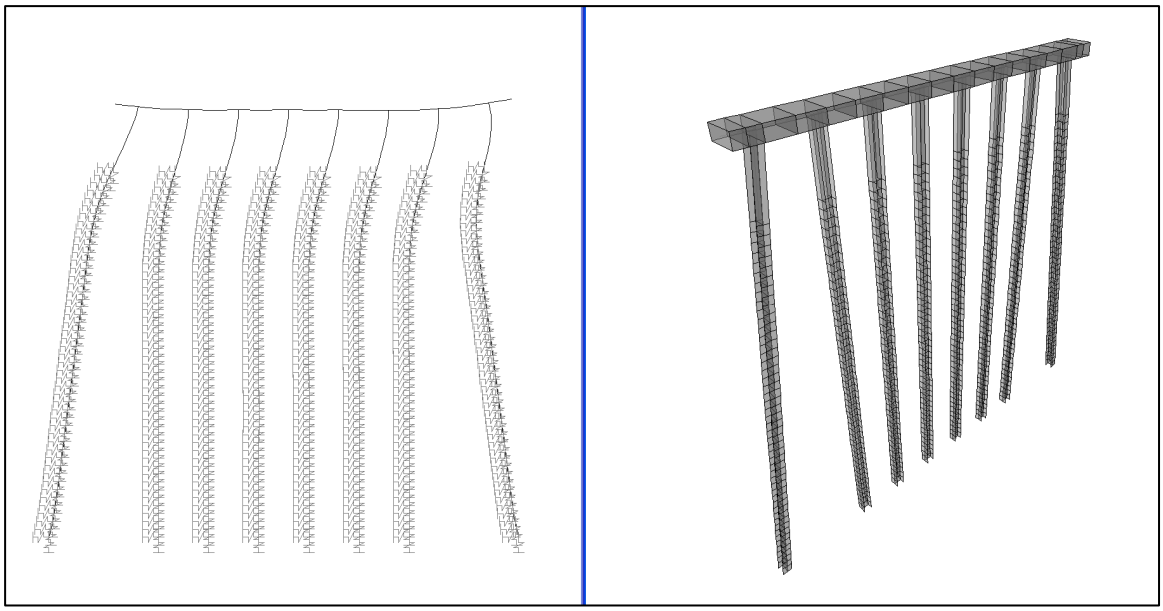

Figure 6. Robeson County Bridge SAP Model from Robinson et al. (2006)

In Robinson et al. (2006), the SAP and MultiPier results were compared, and it was determined that the two programs produced comparable results for driven pile bents when similar modeling assumptions were made. MultiPier was then used to evaluate the possibility of utilizing smaller foundation dimensions or fewer piles for the support of the analyzed bridge cases. In SAP, models were built to evaluate frames with column lengths as obtained from the NCDOT's current point of fixity approach and from the equivalent model discussed in the next section.

Equivalent Model

The methods typically used to estimate a point of fixity from single pile lateral analysis involve running the analysis for a given maximum expected axial, shear, and moment loading combination that is applied to the pile top, then choosing the point of maximum negative moment below the pile top, the point of maximum negative displacement below the pile top, or some other indicator of fixity. The final selection of the location of a point of fixity is however determined by the geotechnical engineer's judgment.

Robinson et al. (2006) noted that the point of fixity determined by the existing methods did not necessarily produce similar moments and displacements in the pile elements when a nonlinear soil-pile model was run in MultiPier or SAP. Indeed, in the four cases

investigated, the moments generated in the pile section were always greater than those generated by the nonlinear model. This leads to the conclusion that the existing point of fixity determination method may be overly conservative.

Robinson et al. (2006) proposed an approach to reduce the conservatism. The overall method is summarized in Figure 7. An equivalent length (L_e) is determined by finding the maximum moment (M_{max}) generated when a lateral load (V) and axial load (P) are applied in a single pile lateral analysis, with a pile head free to translate and rotate and a pile head fixed against rotation but free to translate. The "free head" and "fixed head" condition are assumed for the longitudinal and transverse response of the bridges, respectively. The equivalent length approach yields similar moments and lateral deflection as those generated in more rigorous analysis by numerical methods under the maximum applied design loads. If the same point of fixity is used, however, under lower applied lateral loads, the moment will be overpredicted compared to a nonlinear analysis with soils, i.e. the equivalent model only predicts moments properly at the load for which it is calculated. From a structural analysis standpoint, this should not be an issue as the maximum expected moments and shears are computed correctly.

Lateral pile analyses will calculate a maximum lateral deformation (Δ_t); axial analyses will estimate a vertical deformation (Δ_z). If deformations are also required from the frame analysis, inertial reduction factors for lateral deflections (α) and area reduction factors for vertical deflections (β) are required. These values are calculated using the elastic modulus of the pile materal (E_p) and the area and moment of inertia of the pile section (A_p and I_p, respectively).

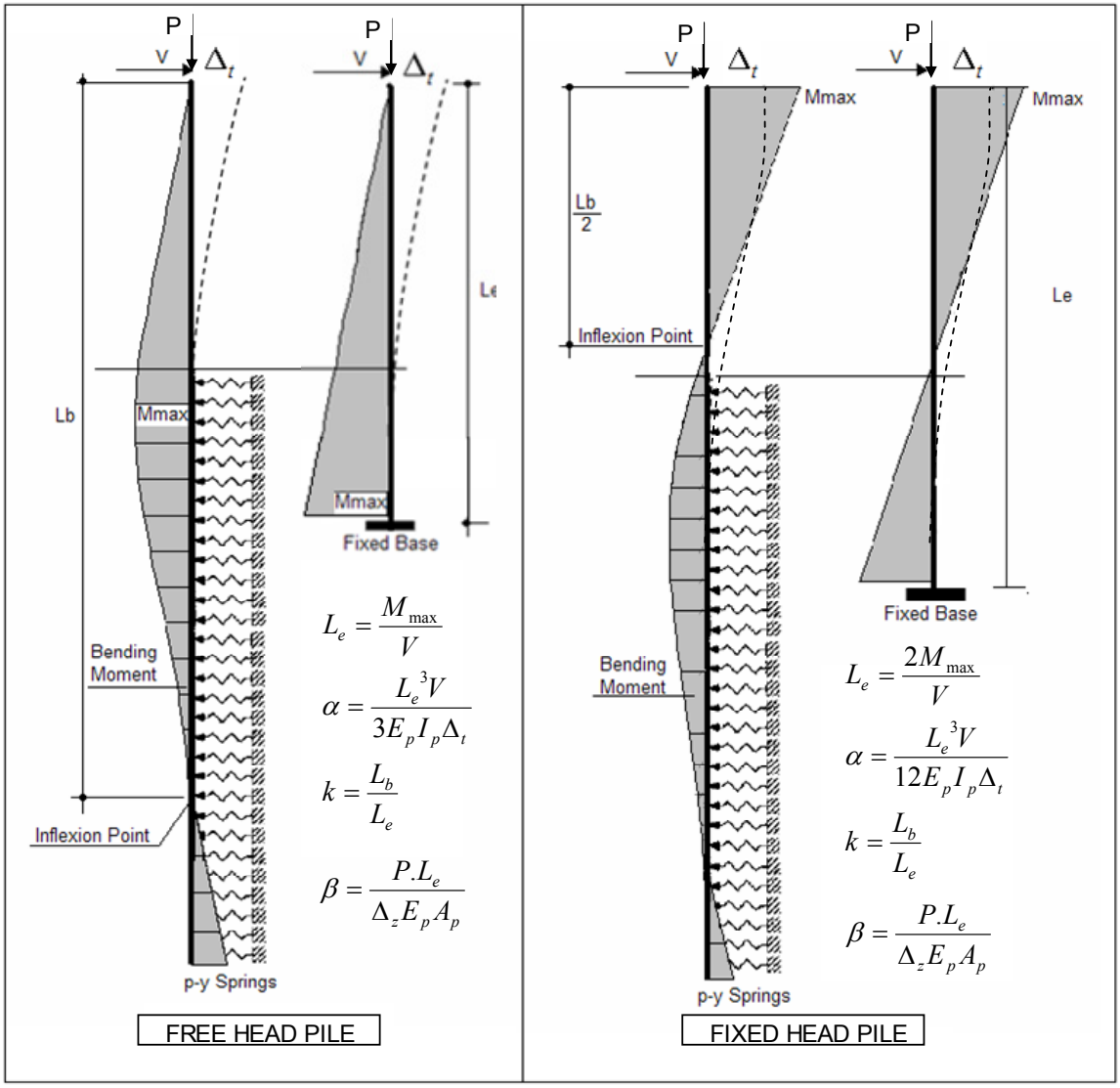

Figure 7. Equivalent Model Parameters for Free (Longitudinal) and Fixed (Transverse) head conditions (from Robinson et al., 2006)

The challenge of the method summarized in Figure 7 is the requirement of two different effective lengths, or restraints, in the longitudinal and transverse directions. Many frame analysis programs allow for a single pile length, but not all allow the addition of very stiff springs to prevent translation in a single direction. SAP does allow for this addition to occur, and a sample equivalent frame is shown in Figure 8. Using the equivalent model based on a properly loaded single pile lateral analysis, much of the behavior of the full nonlinear analysis can be captured in a simple elastic frame analysis approach as proposed by Robinson et al (2006).

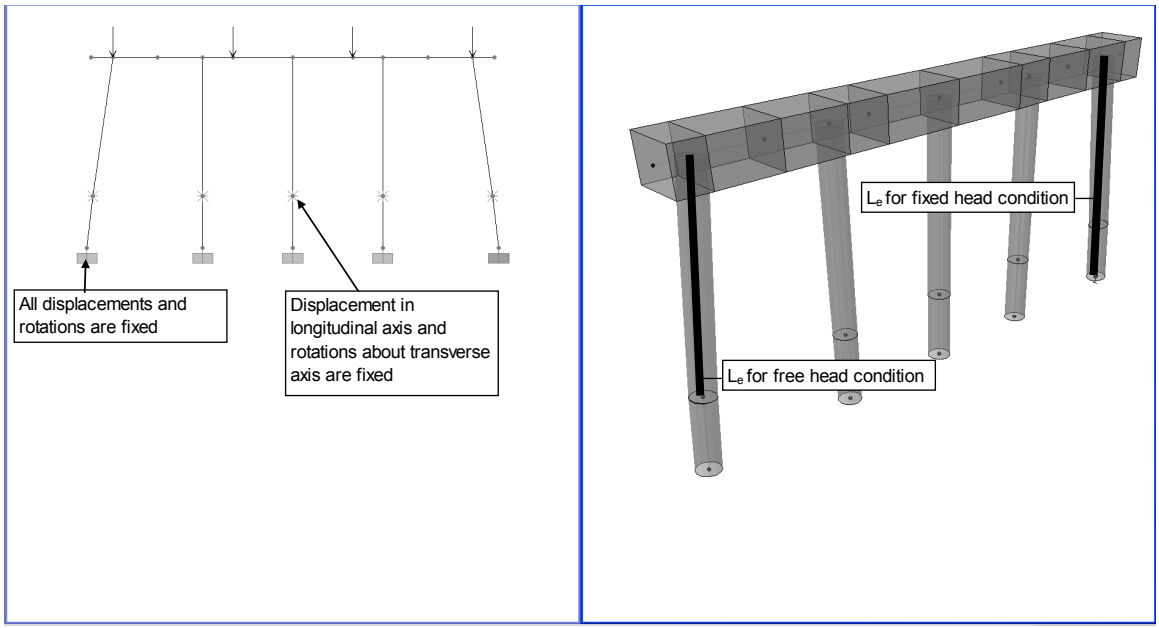

Figure 8. Frame model of Northampton County Bridge using equivalent lengths from Robinson et al. (2006)

The equivalent model, described above, allows the designer to better predict the demands on the overall pile bent structure. While not as versatile as the non-linear soil pile analyses performed in SAP and MultiPier, the equivalent frame analysis allows the designer to capture some of the nonlinear response while maintaining some of the current analysis practices in place at NCDOT.

Limit States

The limit states used by NCDOT were investigated in Robinson et al. (2006). For piles and shafts design, the size of the foundation element is often dictated by the lateral displacement under the assumed lateral load. In NCDOT's case, the lateral displacement of the pile has been limited to one inch. Several studies on the matter were examined, including Moulton's 1986 field survey of 314 bridges from 39 states. Damage to some part of the bridge structure was recorded, as was any observed movement of substructures. Moulton's general observations are summarized in Table 1.

Table 1. Movement Limits for Bridges (from Moulton, 1986)

Direction of Movement Magnitude most likely to cause intolerable damage	
Vertical Only	4 inches
Horizontal (Lateral) Only	2 inches
Both Horizontal and Vertical	
Vertical Component	2 inches
Horizontal Component	1 inch
Angular Distortion (Differential Vertical Displacement : Span Length)	0.004
Multispan structures have a higher frequency of severe structural damage due to foundation movements than single span bridges.	

Robinson et al. (2006) proposed mathematical models to estimate the loads required to cause expansion joints between adjacent bridge spans to close. These models required estimates of the abutment and substructure stiffnesses, as well as the rotation stiffness of the sub- to super-structure connection. These will be reviewed and discussed further in Chapter 6.

Drilled Shaft Bent Design

Drilled shaft bents are conceptually similar to driven pile bents, although the deep foundation elements are different. Drilled shaft bents tend to be selected in the following cases: where lateral loads are significant enough that the cross section and stiffness of a large diameter drilled shaft are required, where lateral resistance must be developed by socketing the shaft into weathered or crystalline rock, or where dense soil strata above the expected required tip elevation make installation of driven piles difficult or impossible without extraordinary secondary measures. Drilled shaft bents differ from pile bents in that the deep foundation elements must be sized for each bridge, instead of selecting from a range of pre-designed or manufactured driven pile types. Thus, drilled shaft design requires sizing of the reinforcement scheme for the shafts.

Geotechnical Design

As for driven pile design, the Geotechnical Unit typically estimates the size and length of the drilled shaft to be installed by performing axial and lateral analyses. The lateral and axial loads can be either assumed or preliminary loads are received from the Structures and Hydrology Units and used in the analyses.

For drilled shafts, geotechnical axial ultimate side resistance is determined in both the soil and in weathered rock. Side and toe resistance in soil profiles are estimated using the procedures outlined in Section 10 of AASHTO (2006) for cohesive or cohesionless soils. These methods are similar to those found in O'Neill and Reese (1999). In weathered rock strata, ultimate side resistance is often assumed to be between 4 and 8 kips/ft^2 while ultimate toe resistance is assumed between 90 and 120 kips/ft^2. These values come from a combination of the experience of the designer and knowledge of the formation from which the weathered rock was produced. These values have been verified in the past by NCDOT and others using field load tests.

Geotechnical lateral resistance is determined using P-y analyses, such as those found in LPILE (Ensoft, 2004), or MultiPier. Design for soil strata is the same as for pile bents. In weathered rock, based on the work of Gabr et al. (2002) in a project funded by NCDOT, the weathered rock is modeled using a stiff clay model with elevated strength properties, or a weak rock model with low unconfined compressive strength values for the rock. In crystalline rock, a Vuggy limestone model with unconfined compressive stresses in the range of 3 kips/in^2 is used These P-y models are selected, in part, based on pragmatism: they are available in LPILE, which is the DOT's current single pile lateral analysis program. Once the drilled shaft is sized based on lateral capacity considerations, the geotechnical unit determines a point of fixity, which is transmitted to the Structures unit along with the Geotechnical unit's other recommendations.

Structural Design

Structural design of drilled shaft bents is similar to those used for pile bent design. Currently, the frame analysis program used is Georgia Pier, although the need to adopt LRFD based design has caused the consideration of RC-Pier (LEAP Software, 2006). The latter program generates live loads due to an AASHTO truck loading on the bridge as a part of the software suite; in Georgia Pier this was done separately. The live and dead loads from the superstructure design and the extreme event loading from wind, stream pressure, vessel impact, and others are then entered into the program to generate the loads in the bent cap and the individual piles. Once the demand on the structural

elements is calculated, the required reinforcement of the drilled shaft section and bent cap are determined and compared to the minimum reinforcement requirements imposed by AASHTO. It should be noted that both RC Pier and Georgia Pier assume the bent is free standing and not necessarily restrained against displacement by the superstructure.

Contribution of Bearing Pad Connections

The geotechnical and structural design of bridge bents considers the substructure to be generally separated from the superstructure, with the superstructure idealized in the bent design as a series of static loads and moments applied to the bearing locations on the bridge bent. Particularly in the bent's longitudinal direction, the current design methodology assumes implicitly that the bent can translate any amount if loaded in that direction. While the point of fixity determination is based on limiting the single pile horizontal deflection to one inch, there is no guarantee that this one inch maxima is: (i) correctly modeled by the traditional point of fixity determination or (ii) acceptable for the bridge as a whole and the superstructure in particular. With these conditions in mind, the true condition of the super to sub structure connection is questioned.

Attention is thus paid to the bearing pads. If the anchor bolt/sole plate/elastomeric bearing pad system can transfer some moment and load between the sub and superstructure, then the condition of the bent is likely not simply "free" or "fixed." The literature was reviewed to examine other studies on elastomeric bearing pads in general and those supporting superstructures with diaphragms in particular.

Bearing pad testing methods were examined and developed by Yura et al. (2001) for determination of shear modulus, as well as for measuring the effect of creep, low temperature and aging on pad performance. Muscarella and Yura (1995) also investigated a number of flat and tapered elastomeric bearing pads from different manufacturers. Through testing, they measured the compressive, shear, and rotation stiffness of the individual pads.

A number of researchers have looked at the effect of bearing pads on the response of a larger system. Abendroth et al (1995) studied the diaphragm effectiveness in prestressed-

concrete girder bridges. They tested a full scale model bridge with different intermediate diaphragm types and locations subjected to vertical and horizontal loads. The girders were supported on elastomeric bearing pads. The results from the tests were then compared with finite element models of the bridge. They determined that the vertical load distribution is independent of the type and location of the diaphragms used in testing. On the other hand, they concluded that the horizontal load distribution is dependent on the type and location of the diaphragms.

Yazdani et al (2000) studied the effect of bearing pads on the response of precast prestressed concrete bridges. They concluded that performance characteristics of AASHTO precast bridge I-beams are slightly enhanced by restraining action from laminated neoprene bearing pads. These effects increase at cold temperatures due to stiffening of the pads, but such increases are minimal. Also, they found out that the horizontal restraint forces transmitted by the bearing pads to the substructure were small in general, within AASHTO limits for the bridge studied.

Eamon and Nowak (2001) conducted research on the effect of secondary elements such as barriers, sidewalks and diaphragms on bridge structural system reliability considering moment capacity. They determined that these elements can affect the live load distribution and increase the bridge loading carrying capacity. The use of typical combinations of secondary systems has varying effects on girder reliability. In addition, the use of diaphragms was shown to be more effective for enhancing the load distribution for bridges with wider girders spacing. In this case, the effect of secondary elements was more pronounced on live load distribution, when the span length was increased.

Green et al (2004) modeled a Florida Bulb Tee 78 precast concrete bridge girder, which is widely used in the state of Florida, to determine the effect of intermediate diaphragms and bearing stiffness on the performance of prestressed AASHTO type bridge girders. Findings from their study indicated that the presence of intermediate diaphragms stiffened the precast prestressed girders and reduced the maximum girder deflection.

Also, increasing bearing pad stiffness led to stiffening of the girders, but this was generally small in magnitude.

Yoon et al (2004) studied the behavior of sole plates in elastomeric bearing systems supporting steel box and/or plates girders. In these types of girders, the bottom flange and the sole plate may act together in dispersing concentrated stresses. The sole plates are important to resist compression and flexural stresses due to bending of the girder and local stress concentration in the diaphragm area. The authors developed several finite element models of the elastomeric bearing system (bearing pads, sole plates, diaphragm and girders). It was found that the sole plate thickness affects the stresses in both the bottom flange immediately under the diaphragm and in the elastomeric bearing pads. Therefore, the sole plate needs to have an appropriate thickness to control the stress concentration in the bottom flange of the girder and to limit stresses in the elastomeric bearing pads.

In general, previous studies have focused on a particular component of the bearing-supported connection systems. Nearly all of the researchers have studied the diaphragm and bearing pad behavior related to load distributions and girder deflection. No one, to the authors' knowledge has studied the moment capabilities of bearing-supported connection systems and tested all the elements of the connection together including the pile or substructure elements.

Load Resistance Factor Design

The shift in practice by state departments of transportation from Load Factor Design (LFD) to Load Resistance Factor Design has not been without controversy. Over the course of this project, the geotechnical resistance factors and the entire chapter on geotechnical design originally printed in AASTHO (2004) were completely revised in the Interim standards of 2006. Even with those changes, strong discussions for and against the prescribed values of resistance factors, in particular, and LRFD design techniques in general are still on-going on at national conferences and committee meetings. With that

in mind, deriving load factors for axial and lateral resistance of drilled shafts in North Carolina soils was undertaken in preparation for the transition.

In 2002, Rahman et al. used data collected from the NCDOT archives to propose resistance factors for axial capacity for driven piles. Parts of this work also resulted in the dissertation work by Kim (2002). These studies compared three geotechnical design methods for driven piles to load capacities from static and high strain dynamic load tests. The result was resistance factors for a variety of geologic situations around the state. Most of the tests were in the coastal plain geologic region.

The resistance factors for axial compressive resistance of drilled shafts outlined in AASHTO (2006) range from 0.40 to 0.60 with a limit of 0.70 depending on the method used to estimate the capacity. Capacities estimated from static load tests in compression, which formed the basis for estimating the resistance factors, are dependent on the number and variability of the sites in which the shafts are installed. Geotechnical resistance for horizontal loading has a recommended resistance factor of 1.0.

Since a framework for evaluating resistance factors is in place for North Carolina soils based on load testing, there is also a need for a similar framework for evaluating resistance factors for drilled shafts based on load tests. However, static load tests for drilled shafts are often cost prohibitive. As such, other methodologies using cast-in-place hydraulic load cells (Osterberg, 1999), explosive driven reaction weights (Mullins et al., 2002) or dropped rams (Robinson et al., 2002) are increasingly popular for estimating the axial and sometimes lateral capacity of drilled shaft foundations. While this report will not compare these methods' efficacy at estimating the loads that would be measured from a conventional static load test, the results from some of these tests will be used to develop resistance factors and calibrate them to existing AASHTO and other design methods typically used by NCDOT.

With the previous NCDOT work, state of practice, and other researchers efforts in mind, the modeling effort for the three bridge case studies can begin. Chapter 3 summarizes the assumptions, modeling efforts and results obtained using the above information.

CHAPTER 3: BRIDGE MODELS AND ANALYSIS RESULTS

Modeling of the bridge structure with shaft bents within the framework of SAP and MultiPier is performed and results are compared with those obtained from current practice to explain issues related to conservatism and design assumptions. The plans and design documents from three bridges were submitted to the project team to analyze using detailed 3-D models in SAP2000 and MultiPier. The bridges were selected to capture a variety of drilled shaft sizes and configurations, superstructure types, and soil conditions. A brief summary of each bridge follows.

Rowan County Bridge, Project R-2911D

The Rowan County Bridge R-2911D allows US 70 to pass over a Norfolk Southern Railroad line. The bridge replaced a structure that was standing at the site prior to the more recent road improvement project. Interior bents were removed and the new bridge consists of a single span with two end bents supported by drilled shafts. One end bent is shown in Figure 9. The abutments also include an anchored tieback wall system to minimize the abutment slope down to the railroad property. While the tieback wall will provide some additional support, NCDOT engineers decided to design the end bents as if they were free-standing bents on drilled shaft that do not rely on the soil resistance behind the tieback walls. Drilled shafts were chosen over driven piles in part due to the magnitude of loads imposed by span length, but also to minimize vibration and disturbance to the active railroad track.

General Information

Designed: 2004

Spans: 1 (170 feet)

Interior Bents: None

End Bents: 2

Shaft Type: Four 48-inch diameter (nominal) drilled shafts, reinforced with 20 #11 bars and spaced 24 feet apart. One HP12x53 brace pile is placed for the wing wall.

Free Shaft Length: None

Bent Cap: 83.5 ft long by 54 inch wide by 60 inch deep (minimum) Class A concrete beam with wing walls

Superstructure: Five steel girders, AASHTO M270 Grade 50W material. Girder flanges: 20 in wide x 2 in thick. Girder web: 77 inches high by 5/8" thick
Super/Substructure Connection: Five elastomeric bearing pads, 3-13/16 in. thick, Type VI (one end bent fixed, one end bent expansion)

Figure 9. Rowan County bridge, under construction in 2005

Geotechnical Summary
For this bridge case study, the westernmost end bent was modeled. The soil profile at this bent was summarized in boring B1-A LT LN. This soil boring shows the ground water level to be approximately 18 feet below the surface. Up to nine feet below the ground surface, medium stiff silty sandy clay was reportedly encountered. The SPT N-value for this layer was 5 blows per foot. Next, medium stiff to stiff micaceous clayey sandy silt was encountered from 9 to 20 feet, with N values averaging 8 blows per foot. Medium to very dense silty sand was reported from 20 to 31 feet, with N values of 19 and 58 blows per foot. Weathered rock with N values in excess of 100 was observed between 31 and 40.5 feet, where the boring terminated.

As designed, the shafts were to terminate in the weathered rock. Based on the project data, capacities along the shaft and at the toe were estimated for the preliminary analysis using drilled shaft t-z and Q-z models originally proposed by O'Neill et al. (1996) for the weathered rock and by BSI (2006) for drilled shafts in sands. P-y models for lateral shaft

resistance in sand were developed by Reese et al. (1974), while the weathered rock model utilized the limestone model was developed by McVay (2004).

Lateral group analysis considered the spacing between the shafts, which for this bridge was 24 feet, or six times the four foot diameter of each shaft (6D). Thus, the P-y multipliers were set to 1. For the 6D spacing, axial group capacity was considered to be unaffected.

Equivalent Model

After a single shaft lateral analysis was performed in MultiPier using the same soil profile used for the full bent analysis, the equivalent model parameters were calculated based on the proposed procedure by Robinson et al. (2006). The equivalent model parameters, including effective length, are shown in Table 2. These effective lengths were then input into a SAP frame without soil and are presented in the next section as "SAP—Equivalent."

Table 2. Equivalent Model Parameters for Rowan County Bridge

EQUIVALENT MODEL PARAMETERS				
Head	Le (ft)	α	B	K
Fixed	36.3	0.92	0.28	1.1
Free	22.9	0.23	0.28	2.1

Analysis Results—SAP and MultiPier

Models of the bridge pier were created in both MultiPier and SAP. Figure 10 shows the MultiPier model. The input files can be found in the Electronic Appendix and results are summarized in Table 3, Table 4 and Table 5 for axial, and lateral responses, and capacity demand, respectively. These tables compare specific critical load cases by considering the predicted maximum moment, shear and axial loads in a particular drilled shaft foundation. The ratio of the demand placed on the shaft due to the AASHTO load cases to the capacity of the shaft based on the combined axial force and moment capacity is also shown.

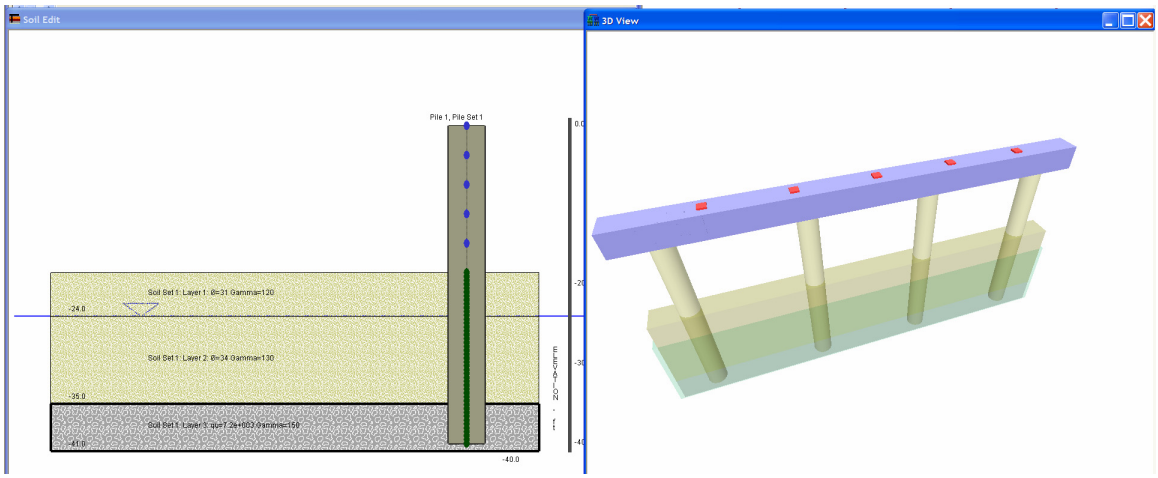

Figure 10. MultiPier Model--Rowan County

Table 3. Rowan County Nonlinear Analysis Results: Maximum Axial Load Case

Model	Maximum Moment (kip-ft)	Maximum Axial Force (kips)	Maximum Shear Force (kips)
SAP—Nonlinear	541	315	21.9
MultiPier	547	306	24.5
SAP—Equivalent	476	306	19.6
AASHTO Group	AASHTO Group I Shaft 4, Demand Capacity Ratio=0.175		

Table 4. Rowan County Nonlinear Analysis Results: Maximum Lateral Load Case

Model	Maximum Moment (kip-ft)	Maximum Axial Force (kips)	Maximum Shear Force (kips)
SAP—Nonlinear	605	257	28.7
MultiPier	529	249	28.7
SAP—Equivalent	573	253	27.7
AASHTO Group	AASHTO Group II Shaft 4, Demand Capacity Ratio=0.171		

Table 5. Rowan County Nonlinear Analysis Results: Maximum Ratio of Demand to Capacity

Model	Maximum Moment (kip-ft)	Maximum Axial Force (kips)	Maximum Shear Force (kips)
SAP—Nonlinear	510	274	22.8
MultiPier	582	290	29.6
SAP—Equivalent	647	298	30.5
AASHTO Group	AASHTO Group III Shaft 4, Demand Capacity Ratio = 0.187		

Table 3 through Table 5 shows reasonable agreement between the two models with full soil models (SAP—Nonlinear and MultiPier). The SAP model using the equivalent point of fixity method, as described by Robinson et al. (2006), also produces a reasonable match compared to the MultiPier results. Differences between the two nonlinear models could be due to the way P-y and t-z models are generated in MultiPier (at each discrete node) versus SAP (linearly interpolated with depth between the P-y or t-z curve at the top of a layer and the P-y or t-z curve at the bottom of a layer.)

Analysis Results—Optimization

After the MultiPier models were verified by SAP, MultiPier was used to optimize the design by reducing the size or number of the shafts in the bridge bent. The bent was constructed using four 48-inch diameter drilled shafts with a reinforcement ratio of 1.6%. First, the four 48-inch shafts were replaced by 42, 36 and 30 inch shafts with reinforcement ratios of 2%. Finally, the number of 48-inch shafts was reduced from four to three, with the 1.6% reinforcement ratio remaining constant.

A summary of the results is shown in Table 6. The values shown are the maxima over all AASHTO load cases analyzed (Groups I, IA, II, and III). As expected, the ratio of the demand placed on the shaft to the capacity of the shaft, based on axial loads and moments applied, steadily increases as the shaft diameter decreases. Similarly, transverse, longitudinal and vertical displacements steadily increase as shaft diameter decreases.

Table 6. Rowan County Alternative Shaft Configurations

	48 in shaft, 1.6% reinf.	42 in. shaft, 2% reinf.	36 in shaft, 2% reinf.	30 in shaft, 2% reinf	3-48 in shafts, 1.6% reinf.
Demand/Capacity Ratio (Shafts)	0.192	0.352	0.423	0.539	0.397
Displacement, transverse (Shaft top, in)	0.13	0.16	0.24	0.41	0.24
Displacement, longitudinal (Shaft top, in)	0.26	0.36	0.58	1.17	0.38
Displacement, axial (Shaft top, in)	0.27	0.34	0.46	0.67	0.49

Robinson et al. (2006) compared relative cost savings of reducing the number or size of foundation elements using NCDOT bid averages (NCDOT, 2004). For drilled shafts, there is tremendous variation in the bid average for drilled shafts in soil and in rock. For example from the 2005 NCDOT bid averages (NCDOT, 2005), installing a 48 inch drilled pier in soils ranged in cost from $189/linear foot to $752/linear foot. Drilling in rock (all size shafts) ranged from $686 to $2750/linear foot.

This wide variation in cost certainly reflects differing site conditions, as well as the contractor's available drilling equipment. Such wide variation, however, makes determining possible cost savings problematic. Thus, cost savings will not be estimated in this report.

Wake County Bridge, Project R-2809D

This case study analyzed the bridge that spans Richland Creek on the NC 98 bypass between US 1 and US 1A. The concrete girder bridge is supported by three interior drilled shaft bents and two end bents with vertical and battered HP 12x53 (HP 310x79) driven piles. A photograph is shown in Figure 11.

Figure 11. Wake County Bridge R-2809D, 2006.

General Information

Designed: 2003

Spans: 4 (100.8, 98.4, 98.4 and 100.8 feet)

Skew: 130^{o}

Interior Bents: 3

Shaft Type: Seven 4.5 ft (1372 mm) diameter drilled shafts, spaced 18.3 ft (5.58 m)

Free Shaft Length: Cast after shafts are completed with 4 ft (1220 mm) diameter, 39.4 feet (12 m) long columns

Bent Cap: 56 inch (1420 mm) wide by 51 inch (1300 mm) deep by 80.44 ft (24.517 m) long Class A concrete beam

Cap Reinforcement: Seven #36 (metric) bars (top and bottom), four #16 (metric) on each face

End Bents: 2

Pile Type: 28 HP12x53 (310x79); Eight brace piles battered 1:4

Free pile Length: None

Bent Cap: 160 ft (48.7 m) long by 49 inch (1250 mm) wide by 30 inch (760 mm) deep (minimum) Class A concrete beam with wing walls

Superstructure: Seventeen 4.5 ft **(**1372 mm**)** prestressed concrete girders with cast-in-place concrete deck slab**.** Diaphragms are constructed between girders at the end bents, the interior bents and between bents.

Interior Bents Super/Substructure Connection: Two rows of 17 elastomeric bearing pads (Type V pads with 2 inch diameter anchor bolts)

End Bent Super/Substructure Connection: One row of 17 elastomeric bearing pads (Type V, 2-1/4 inch or 57 mm thick)

Bearings: Bearings at the end bents are expansion. Bearings at Bents 1 and 3 are all expansion. All bearings at Bent 2 are fixed.

Geotechnical Summary

For this analysis, one of the three interior drilled shaft bents was modeled. Five soil borings were performed by NCDOT for each of the interior bents. For Bent 1, they were labeled B1-A, B1-B, B1-C, B1-D, and B1-E. All borings showed similar profiles, except B1-E.

The profiles can generally be characterized as residual and composed of approximately 10 feet (3.2 m) of low N-value material overlying weathered and parent rock. The groundwater table was encountered approximately 10 inches (0.25 m) below the ground surface. Scour effects are considered because the bridge crosses a small stream that has a relatively high flood elevation.

The borings indicate a ten foot thick layer of clayey silt and sandy clay which has N-values between 7 and 17 blows per foot. Below that, weathered or slightly to severely fractured black gneiss was encountered. Recovery ratios were between 0 and 45% in the weathered material, and generally 100% in the parent material. RQD values were typically 0% in the weathered rock and between 50 and 90% in the sound gneiss.

Boring B1-E shows silty clay and silty sands were encountered to depths of 10 ft (3.1 m) with N values averaging 10 blows per foot. This layer is underlain by pea sized alluvial gravels and sandy clays with N values of 46 and 68, respectively. Finally, very dense silty sands (likely weathered rock) with N values in excess of 100 are encountered. Scour elevations on this boring are indicated to depths of 22.5 ft (7 m), which leaves

approximately 10 ft (3.2 m) of weathered rock underlain by gneiss and granite parent rocks.

According to the provided plans, the 30 to 45 foot (9 to 14 m) long shafts were installed with a socket in the weathered and parent rock material. After the shafts were completed, a 35 ft (11 m) column was cast on top of the shaft with a reduced diameter. In MultiPier, the soils were modeled using Reese's P-y curves for stiff clay below the water table, with a 4 ksf unconfined compressive strength for the weathered rock and McVay's (2004) limestone model for P-y curves of the parent material. Axial curves were developed using O'Neill's and Reese (1999) model for drilled shafts in intermediate geomaterial.

Equivalent Model

After a single shaft lateral analysis was performed in MultiPier using the same soil profile used for the full bent analysis, the equivalent model parameters were calculated based on the model presented by Robinson et al. (2006) and recreated in Figure 4 in Chapter 2. The equivalent model parameters are shown in Table 7. These parameters were then input into a SAP frame without soil and are presented in the next section as "SAP—Equivalent."

Table 7. Equivalent Model Parameters for Wake County Bridge

EQUIVALENT MODEL PARAMETERS				
Head	Le (ft)	α	B	K
Fixed	20.00	1.16	0.24	1.1
Free	29.42	1.16	0.24	2.1

Analysis Results—SAP and MultiPier

The models for the Wake County bridge were developed in MultiPier and SAP. A sample set-up is shown in Figure 12. Input files are included in the Electronic Appendix. Table 8 shows the maximum moment, shear and axial forces developed in the most critical shaft for each model. Both the MultiPier and SAP models yielded consistent shaft responses under the applied load cases.

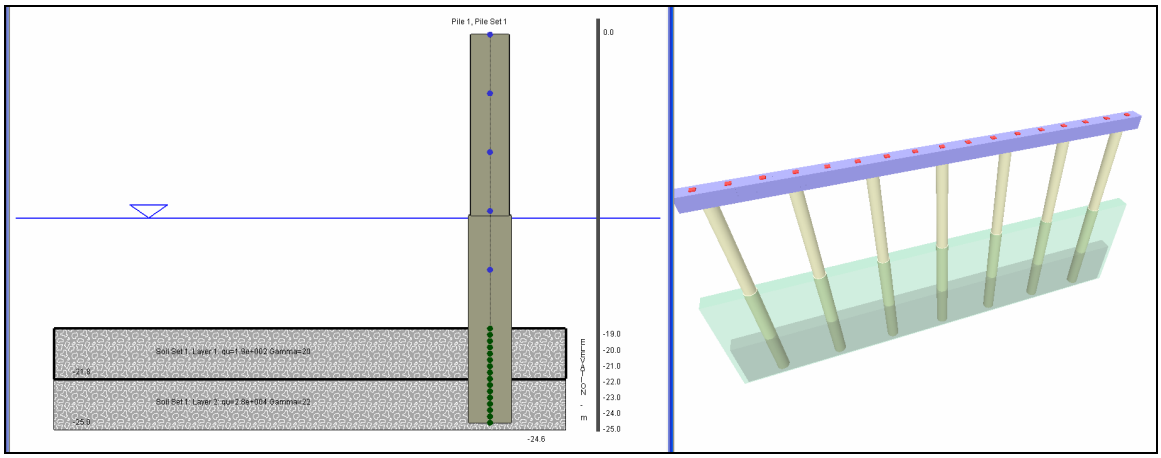

Figure 12. Wake County Bridge MultiPier Model

Table 8. Wake County Nonlinear Analysis Results at Top of Shaft: Maximum Lateral Load Case

Model	Maximum Moment (kip-ft)	Maximum Axial Force (kips)	Maximum Shear Force (kips)
SAP--Nonlinear	442	4052	40
MultiPier	450	4100	45
SAP—Equivalent	398	4053	41
AASHTO Group	AASHTO Group II Shaft 4, Demand Capacity Ratio=0.226		

Analysis Results—Optimization

Once the MultiPier result was verified, the model was then optimized by reducing the number or size of the shafts while maintaining the same load cases. For this bridge, seven 54 inch diameter drilled shafts were used. Table 9 shows the results from reducing the number of shafts. Demand capacity ratios tend to be between 0.2 and 0.3, although displacements in the transverse and longitudinal directions begin to exceed 1 inch when 42 inch diameter shafts are considered. The highest demand capacity ratio, in the original layout, occurs due to the reduction in shaft area between the shaft and the column.

Table 9. Wake County Alternative Shaft Configurations, based on AASHTO Groups I, IA, II and III

	Seven 54 in. shafts, 48 in. columns	Seven 48 in. shafts uniform	Seven 42 in. shafts uniform	Seven 36 in. shafts uniform	Seven 30 in. shafts, uniform	Six 42 in. shafts uniform
Demand/Capacity Ratio (Shafts)	0.32	0.21	0.26	0.36	0,49	0.29
Displacement, transverse (Shaft top, in)	0.43	0.47	0.75	1.28	2.5	0.91
Displacement, longitudinal (shaft top, in)	0.67	0.75	1.22	2.18	4.4	1.46
Displacement, axial (shaft top, in)	0.24	0.24	0.28	0.38	0.53	0.35

Pitt County Bridge, Project B-3684

This bridge spans the Tar River and its overflow area on state route 1565. It consists of two end bents and 19 interior bents, for a total length of 1952 feet.

General Information

Designed: 2005

Spans: 20 (Span between end bent 1 and Bent 1 is 101 ft-1 inch, 14 are 100 feet, four are 90 feet, final span is 91 ft-1 inch)

Skew: 90^{o}

Interior Bents: 19

Drilled Shaft Bent (Bents 1, 4, and 5: Bent 4 summarized below)

Shaft Type: Two five ft (1524 mm) diameter drilled shafts, reducing to 4.5 ft (1.37 m) diameter for the free column above the ground surface, spaced 19.5 ft (6 m)

Free Shaft Length: Cast after shafts are completed with 4.5 ft (1.37 m) diameter, 35 feet (10.67 m) long columns

Bent Cap: 62 inch (1575 mm) wide by 48 inch (1219 mm) deep by 30 ft (9.14 m) Class A concrete beam

Cap Reinforcement: Eight #11 bars on top, eight #11 bars on the bottom, and eight #5 on each face.

Drilled Pile Footings or Vessel Impact Bents(Bents 2 and 3)

Not in this study.

Driven Steel Pile Footings and Bents (Bents 6 through 20)

Not in this study

End Bents: 2

Pile Type: H-Pile

Free Pile Length: Not available

Bent Cap: 39.25 ft (12 m) long Class A concrete beam with wing walls

Superstructure: Four 54 inch prestressed concrete girders with cast-in-place concrete deck slab**.** Diaphragms are constructed between girders at the end bents, the interior bents and between bents.

Interior Bents Super/Substructure Connection: Two rows of four elastomeric bearing pads (Type V pads with 2 inch diameter anchor bolts)

End Bent Super/Substructure Connection: One row of four elastomeric bearing pads (Type V, 2-1/4 inch or 57 mm thick)

Bearings: Bearings at the end bents are expansion. Odd numbered bents have two rows of fixed connections; even numbered bents have two rows of expansion connections.

Geotechnical Summary

For this analysis, one of the three interior drilled shaft bents was modeled. Two soil borings were performed by NCDOT at this bent. For Bent 4, they were labeled B4-A and B4-B. Both borings showed similar profiles, although B4-A was more detailed and included SPT testing.

The profile is typical of the coastal region, consisting of alternating layers of sands and clayey silts. At a depth of approximately 25 feet, the PeeDee Formation was encountered. Generally, this stratum consists of soils described as sands or sandy silts with intervals of sandy limestone.

The boring indicates a three foot thick layer of clayey silt which has an N-value of 2 blows per foot. This is underlain by saturated fine sands and wet sandy clayey silts with N-values between 8 and 15 blows per foot that extend to a depth of 24 ft. The PeeDee formation follows the saturated fine sand. It is described as fine to coarse sand, fine to coarse sandy silt, fine sandy clay and fine sandy clayey silt, all with intervals of sandy limestone. The limestone layers tend to be no more than 12 inches thick, and are indicated in the boring log. N-values are highly variable depending on whether the SPT struck a limestone layer (N-values greater than 100 blows per foot) or one of the sandy layers (N-values of around 10 to 20 blows per foot). In this boring, the PeeDee formation reportedly extends from a depth of 24 feet to the termination of the boring at 98.9 feet.

The shafts at Bent 4 were expected to be installed to depths of 100 feet (30.5 m) below the ground surface, well into the PeeDee formation. After the shafts were completed, a 37 ft (12 m) column was cast on top of the shaft with a reduced diameter. In MultiPier, the upper 25 ft of the soil profile was removed for scour considerations. The soils were modeled using Reese's P-y curves for sand, with a 32^{o} friction angle in the PeeDee formation's soils and 45^{o} friction angles in the sandy limestone. Axial curves were developed using BSI's (2004) model for drilled shafts in sands. The soil profile for this bridge was the same used by NCDOT in the original MultiPier analysis performed for the bridge design.

Equivalent Model

After a single shaft lateral analysis was performed in MultiPier using the same soil profile used for the full bent analysis, the equivalent model parameters were calculated based on the approach presented by Robinson et al. (2006). The equivalent model parameters are

shown in Table 10. These parameters were then input into a SAP frame without soil and are presented in the next section as "SAP—Equivalent."

Table 10. Equivalent Model Parameters for Pitt County Bridge

EQUIVALENT MODEL PARAMETERS				
Head	Le (ft)	A	β	K
Fixed	73.4	0.30	.20	2.1
Free	84.2	0.47	.20	1.1

Analysis Results—SAP and MultiPier

The models for the Pitt County bridge were developed in MultiPier and SAP. A sample profile set-up is shown in Figure 13. Input files are included in the Electronic Appendix. Table 11 shows the maximum moment, shear and axial forces developed in the most critical shaft for each model. Both the MultiPier and SAP models yielded consistent responses under the applied load cases.

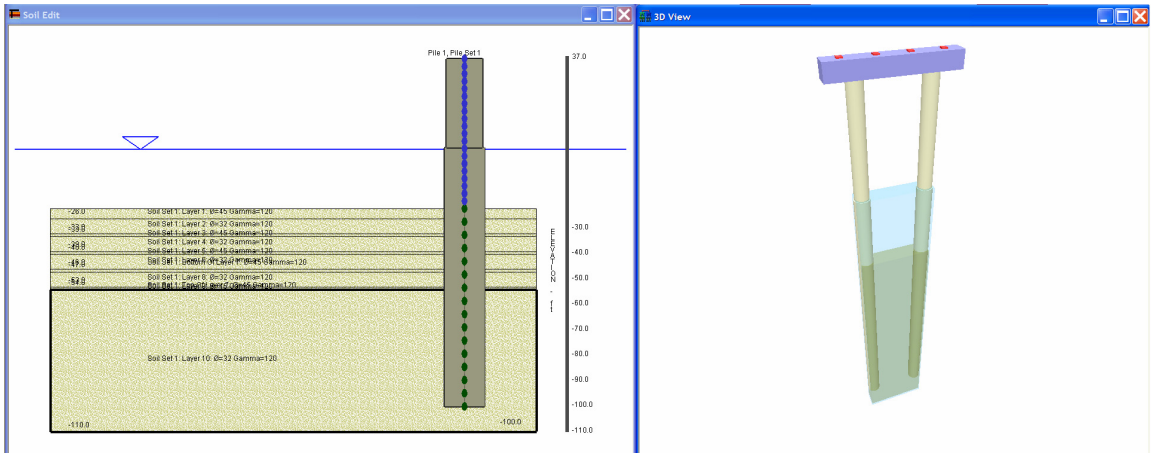

Figure 13. Pitt County Bridge MultiPier Model

Table 11. Pitt County Nonlinear Analysis Results at Top of Shaft: Maximum Lateral Load Case

Model	Maximum Moment (kip-ft)	Maximum Axial Force (kips)	Maximum Shear Force (kips)
SAP—Nonlinear	978	832	35.7
MultiPier	1098	807	33.3
SAP—Equivalent	1245	790	35.4
AASHTO Group	AASHTO Group II Shaft 2, Demand Capacity Ratio=0.302		

Analysis Results—Optimization

Once the MultiPier result was verified, the model was then optimized by reducing the number or size of the shafts while maintaining the same load cases. For this bridge, two 60 inch diameter drilled shafts were used. Table 12 shows the results from reducing the number of shafts. Demand versus capacity ratios tend to vary greatly, approaching as high a value as 0.7 for the 48 inch shafts.

Table 12. Pitt County Alternative Shaft Configurations, based on AASHTO Groups I, IA, II, III and IV

	Two 60 in. shafts, 54 in. columns	Two 54 in. shafts uniform	Two 48 in. shafts uniform
Demand/Capacity Ratio (Shafts)	0.308	0.386	0.70
Displacement, transverse (shaft top, in)	1.3	1.7	2.6
Displacement, longitudinal (shaft top, in)	2.1	3.6	8.4
Displacement, axial (shaft top, in)	0.7	0.7	1.0

In this case, model for the original 60 inch diameter shaft layout resulted in longitudinal displacements of approximately two inches. It should be noted, however, that the worst

case soil profile was used, where maximum scour was assumed. With that in mind, the analysis based on the modeling configuration yielded displacements that are significantly greater than the normal 1 inch limit especially in the longitudinal direction.

Summary

The results presented herein have shown that the MultiPier model can be approximately reproduced in the 3-D SAP program. This essentially verifies the output results for computed drilled shafts responses from the MultiPier model. Coupled with the results from the driven piles project as reported by Robinson et al (2006), MultiPier appears to be capable of modeling a wide range of commonly used deep foundation solutions.

Similarly, the equivalent frame model proposed in Robinson et al. (2006) provides results that are comparable to those obtained from both the SAP and MultiPier analyses, provided that the most critical lateral load case is used to evaluate the parameters for the equivalent model. If nonlinear analyses are not eventually adopted by NCDOT, then an equivalent frame model that is built using Robinson et al (2006) approach will result in similar moments, axial loads and shear loads in the most critical case. This should lead to more optimal and possibly reduced sizing of the structural elements.

An optimization analysis was conducted for each bridge by reducing the number, or size, of the shafts. In all three cases, it was shown that some savings in material and installation costs can be realized using the nonlinear analysis. Thus, compared to the point of fixity methods traditionally used by NCDOT, there is some room for cost and material savings by using the nonlinear or equivalent models.

These analyses have considered the drilled shaft bents as free standing. The next chapter will investigate the moment transfer capabilities of the anchor bolt-sole plate-bearing pad connection between super- and sub-structure. Full scale lab tests and their results will be described.

CHAPTER 4. EXPERIMENTAL PROGRAM: BEARING PADS

In cases of bearing supported bridge superstructures with diaphragms connecting adjacent girders, it is important to identify the stiffness of the connection as well as its moment transfer capacity. This aspect is often not considered in design and its quantification facilitates the optimization of the design process. The rotational stiffness of the connection directly impacts the assumptions of the boundary conditions and the effective length or buckling factor used in the pile or substructure design. As mentioned earlier, the NCDOT assumes the K-factor for effective length calculations is 2.1 (free head) in the longitudinal direction. If it can be shown that current details can accommodate an effective length less than 2.1, then this would be advantageous and can possibly be translated into cost savings.

Figure 14 shows different pile boundary conditions used in the design of the bridge substructure (AISC, 2002). The last case in Figure 14 is the one assumed for analysis in the longitudinal direction. As the effective length factor (K) increases, the critical buckling load decreases. Therefore, as the K-factor increases there is a need to design stiffer deep foundation elements, which becomes more expensive.

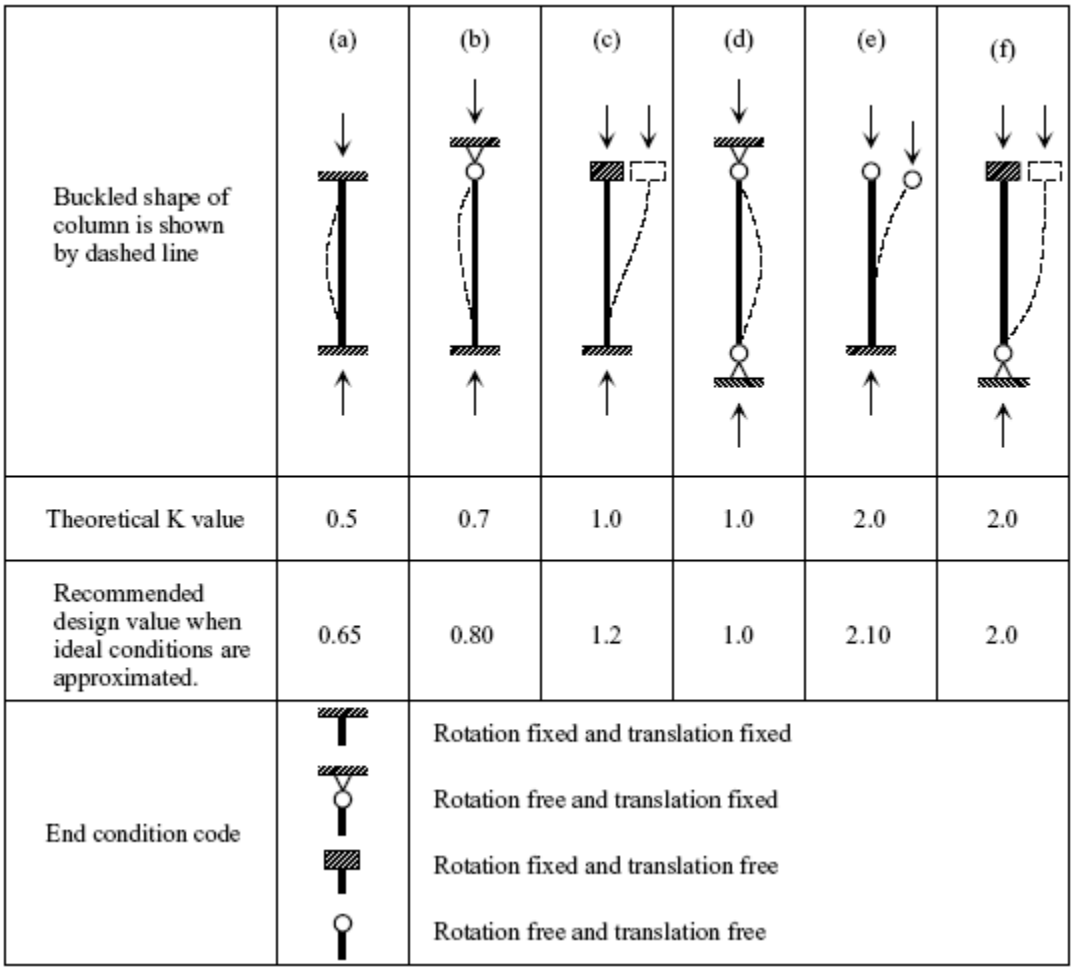

Figure 14. Boundary conditions for pile design (after AISC. LRFD Manual of Steel Construction, 2001)

The experimental program for characterization of the bearing pad stiffness was divided into two phases. The first included testing of the bearing pads under the combined action of shear and axial loads. The second consisted of several full scale tests on a typical substructure/bearing pad/diaphragm/superstructure connection to study the moment transfer capabilities of the bearing connection between the super- and sub-structure. The connection is tested simulating field conditions of NCDOT bridges. These tests are described in detail in the next sections.

Index Testing

The primary purpose of this phase of the experimental program is to investigate the behavior of the bearing pads supplied by NCDOT under the combined action of shear and

axial forces. Results from the experimental program are used to estimate the shear modulus and the force-deformation response of the bearing pads under the effects of combined load levels. The properties of the bearing pads tested in this study are shown in Table 13. The hardness/durometer nominally gives an indication of the shear modulus of the material. According to Mucarella and Yura (1995), for a material with a durometer between 55 and 65, the shear modulus should range between 110 and 150 psi (0.76 and 1.03 MPa). Nonetheless, in some cases the shear modulus values can vary as these values are determined by testing unreinforced vulcanized rubber. A picture of the bearing pads used in the testing program is shown in Figure 15.

Table 13. Properties of the Bearing Pads

Type	Durometer	Thickness in (mm)	Area in^2 (m^2)
V	50	3.56 (90.5)	325 (0.210)
VI	60	2.50 (63.5)	253 (0.163)

Figure 15. Bearing Pads provided by NCDOT

A series of displacement-controlled lateral load tests were performed on the bearing pads under varying levels of axial load. The tests were performed under axial loads of 50 (222 kN), 100 (444 kN), and 150 kips (667 kN). The lateral loading history for all the tests consisted of reversed single displacement cycles with increments of 0.25 inches (6.35 mm) until a target displacement of 2 in (50.8 mm) is achieved. The loading history is shown in Figure 16.

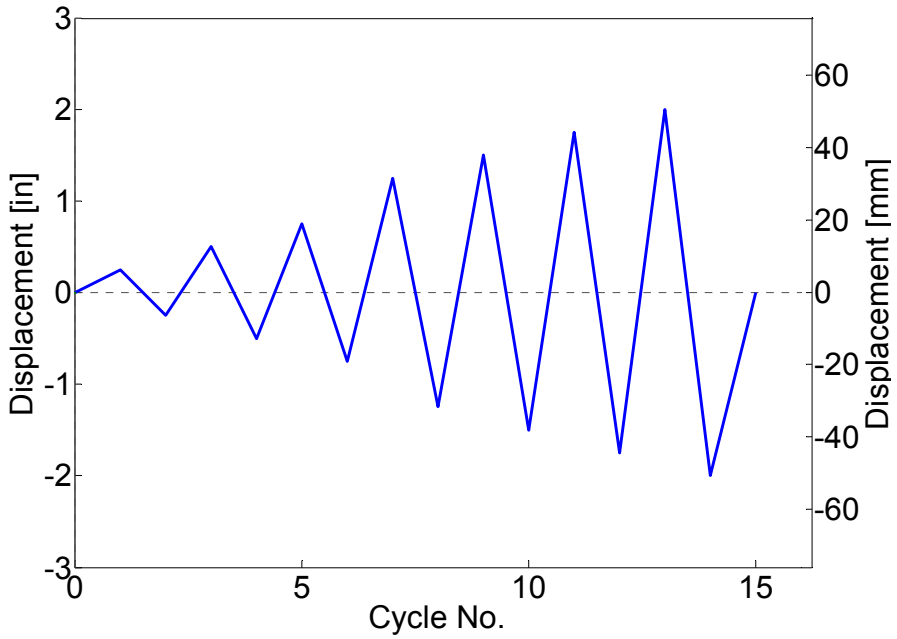

Figure 16. Example Lateral Loading Scheme

Experimental Test Setup

A schematic drawing and a photograph of the experimental setup are shown in Figure 17. The setup consisted of a steel frame to which a 110 kip (489 kN) hydraulic actuator was connected. The actuator (labeled "4" on Figure 17) was used to apply the lateral load during testing. The steel frame was rigidly attached to the laboratory strong floor using four Dywidag bars. Then, a concrete block (labeled "5") with dimensions of 31.5 inches (0.8m) by 18.5 inches (0.47m) by 18.5 inches (0.47m) was connected to the actuator by means of four 1 inch (0.025 m) Dywidag bars and four 1 inch (0.025 m) square steel plates applied as washers to the bottom of the concrete block.

Next, two bearing pads (labeled "6") were centered on two sides of the concrete block to simulate the bearing pad connection with a bridge bent cap. Later, two steel plates (labeled "1") were placed adjacent to the bearing pads to simulate the bearing pad connection with a sole plate. Four 1-3/8 inch (0.034 m) Dywidag bars (labeled "3") were installed through the steel plates (but not the bearing pads) and tied with steel plates and nuts. Then, two steel beams (labeled "7") were placed on the top of the steel plates to restrain any vertical movement of the plates. With everything together, four 60-ton (534

kN) jacks and 3 load cells (labeled "2") were positioned between 1 inch (0.025 m) steel plates and nuts. The load cells were used to measure the axial load applied during the tests. An electric pressure pump was connected to the jacks to apply the axial load. Figure 18 shows the load cell and 60-ton (534 kN) jack used in the test.

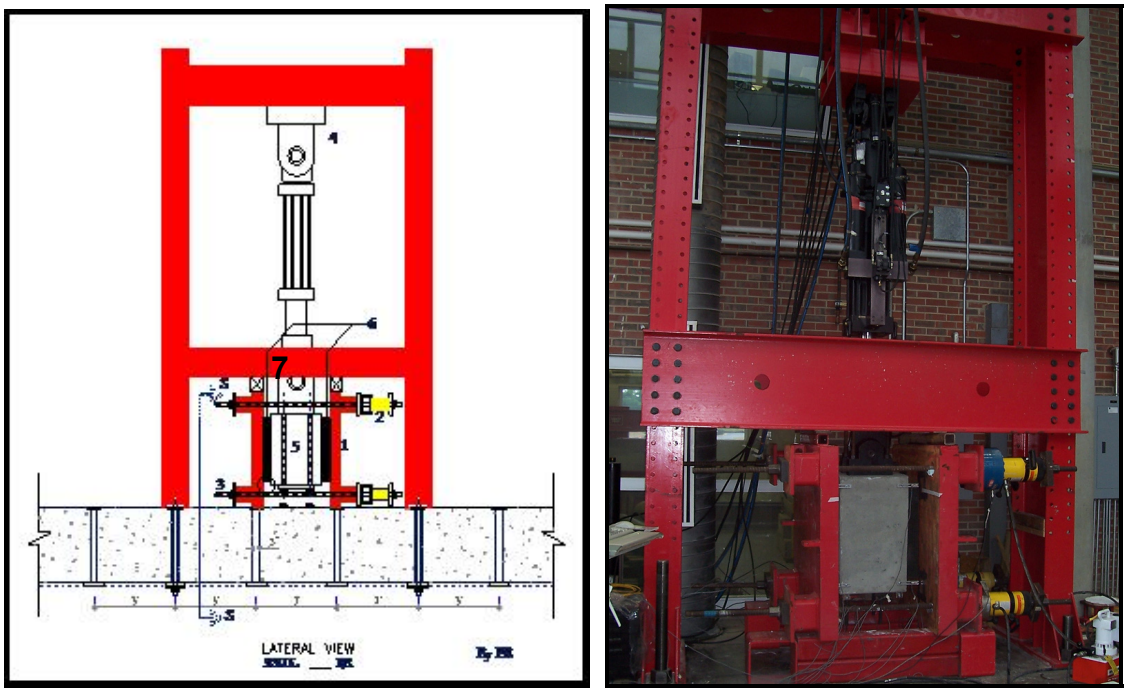

Figure 17. Experimental setup sketch (provided by Pablo Robalino) and test picture

Figure 18. Load cell and 60-ton jack

Instrumentation

Instrumentation consisted of a total of eight string potentiometers and eight linear potentiometers. The string potentiometers were used to measure the vertical displacements of the concrete block and bearing pads during the cyclic loading history. The linear pots were used to record any horizontal movement of the block in order to have an indication of the block's rotation during the tests. The linear pots were placed at 2 inches (0.0508 m) from the top and bottom of the concrete block (for a total of four on each face of the block).

Figure 19 and Figure 20 show the location of the string and linear pots, respectively. Four of the string potentiometers were located near the four corners of the concrete block and the rest were connected to the bearing pads (two per pad). They were fixed to the floor with Hydro-Stone® (gypsum cement) to prevent movement during testing**.** Figure 21 presents a closer view of the instrumentation and experimental setup used in the testing program.

Figure 19. String Potentiometers

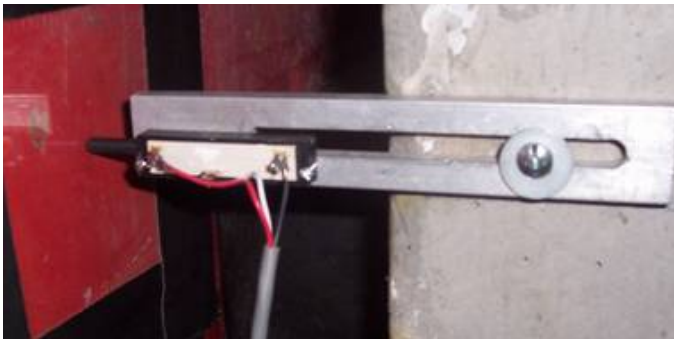

Figure 20. Linear Potentiometers

Figure 21. Closer view of the instrumentation

Experimental Results

A summary of the results is presented in this section. A total of six testing cases are presented (three for each bearing pad type). The shear force versus displacement was recorded during each test along with the applied axial load.

Bearing Pad Type V – Axial Load 50 kips (222 kN)

Figure 22 (a,b,c,d) shows the lateral force-displacement hysteretic response for the two bearing pads studied during these tests. These responses were obtained by displacing the concrete block using the displacement-controlled loading history as shown in Figure 16.

Figure 22 (a,b,c,d) shows the response obtained for the left and right bearing pad, respectively. The displacements were obtained with the string pots, located at the following positions: at 10/16 inch (15.87 mm) from the left edge and 1-1/2 inch (38.1 mm) from the concrete right edge for the left bearing pad, and at 15/16 inch (23.81 mm) from right edge, 1-5/16 inch (33.33 mm) from concrete left edge for the right bearing pad.

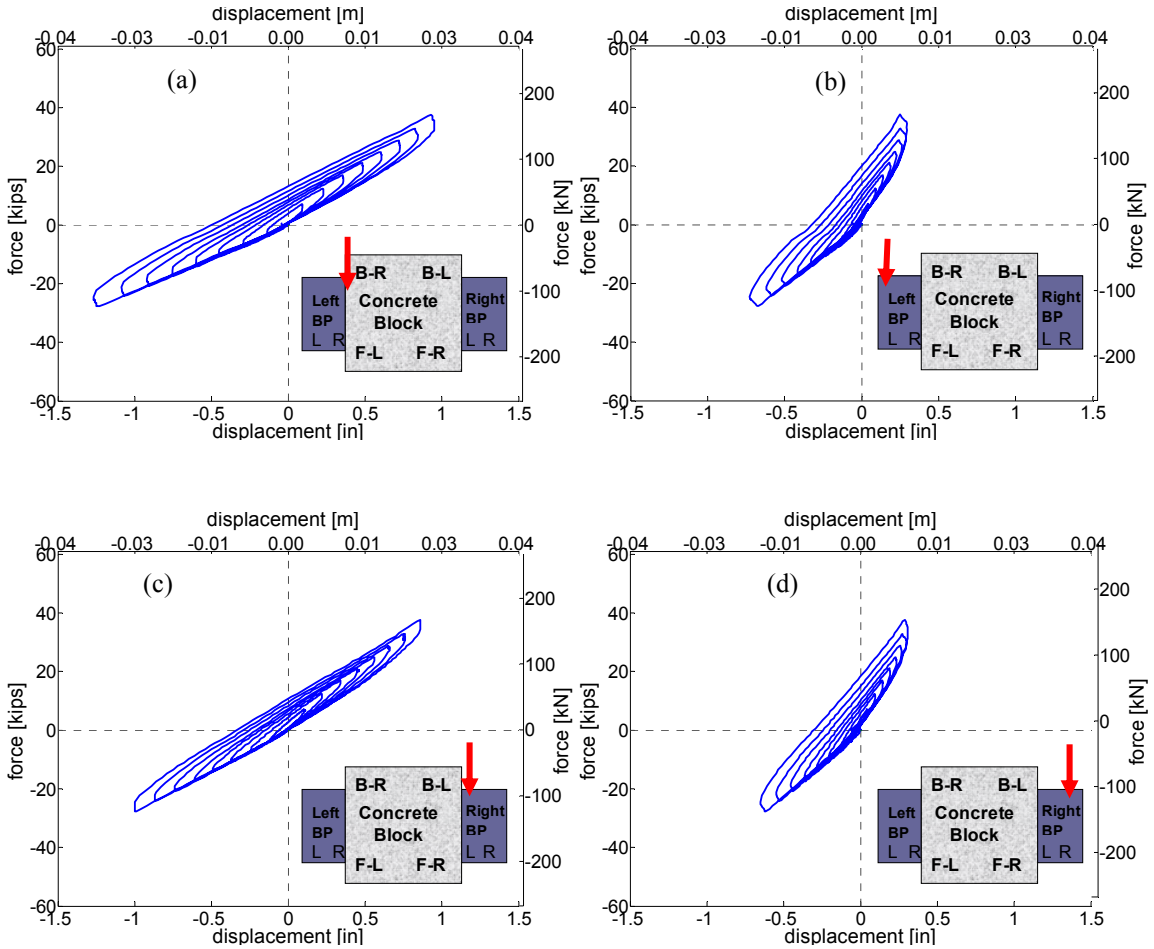

Figure 22. Force-displacement hysteretic response Type V-axial load 50 kips (222 kN)

The bearing pad displacements are higher nearer to the concrete surface as expected (right (R) and left (L) side for Left and Right bearing pad, respectively. The load-displacement responses (Figure 22) show the typical nonlinear behavior of elastomers under the influence of shear forces.

Bearing Pad Type V – Axial Load 100 kips (444 kN)

Figure 23(a-d) shows the force-displacement responses for Type V bearing pad. In this case an axial load of 100 kips (444 kN) was applied to the bearing pads. The displacements were recorded at the same points of the previous case.

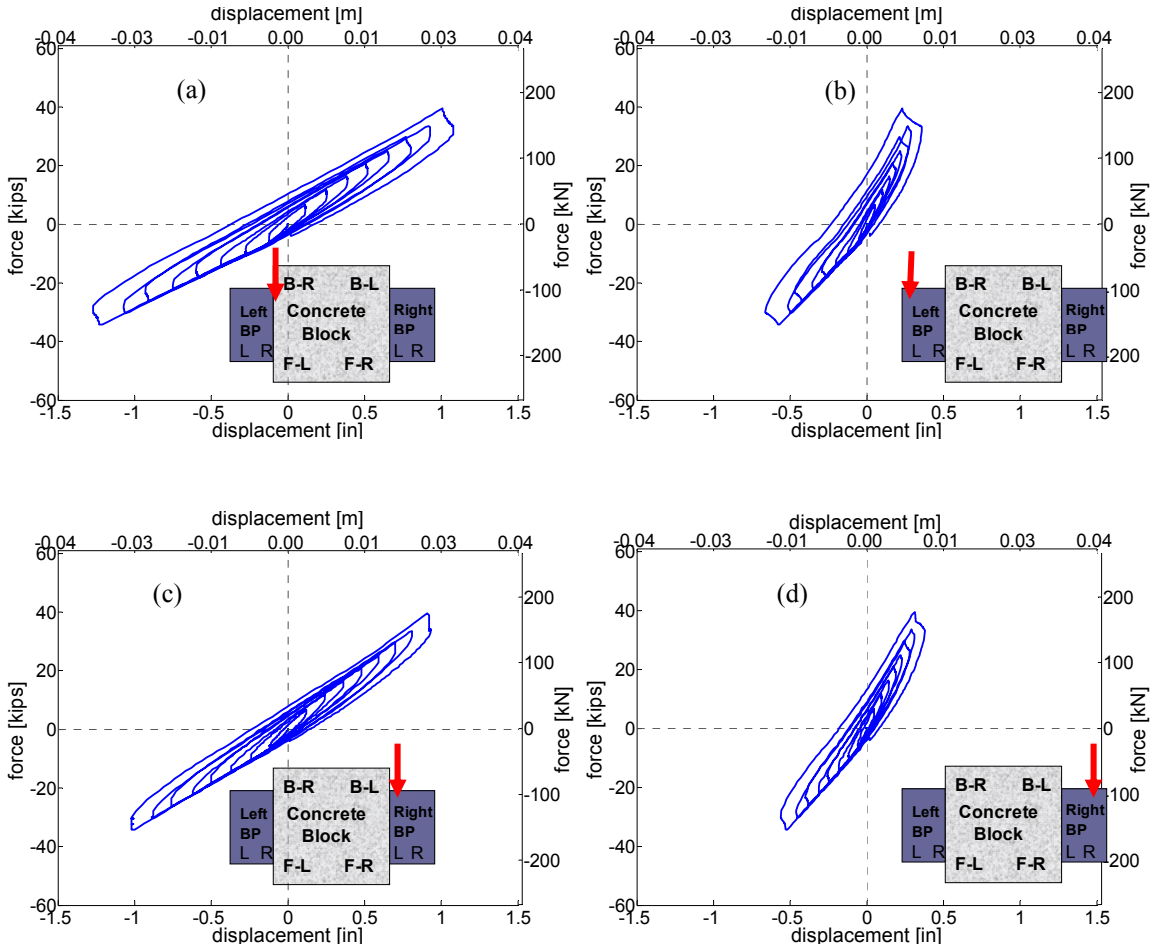

Figure 23. Force-displacement hysteretic response for Type V-axial load 100 kips (444 kN)

It can be noticed that when the axial load increases, the size of the loops in the load-displacement response also increases. This is an indication that the bearing pads are dissipating more energy from the shear loads as axial loads get higher. In addition, a slight increase in the applied lateral force was observed for the higher axial load (compare Figure 22 to Figure 23).

Bearing Pad Type V – Axial Load 150 kips (667 kN)

Figure 24(a-d) shows the force-displacement responses for Type V bearing pad with an applied axial load of 150 kips (667 kN). The displacements were recorded at the same points of the previous cases.

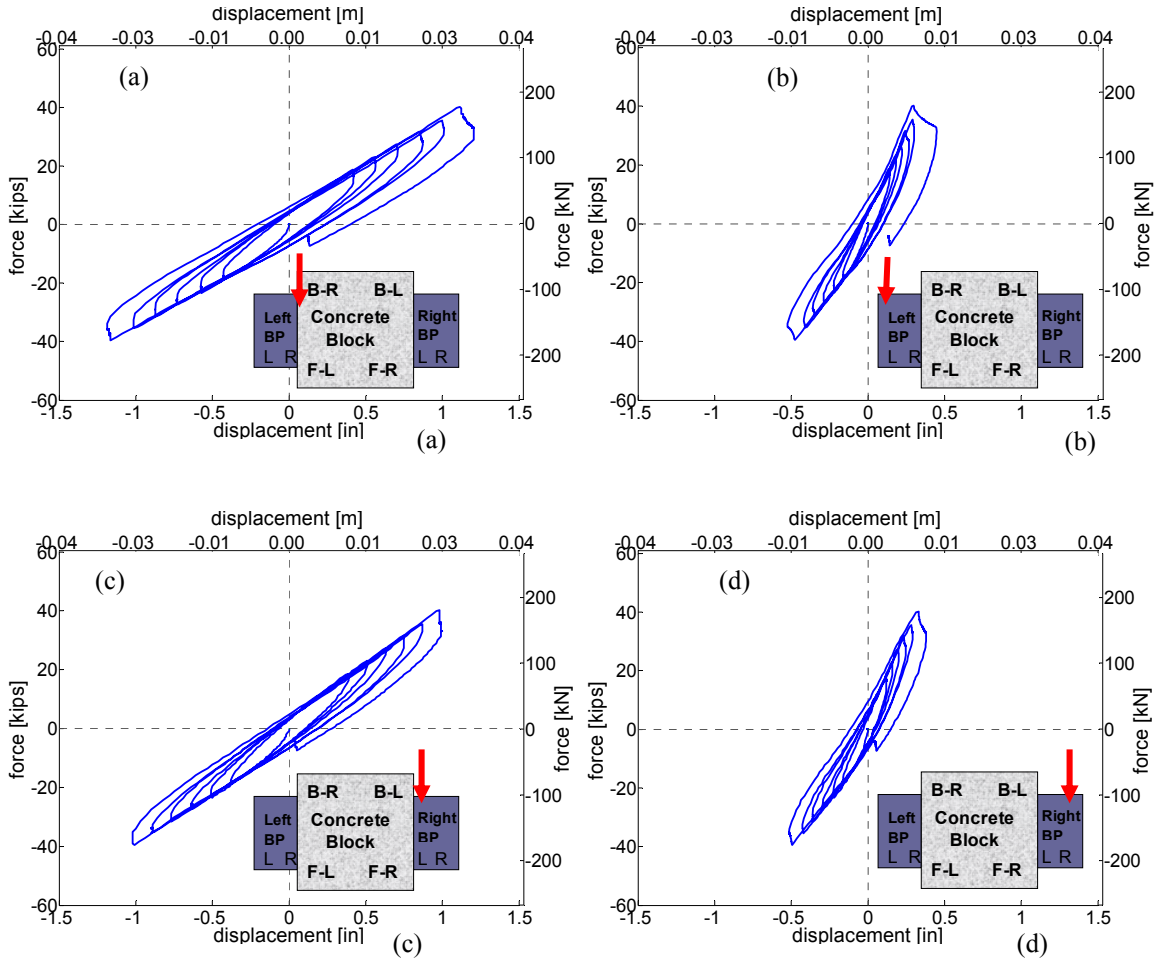

Figure 24. Force-displacement hysteretic response for Type V-axial load 150 kips (667 kN)

Basically, Figure 24 shows the same pattern in the response obtained for previous cases. The sizes of the loops in the load-displacement response become larger and consequently the dissipated energy increases.

Bearing Pad Type VI – Axial Load 50 kips (222 kN)

Figure 25 (a,b,c,d) presents the lateral force-displacement hysteretic response for the Type VI bearing pad. The displacements were obtained with the string pots, located at the positions schematically shown on the figure.

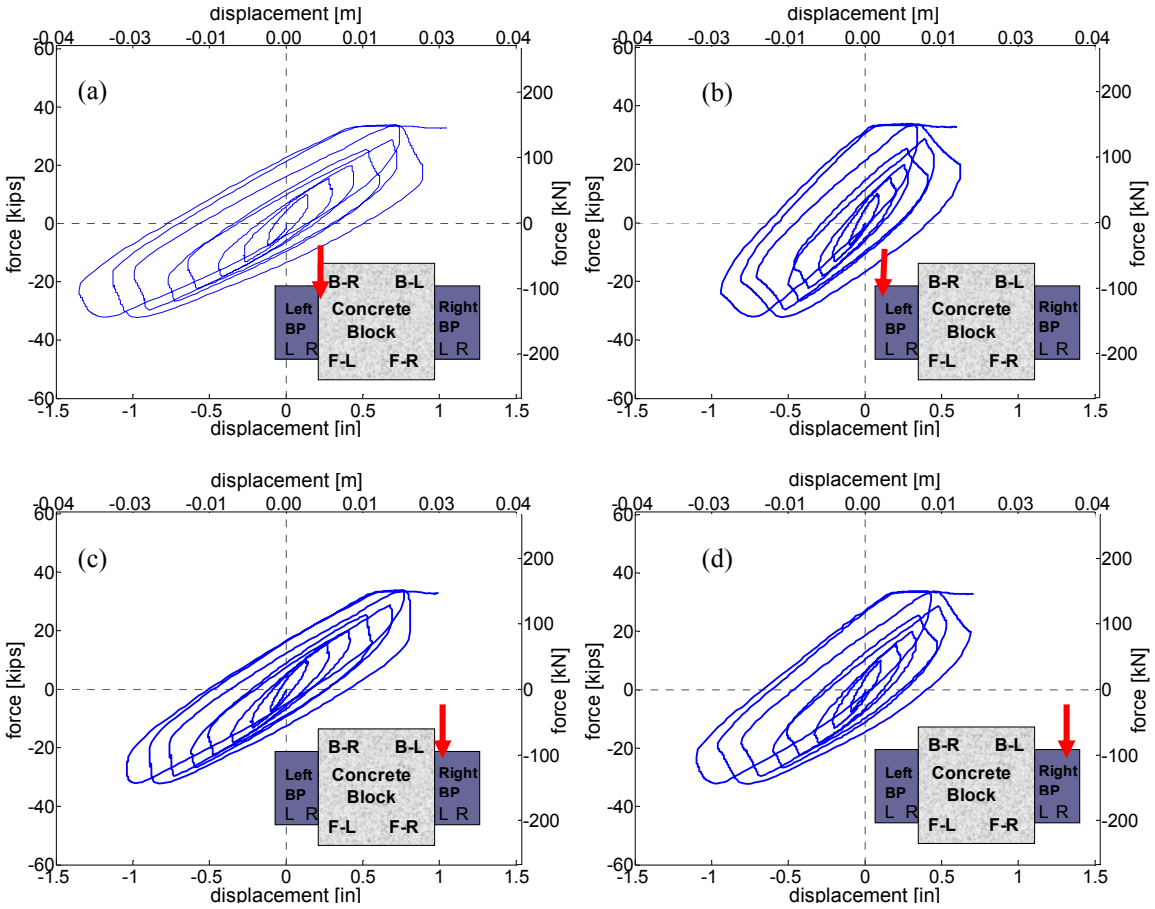

Figure 25. Force-displacement hysteretic response for Type VI – 50 kips (222 kN)

Figure 25 shows the lateral load-displacement response for Type VI bearing pad with an applied axial load of 50 kips (222 kN). It is observed that this type of bearing pad shows greater nonlinearity characteristics than the Type V pad, which in turn implies that the shear modulus will vary depending on how it is calculated. The different methods used for the shear modulus calculation will be explained in the next section.

At Bearing Pad (Left):

i. 0.75 inches (19.05 mm) from left edge
ii. 1.0 inch (25.4 mm) from concrete (right) edge

At Bearing Pad (Right):

i. 1.0 inch (25.4 mm) from right edge
ii. 0.25 inch (6.35 mm) from concrete (left) edge

Bearing Pad Type VI – Axial Load 100 kips (444 kN)

Figure 26 (a-d) shows the force-displacement responses for Type VI bearing pad with an applied axial load of 100 kips (444 kN). Figure 26 also shows that, for a Type VI bearing pad, the size of the loops of the lateral force-displacement hysteretic response increases with the applied axial load. The lateral force required to displace the bearing pad also increases significantly compared to the less stiff Type V pads.

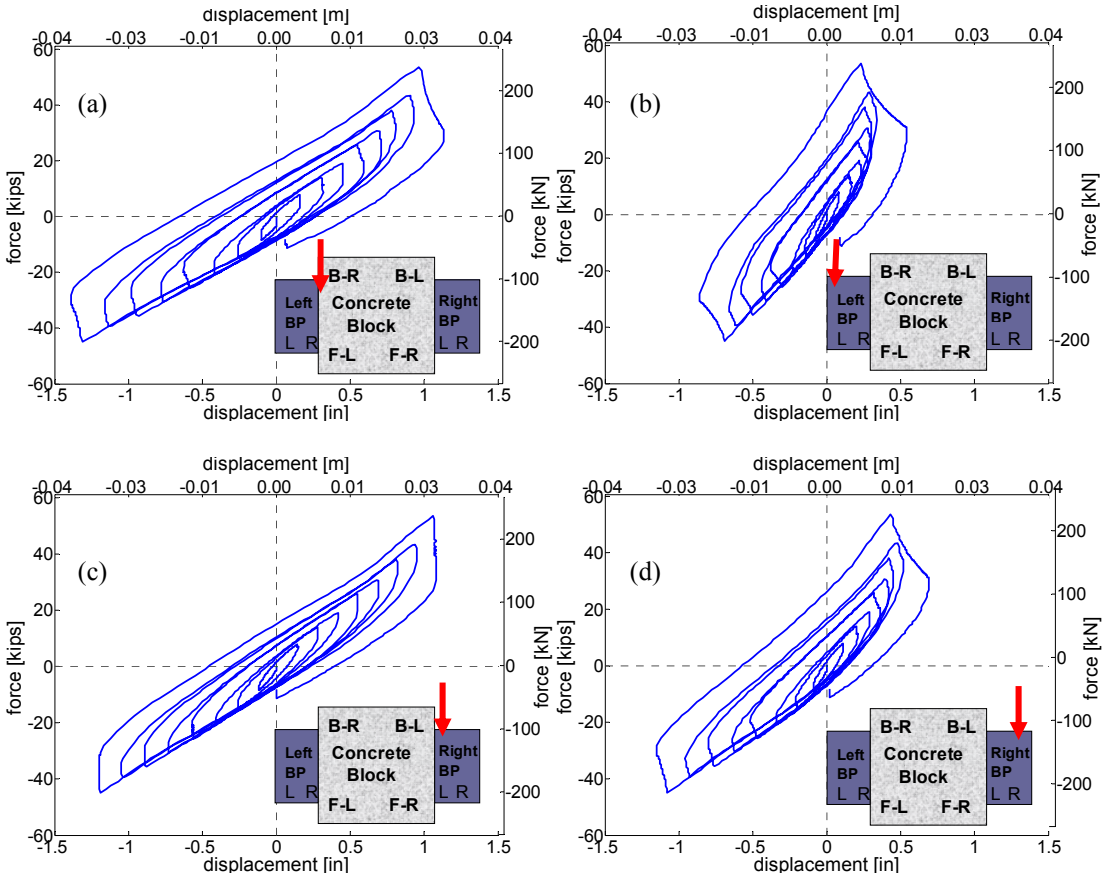

Figure 26. Force-displacement hysteretic response for Type VI – 100 kips (444 kN)

Bearing Pad Type VI – Axial Load 150 kips (667 kN)

Figure 27 shows the lateral load-displacement response for Type VI bearing pad with an applied axial load of 150 kips (667 kN). This test was stopped at a displacement in the concrete block of 1.25 inches (31.75 mm). The cycle in the pull direction was not completed due to instability in the test set up and failure of both bearing pads by delamination of the steel plates and elastomer. The force required to finish the loading history was too high for Type VI bearing pad with this level of axial load.

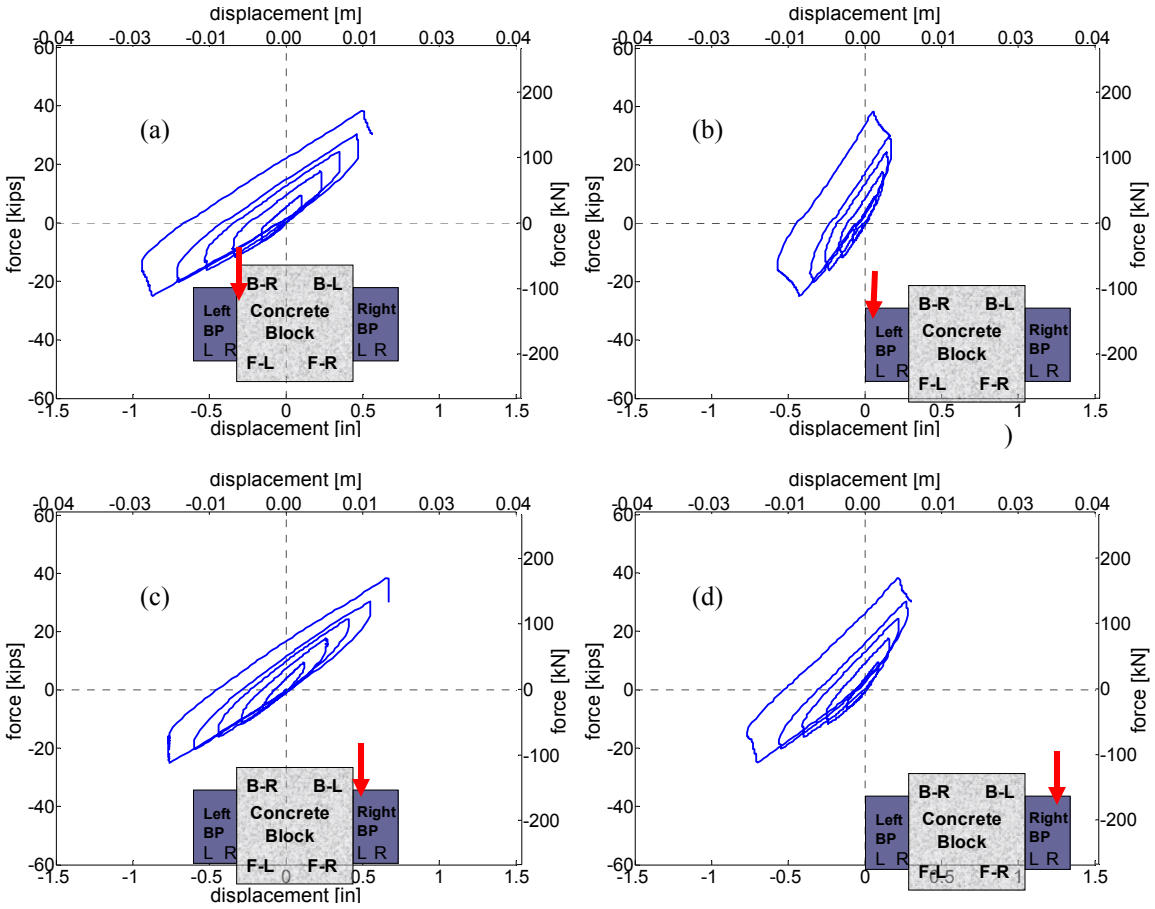

Figure 27. Force-displacement hysteretic response for Type VI-150 kips (667 kN)

In summary, Figure 22-Figure 27 presents the response of the bearing pads under study due to the combined action of axial and shear forces. As noted in the plots, the bearing pads exhibit a nonlinear response. This is characteristic of elastomers under shear, and consequently the value of the shear modulus changes accordingly; several definitions were established in the literature (Yura et al, 2001 NCHRP Report 449) to describe such behavior. Yura et al summarized several test definitions such as one way (pushover type), two way (cyclic type), and low temperature, each with different increment of strains.

The loops of the hysteretic response for the Type V bearing pads are narrower than the loops of the response for Type VI bearing pads. This indicates that the Type VI bearing pads dissipated more energy during the application of the lateral load. To induce the same displacement magnitude under shearing, Type VI requires a higher force compared to Type V since it is manufactured using a stiffer elastomeric material.

Shear Modulus Calculation

Theoretically, the shear modulus is obtained as follows:

Equation 6 $$F = \frac{(G)(A)(\Delta)}{t}$$

Equation 7 $$G = \frac{(t)(F)}{(A)(\Delta)}$$

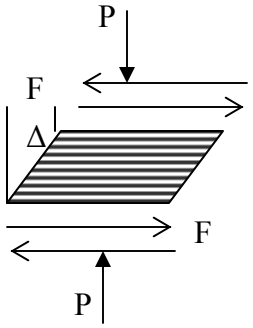

Figure 28. Forces acting at the bearing pad

G = Shear Modulus

F = friction force required to deform an elastomeric pad

A = contact area

Δ = deflection of the pad

$$\gamma(Shear\_Strain) = \Delta / t$$

As indicated before, because the shear modulus changes with the definition used to calculate it, it is necessary to clarify the way that this parameter was obtained in this study. Yura et al in the NCHRP report 449 (2001) presented several approaches to obtain the shear modulus for bearing pads. Shear modulus is usually determined as the slope of a line between two points on the stress (defined as shear force /contact area) - shear strain (displacement /total elastomer thickness) curve. In general, a secant modulus at 50-percent strain is used to calculate the shear modulus. According to Yura et al (2001), the 50-percent secant modulus definition yields the correct value of the maximum shear force when the bearing is strained to the maximum design level, which is an important performance (design) limit. Another definition is the ASTM quad shear at 25% strain which gives usually a value that is approximately 10% higher than the 50% secant modulus, which is recommended as a design level. Both definitions can be used to calculate the shear modulus (G) for bearing pads strained in one or two directions. In this study the bearing pads were subjected to strains in both directions (reverse cyclic loading).

In this study, the shear moduli were computed for the laboratory test data using methods described in NCHRP report 449 (2001) by Yura et al. Four different methods were used to obtain the shear modulus for Type V and VI bearing pads. These are defined as follows:

- **Definition 1:** Slope of a line between 0 to 50% shear strain in the stress vs. shear strain relationship (one way)
- **Definition 2:** Slope of a secant line between -50% and 50% shear strain in the stress vs. shear strain relationship (two way)
- **Definition 3:** Slope of a tangent line between -25% and 25 % shear strain (top line of in the stress vs. shear strain relationship)
- **Definition 4:** Slope of a tangent line between -25% and 25 % shear strain (bottom line of in the stress vs. shear strain relationship)

The shear moduli evaluated using these methods are presented in Table 14 through Table 19 for the six cases tested in this study. For brevity, the stress vs. shear strain relationships were presented for the right bearing pad for Type V cases, and for the left bearing pad for Type VI cases (Figure 30 to Figure 35). Similar plots can be obtained for the other pads. Figure 29 shows a sketch of the position of the bearing pads in relation to the concrete block and nomenclature used in the discussion. L and R mean left and right, respectively, for each bearing pad. B-R, B-L, F-L, F-R indicate back-right, back-left, front-left, and front-right sides of the concrete block.

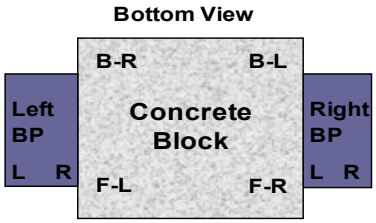

Figure 29. Nomenclature of the bearing pads test set up

Figure 30 shows the stress-shear strain relationship for a Type V bearing pad with an axial load of 50 kips (222 kN). The four different lines used for the calculation of the shear modulus are shown on the plot. Line 0-d is for definition 1 (between 0 to 50% shear

strain). Line b-c is for definition 2 (secant line -50% /50 % shear strain). Lines a-e and f-g are for definition 3 and 4, respectively. The values of shear modulus (G) for this case are presented in Table 14(a-c). The calculation was performed for each of the right and left bearing pads. Then, the shear modulus values obtained between both pads were averaged and presented in Table 14(c) as $G_{average}$ for all the different definitions. In this case, $G_{average}$ was estimated to range from 0.56 to 0.7 MPa.. The applied force was divided by 2 since the tests were performed using two bearing pads and assuming an ideal situation in which each bearing pad accounts for half of the total applied force.

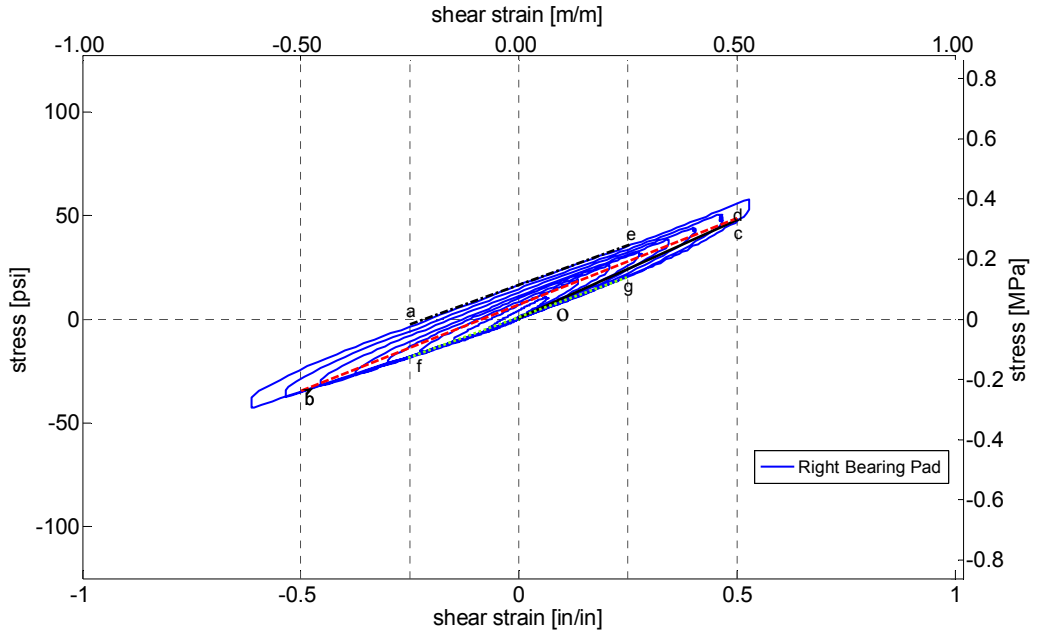

Figure 30. Stress vs. shear strain relationship for Type V- 50 kips (222 kN)

Table 14.(a-c) Shear Modulus according to several test definitions for Type V- 50 kips (222 kN)

Left Bearing Pad						
Shear Modulus Definition	**Direction**	**stress** (psi)	**stress** (MPa)	**G** (psi)	**G** (MPa)	**$G/G_{(0/+50)}$**
0/+.50	One way	53	0.3656	106.00	0.7311	1
+/- 50 secant	Two way	53/-36.66	.3656/-.2529	89.66	0.6184	0.846
+/- .25 tangent (top line)	Two way	41.49/-0.707	.2862/-.0049	84.39	0.5821	0.796
+/- .25 tangent (bottom line)	Two way	23.18/-18.35	.1599/-.1266	83.06	0.5729	0.784

Right Bearing Pad						
Shear Modulus Definition	**Direction**	**stress** (psi)	**stress** (MPa)	**G** (psi)	**G** (MPa)	**$G/G_{(0/+50)}$**
0/+.50	One way	48	0.3311	96.00	0.6622	1
+/- 50 secant	Two way	48/-35.3	.3311/-.2435	83.30	0.5746	0.868
+/- .25 tangent (top line)	Two way	36.1/-3.88	.2489/-0.0267	79.96	0.5515	0.833
+/- .25 tangent (bottom line)	Two way	21.5/18	.1483/-.1242	79.00	0.5449	0.823

Shear Modulus Definition	**$G_{average}$** (psi)	**$G_{average}$** (MPA)
0/+.50	101.00	0.6966
+/- 50 secant	86.48	0.5965
+/- .25 tangent (top line)	82.18	0.5668
+/- .25 tangent (bottom line)	81.03	0.5589

The last column in Table 14 through Table 19 shows the ratio of each shear modulus over the shear modulus obtained using definition 1 (slope from 0 to 50% shear strain). Yura et al (2001) recommended using this quantity as a reference parameter. The shear modulus value consistently varied depending on the method used for its calculation.

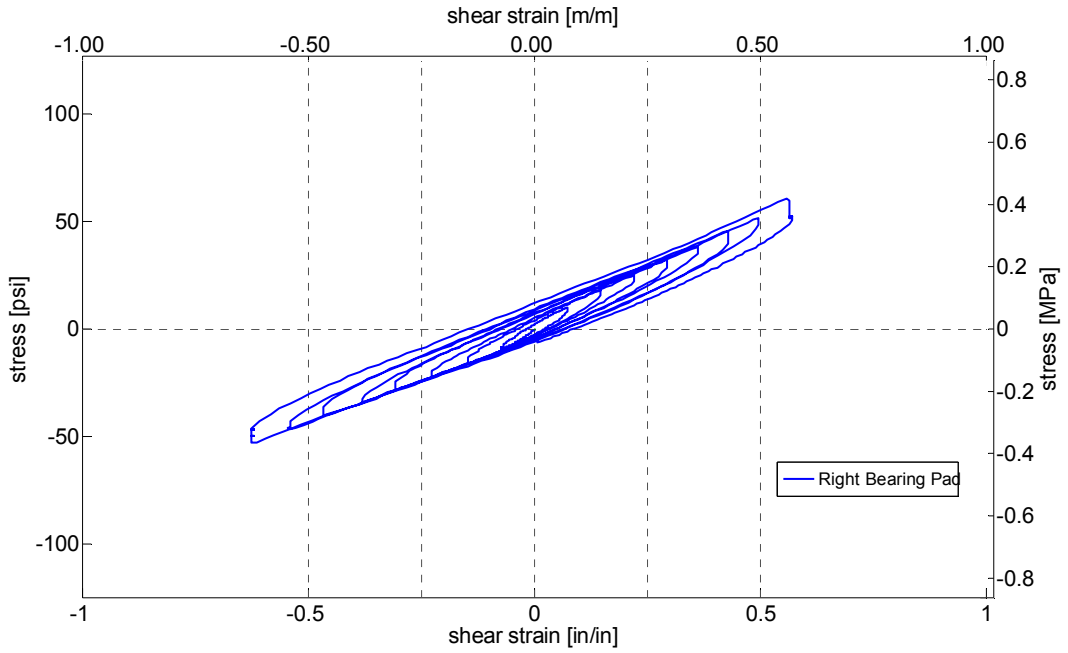

Figure 31. Stress vs. shear strain relationship for Type V- 100 kips (444 kN)

Table 15. (a-c) Shear Modulus according to several test definitions for Type V- 100 kips (444 kN)

Left Bearing Pad						
Shear Modulus Definition	**Direction**	**stress** (psi)	**stress** (MPa)	**G** (psi)	**G** (MPa)	**$G/G_{(0/+50)}$**
0/+.50	One way	56.62	0.3905	113.24	0.7811	1
+/- 50 secant	Two way	56.62/-45.99	.3905/-.3172	102.61	0.7078	0.906
+/- .25 tangent (top line)	Two way	38.62/-6.65	.2664/-.0459	90.54	0.6245	0.800
+/- .25 tangent (bottom line)	Two way	15.13/-25.99	.1044/-.1793	82.24	0.5672	0.726

Right Bearing Pad						
Shear Modulus Definition	**Direction**	**stress** (psi)	**stress** (MPa)	**G** (psi)	**G** (MPa)	**$G/G_{(0/+50)}$**
0/+.50	One way	51.55	0.3556	103.10	0.7111	1
+/- 50 secant	Two way	51.55/-42.5	.3556/-.2931	94.05	0.6487	0.912
+/- .25 tangent (top line)	Two way	32.32/-9.80	.2229/-0.0676	84.24	0.5810	0.817
+/- .25 tangent (bottom line)	Two way	13.42/24.76	.0.0926/-.1708	76.32	0.5264	0.740

Shear Modulus Definition	**$G_{average}$** (psi)	**$G_{average}$** (MPA)
0/+.50	108.17	0.7461
+/- 50 secant	98.33	0.6782
+/- .25 tangent (top line)	87.39	0.6028
+/- .25 tangent (bottom line)	79.28	0.5468

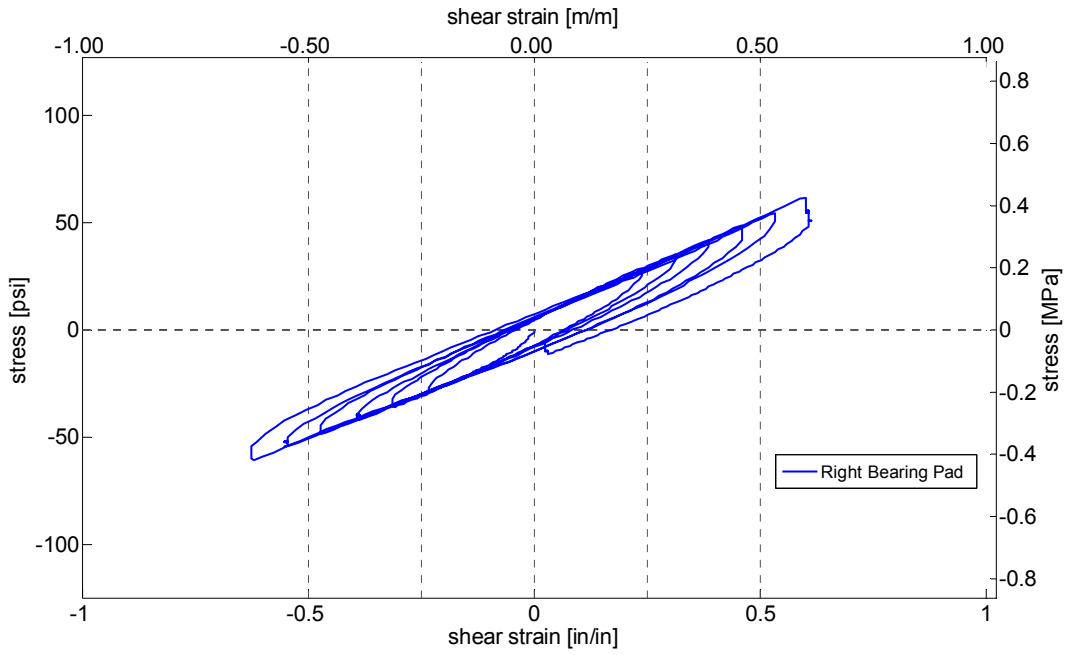

Figure 32. Stress vs. shear strain relationship for Type V- 150 kips (667 kN)

Table 16 (a-c) Shear Modulus according to several test definitions for Type V- 150 kips (667 kN)

Left Bearing Pad						
Shear Modulus Definition	**Direction**	**stress** (psi)	**stress** (MPa)	**G** (psi)	**G** (MPa)	**$G/G_{(0/+50)}$**
0/+.50	One way	57.62	0.3974	115.24	0.7949	1
+/- 50 secant	Two way	57.62/-55.46	.3974/-.3825	113.08	0.7800	0.981
+/- .25 tangent (top line)	Two way	33/-13.46	.2276/-.0928	92.92	0.6409	0.806
+/- .25 tangent (bottom line)	Two way	33/-13	.2276/-.0897	92.00	0.6346	0.798

Right Bearing Pad						
Shear Modulus Definition	**Direction**	**stress** (psi)	**stress** (MPa)	**G** (psi)	**G** (MPa)	**$G/G_{(0/+50)}$**
0/+.50	One way	52.08	0.3592	104.16	0.7184	1
+/- 50 secant	Two way	52.08/-49.8	.3592/-.3435	101.88	0.7027	0.978
+/- .25 tangent (top line)	Two way	30.08/-13.66	.2075/-0.0942	87.48	0.6034	0.840
+/- .25 tangent (bottom line)	Two way	7.169/-31	.0.0494/-.2138	76.34	0.5265	0.733

Shear Modulus Definition	**$G_{average}$** (psi)	**$G_{average}$** (MPA)
0/+.50	109.70	0.7567
+/- 50 secant	107.48	0.7413
+/- .25 tangent (top line)	90.20	0.6222
+/- .25 tangent (bottom line)	84.17	0.5806

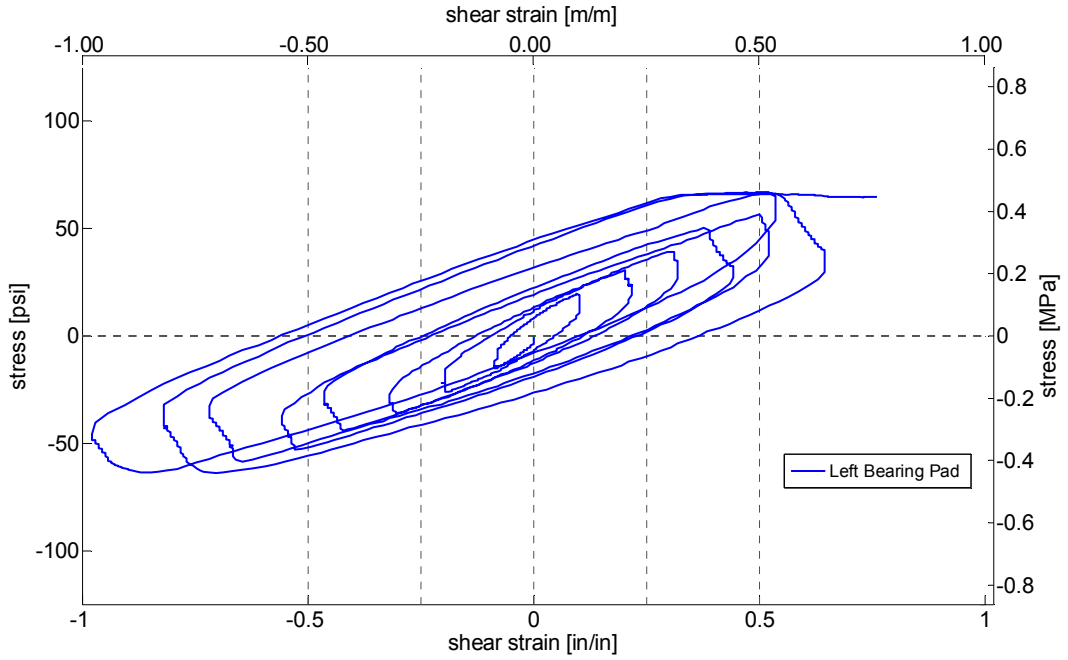

Figure 33. Stress vs. shear strain relationship for Type VI- 50 kips (222 kN)

Table 17. (a-c) Shear Modulus according to several test definitions for Type VI- 50 kips (222 kN)

Left Bearing Pad						
Shear Modulus Definition	**Direction**	**stress** (psi)	**stress** (MPa)	**G** (psi)	**G** (MPa)	**$G/G_{(0/+50)}$**
0/+.50	One way	66.84	0.4610	133.68	0.9221	1
+/- 50 secant	Two way	66.84/-55.69	.4610/-.3841	122.53	0.8451	0.917
+/- .25 tangent (top line)	Two way	60.91/-24.55	.4201/-.1693	170.92	1.1789	1.279
+/- .25 tangent (bottom line)	Two way	-8.6/-41.26	.0593/-.2846	65.32	0.4505	0.489

Right Bearing Pad						
Shear Modulus Definition	**Direction**	**stress** (psi)	**stress** (MPa)	**G** (psi)	**G** (MPa)	**$G/G_{(0/+50)}$**
0/+.50	One way	-	-	-	-	-
+/- 50 secant	Two way	-	-	-	-	-
+/- .25 tangent (top line)	Two way	64.66/-4.387	.4456/-0.0303	138.09	0.9525	-
+/- .25 tangent (bottom line)	Two way	9.84/-54.31	.0679/-.3746	128.30	0.8849	-

Shear Modulus Definition	**$G_{average}$** (psi)	**$G_{average}$** (MPA)
0/+.50	133.68	0.9221
+/- 50 secant	122.53	0.8451
+/- .25 tangent (top line)	154.51	1.0657
+/- .25 tangent (bottom line)	96.81	0.6677

- shear strains did not reach a value higher of 50%.

The right bearing pad for the Type VI pad tests did not reach shear strains higher of 50%. Consequently, there is not enough information to obtain the shear modulus using definition 1 and 2 (blank spaces in Table 17 through Table 19).

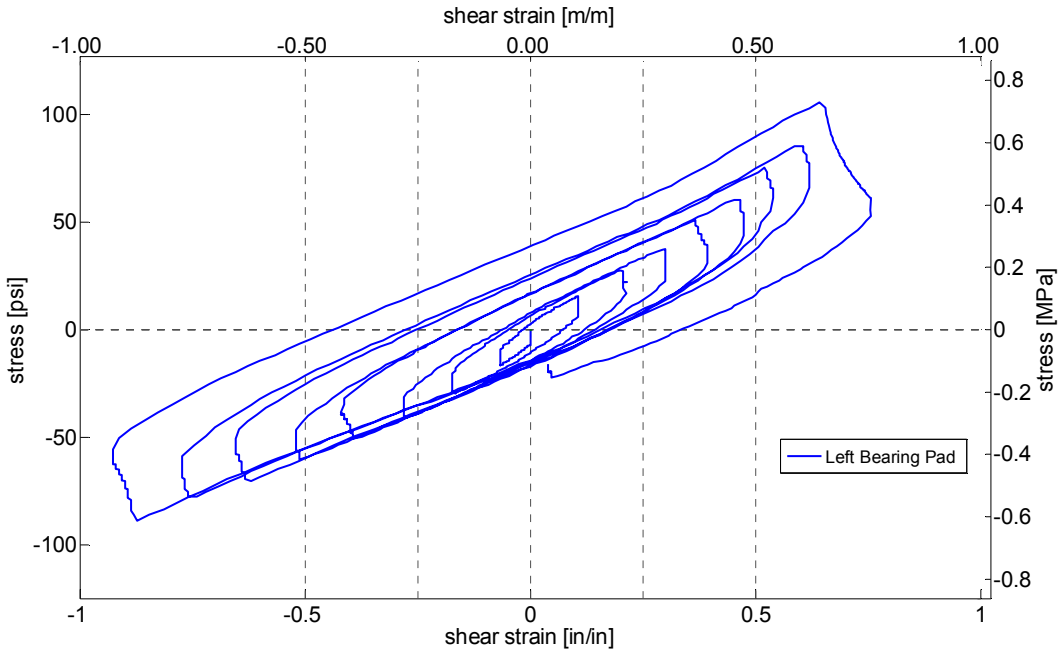

Figure 34. Stress vs. shear strain relationship for Type VI- 100 kips (444 kN)

Table 18.(a-c) Shear Modulus according to several test definitions for Type VI- 100 kips (444 kN)

Left Bearing Pad						
Shear Modulus Definition	**Direction**	**stress** (psi)	**stress** (MPa)	**G** (psi)	**G** (MPa)	**$G/G_{(0/+50)}$**
0/+.50	One way	88.14	0.6079	176.28	1.2159	1
+/- 50 secant	Two way	88.14/-59.09	.6079/-.4076	147.23	1.0155	0.835
+/- .25 tangent (top line)	Two way	62.06/-6.67	.4281/-.0460	137.46	0.9481	0.780
+/- .25 tangent (bottom line)	Two way	8.02/-39.53	.0553/-.2727	95.10	0.6560	0.539

Right Bearing Pad						
Shear Modulus Definition	**Direction**	**stress** (psi)	**stress** (MPa)	**G** (psi)	**G** (MPa)	**$G/G_{(0/+50)}$**
0/+.50	One way	-	-	-	-	-
+/- 50 secant	Two way	-	-	-	-	-
+/- .25 tangent (top line)	Two way	64.62/-6.67	.4457/-0.0460	142.58	0.9834	-
+/- .25 tangent (bottom line)	Two way	.248/-49.8	.0017/-.3435	100.10	0.6904	-

Shear Modulus Definition	**$G_{average}$** (psi)	**$G_{average}$** (MPA)
0/+.50	176.28	1.2159
+/- 50 secant	147.23	1.0155
+/- .25 tangent (top line)	140.02	0.9658
+/- .25 tangent (bottom line)	97.60	0.6732

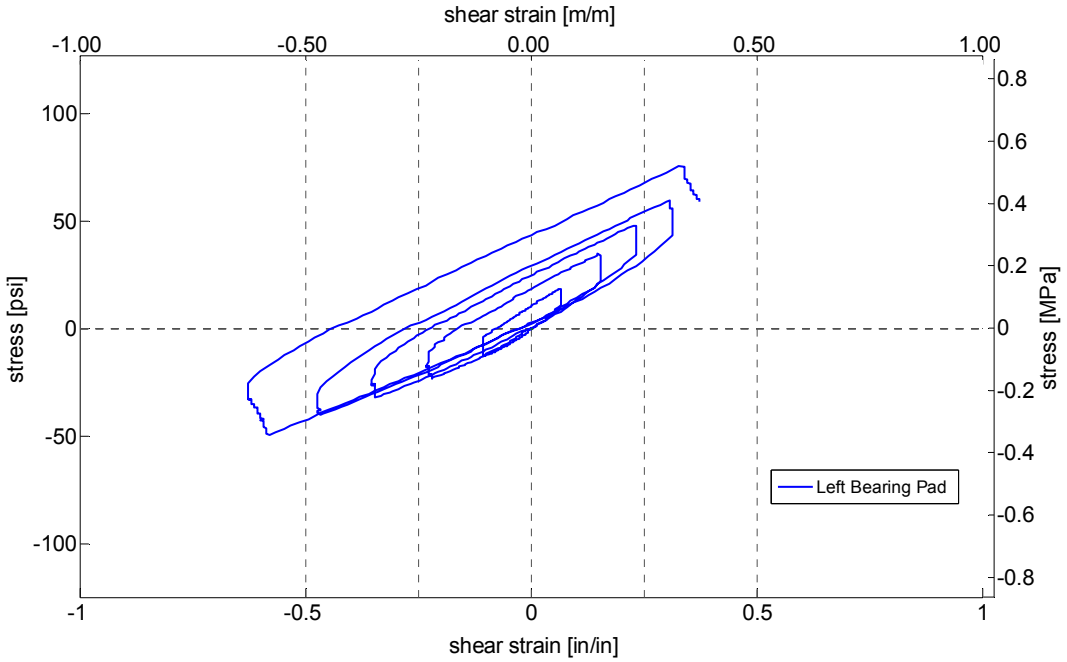

Figure 35. Stress vs. shear strain relationship for Type VI- 150 kips (667 kN)

Table 19.(a-c) Shear Modulus according to several test definitions for Type VI- 150 kips (667 kN)

Left Bearing Pad						
Shear Modulus Definition	**Direction**	**stress** (psi)	**stress** (MPa)	**G** (psi)	**G** (MPa)	$G/G_{(0/+50)}$
0/-.50	One way	42.13	0.2906	84.26	0.5812	1
+/- 50 secant	Two way	-	-	-	-	-
+/- .25 tangent (top line)	Two way	68.14/18.48	.470/-.1275	99.32	0.6851	1.179
+/- .25 tangent (bottom line)	Two way	31.88/-24.15	.2199/-.1666	112.06	0.7729	1.330

Right Bearing Pad						
Shear Modulus Definition	**Direction**	**stress** (psi)	**stress** (MPa)	**G** (psi)	**G** (MPa)	$G/G_{(0/+50)}$
0/+.50	One way	-	-	-	-	-
+/- 50 secant	Two way	-	-	-	-	-
+/- .25 tangent (top line)	Two way	69.72/-8.0	.4809/-0.0552	142.58	0.9834	-
+/- .25 tangent (bottom line)	Two way	50.36/-38.58	.3474/-.2661	100.10	0.6904	-

Shear Modulus Definition	$G_{average}$ (psi)	$G_{average}$ (MPA)
0/+.50	84.26	0.5812
+/- 50 secant	-	-
+/- .25 tangent (top line)	120.95	0.8343
+/- .25 tangent (bottom line)	106.08	0.7317

The test on the Type VI bearing pad with 150 kips (667 kN) of axial load was stopped at 1.25 in (31.75 mm) of displacement because the test-set up became unstable and the bearing pad failed (Figure 34). The higher force required to displace this bearing pad caused significant rotation of the steel plates and steel beams at the bottom of the plates. The bearing pads failed when the elastomer and the steel separated in the bearing pad. Table 19 (a-c) show a decrease in shear modulus for this particular case. Failure of this pad likely caused the degradation in the shear modulus properties.

In summary, the Type VI bearing pad was observed to have a higher shear modulus than the Type V pad. Higher hardness is a rough indicator of a higher shear modulus, and the Type V and VI pads used in these tests have a hardness magnitude of 50 and 60, respectively.

It was noted that the concrete block slightly rotated during the tests. This situation could contribute to the non-uniform application of the load on the bearing pads. Here, it is assumed that the force transferred to each bearing pad is the same (half of the total force). As this assumption may not be exactly the case, the slight rotation could explain the

differences in the shear modulus values between the right and left bearing pads in addition to differences resulting from manufacturing variation.

Yura et al (2001) recommended the use of the shear modulus calculated between 0 to 50% or between -50% and 50% shear strain. This approach is based in the shear strain limit criteria established in the AASHTO LRFD Bridge Design Specifications. The maximum design strain at serviceability level specified by AASHTO is calculated at a displacement of +/- 0.5 times the thickness of the bearing pad, which corresponds to a 50% shear strain. Strains higher than 50% could cause significant rollover of the edges and delamination due to fatigue. Under such situation, the effectiveness of the bearing pads in transferring the forces of the girders may diminish.

Comparison

Yura et al (2001) performed several tests on tapered and non tapered bearing pads and reported the values shown in Table 20 for shear modulus according to the 50% shear strain definition. The NEO nomenclature in Table 20 stand for bearing pads made from neoprene, the same material type as the bearing pads tested in this study. Table 20 shows the values of shear modulus at different levels of hardness compared to values specified by the manufacturer using an approximate axial load of 57 kips.

Table 20. Shear modulus obtained in the Yura et al tests (2001) from NCHRP report 449

Specimen Type	Shear Modulus MPa (psi)		Hardness (Durometer)
	Specified	Report	
NEO100	0.69 (100)	0.63 (92)	53
NEO150	1.03 (150)	1.06 (154)	66
NEO200	1.38 (200)	1.25 (182)	70

Table 21. Comparison of the shear modulus (G) obtained in all the tests for Type V and Type VI bearing pads

	Type V			Type VI		
Test Name	P_{ave} kips (kN)	G (psi)	G (MPa)	P_{ave} kips (kN)	G (psi)	G (MPa)
50	58.54 (260)	101.00	0.70	44 (196)	133.68	0.92
100	94.5 (420)	108.70	0.75	100.05 (444)	176.28	1.22
150	153.39 (680)	109.70	0.76	140 (623)	84.26	0.58

The shear modulus obtained for a hardness of 53 and 66 was 92 psi (0.63 MPa) and 154 psi (1.06 MPa), respectively as shown in Table 20. In this study, for the Type V bearing pad (50 hardness) the shear modulus obtained ranges between 101 to 109.7 psi (0.70-0.76 MPa) using the 0-50% shear modulus definition. For the Type VI bearing pad (60 hardness) the values range between 133.7 to 176.3 psi (0.92-1.22 MPa). Values for the Type VI bearing pad with applied axial load of 150 kips (667 kN) are not used for comparison due to failure of the pad during this test. Although the compounds in the neoprene material vary among manufacturers, values obtained in this study are comparable to those found in the literature when the 150 kip load Type VI test is ignored as a possibly isolated incident.

Bearing pads shear deformation modes

Figure 36 (a-b) and Figure 37 (a-b) present the shear deformation of the bearing pads for several displacement levels of the concrete block. Figure 36 shows the deformation of the bearing pad for one inch of displacement. Figure 37 shows the shear deformation pattern when the concrete block reaches a displacement of 1.5 inch. It is noted in the pictures that the displacement profile of the bearing pad is generally non uniform as the load is increased.

Figure 36. (a-b). Bearing pad shear deformations for 1 inch (25.4 mm) block displacement (Type V)

Figure 37. (a-b) Bearing Pad deformations for 1.5” inch (38.1 mm) block displacement (Type V)

(Type VI Bearing Pads)

Figure 38. (a-b) Bearing Pad deformations for 1 inch (25.4 mm) block displacement (Type VI)

Figure 39. (a-b) Bearing Pad deformations for 0.75 inch (19.05 mm) block displacement (Type VI)

Figure 38 (a-b) and Figure 39 (a-b) present the shear deformation of the Type VI bearing pads at different points during the test. The first set (Figure 38) show the deformation of the bearing pad for 1 inch of block displacement, with 50 kips of axial load. Figure 39 shows the shear deformation pattern when the concrete block reaches a displacement of 0.75 inch.

Bearing Pad Compression Tests

The response of the bearing pad under pure compression forces was also evaluated. One Type V and one Type VI elastomeric bearing pad was tested under a uniform compressive load. The elastomeric bearing pads were loaded to 200 kips while the vertical compression was monitored in four locations, each being 8-¼ inches from the corner of the bearing pad. Figure 40 illustrates the linear potentiometer layout and Figure 41 presents a picture of the actual test set up.

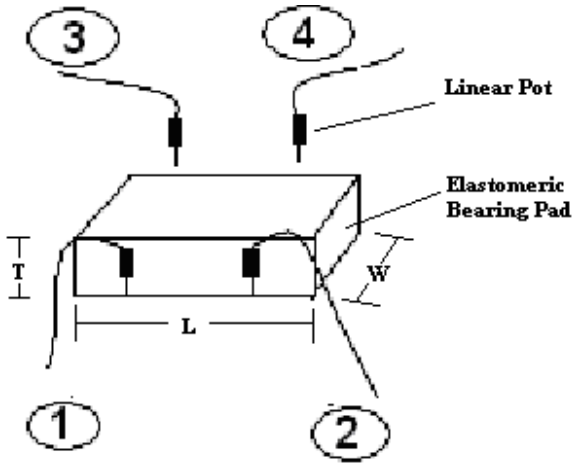

Figure 40. Illustration of linear pot layout on elastomeric bearing pad

Figure 41. Test setup of compression test on elastomeric bearing pad

For the Type V bearing pad, one of the linear pots did not record accurately and is not presented in the response data. Figure 42 and Figure 43 show the compressive stress versus compressive strain of Type V and Type VI bearing pads, respectively.

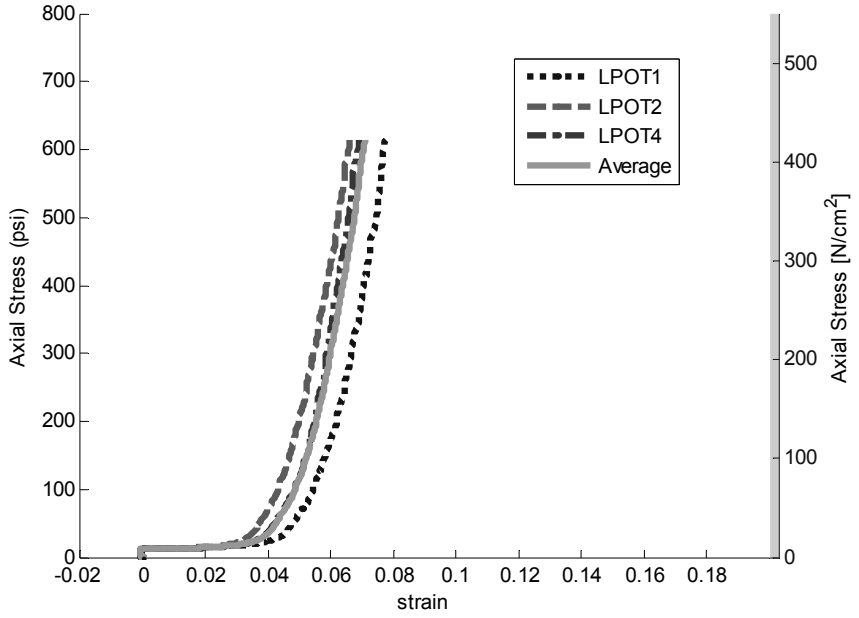

Figure 42. Compression test results for Type V BP

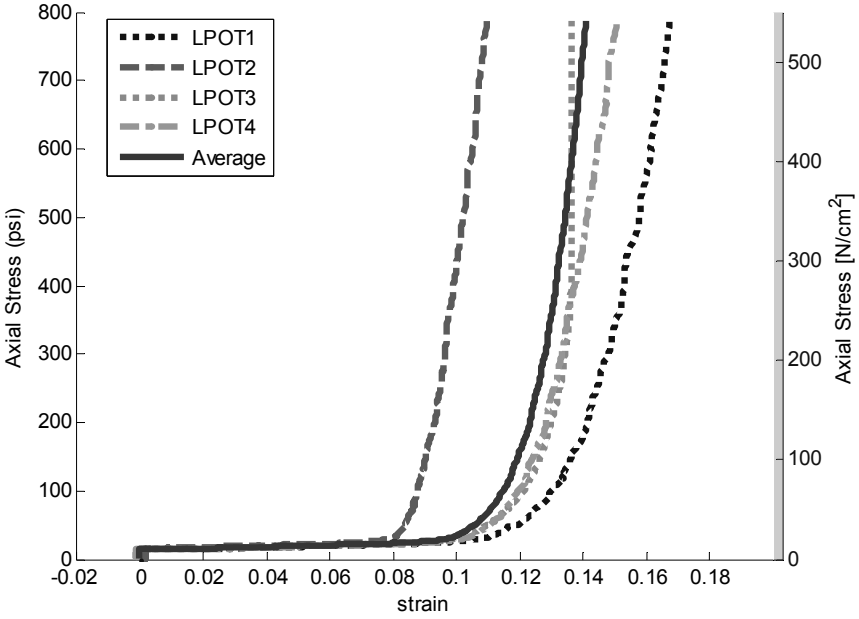

Figure 43. Compression test results for Type VI BP

The test data show that initially the bearing pad is not sustaining the applied load due to the compression of the soft neoprene materials. As the applied load continues to increase, the compressive strength is mobilized. As shown in Figures 42 and 43, the compressive strain where this situation occurs depends on each measuring device and is most likely to be affected by the slight uneven compression surfaces of the plates used in the test setup (Figure 41). Based on the averages of these measurements it was determined that the compressive stiffness starts to increase at a compressive strain of 0.035 inch/inch and 0.9 inch/inch for the Type V and Type VI bearing pads, respectively. It can also be observed that the Type VI bearing pad has a higher compressive capacity than the Type V bearing pad. In this case, the compressive modulus for the Type V is estimated equal to approximately 3000 psi versus 6000 psi for the type VI. According to Yura et al (1995), the hardness of the material and the shape factor influence the bearing pad compressive behavior. The compressive stiffness increases with the increase of hardness values.

Summary

The performance testing program aimed at characterizing the rotational stiffness of the substructure to superstructure connection within the bridge system taking into the account the relative stiffness of the other components. The program included testing of Type V and VI bearing pads under the combined action of compression and shear, and testing of the bearing pads in pure compression.

The shear index testing provided shear modulus values of Type V and Type VI bearings pads. In general, these measurements were similar to those measured by Yura et al. (2001), but extended those results to higher axial loads. The data also indicated that the behavior of these bearing pads under combined shear and compression was highly nonlinear, and that energy dissipation tended to increase as the axial load was increased.

Data from the compression tests provided some compressive properties of the bearing pads under study. Measured elastic moduli of the Type V pads were approximately half that measured for the Type VI pad. The information from these index tests will be used

to characterize the compressive and rotational stiffness properties of the entire connection for the full-scale model in Chapter 5.

CHAPTER 5. FULL SCALE TESTING

A series of full scale tests were performed to study the behavior of the substructure to superstructure connections in bearing–supported bridge superstructures with diaphragms connecting adjacent girders. A bearing–supported connection has several important elements including the bearing pads, sole plates, anchor bolts and diaphragm. These are described as follows:

Bearing Pads

Bearing pads are mechanical devices that are used to transmit the forces or loads from the superstructure to the substructure (piles or drilled shafts). This study was focused on connections using elastomeric reinforced bearing pads, shown in Figure 44. The general properties of elastomeric bearing pads are identified by the durometer number, which is a measure of the stiffness or shear modulus of the material. The performance testing program was conducted using the same Type V and Type VI bearing pads used in the index testing program described in Chapter 4. The properties of the pads used in testing were shown in Table 13.

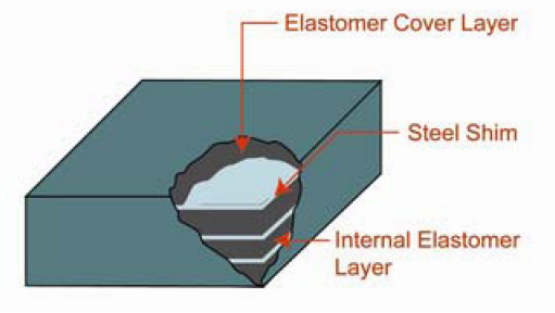

Figure 44. Components elastomeric reinforced bearing pad (from www.hdrinc.com)

Sole Plates and Anchor bolts

The sole plates and anchor bolts connect the girders and cap beam. The bearing pads are placed at the girder locations on the top of the cap beam, and the sole plates are placed on the top of the bearing pad. Steel anchor bolts of 2 inch (50.8 mm) diameter previously embedded 18 inch (0.46 m) into the cap beam are bolted to the sole plates. Next, the sole plates are welded to an embedded plate cast into the bottom of the girders. Normally, the

sole plate is welded to the girder plate on each side of the girder, parallel to the girder length. Because that weld would have to be performed upside down, the weld length in this test was perpendicular to the girder on each side of the diaphragm. Figure 46 shows how all the components are placed together.

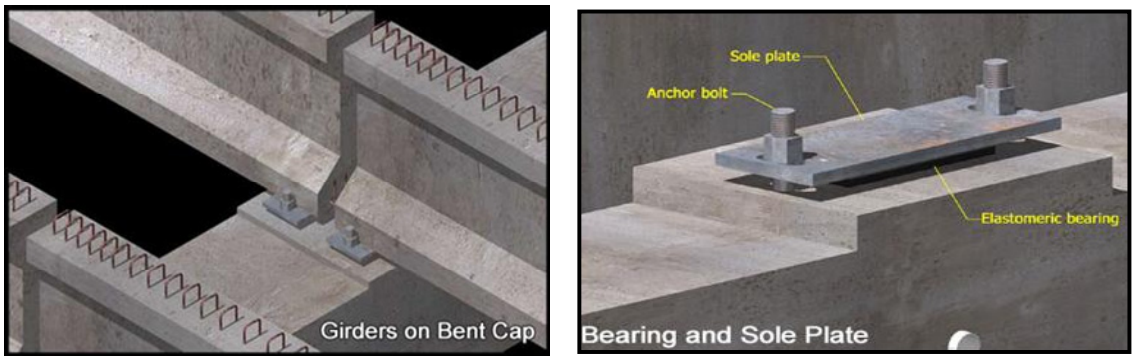

http://www.ncdot.org

Figure 45. Connection details (from www.ncdot.org)

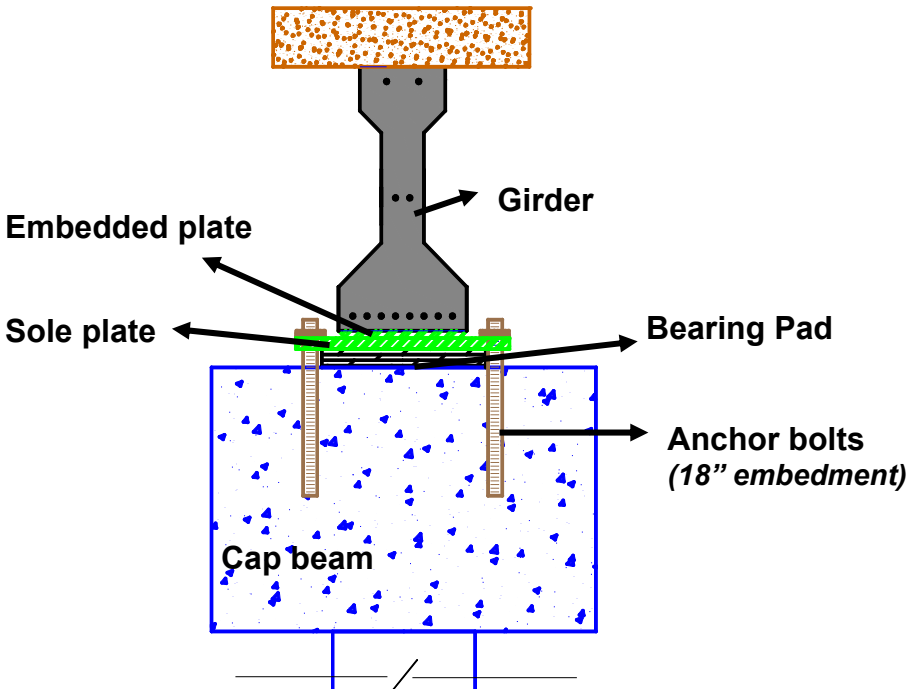

Figure 46. Connection elements in a bearing-supported bridge

Diaphragm

A diaphragm is used to connect two girders together and to form a system that behaves as a single unit. The diaphragm also distributes the forces or loads throughout the girders. In addition, the girders are made continuous for live load by the use of a diaphragm, which provides benefits such as the ability to construct longer spans, improve durability and lower the bridge costs. Figure 47 presents a diagram of how the reinforcing steel is placed throughout the diaphragm. The reinforcing steel consists of several longitudinal bars running all the way through the diaphragm and stirrups that are extended into the deck slab.

Figure 47. Diaphragm reinforcing steel (from www.ncdot.org)

Experimental Test Set-Up

The tests were performed in the North Carolina State University Constructed Facilities Laboratory (CFL). The connection was tested upside down as shown in Figure 48. The setup consisted of a steel frame to which a 220 kip (979 kN) actuator was connected. The actuator was used to apply the lateral load during the tests. The steel frame was rigidly attached to the laboratory strong floor using four 1-3/8 inch (34.9 mm) Dywidag bars and a bracing system was provided for stability. Five 60 ton (534 kN) jacks were used to apply axial loads to the column and bearing pads to simulate gravity effects. The axial load at the bearing pads was distributed by the use of two HSS beams at each bearing pad location (Figure 49). Figure 50 and Figure 51 show photographs of the test setup taken from various angles.

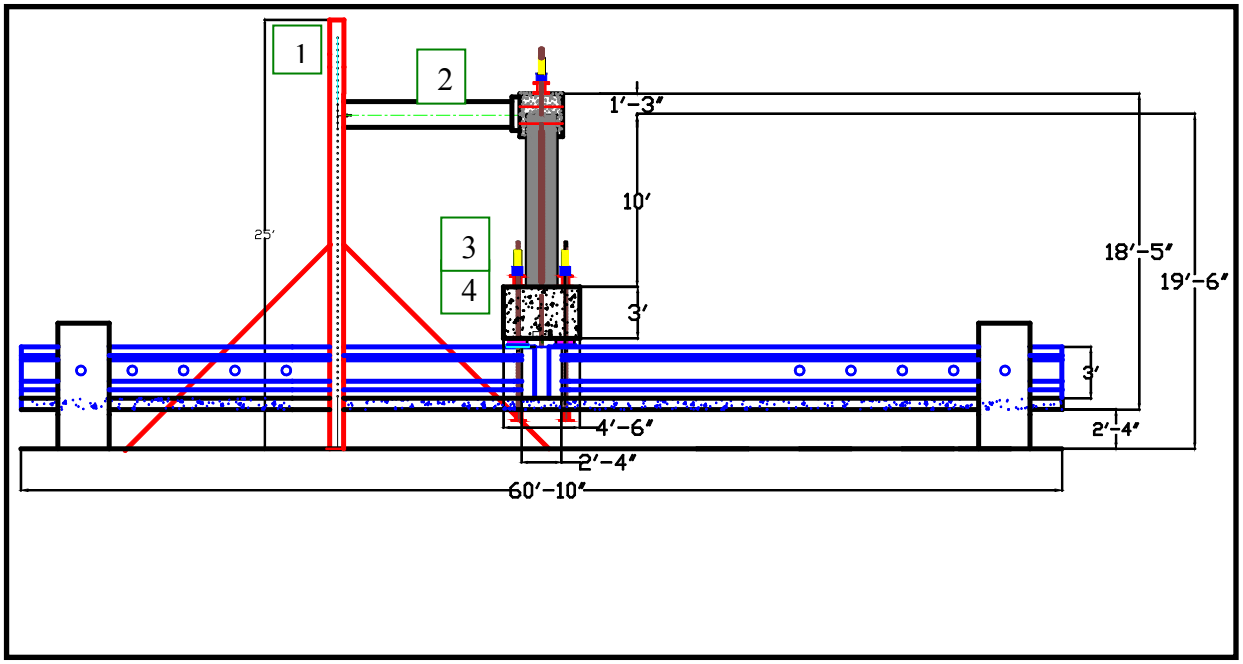

1. Steel Frame and braces
2. 220 kips actuator (40” stroke)
3. Five (5) 60 ton hydraulic jacks
4. Four (4) HSS beams (48 “ length)

Figure 48. Experimental test set-up (lateral view)

Figure 49. View of the four 60 ton jacks used to apply axial load to the bearing pads.

Figure 50. Views of the test set-up

Figure 51. General View of Test set-up

Figure 50 shows the actuator as attached to the pile/shaft to apply the lateral load.

Figure 51 shows the prepared sample ready for testing. .

Figure 51 also shows, at the far left, the support connection for the girder where pins were inserted into pre-drilled holes to create a pin connection that allows rotation but no translation.

Two AASHTO Type II girders of 30 ft (9.14 m) long were used during the tests. The dimensions of these girders as well as the number of prestressed tendons in each girder are shown in Figure 52. The girders were made continuous with a diaphragm following the NCDOT specifications described above.

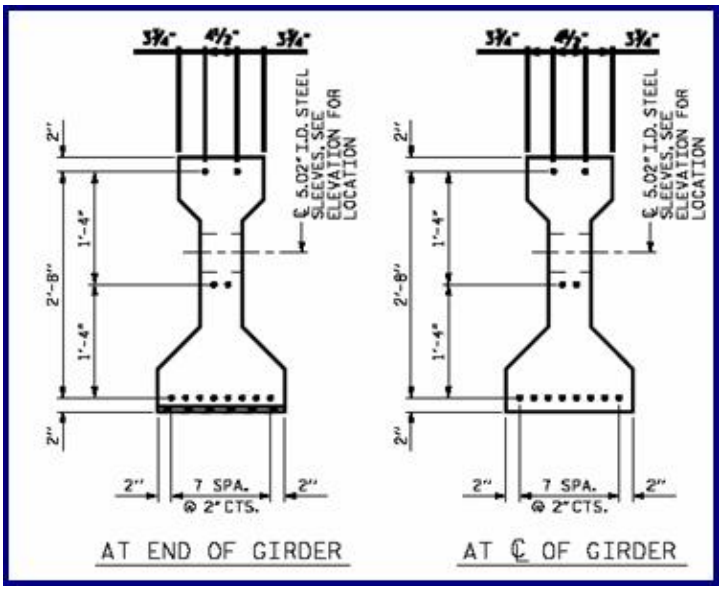

Figure 52. AASHTO Type II girder details

The girders ends were connected by means of a pinned connection. Figure 53 shows a detailed cross section of the pinned connection which consists of two L-shaped concrete blocks at each end and a steel rod of 5 in (127 mm) diameter. The steel rod was inserted through a cast in place steel guide tube of 5.02 in diameter (127.64 mm) to minimize any movement other than rotation of the girder relative to the steel rod and support blocks. Thus, the location of the pin represents a point of inflection in the moment profile.

Figure 54 and Figure 55 show the alignment of the support blocks and placement of the pin rod throughout the girders.

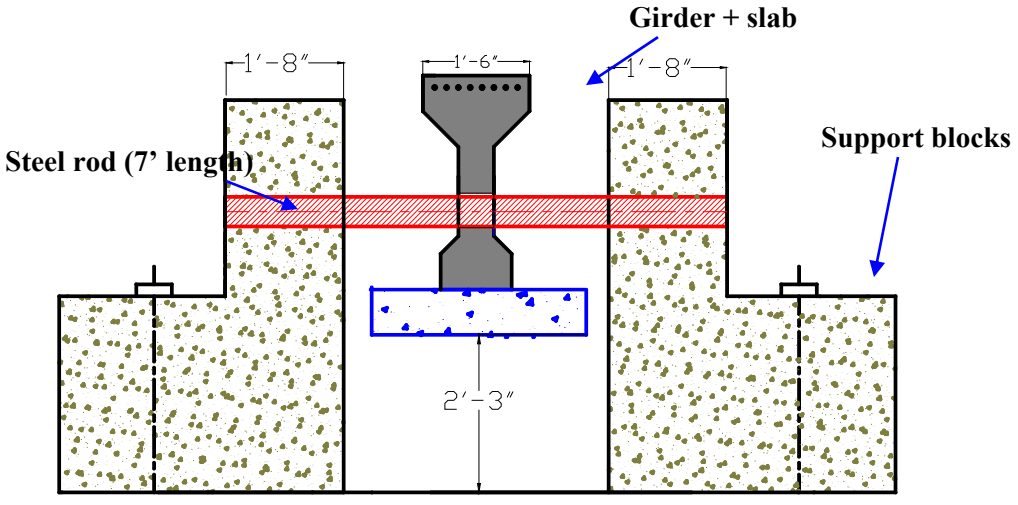

Figure 53. Pinned connection at girder ends

Figure 54. Support block alignment

Figure 55. Preparation for pin placement

As mentioned earlier, three different types of piles that were 10 ft (3.05 m) long were tested. The test piles were circular steel reinforced, square steel reinforced, and HP steel sections. Figure 56 shows the three sections used during testing; Figure 57 and

Figure 58 present the construction and casting phase of the test pile specimens including the caps.

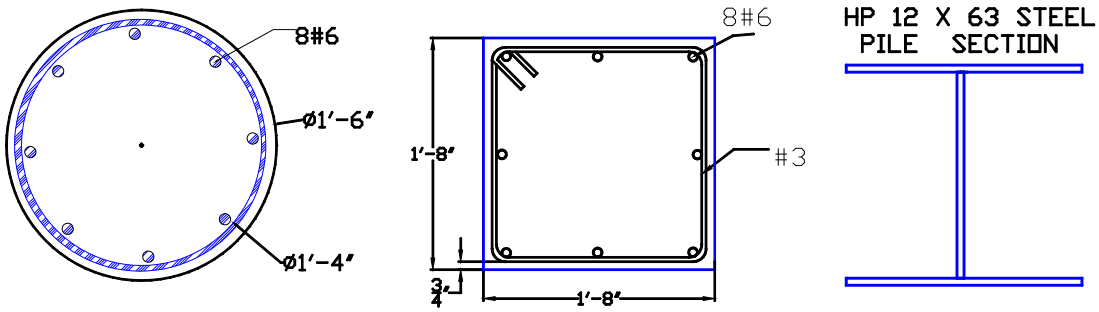

Figure 56. Test piles cross sections

Figure 57. Construction of the test piles

Figure 58. Casting of the test piles

Instrumentation

The instrumentation used to monitor the system response under the applied loading consisted of a total of 55 sensors for monitoring strain, deformation, and stresses. Three load cells were used to monitor the axial load in the bearing pads and test pile (will be referred to as "column.") String potentiometers ("pots") were used to measure displacements at the bottom of the slab/girder, and at the cap beam and top of the column. Linear potentiometers were used to measure displacements/curvatures at the column, compression, and shear deformation of the bearing pads. Linear potentiometers were also used to measure any displacement/slippage of the bearing pads in the transverse direction to the lateral load. Twelve strain gages were used to monitor the strain in the longitudinal reinforcing bars in the columns. Also, three inclinometers were used to measure rotation at the diaphragm, at the top of the column and at the cap beam. Figure 59 shows a diagram of the position of all the instruments in the test set-up. In this figure, LC, SP, P, CLIN-# stand for load cell, string pot, linear pot, and inclinometer, respectively.

Test Matrix

A total of 42 tests were performed with the different piles and bearing pad types utilized in the study. Each concrete pile was subjected to three different levels of axial load ratio (ALR). The H-Pile was not loaded axially due to the insensitivity of steel stiffness to axial loads. In addition, for each ALR, the axial load on the bearing pads was varied to three levels (P1, P2, P3). Testing was performed for each bearing pad/pile combination. Lateral load was applied to the test samples until the yield displacement of the pile, and in some of the cases in the inelastic range (the starred cases in Figure 60). The lateral loading scheme is explained in detail in the next section.

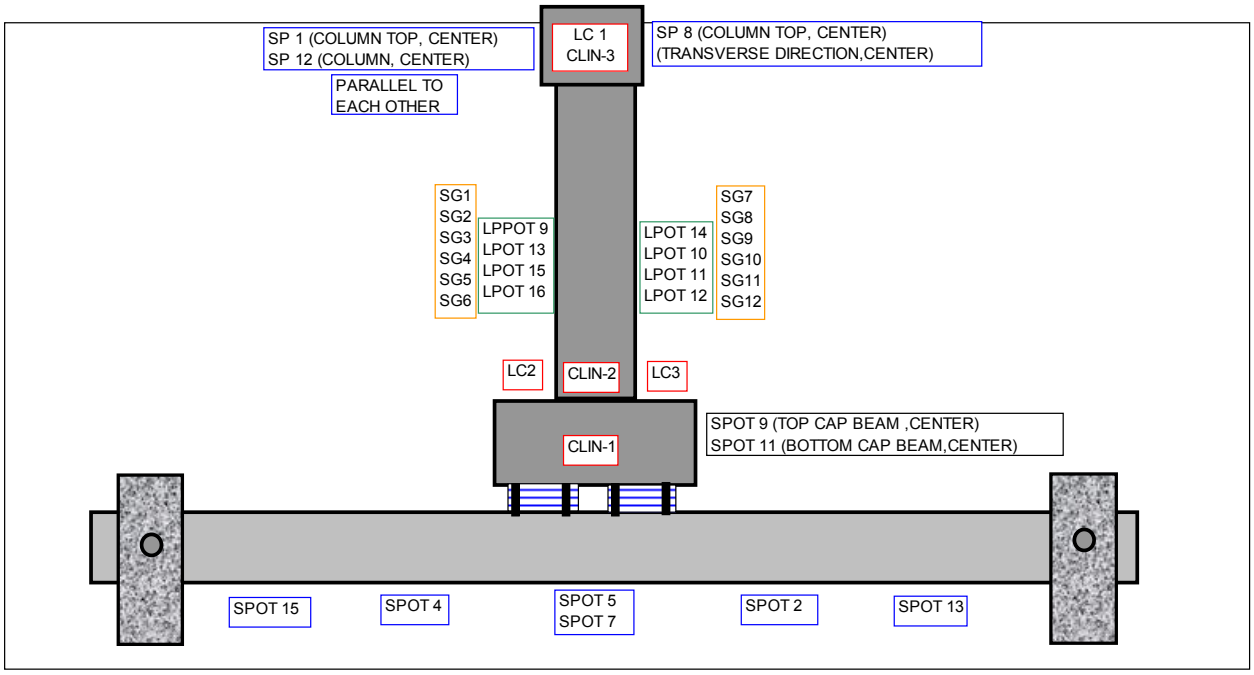

(a)

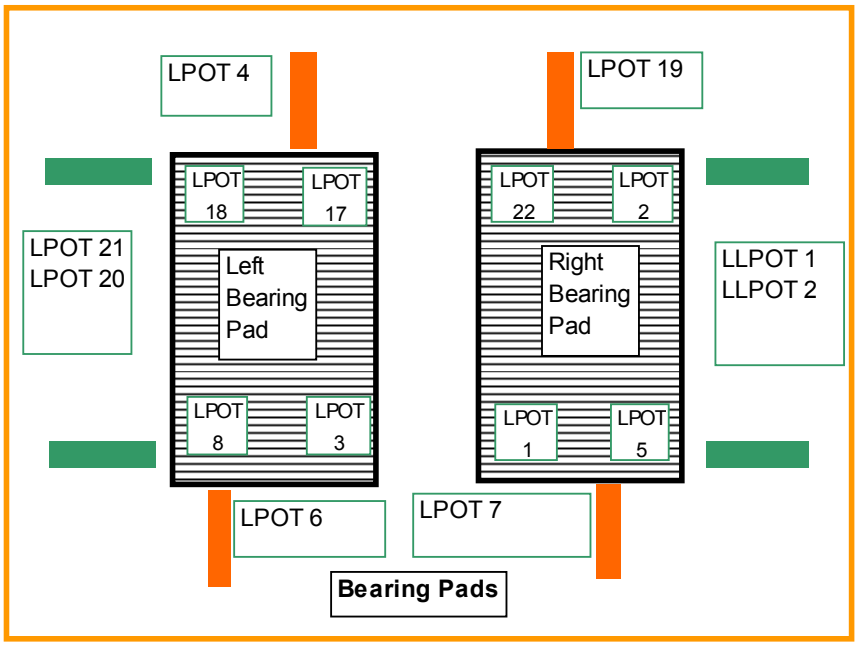

(b)

Figure 59. Schematic showing positions of sensors a) section view of the test sample and b) plan view of the bearing pads.

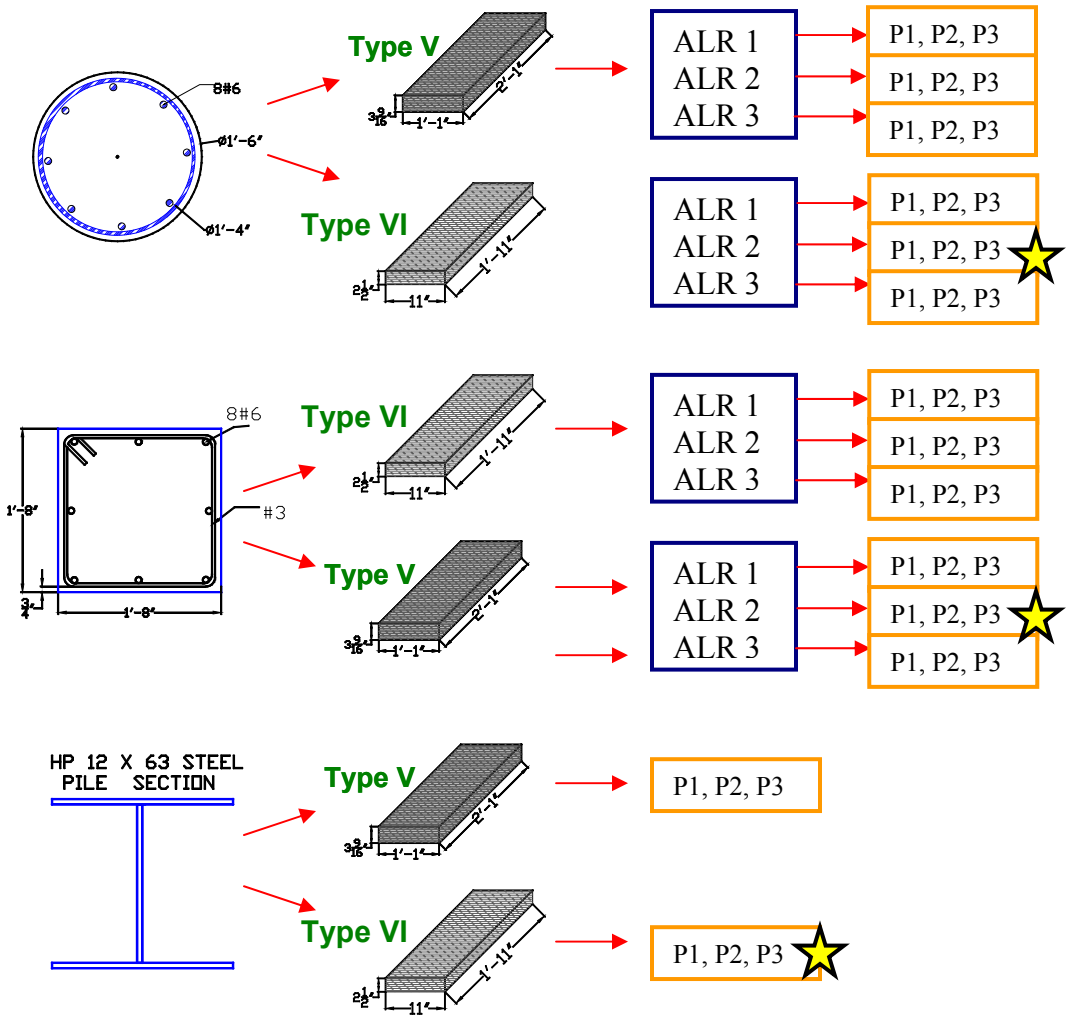

Figure 60. A Summary of number and type of tested performed for each Pile section: Test Matrix

Loading Protocol

The lateral loading history for all the tests consisted of reversed single displacement cycles to increments of 0.75 inches (19.05 mm) until the yield displacement for each case was reached. The computed yield displacement for square and circular piles was approximately 3 inches (76.2 mm). For the H-pile, the yield displacement was computed to be approximately 6.0 inches (152.4 mm). The loading history is shown in Figure 61 for the concrete piles. One case with each pile was subjected to inelastic/ductility cycles (see the starred cases in Figure 60).

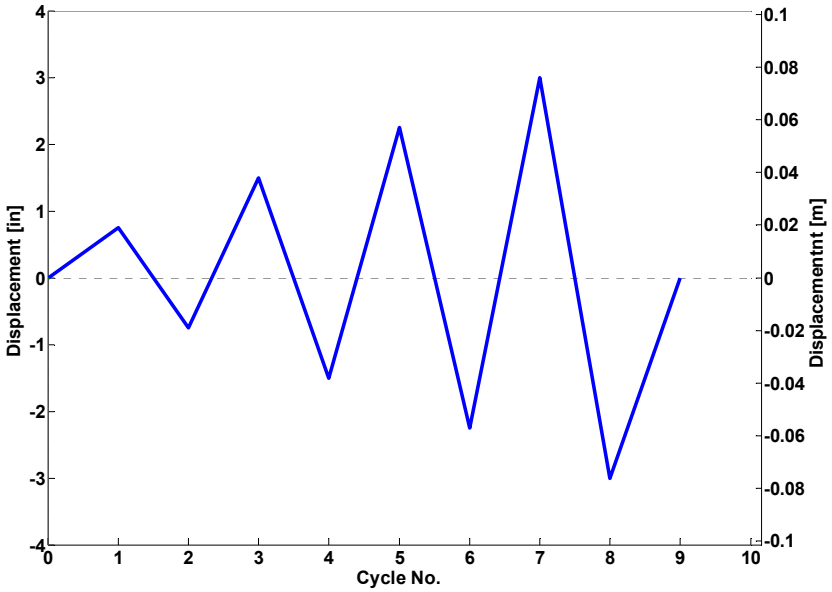

Figure 61. Lateral loading history of concrete piles for elastic cycles

Table 22, 23, and 24 present the axial loads that were applied during each test case. Three different axial load ratios (ALR) were applied (4, 6 and 8 %) to the circular pile. The axial load ratios were changed to 3, 4 and 5 % for the square pile. This was due to limitations in the yield force of the bar and load cell capacity which may be exceeded with the use of 6% or higher axial load percentage in this case. The axial load at the bearing pads (P1, P2, and P3) were obtained by relating the pile to the number of girders/pads in a real bridge. The H-Pile cases were tested without any axial load in the column. The relationship between the axial load in the pile to axial load in the bearing pads was performed assuming an axial load in the pile of 109 kips (485 kN).

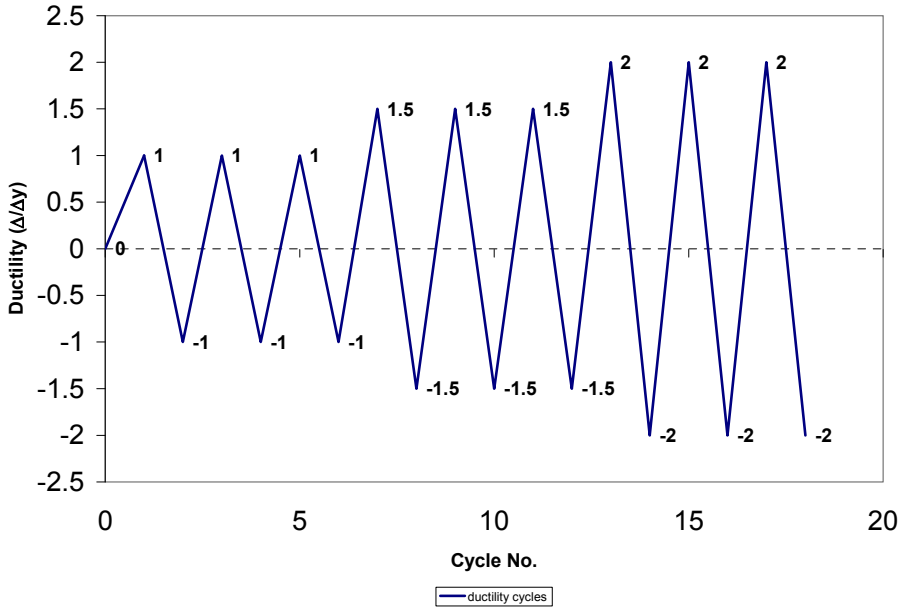

Figure 62. Lateral loading history for ductility cycles

Table 22. Loads for circular pile cases

Case	ALR (%)	Column	Load on one Bearing Pad		
		P kips (kN)	P1 kips (kN)	P2 kips (kN)	P3 kips (kN)
1	**4**	46 (205)	11 (51)	17 (76)	23 (102)
2	**6**	69 (307)	17 (76)	26 (116)	34 (151)
3	**8**	92 (409)	23 (102)	34 (151)	46 (205)

Table 23.Loads for square pile cases

Case	ALR (%)	Column	Load on one Bearing Pad		
		P kips (kN)	P1 kips (kN)	P2 kips (kN)	P3 kips (kN)
1	**3**	54 (240)	13.5 (60)	20 (89)	27 (120)
2	**4**	72 (320)	18 (80)	27 (120)	36 (160)
3	**5**	90 (400)	23 (102)	34 (151)	45 (200)

Table 24. Loads for HP pile cases

Case	Column	Load on one Bearing Pad		
	$P_{assumed}$ kips (kN)	P1 kips (kN)	P2 kips (kN)	P3 kips (kN)
1	109 (485)	27 (120)	41 (182)	55 (245)

The first case tested was for the circular pile under 4% axial load ratio with Type V bearing pads with pad load of P1 (see Figure 62.) The testing continued after increasing the bearing pad loads for a given axial load ratio on the pile. Once testing on the Type V bearing pad was completed, the Type VI bearing pad was tested. The same testing sequence was applied on the Type VI bearing pad within the system, except that after completion of the first loading protocol (elastic cycles), the second loading protocol was applied until a ductility of 1.5 was achieved on the column with an axial load ratio (ALR) of 6% and a bearing pad load of P3.

The second phase utilized the square pile. This phase began with using the Type VI bearing pad with increasing bearing pad load and then increasing the axial load ratio. For the testing on the Type V bearing pad, the axial load sequence followed was 3%, 5%, and 4%, respectively. The inelastic cycles were performed on the Type V bearing pad at load level of P3, using the 4% axial load ratio.

The third testing phase concluded with testing of the H-Pile. Axial load was not applied to the H-pile as no change in its stiffness is expected with varying axial load. The first testing protocol utilized Type V bearing pad and the second utilized Type VI pad.

Calculation of theoretical first yield

The theoretical first yield displacement of a reinforced concrete section is defined at the point in which first yield of the tensile reinforcement occurs. The yield strain of the tensile reinforcement is expressed in Equation 8,

Equation 8

$$\varepsilon_y = \frac{F_y}{E} = 0.002$$

Where, F_y and E are the yield strength and modulus of elasticity of the steel, respectively.

This point can be represented graphically in a moment-curvature relationship or in a strain profile of a reinforced concrete section as shown in Figure 63.

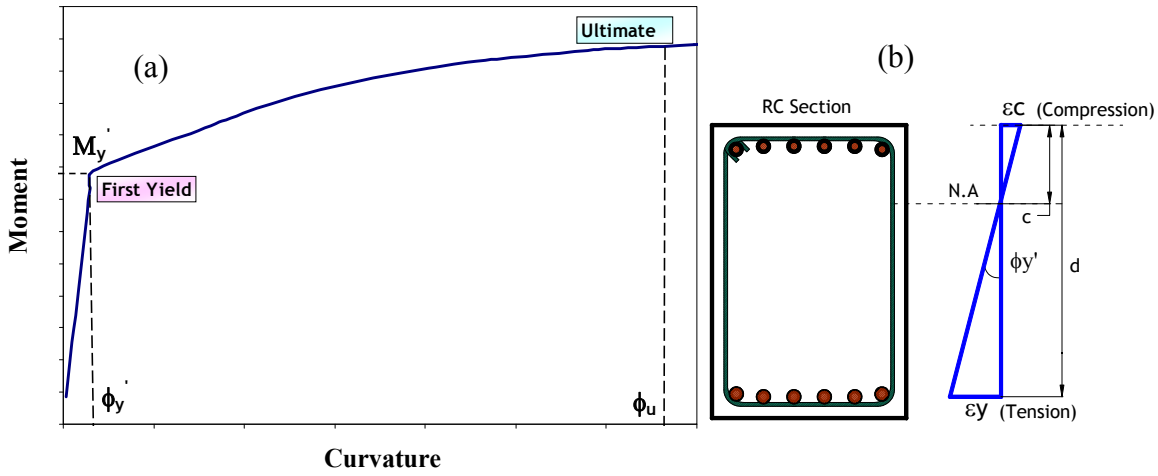

Figure 63. Moment-curvature (a) and strain profile of a RC section at first yielding (b)

The first yield curvature is needed in order to obtain the first yield displacement. Moment-curvature analyses are performed on the desired section to obtain the curvature at first yield of the reinforcement. Then, the first yield curvature is obtained through Equation 9.

Equation 9

$$\phi_y' = \frac{\varepsilon_y}{(d - c)}$$

Where, ε_y is yield strain in Equation 8, d is the depth of the section to the centroid of the tensile reinforcement, and c is the corresponding neutral axis depth.

Then, the first yield displacement can be computed using the following relationship.

Equation 10

$$\Delta_{y'} = \frac{\phi_y' l^2}{3}$$

Where, l is the length of the pile/column including the strain penetration length. Equation 10 was obtained by using the moment area method and assuming a linear curvature relationship (Figure 64). Therefore, the first yield displacement is obtained by multiplying the area of the curvature profile (triangular region in Figure 64) by the centroid of the curvature area from the loading point.

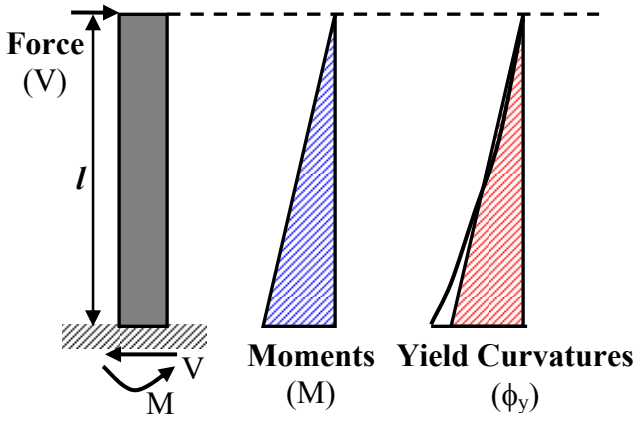

Figure 64. Moment and curvature profiles for a cantilever reinforced concrete pile/column

Physical Observations from Full Scale Testing

Several physical observations were made throughout the testing. The first yielding observed of the longitudinal steel bars in the square and circular piles occurred at approximately 3 in (76 mm) top deflection of the pile. The theoretically-estimated first yield displacement was 1 inch (25.4 mm) with the assumption of a fixed base column. It seems that the connection under study provides an additional ductility to the system. This initial testing observation led to the testing sequence design of intervals of 0.75 in (19 mm) and ending the elastic cycle tests at 3 in (76 mm) top deflection.

Throughout the elastic cycles (first loading protocol) on the concrete pile, the cracks that developed in the pile and pile cap were monitored as well as the behavior of the bearing pad and connections. As testing progressed on the circular pile, flexural cracks developed initially near the base of the connection between the cap beam and pile. The cracks started developing at 7 inches (178 mm) above the pile cap and continued further up the pile at a spacing of 7 to 8 inches (178-203 mm), as shown in Figure 66, as the bearing pad load and the pile axial load increased. A total of eight cracks on each side (pushing/pulling) were observed. This same behavior occurred during testing of the square pile except that the cracks developed on spacing ~12in (305 mm) starting from the pile to pile cap connection.

Figure 65. Flexural cracks produced in the square pile

It was noticed that during the circular pile test at 8% axial loading case, with P3 load level applied to the Type V bearing pad, that the pile cap rotation produced a visible gap ~1/8 in (3 mm) between the bearing pad and pile cap. Figure 66 show the gaps between the pile cap and bearing pad and the bearing pad and sole plate during a loading. As testing continued more visible gaps were noticed near the peak of each elastic cycle for the different circular pile load cases. During some cases, the edge of the bearing pad was not touching the pile cap or the sole plate.

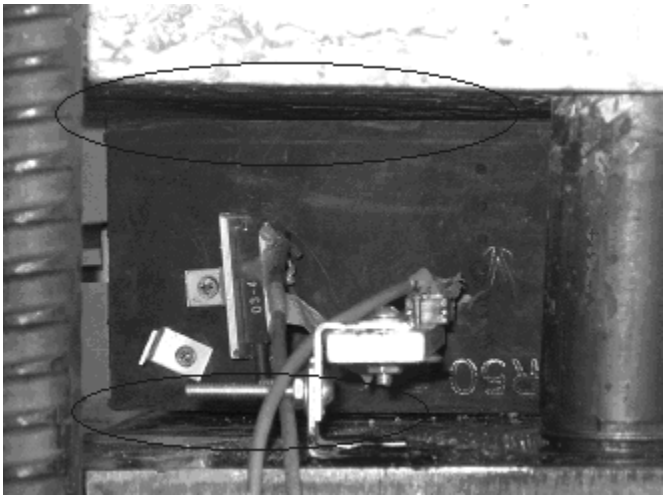

Figure 66. Visible gap between pile cap and bearing pad

As the testing sequence progressed, the deformation of the bearing pad became more notable as the axial load and bearing pad load were increased for all three piles. Figure 67 shows the deformation of the Type VI bearing pad furthest away from the actuator during pushing the circular pile under the inelastic cycles.

Figure 67. Shear deformation of the type VI bearing pad

As testing progressed into the inelastic cycles for each pile, specific observations are as follows:

Circular Pile

As loading increased it was observed that a deflection of 3.26 inches (83 mm) at the top of the pile produced yielding of the longitudinal steel. When the pile was loaded to

ductility 1.5 (4.89 inches displacement) the testing was terminated because bending was noted around the weak axis of the sole plate. It was observed that the weakest link for this connection was the sole plate that is located at the top of the bearing pad. The force produced by the bending of the sole plates caused a gap between the embedded plate and the girder because of the pulling action. However, the force experienced during this test was not enough to pull out the embedded plate from the girder. Figure 68 shows the gap produced between the embedded plate and the girder as well as the gap between the bearing pads and sole plate. Figure 69 shows that there are four anchor studs embedded seven inches into the girder, which prevent the embedded plate from pulling out when the bond force is not exceed. The bending of sole plates caused crushing of the concrete around the diaphragm area (Figure 70 a- b).

Figure 68. Pullout of embedded plate in girder

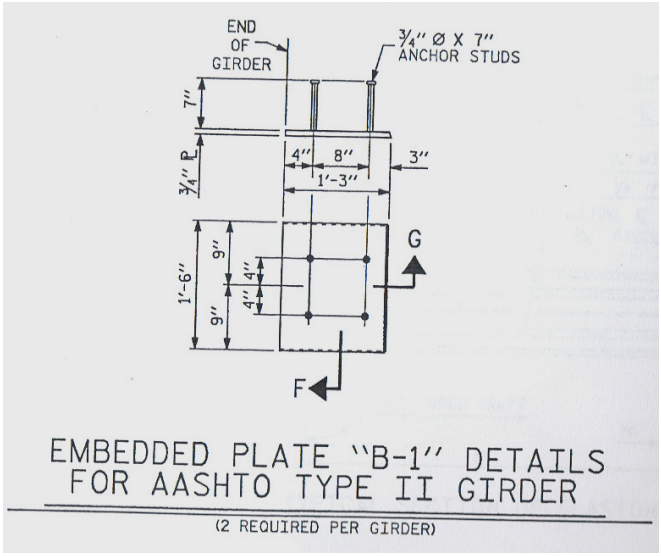

Figure 69. Detailed design of embedded plate from NCDOT drawings for Wake County Bridge

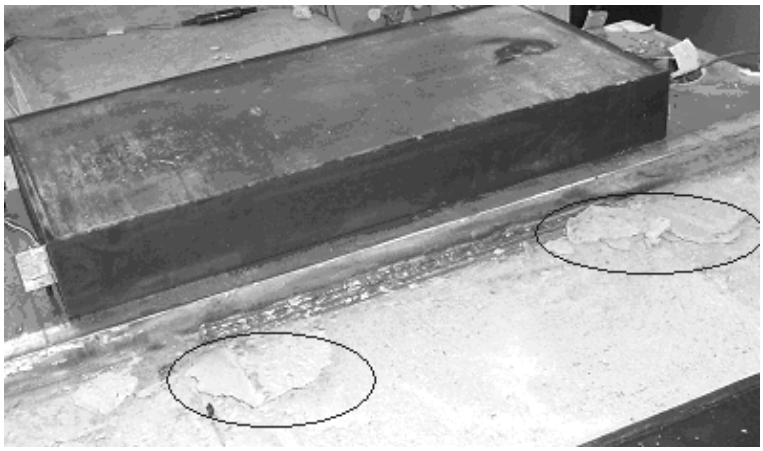

(a)

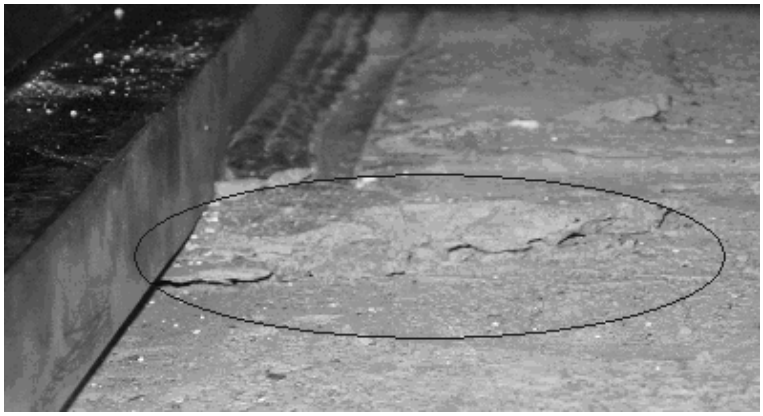

(b)

Figure 70. Concrete cracking in the diaphragm under the pile cap (a-b)

While the inelastic (ductility) loading progressed, the sole plate bent approximately to ½ in (12.7 mm) as the applied force increased. This behavior as well as the pullout of the embedded plate in the girders occurred in the square pile, as well as in the H-Pile, as elastic testing cycles progressed into inelastic cycles (second loading protocol).

Square Pile

The square pile seems to sustain top deflections at first yield of the longitudinal reinforcing steel similar to the circular pile (3.26 inches, or 83 mm). Testing in the ductility cycles continued where embedment plate pullout and sole plate bending was noticeable due to the weakening of the connection. The square pile is stiffer than the circular one, thus it requires higher forces to displace the same amount as the circular pile. Figure 71 shows the increase in cracks in the diaphragm due to bending of the sole plates and pulling out of the embedment plate. Also, Figure 72 captures the bending of the sole plate during the second loading protocol (ductility cycles) of the square pile.

Figure 71. Cracks in diaphragm from pullout of embedded plate

Figure 72. Bending of sole plate

Figure 71 and Figure 72 show the cracks at the diaphragm and bending of the sole plate at ductility 2 (6.52 inches (166 mm)). Testing of the square pile was ended after one cycle of ductility 2 (push only) because significant cracking of the concrete cap was observed above the anchor bolt on the back side of the pile cap. Figure 73 reveals the cracking of the concrete at this location.

Figure 73. Significant cracking in the pile cap

H-Pile

During the first protocol of testing for the H-Pile, similar behavior was noticed as for the circular and square piles. It was observed that there was more significant shear deformation of the bearing pad, sole plate bending, and embedment plate pull out action with increasing lateral load. After completion of the elastic cycles, the most noteworthy difference in the behavior of the H-Pile was that at the final peaks of the loading elastic cycles, cracks developed between the H-Pile and the pile cap. These cracks became more pronounced as the second loading protocol began as a top deflection of 6.23 inches (158 mm) at a horizontal load of ~18 kips was needed to reach the first yielding of the H-Pile. Testing continued to the completion of a ductility of 1.5 where the top deflection of the pile reached 9.34 inches (237 mm). The prying action of the embedded part of the HP pile caused large damage in the cap beam and the test was stopped for this reason. At this point of testing, accurate measurements of top deflection could not be further made due to the configuration of the test setup and lack of instruments at the embedded part of the HP pile. Also the pile was rotating significantly, independent of the pile cap as displayed in Figure 74. Figure 75 through Figure 77 show the damage at different points in the specimen at a top deflection of 9.34 inches.

Figure 74. Rotation of the H-Pile independent of the pile cap

Figure 75. Pullout of the H-Pile from the pile cap

Figure 76. Cracks in the pile cap due to the prying action of the HP pile embedded part

Figure 77. Gaps generated between sole plate / cap beam and bearing pad

Deformation and Stiffness

The measured results were analyzed to determine the contribution of the various system components to the total top lateral displacement of the pile. A string pot was attached at

the pile top and measured the total top deflection throughout the testing sequence. The results of the test revealed that the total top deflection of the pile was a sum of the following components: pile bending, bearing pad shear deformation, girder rotation, and pile cap rotation as schematically shown in Figure 78.

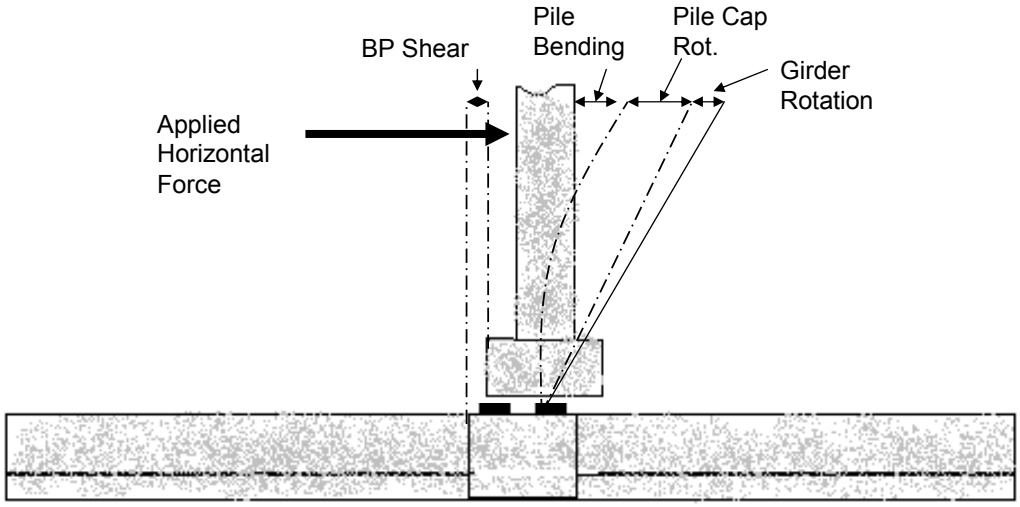

Figure 78. Components of Contributing Pile Top displacement

Figure 79 through Figure 81 show example hysteretic responses of the top of the piles throughout the lateral loading sequence. For the rest of the force-displacement responses see Appendix A.

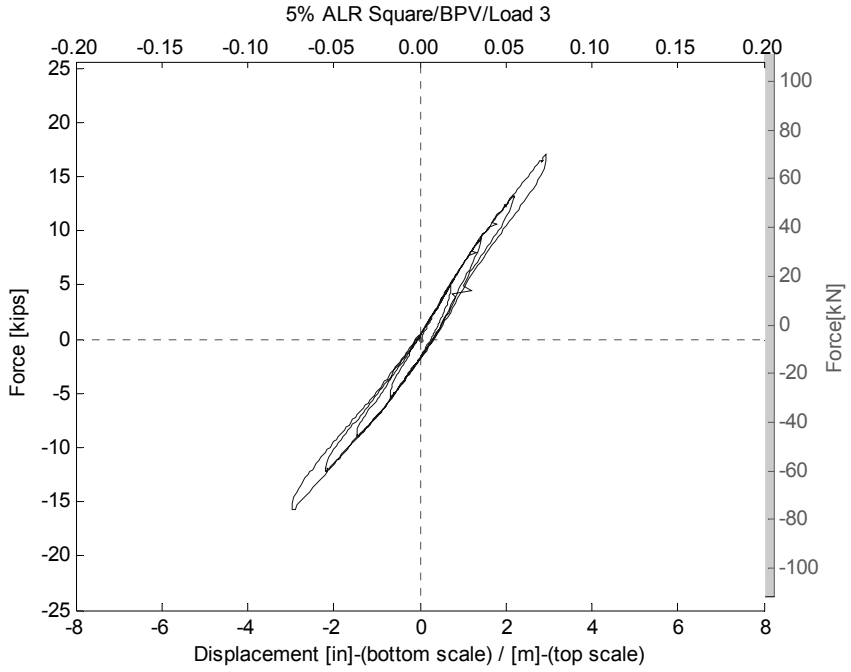

Figure 79. Example square pile top displacement vs applied lateral load

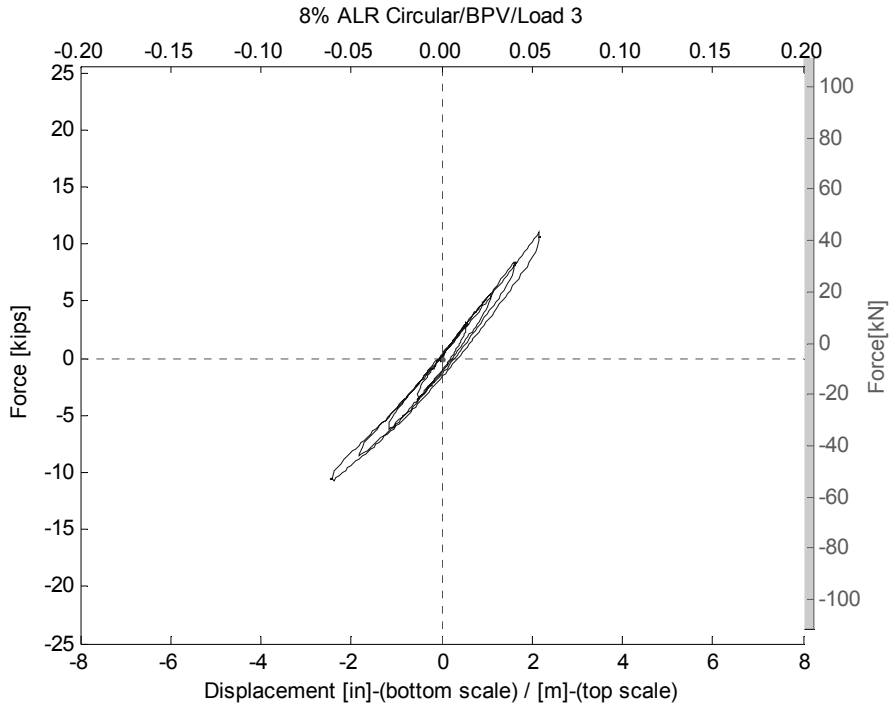

Figure 80. Example circular pile top displacement vs applied lateral load

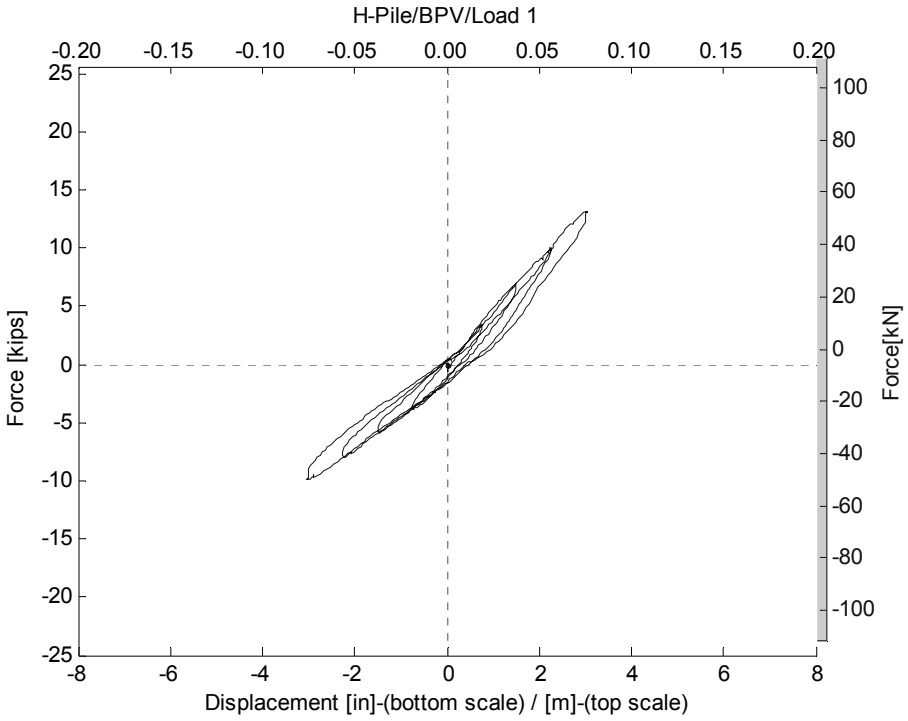

Figure 81. Example H-pile top displacement vs applied lateral load

The measurements of the contributing displacements were obtained at the peaks of each testing protocol for both pushing and pulling of the piles during the elastic and ductility cycles. The rotation of the girder was determined from the inclinometer data indicated by the CLIN-1 on Figure 59. Also, the rotation of the pile cap was determined from two string pots (SPOT 9 and SPOT 11) located at the top and bottom of the pile cap. The contributing top displacement from pile bending was determined from estimating the curvature of the pile from the compressive displacement measurements at four points along either side of the pile (LPOT 9 through 16). The last component of contributing pile top displacement was from the shear deformation of the pile measured by linear pots, two pots per bearing pad as indicated in Figure 59 by LLOT 2, LLPOT1, LPOT 20, and LPOT 21. Figure 82 shows the calculated contributing top displacement of each component with respect to the overall measured top displacement at the peaks of each loading cycle. See Appendix A for all full scale testing calculated contributing top displacement figures.

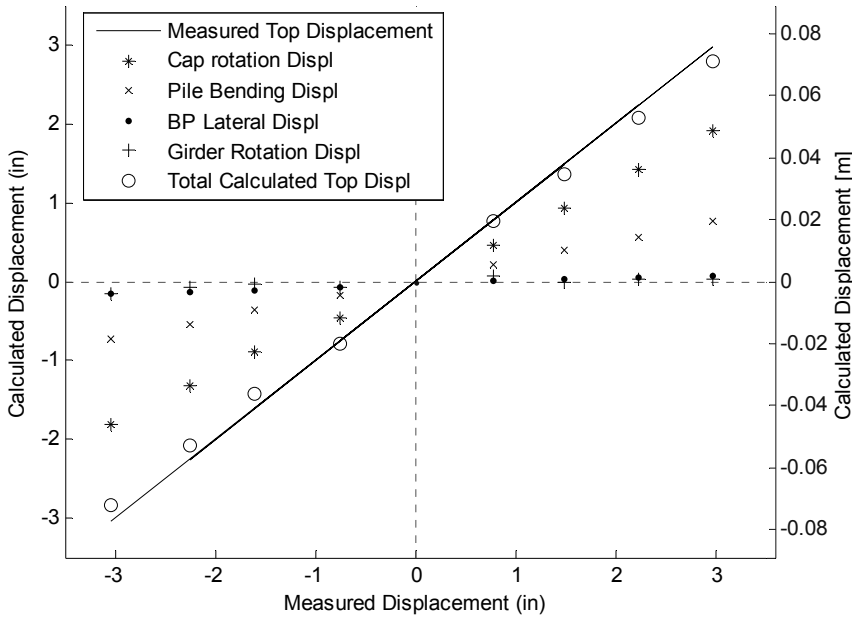

Figure 82. Top Displacement Components for Square Pile with 0.03 axial load ratio/BP V/Load P1

From Figure 82 it is evident that the sum of the contributing components, indicated by the circles, matches the measured top lateral displacement of the pile. Figure 83 shows the

measured top displacement versus the calculated top displacement throughout the history of one elastic loading cycle on the square pile.

Figure 83 shows that the calculated top displacement associated with each contributing displacement component is very similar to the measured top displacement during testing. Also, the test results revealed that the pile cap rotation had the most significant contribution to the top displacement of the pile, followed by the bending of the pile, and then the bearing pad shear and girder rotation contributed the least. Figure 84 shows the percentages of the contributing components of the total top deflection of 0.75 in (19 mm) for the square pile under an axial load ratio of 3% and Type V bearing pad load level of P1. See Appendix A for all full scale test results of measured versus calculated top displacement results and for all pie charts of contributing displacements.

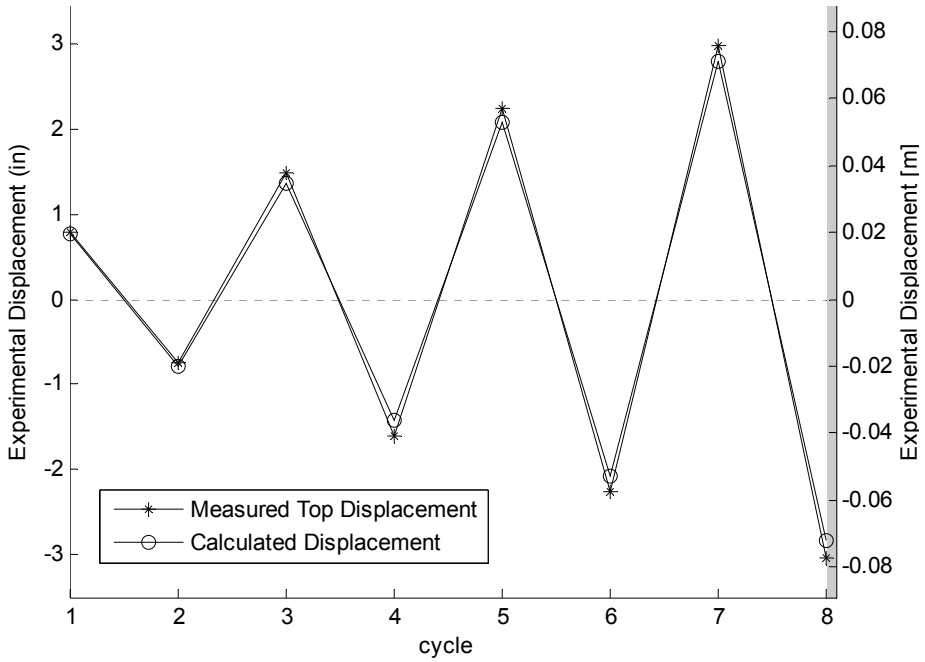

Figure 83. Measured versus Calculated Top Displacement for Square Pile with 0.03 axial load ratio/BP V/Load P1

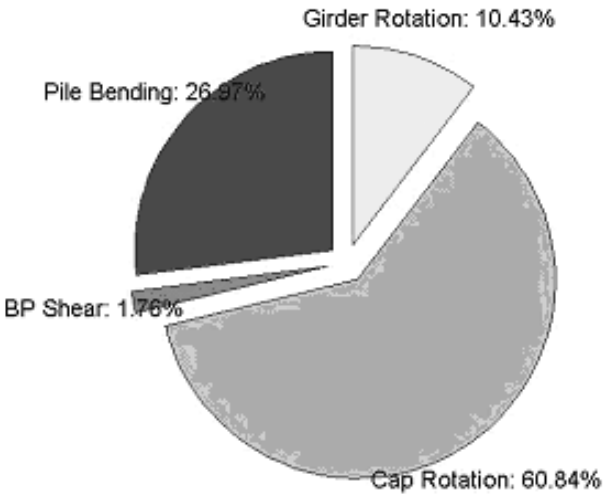

Figure 84. Pile Top Displacement Component Percentages for Square Pile with 0.03 ALR/BP V/Load P1/0.75 in (19 mm) top displacement

Test data indicated that the rotation of the pile cap is significant in the overall response of the pile. Therefore, it is important that the degree of fixity of the pile cap be modeled appropriately in the structural analyses. In order to determine the pile cap fixity effect, the results and measurements of the cap rotation and moment at the pile cap are analyzed. Figure 85 to Figure 90 show the moment in the pile cap versus the measured rotation for the different elastic loading cases for each pile and bearing pad type. These plots show the envelope of the moment-rotation response for the different cases.

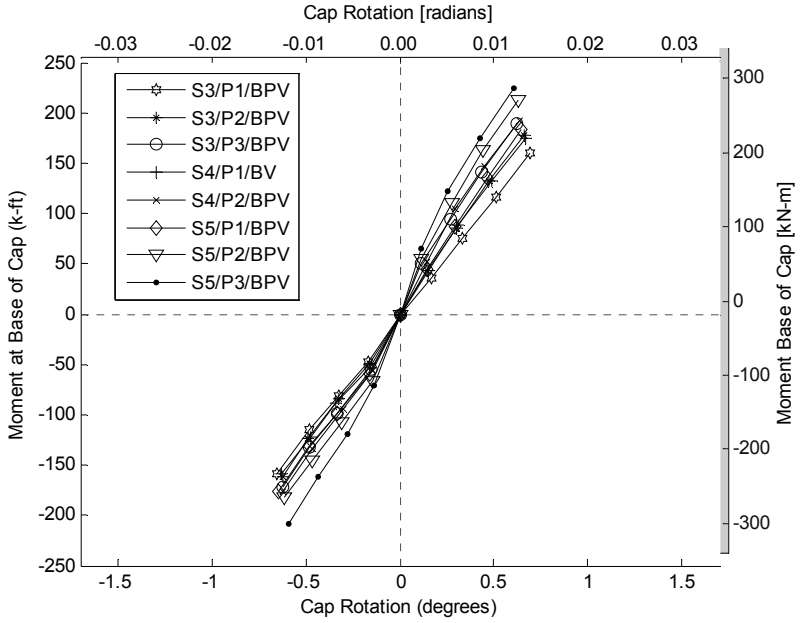

Figure 85. Square Pile/BP V: Cap Moment versus Cap Rotation

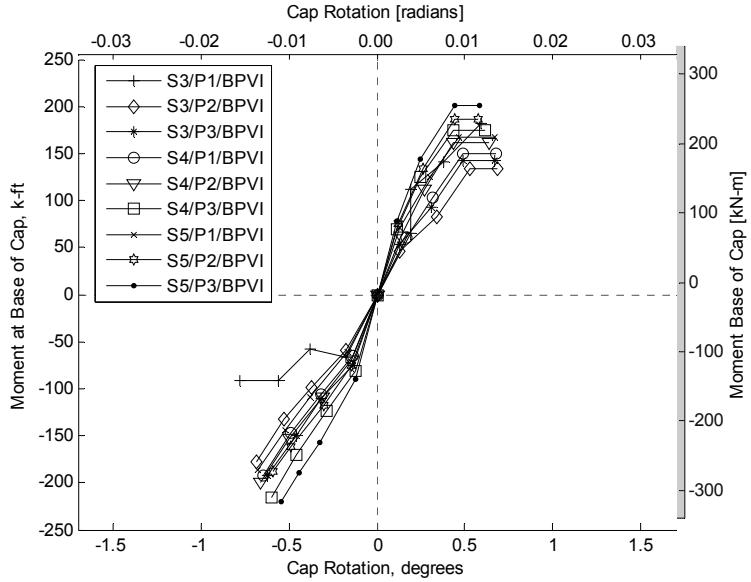

Figure 86. Square Pile/BP VI: Cap Moment versus Cap Rotation

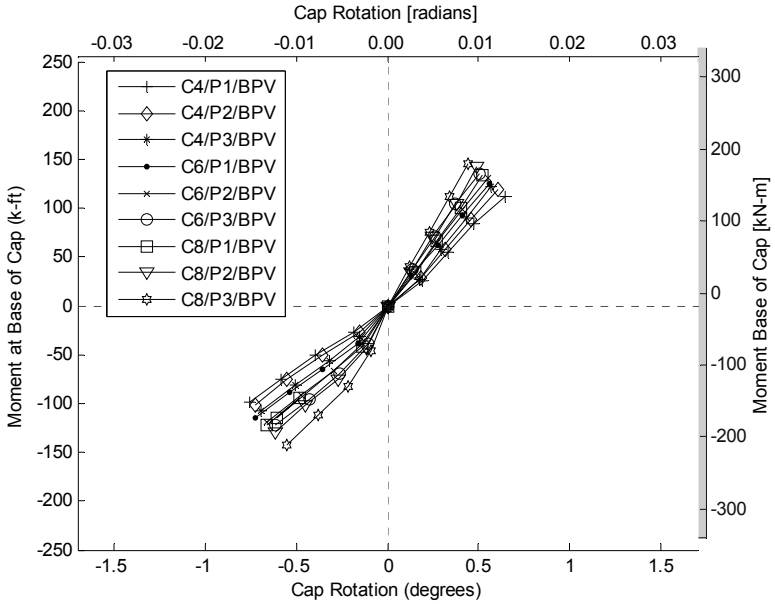

Figure 87. Circular Pile/BP V: Cap Moment versus Cap Rotation

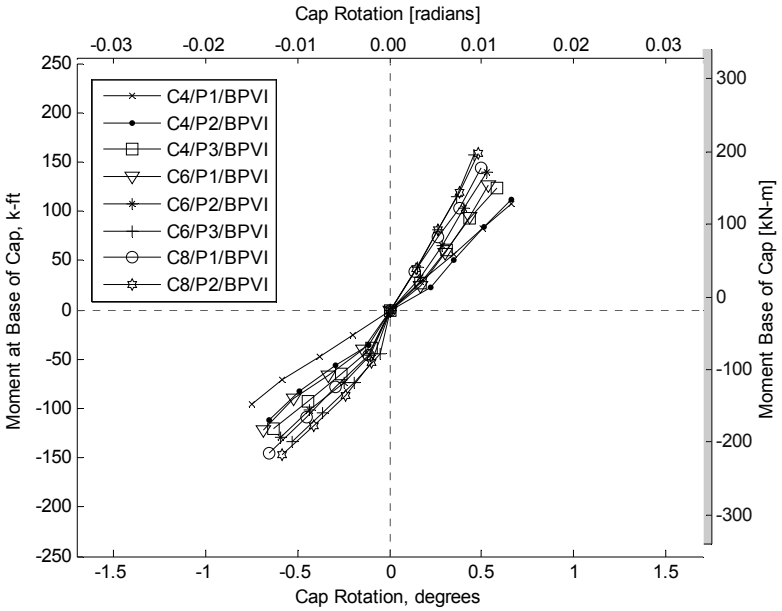

Figure 88. Circular Pile/BP VI: Cap Moment versus Cap Rotation

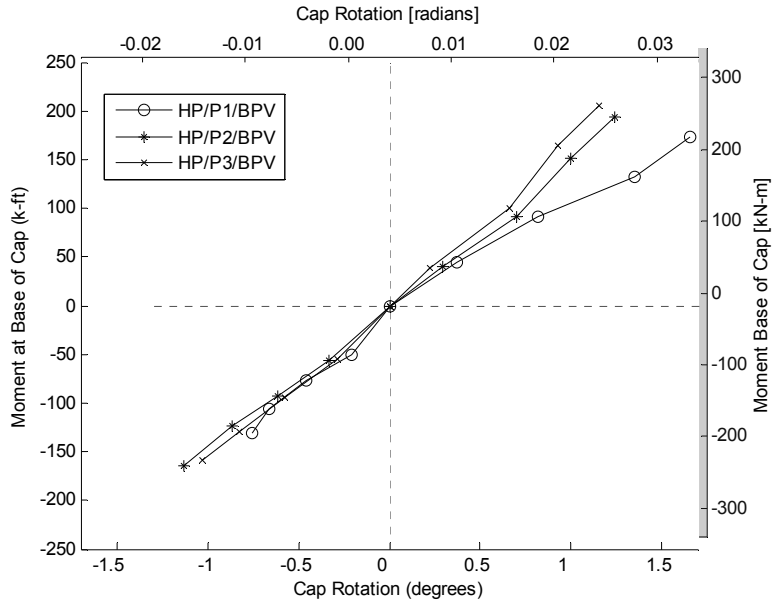

Figure 89. HP/BP V: Cap Moment versus Cap Rotation

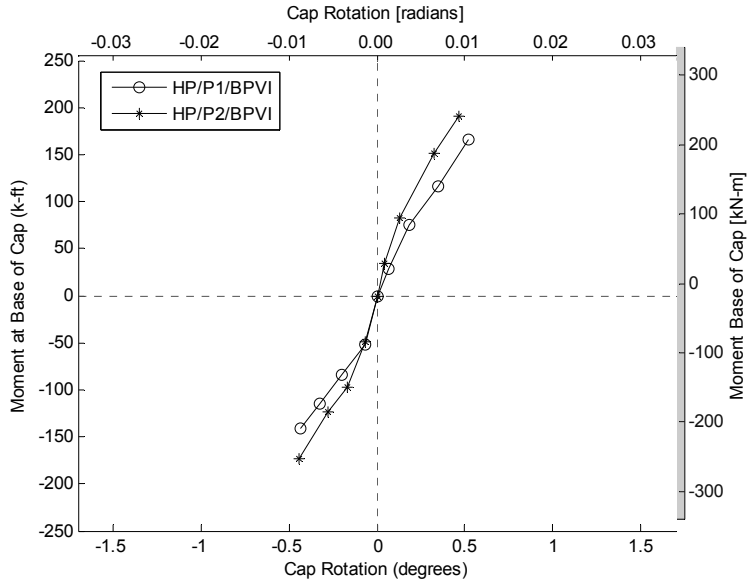

Figure 90. HP/BP VI: Cap Moment versus Cap Rotation

The moment versus rotation results show that for each loading case, the behavior of the bearing pads is generally consistent. Increasing the load in the bearing pad and in the pile causes an increase in cap moment which generated cap rotation. The maximum moment in the pile cap for all of piles testing and loading cases was between 150 (218.5) and 225(327.8) k-ft (kN/cm). The maximum cap rotation was approximately 0.5 degrees for all the loading cases except for the H-pile tests on the Type V bearing pad where the maximum pile cap rotation was more than double that experienced in the other cases.

From the moment and rotation at the pile cap for each loading case, the secant rotational stiffness at the peak of each loading cycle is determined. The secant rotational stiffness for each loading case in each bearing pad at the elastic displacement interval was determined by dividing the measured cap moment by the cap rotation ($K_\theta = M/\theta$). Figure 91 through Figure 102 present the secant rotational stiffness determined at each top displacement peak. These values are presented for the pulling (positive) and pushing (negative) directions. For simplicity, rotational stiffnesses versus displacements are shown always positive with the direction specified in the figures.

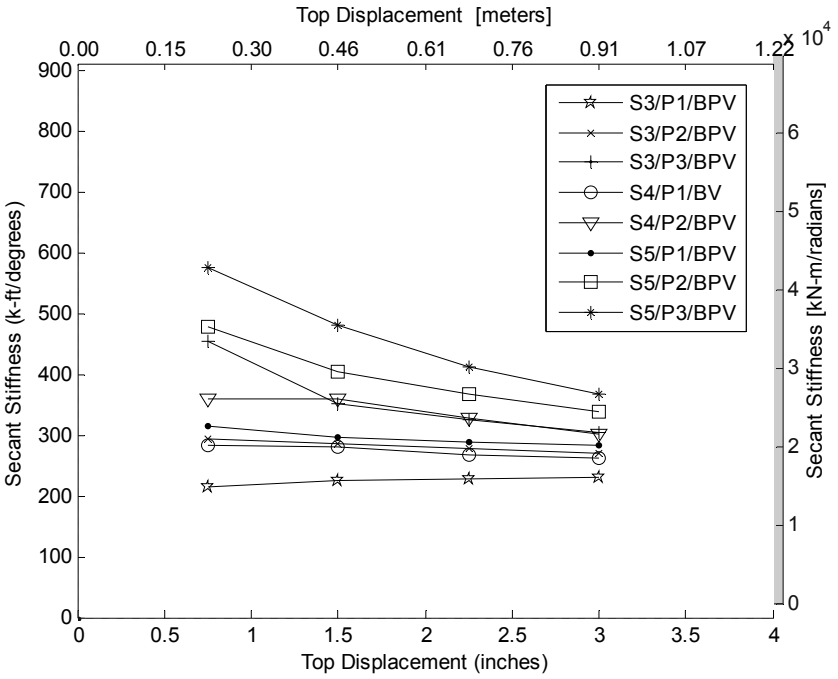

Figure 91. Secant Stiffness of Square pile / BP V (pushing direction)

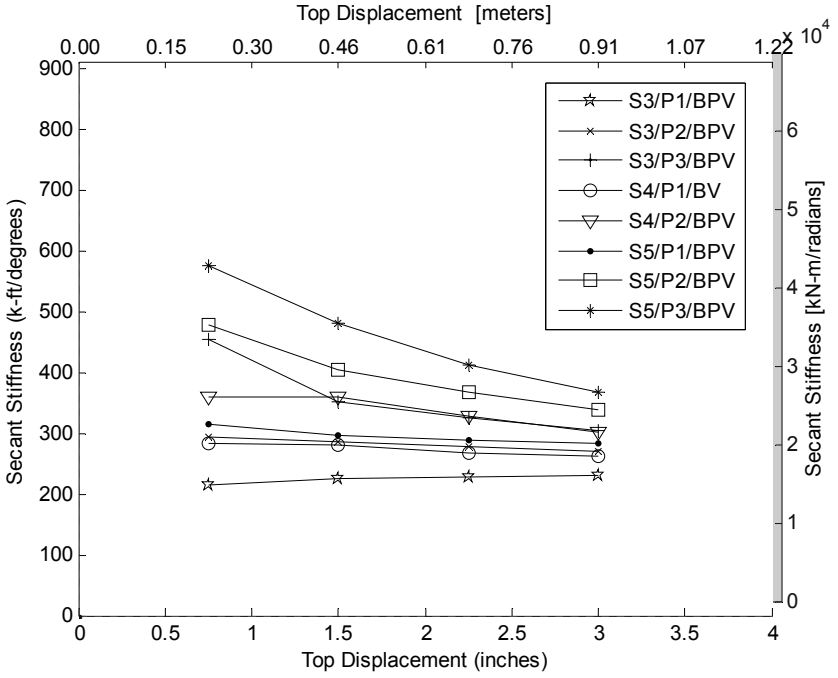

Figure 92. Secant Stiffness of Square pile /BP V (pulling direction)

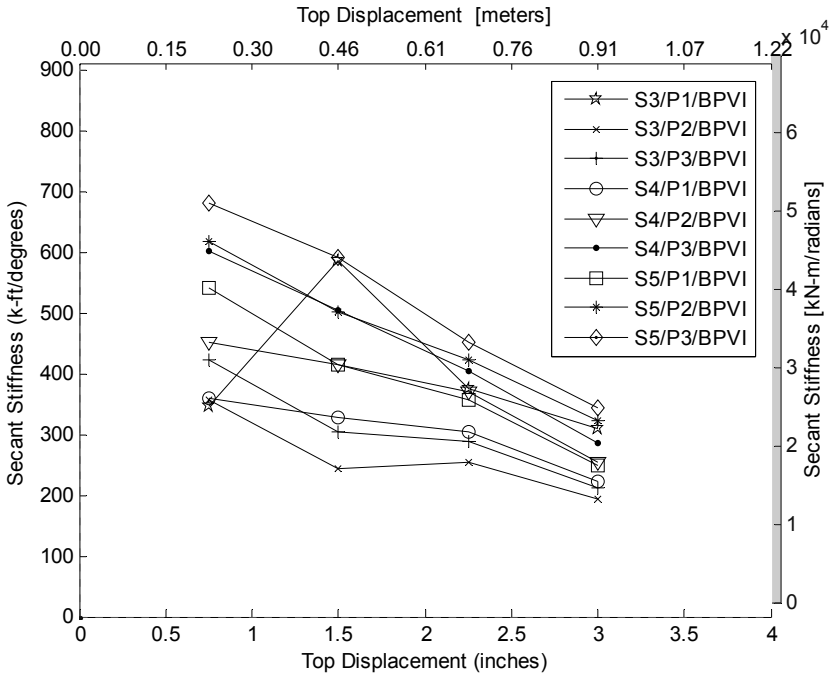

Figure 93. Secant Stiffness of Square pile / BP VI (pushing direction)

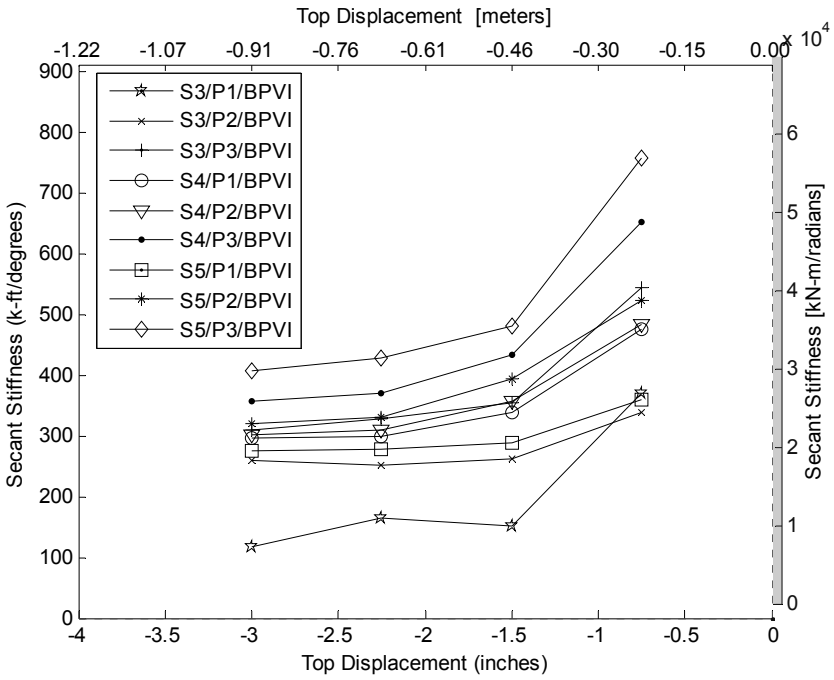

Figure 94. Secant Stiffness of Square pile / BP VI (pulling direction)

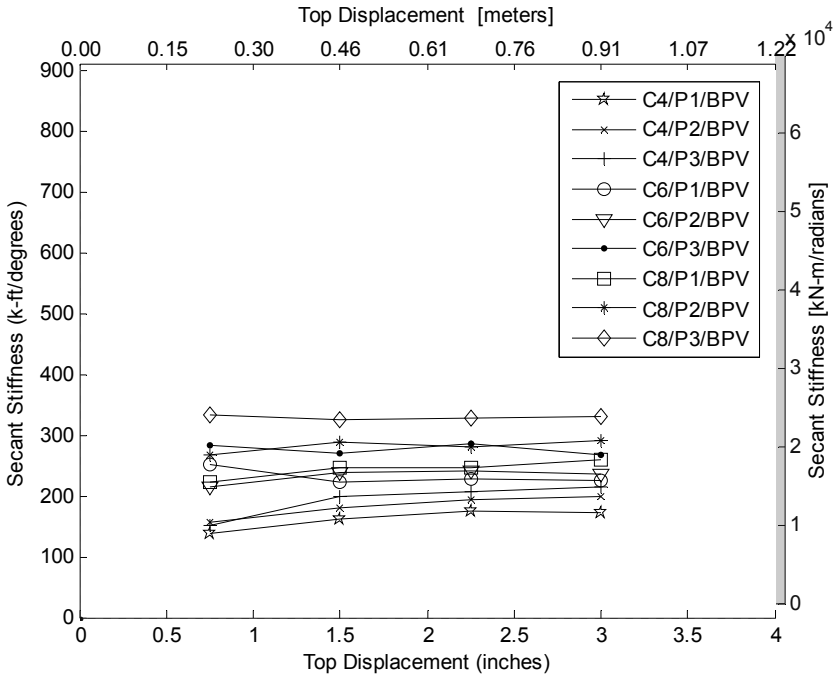

Figure 95. Secant Stiffness of Circular pile / BP V (pushing direction)

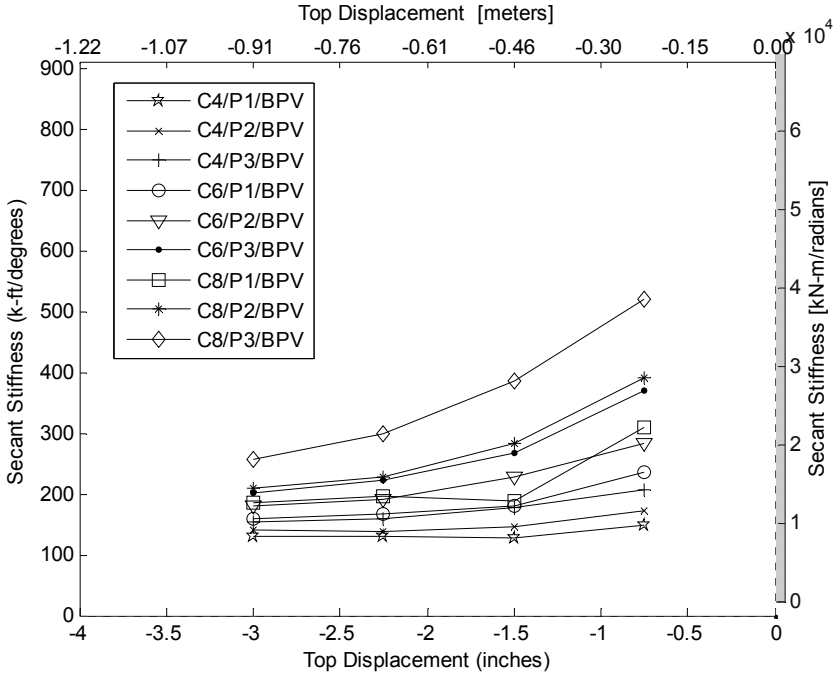

Figure 96. Secant Stiffness of Circular pile/ BP V (pulling direction)

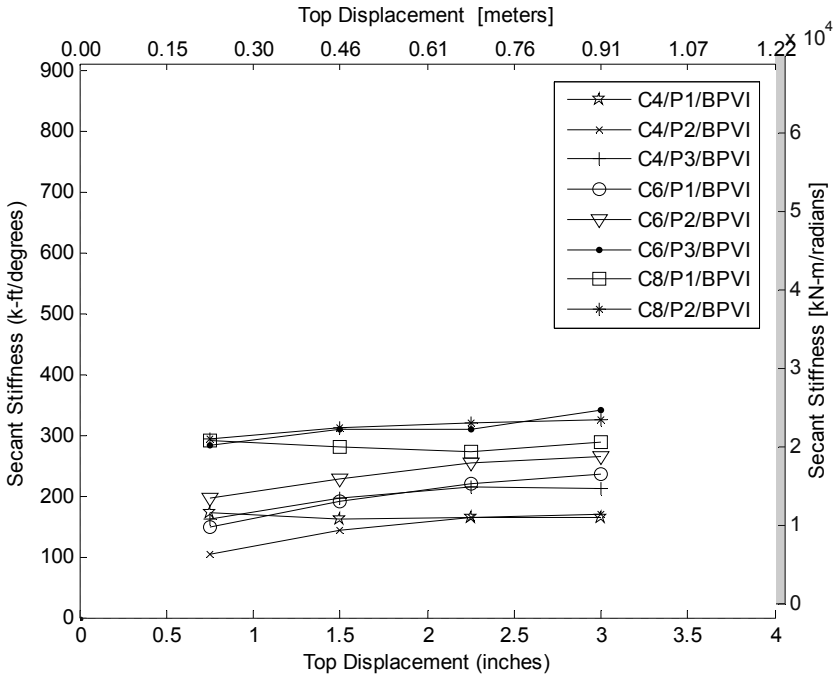

Figure 97. Secant Stiffness of Circular pile/ BP VI (pushing direction)

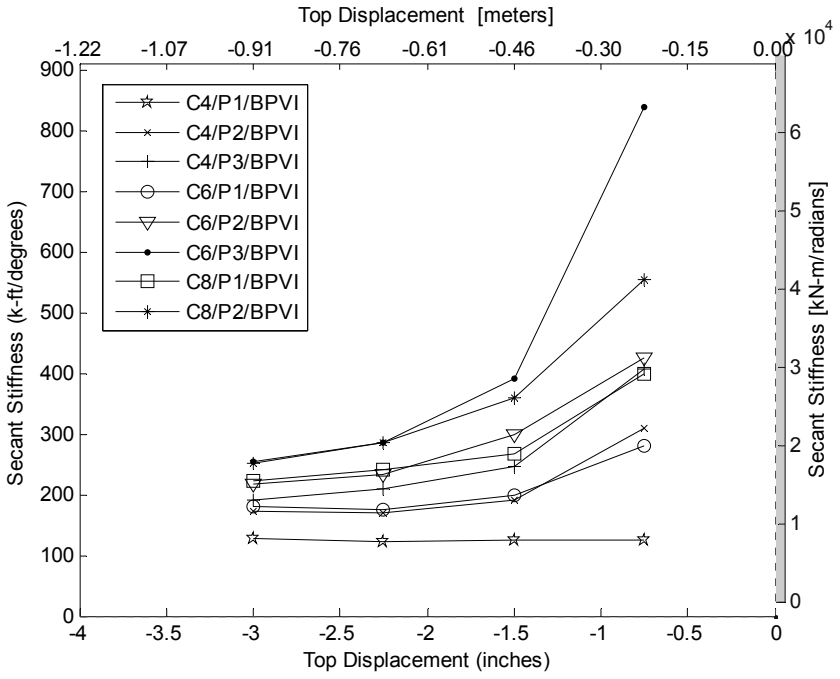

Figure 98. Secant Stiffness of Circular pile / BP VI (pulling direction)

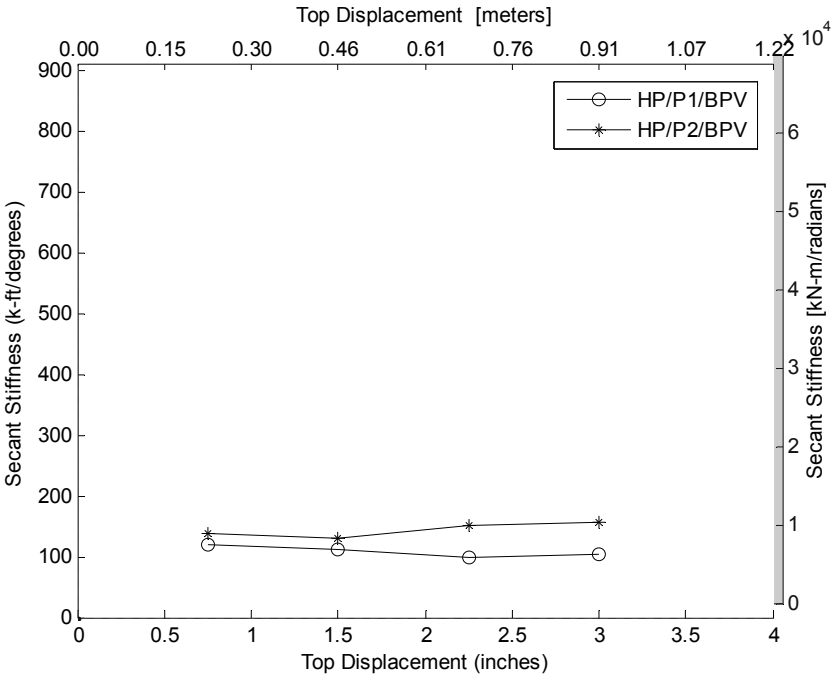

Figure 99. Secant Stiffness of H-pile / BP V (pushing direction)

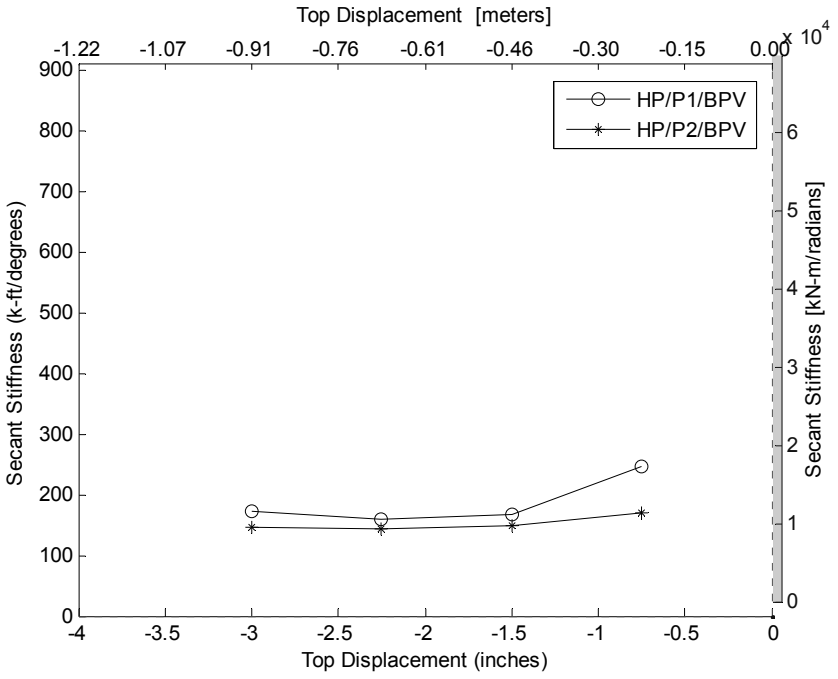

Figure 100. Secant Stiffness of H-pile / BP V (pulling direction)

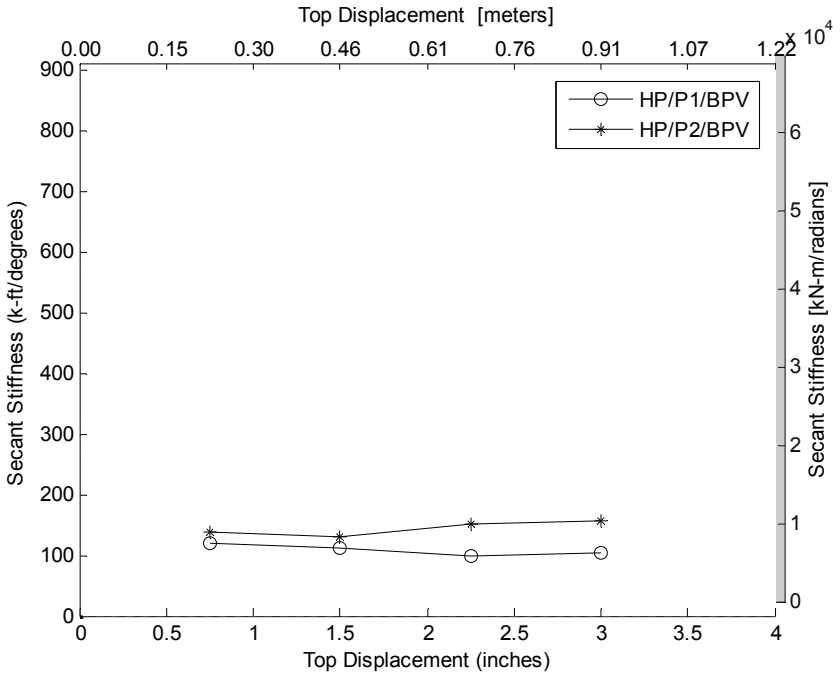

Figure 101. Secant Stiffness of H-pile/ BP VI (pushing direction)

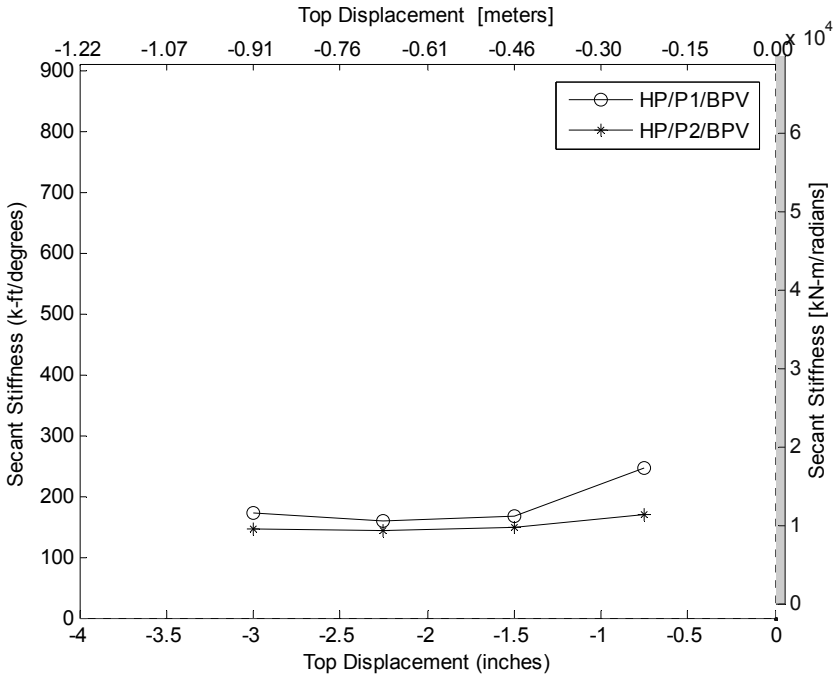

Figure 102. Secant Stiffness of H-pile/ BPVI (pulling direction)

The rotational secant stiffness data obtained from testing on the three different piles show reasonable trends. When the actuator was pulling the piles, there was a more significant decrease in the rotational secant stiffness in the pile cap as opposed to the pushing

direction. This situation was especially evident during testing the circular pile cases and may be due to the unleveled surface of the bottom of the cap beam acquired during the casting process. During the different loading cases in for the circular and square piles, the difference in the rotational stiffness became less and less as the pile was pushed/pulled further away. This trend may indicate a threshold rotational stiffness in the case of the concrete piles at very large pile displacements. The stiffness results for the H-pile remained largely uniform throughout the lateral loading protocol.

It can also be noticed that the secant rotational stiffness is higher for the square pile cases with Type VI pad. The square pile is stiffer than both the circular and HP piles, which is contributing more to the stiffness of the connection. Similarly, the Type VI pad has a higher shear modulus which provides a higher resistance to the lateral force, and thereby increasing the stiffness of the connection. As the axial load on the bearing pad and pile was increased, the rotational stiffness also increased.

Summary

This performance testing program aimed at characterizing the rotational stiffness of the sub-super structure connection within the bridge system taking into the account the relative stiffness of the other components. For this program, a slice of a deck-girder-diaphragm-sole plate-anchor bolt-bearing pad-bent cap-pile bridge system was constructed upside down to test the longitudinal behavior of the substructure to superstructure connection in full scale. Loading was displacement controlled and was monitored using 55 separate measuring devices. The full scale test results for the various loading cases for each pile can be found in Appendix A.

The results from the full scale testing show the capability of this type of connection to sustain and transfer the applied moments. Given the test components strength and stiffness parameters, it was found from test observations that the weakest link in this connection was the steel sole plates located at the top of the bearing pads. As these plates were bent during load application, crushing of the concrete occurred at the diaphragm area. Under the applied lateral loads, the sole plates bending action lead to pulled out of the embedded plate on the girder. The embedded plate has four studs of 178 mm (7 in) in

length, which provided enough strength against the pulling force produced by the bending of the sole plates during. At displacements in excess of the elastic yield load, additional weak links were found at the H-Pile to cap connection.

The increase in the test pile and bearing pad stiffness, induced by applying higher axial loads, increased the rotational stiffness of the connection. For the conditions simulated in this testing program, the largest contributors to the total displacement response of the tested system were cap beam rotation (approximately 60%), followed by the pile lateral deformation (approximately 25%).

CHAPTER 6: DESIGN APPLICATION AND LIMIT STATES

Theoretical Rotational Stiffness

From the full scale testing, rotational stiffness values were determined for the loading configuration simulated in the laboratory. The results from the experiments are compared to results from an equation derived from static equilibrium considerations in an attempt to provide a framework for estimating connection rotational stiffness for other bridge assemblies with different bearing pads.

The model proposed to predict the rotational stiffness of the measured test results assumes that the pile cap is a rigid structure, and that the rotation of the connection joint is a function of the compressive stiffness of the bearing pad and the tensile stiffness of the anchor bolts attached from the pile cap to the sole plate. The model simulates loading in one direction where, as the bearing pad is compressed on one side, the other side experiences tension. Figure 103 shows an illustration of the idealized connection configuration.

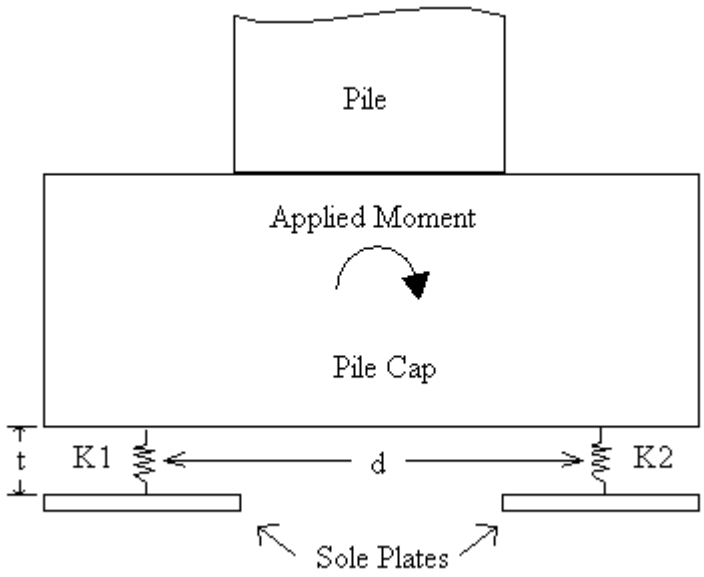

Figure 103. **Schematic illustration of rotational component of connection joint**

In this case, the following parameters are defined:

t = thickness between the sole plate and the pile cap

d = distance between the compressive and the tensional stiffness elements

K1 = stiffness of the tensile element (anchor bolts)

K2 = stiffness of the compressive element (elastomeric bearing pad)

The model in Figure 103 is implemented into Equation 13 to combine the contribution of the anchor bolts and the bearing pad towards the overall connection rotational stiffness. The robustness of Equation 13 was verified through the principles of statics and through the use of the computer program SAP 2000.

Equation 11 $$K1 = \frac{EsAs}{t}$$

Equation 12 $$K2 = \frac{EpAp}{t}$$

Equation 13 $$Kr = \frac{d^2}{t\left(\frac{1}{EsAs} + \frac{1}{EpAp}\right)}$$

Where:

Es = Elastic Modulus of the anchor bolt steel

As = Cross sectional area of the anchor bolt

Ep = Elastic Modulus of the bearing pad

Ap = Cross section of the bearing pad

The proposed model to predict the rotational stiffness is applied and results are compared to the rotational stiffness from the 3% Axial Load Ratio cases of the square pile with bearing pad type V. Limitations of the theory in predicting the measured response are presented and discussed.

The parameters implemented in Equation 13 are defined. From the bearing pad compressive test results presented in Chapter 4, an elastic modulus was determined by taking a secant modulus from a strain range of 0.03 to .065. The estimated elastic

modulus value does not include the initial part of the stress-strain curve because this deformation was due to a seating error. Table 25 presents the input values for the predicted rotational stiffness.

Table 25. Input parameters for rotational stiffness model

Parameters	Values	Units	Values	Units
t	3.563	inch	9.05	cm
d	28	inch	71.12	cm
Es	29000000	psi	19957840	kN/cm^2
Ep	16714	psi	11503	kN/cm^2
As	6.28	$inch^2$	40.5	cm^2
Ap	325	$inch^2$	2097	cm^2

Using the parameters in Table 25, a rotational stiffness was calculated and directly compared to the results from full scale testing in Figure 104. The comparative results show that the theoretical equation overestimates the measured response from the full scale tests. The predicted rotational stiffness from Equation 13 yielded a rotation stiffness of approximately 1700 k-ft/degree (131,000 kN-m/rad) which is roughly five times greater than the average rotational stiffness from the measured results.

Possible reasons the predicted rotational stiffness was greater than the measured results could be attributed to several factors. Below is a list of possible sources of error:

i. The elastic modulus assumed for the bearing pad has a significant effect on the connection's rotational stiffness. The elastic modulus was taken from independent, compressive tests, with stress applied uniformly on the bearing pads. In the full scale testing, the bearing pad experienced non-uniform compressive stresses.

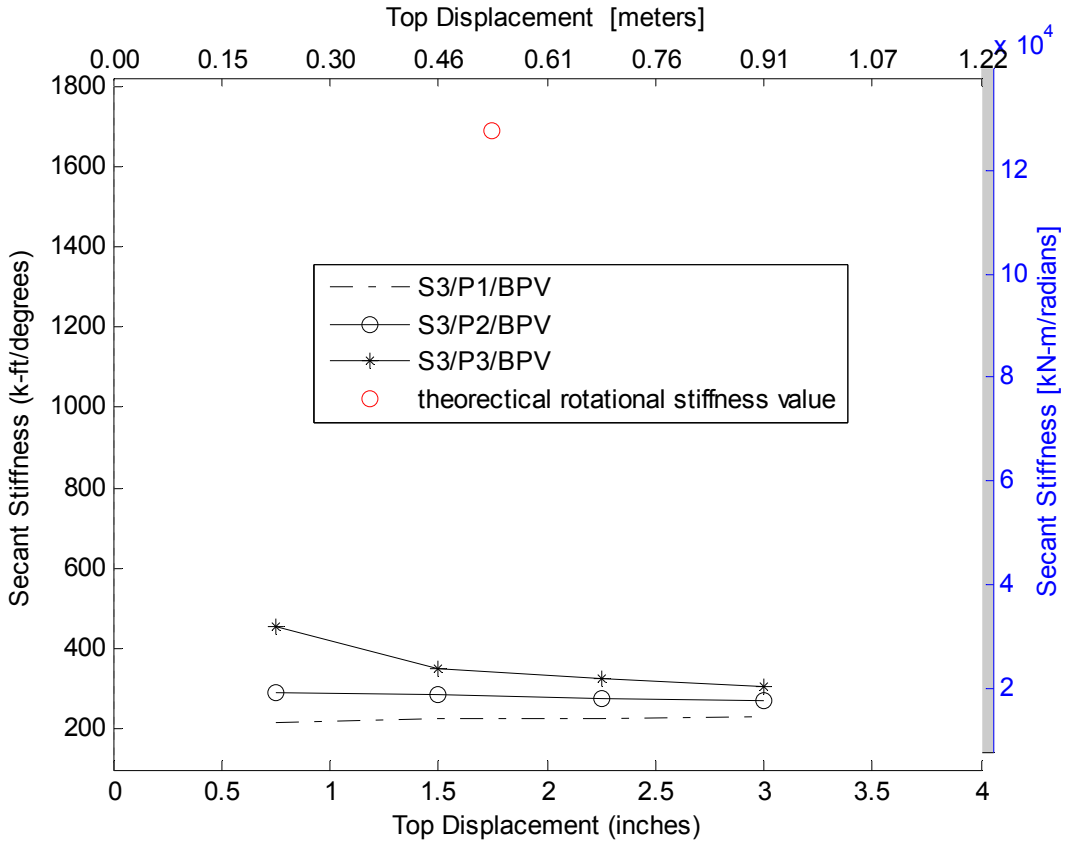

Figure 104. Theoretical rotational stiffness compared to measured results

ii. The model in Figure 103 assumes that the point of rotation is at the center of the pile cap. In comparison, this may not have been the case during the full scale testing where the pinned girder connection allowed some rotation even though this rotation was minimal.

iii. The theoretical model does not take into account the load magnitude which was applied to the bearing pad. The data from the full scale testing indicated that increasing the load on the bearing pad increases the rotational stiffness. This load is not modeled in Equation 11 through Equation 13, which may explain the difference between the measured and predicted rotational stiffnesses.

iv. It was noticed that the sole plate bent significantly and pulled away from the girder during testing. The result of this action is to increase the allowed rotation and cause the model from Equation 13 to over predict the stiffness.

v. Throughout testing, cracks developed along the length of the pile cap where the anchor bolts were connected. As the bond between the anchor bolt and concrete deteriorated, the stiffness contribution of the anchor bolt is significantly reduced and, accordingly, Equation 13 would over predict the rotational stiffness.

Given the range of rotational stiffness values measured and calculated for the Type V bearing pad in Figure 104, a parametric study was undertaken to determine the effects of a range of rotational stiffness as applied to the pile bents previously modeled in Robinson et al. (2006) and in Chapter 3. These results were compared to models that were free to translate and rotate (a free head condition) and free to translate but not rotate.

Wake and Halifax County bents with rotational springs

Rotational springs were attached to the bearing pad locations in the MultiPier Wake County bridge model described in Chapter 3. First, the bent was modeled as free standing with the AASHTO load cases applied as in Chapter 3. Next, rotational stiffness springs were added to resist moments along the bent cap transverse and longitudinal directions, with stiffness values similar to those measured in the longitudinal direction in the full scale tests presented Chapter 5. This model is shown in Figure 105 and the range of rotational stiffnesses used in MultiPier was obtained from Figure 104. Finally, these rotational springs were made extremely stiff, or fixed against rotation. The results from these models are presented in Table 26.

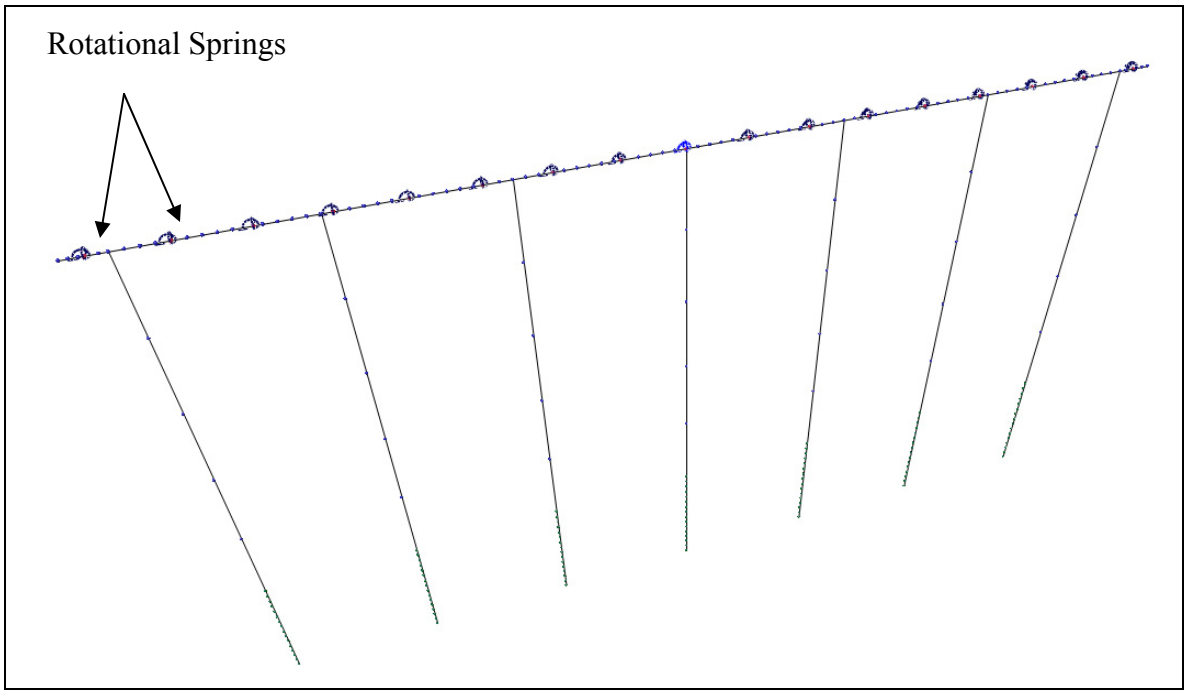

Figure 105. Wake County MultiPier Model with rotational springs

Table 26. Results of varying rotational spring attached to Wake County Bridge Model

	Moment kip-ft	Shear kips	Axial Force kips	Demand Capacity Ratio	Transverse Disp. In	Longitud. Disp. in
Free standing	538	40	1661	0.319	0.43	0.67
200 kip-ft/deg	536	40	1660	0.318	0.43	0.57
500 kip-ft/deg	534	40	1658	0.318	0.43	0.49
1700 kip-ft/deg	527	39	1650	0.317	0.43	0.35
Fixed spring	400	33	1375	0.266	0.43	0.18

Table 26 shows that adding a rotational spring based on the Type V bearing pad resulted in loads and displacements that were only slightly lower than those predicted by a free standing bent. A bent with springs fixed against rotation had moments, shear and axial forces that were considerably lower than the freely rotating or restrained bents. Thus, in

this case, current NCDOT practice of assuming a free standing bent appears to be reasonable.

The Wake County bent was constructed using several large diameter drilled shafts. For comparison, a bent using significantly more slender driven prestressed concrete piles is also presented. From Robinson et al. (2006), the Halifax County bridge was checked using the same bearing pads rotation stiffnesses. While these Type V bearing pads are larger than those used in the construction of this structure, the comparison between the Wake and Halifax County bridges using the same bearing pads will highlight what will drive design decisions.

As before, the Halifax county bridge was modeled as a free standing bent that is free to rotate, fixed against rotation and with rotational stiffnesses as measured by the full scale testing. Figure 106 shows the model with rotational springs attached at the bearing pad locations. The results from the five models analyzed are included in Table 27.

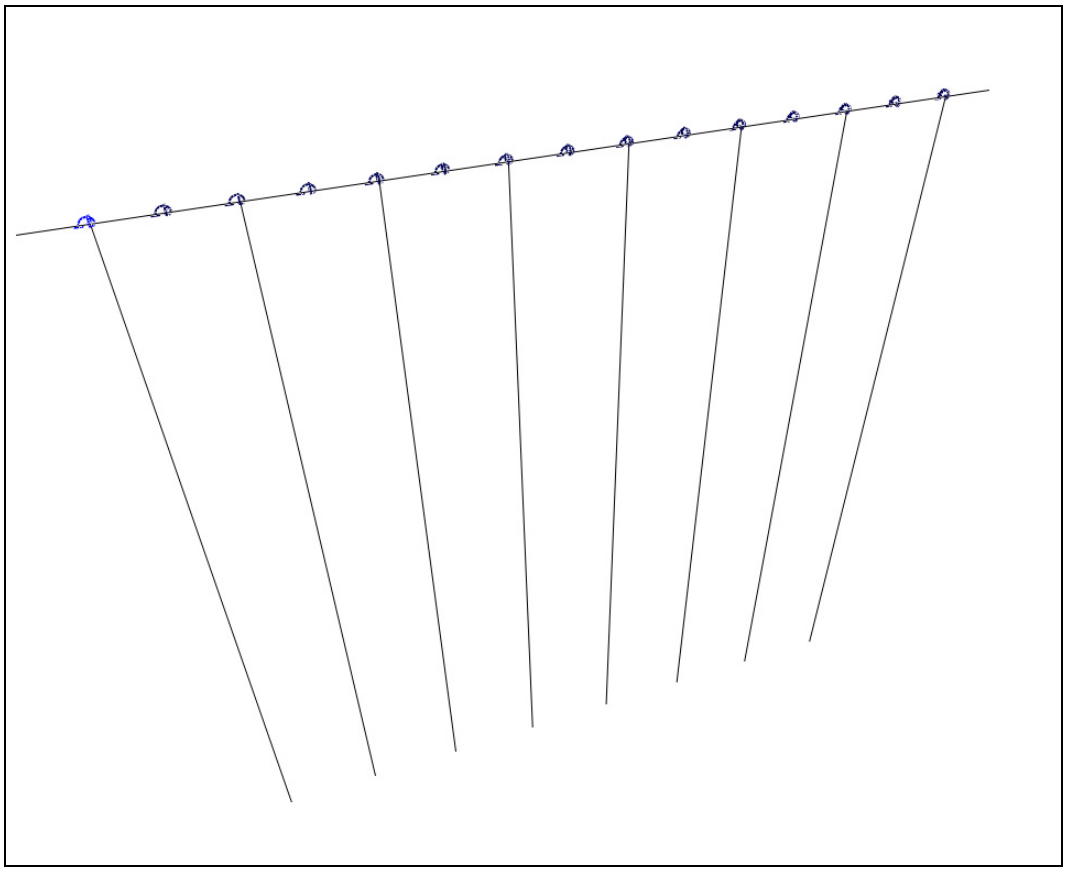

Figure 106. Halifax County MultiPier model with rotational springs (after Robinson et al. 2006).

Table 27 shows that, in the Halifax case, the addition of the rotational restraint at the bearing pad location results in moments, shears and axial forces that are more similar to the fixed rotation bent than the free standing bent. This is particular true for displacements in the longitudinal direction, where the free standing bent was predicted to be 0.6 inches, while displacements for the rotationally restrained bents was closer to 0.15 inches.

Table 27. Results of varying rotational spring attached to Halifax County Bridge Model

	Moment kip-ft	Shear kips	Axial Force Kips	DCR	Trans. in	Long. in
Free standing	40.2	3	297	0.3	0.15	0.6
200 kip-ft/deg	32.1	2.5	281	0.29	0.14	0.15
500 kip-ft/deg	31	2.4	268	0.27	0.14	0.14
1700 kip-ft/deg	29	2.3	248	0.25	0.14	0.14
Fixed spring	28	2.2	225	0.23	0.14	0.14

Considering the differences between the Wake and Halifax County bent results when rotational restraint is included, it would appear that the relationship between the stiffness of the connection and the stiffness of the pile or shaft section is the determining factor in the behavior of the bridge. The stiffness of the Wake and Halifax County foundation elements (EI/L_{free}) are 506,615 kip-ft/rad and 1007 kip-ft/rad (8842 and 18 kip-ft/deg, respectively). For these stiffnesses, the moment of inertia used was a gross or uncracked moment of inertia and the length was the modeled length from the top of the pile or shaft to the ground surface.

The ratio of bearing pad to foundation element stiffness for the Wake County model ranges from 1:50 to 1:5 while for the Halifax county model this ratio ranges from 11:1 and 97:1. It appears that the more appropriate model to use (fixed or free to rotate) depends on the relative stiffness of the pads to the foundation elements. Alternatively, Figure 107 and Figure 108 show how moment, axial force, demand capacity ratio and longitudinal displacement change relative to a free and fixed rotational bent conditions as the stiffness changes. The y-axis can be interpreted by Equation 14, where in this example, M is moment and M_{fixed} and M_{free} are those shown in Table 26 or Table 27, respectively.

Equation 14

$$Ratio = \frac{M_{rotational} - M_{fixed}}{M_{free} - M_{fixed}}$$

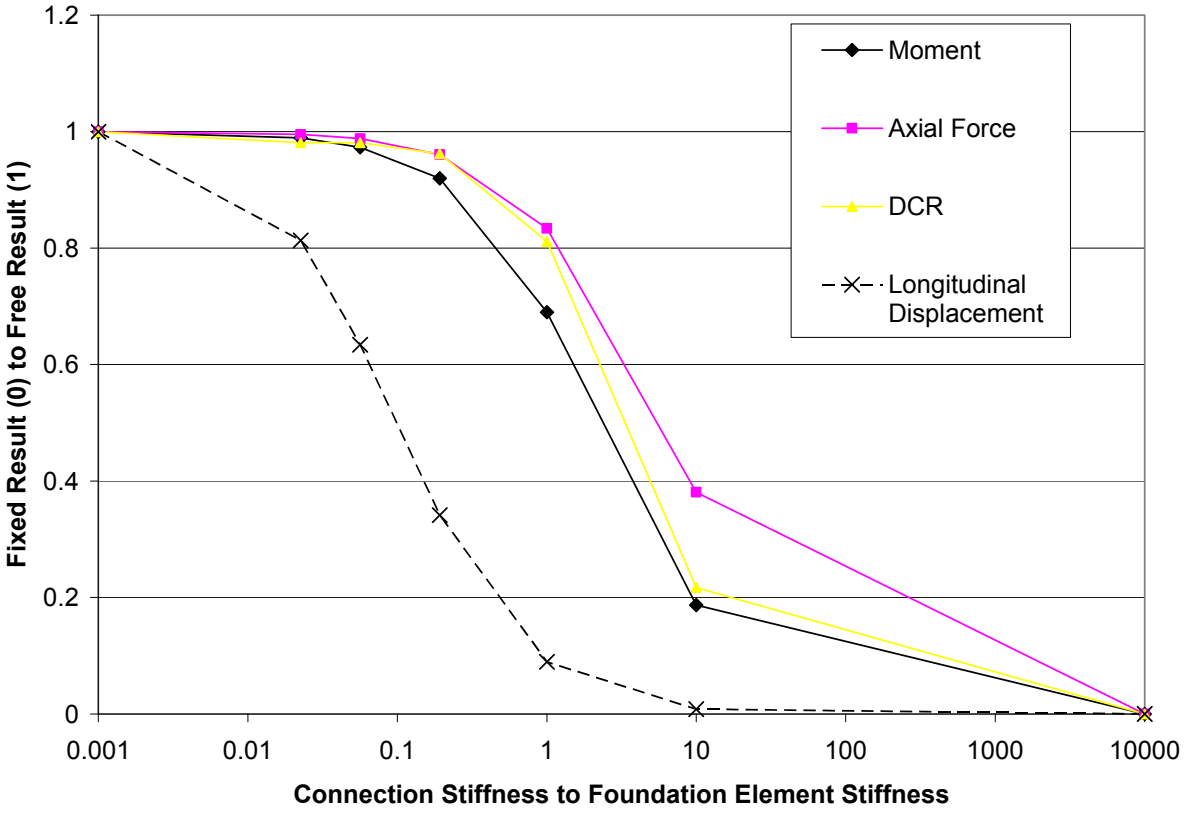

Figure 107. Effect of Stiffness Ratio on Wake County Bridge, normalized to fixed and free results from Table 26.

Figure 107 shows the effect of the connection stiffness on the overall result as the foundation element stiffness changes. The moment, axial force and demand capacity ratio curves are quite similar to one another. The longitudinal displacement, however, drops much more quickly—connections ten or more times stiffer than the foundation element offer no extra benefit for reducing displacements.

Comparing Figure 107 to Figure 108, the shapes of the curves are similar, but the Halifax county bridge (which has a less stiff foundation element than Wake County) tends to be shifted to the right. For a comparison of selected quantities, see Figure 109.

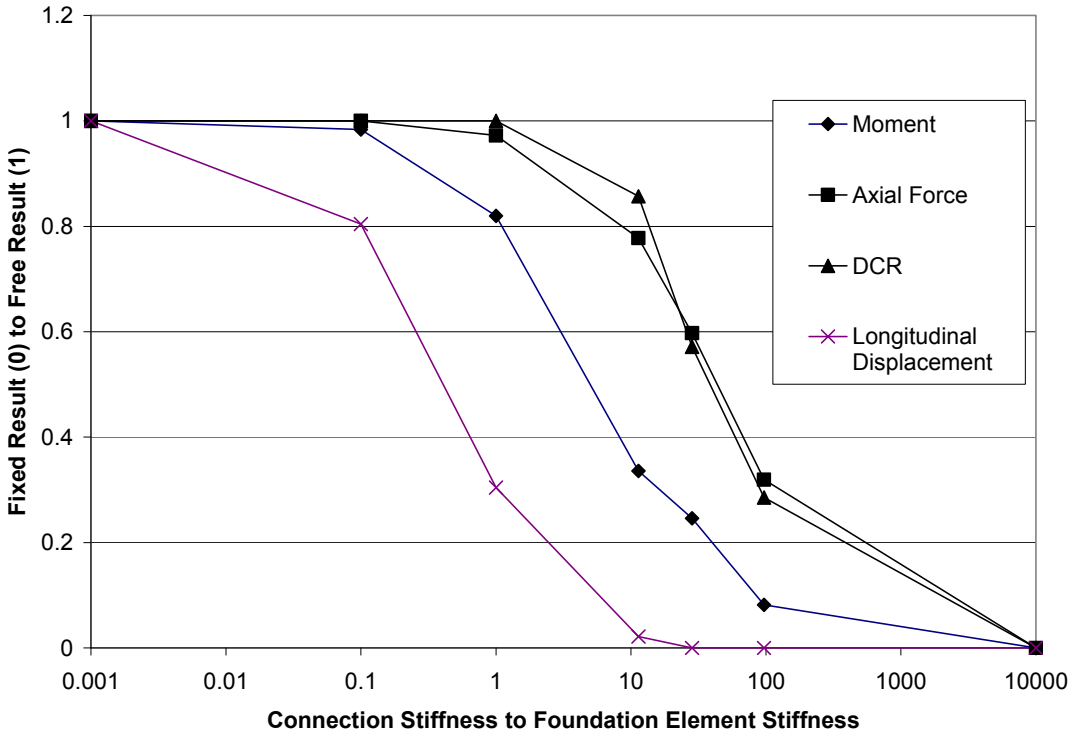

Figure 108. Stiffness Ratio Effect on Halifax County Bridge, normalized to fixed and free results from Table 27

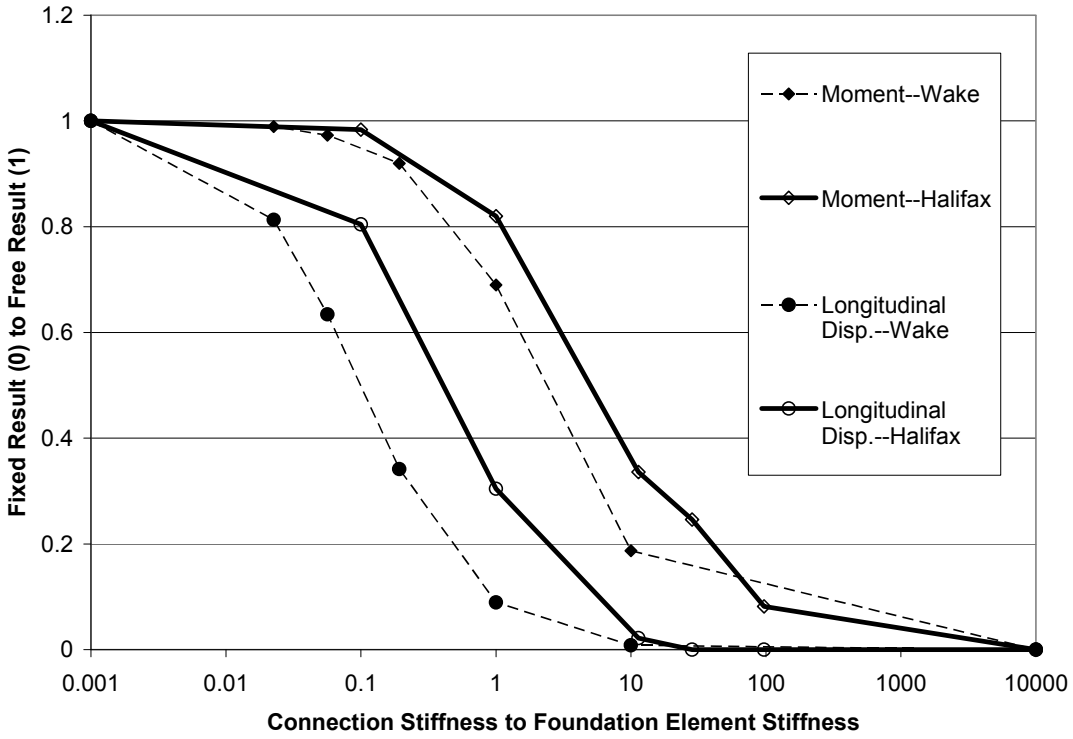

Figure 109. Comparison between Halifax and Wake County Results Normalized to fixed and free heads.

Determining Effective Length Factors

To additionally investigate the effects of a rotational spring on top of a foundation element, another series of MultiPier runs were made. First, an elastic column with a rotational spring at the top and a fixed bottom was modeled to determine the effects on the effective length factor, k, and the overall behavior of the model. This model was free to translate laterally.

Next, a single pile lateral analysis was performed in MultiPier with rotational springs at the pile top in a variety of soil conditions. In this case, the effects on the effective length required to match maximum moments, L_e, and the effective length factor were investigated.

Finally, the effects of rotational springs at the bearing locations of certain pile and shaft bents were examined.

Elastic column analyses

An elastic column was modeled in MultiPier with the same section properties as the Halifax County bridge's precast concrete piles from Robinson et al. (2006). The length was initially set at 10 feet, a typical free length for the piles in that pile bent. That, including the concrete properties and uncracked section resulted in an EI/L of 424,766 kip-in. The base of the column was fixed against rotation and translation; the top of the column was free to translate. The rotational stiffness of the top of the column was varied from free (rotational stiffness of the top spring was zero) to fixed (rotational stiffness of the top spring was very large. Between fixed and free, the rotational stiffness varied as a percentage of EI/L in kip-in/radian.

For a beam fixed at one end and free to translate, but not rotate, at the other end, beam theory says the effective length factor, k, is 1.0. (Gambhir, 2004) For a beam fixed at one end and free to translate and rotate at the other, k is 2.0. If a rotational spring is added, k will vary between 1 and 2.

From the MultiPier numeric results, k can be calculated by determining where the rotation of a particular element reaches an inflection point (the absolute value of the rotation is at a maxima) or where the moment in the section is zero. The two times the distance from the bottom of the column to the point of zero moment divided by the total column length is k. For example, for the free top case, the point of zero moment is at the top of the column, and twice the column length divided by the column length is 2. For the fixed case, the point of zero moment is at the midpoint of the column, so k is 1.

The deflected shape of the laterally loaded column with different rotational stiffnesses applied to the top of the column is shown in Figure 110. The points of zero moment are identified with a data point, which is used to determine the values of k shown in the legend. When the rotational stiffness of the spring is equal to EI/L, k is 1.5.

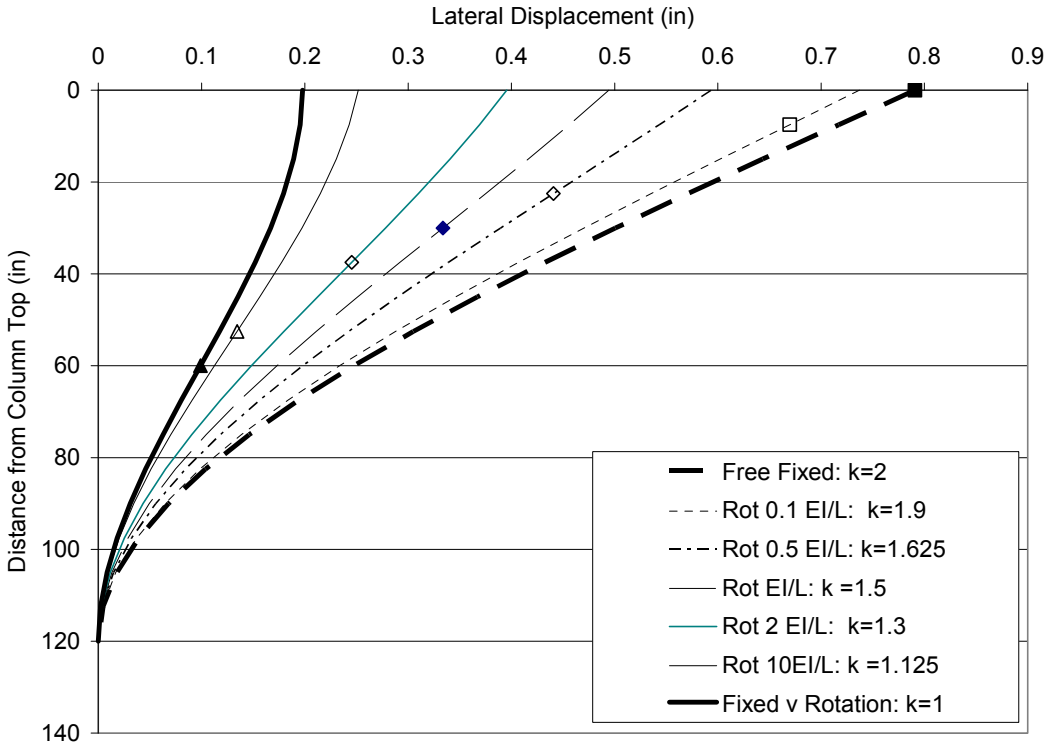

Figure 110. Determination of k for a column (10 ft long, EI/L = 424776 kip-in, 70 kip lateral load). Point of inflection noted in each case by data point.

It should be noted that, in the transverse direction, NCDOT currently assumes a K value of 1.4, which indicates fixity of the connection. Such an assumption seems to be conservative in that direction, and no investigation is focused on the behavior in the transverse direction. Furthermore, POT and TFE bearing pads are not included in this investigation as NCDOT does not use a diaphragm to connect adjacent girders with these types of bearings. Without a diaphragm, such connections will not transfer moment, and a K factor of 2.1 is deemed appropriate, compared to 2.0 calculated using elasticity arguments.

When a rotational spring is applied in the longitudinal direction, the K factor varies from 2 to 1 as a function of the ratio of the rotational stiffness of the spring to the stiffness of the pile. When the pile is changed from a column to a 50 foot long pile, embedded 40 feet in a sand with a friction angle of 30 degrees. The stiffness of the pile remained unchanged. Table 28 shows the results of this analysis, which implies the additional restraint provided by the soil and the increased pile length tend to increase the k value when the pile top rotational springs have similar stiffnesses.

Table 28. Pile embedded in sand: equivalent lengths and k factor

Rotational Spring as EI/L of pile	Le (ft) per Figure 7, fixed head	K per Figure 7, fixed head
10%	10.5	2.0
50%	12.0	1.8
100%	14.8	1.4
Fixed	15.6	1.3

Limit States

Lateral displacement limit based on pile or shaft yield

The yield displacement Δ_y is defined as the lateral displacement at which drilled shafts or piles reach their yield moment capacity. The yield displacement marks the onset of inelastic behavior and damage in the piles of shafts and can be accurately determined from a lateral inelastic static analysis of the structure, often called pushover analysis. Alternatively, Δ_y can be estimated by integration of the curvature profile of the pile or shaft at yield. However, due to the complex shape of the curvature profile, this could be difficult to achieve unless the soil-pile system is replaced by an equivalent column, for which the integration of curvature has a closed form solution.

The yield displacement of a fixed base column with free or fixed head can be estimated with Equation 15 and Equation 16 respectively. In these equations L_e is the equivalent length calculated with the formulation proposed by Robinson et al. (2006).and ϕ_y is the yield curvature of the shaft of pile section.

Equation 15

$$\Delta_y = \frac{\phi_y L_e^{\,2}}{3}$$

Equation 16

$$\Delta_y = \frac{\phi_y L_e^{\,2}}{6}$$

The yield curvature of reinforced concrete, steel or composite sections can be estimated by Equation 17 in terms of the yield strain of the steel in the section ε_y and the section diameter D

Equation 17

$$\phi_y = 2.\frac{\varepsilon_y}{D}$$

Then, the yield displacement is determined for free and fixed head conditions, as shown in Equation 18 and Equation 19 respectively, by substitution of Equation 17 into Equation 15 and Equation 16.

Equation 18

$$\Delta_y = \frac{2\varepsilon_y L_e^{\,2}}{3D}$$

Equation 19

$$\Delta_y = \frac{\varepsilon_y L_e^{\,2}}{3D}$$

According to Equation 18 and Equation 19, Δ_y is a quadratic function of Le. This formulation is approximate and conservative since it does not account for the real shape of the curvature profile nor the rotation at the point of fixity that exist in the real soil-pile system.

It was mentioned before that the most accurate way of determining yield displacement is a pushover analysis of the structure; such an analysis can be performed using MultiPier with a nonlinear model of the bent and surrounding soil. The pushover analysis in MultiPier is force-based; therefore the total lateral force acting in the structure is applied, after gravity load, in a given number of increments going from zero to the full load value. Each loading increment returns displacements and forces along the piles and in the soil. The solution is iterative and convergence will depend on the level of displacement and convergence tolerance set by the analyst.

The yield displacement is found in MultiPier when the moment profiles show that any section has reached the yield moment, M_y. This will be close but generally less than the displacement at which the demand/capacity ratio approaches one. The reason is that the latest limit is related to the pile or shaft section reaching its ultimate flexural capacity, as defined by design codes. The yield displacement M_y should be obtained from a separate moment-curvature analysis of the pile or shaft section.

As an example, the moment-curvature response of the reinforced concrete drilled shaft of Wake County Bridge has been found with the section analysis program USC-RC (Esmaeily, 2000) and it is shown in Figure 111. From the M-C response, the yield moment, M_y related to the yield curvature, ϕ_y that should be checked in MultiPier is found with the following procedure:

1) The first yield moment M_y' and the nominal strength moment M_n are determined in the M-C response. M_y' is found when the reinforcing steel first reaches ε_y. M_n if found when the concrete reaches a compression strain of 0.003.
2) A bilinear representation of the M-C response if developed with one line segment going from the origin and intercepting the M-C curve in M_y'. The second segment is drawn from the M_n point to intercept the first segment balancing the areas formed with the M-C curve above and below.
3) The intersection of the two segments of the bilinear diagram gives the yield curvature of the section ϕ_y. A vertical line drawn from this point to cut the M-C curve will give the yield moment M_y

For the four bridges studied by Robinson et al. (2006) and the three covered in this report, Table 29 and Table 30 show the yield displacement calculated with the Equation 18 and Equation 19 and also the yield displacement found with a pushover analysis. It is observed that the approximate procedure presented at the beginning of this section gives a conservative estimate of yield displacement for both transverse and longitudinal response that for all cases is higher than the one inch limit generally used by the NCDOT. The yield displacement based on Pushover analysis for Wake County and Pitt County Bridges were not found since the pushover analysis failed to converge before reaching this point. This was due to the high flexibility of these structures.

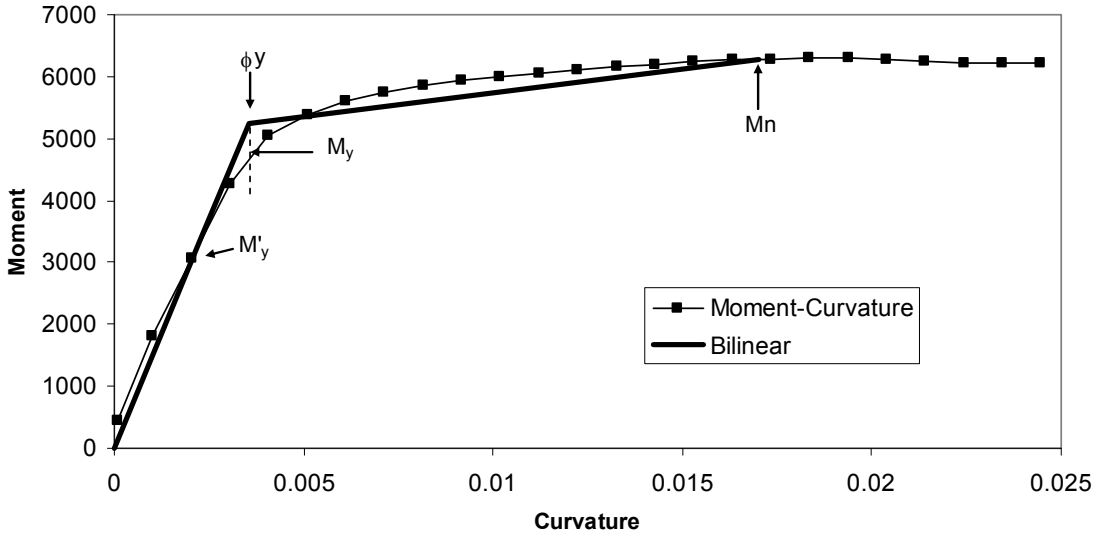

Figure 111.Moment-Curvature response of drilled-shafts in the Wake County Bridge

Table 29. Transverse yield displacement based on equivalent model parameters

Bridge	Pile Type	ε_y	h or D (in)	Le (ft)	Δ_y (in)	Δ_y (in) Mpier
Robeson	H14x73	0.0022	14	14.50	1.59	4.56
Northampton	24in SPP	0.0022	24	22.20	2.17	2.62
Halifax	18in S-PCP	0.0015	18	22.60	2.04	2.18
Rowan	RC Drilled Shaft	0.0022	48	36.30	2.90	5.40
Wake	RC Drilled Shaft	0.0022	48	65.62	9.47	not found
Pitt	RC Drilled Shaft	0.0022	60	73.40	9.48	not found
Bridge		ε_y	**h or D (m)**	**Le (m)**	Δ_y **(m)**	Δ_y **(m) Mpier**
Washington	406mm S-PCP	0.0015	0.406	6.28	0.10	0.07

Table 30. Longitudinal yield displacement based on equivalent model parameters

Bridge	Pile Type	ε_y	h or D (in)	Le (ft)	Δ_y (in)	Δ_y (in) Mpier
Robeson	H14x73	0.0022	14	10.80	1.76	13.00
Northampton	24in SPP	0.0022	24	16.20	2.31	8.14
Halifax	18in S-PCP	0.0015	18	16.80	2.26	4.06
Rowan	RC Drilled Shaft	0.0022	48	22.90	2.31	11.80
Wake	RC Drilled Shaft	0.0022	54	96.52	36.44	not found
Pitt	RC Drilled Shaft	0.0022	60	84.20	24.96	not found

Based on these results, it can be concluded that a conservative estimate of yield displacement, that can be used as a design limit state, can be easily calculated with Equation 18 and Equation 19 for free head and fixed head response respectively. The yield displacement is directly proportional to the square of the equivalent length and inversely proportional to the diameter of the section. For the seven bridges studied in this

report, the yield displacement calculated by equation and by pushover analyses are higher than the one inch design limit generally used by the NCDOT.

Transverse Displacements Required to Close Expansion Joints

As outlined in Robinson et al (2006), serviceability limit state was proposed on the basis of joint closure. The bridge system is treated as a multi-span support system with foundation and abutments represented as springs. Limit state is established on the basis of the distance that a joint gap would close due to an applied lateral load in the transverse direction. Figure 112 and Equation 20 through Equation 22 show one configuration with the various parameters associated with determining the joint closure.

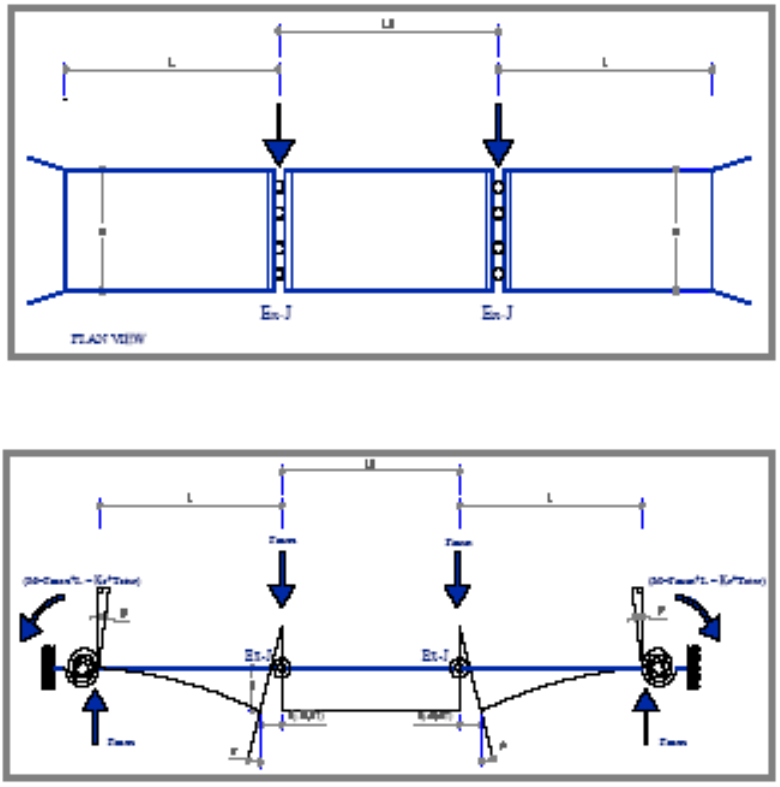

Figure 112. Joint Closure Model for 3 spans supported by 2 interior pile bents at the expansion joints (Robinson et al 2006)

Equation 20

$$P\max = \frac{\left(\delta j - \alpha(\Delta T)\left(L + \frac{L2}{2}\right)\right)}{\left(\frac{w}{2}\right)\left(\frac{L^2}{2EI} + \frac{L}{Kr}\right)}$$

Equation 21

$$\delta tot = \frac{P\max L^3}{3EI} + \frac{P\max L^2}{Kr} + \frac{P\max}{K1}$$

Equation 22

$$FL = P\max + \left(K2 * \delta tot\right)$$

Where,

Pmax = Force required to close the expansion joint (force units)

δtot = Lateral displacement limit (length)

δj = Joint width (length)

K1 = Abutment stiffness (trans-rot) (force/length)

K2 = Pile group stiffness (trans-rot)(force/length)

Kr = rotational stiffness of the bearing pad in the transverse direction (force-length/rad)

L = exterior span lengths (length)

L2 = interior span length (length)

w = width of span (length)

EI = flexural stiffness of the superstructure (trans-rot)(force-lenght^2)

α = coefficient of thermal expansion (1/Temperature)

ΔT = Temperature

An important parameter for the application of equations 15, 16 , and 17 to establish limit state is the rotational stiffness at the key joint locations. Results from full scale testing conducted herein provided data on super to sub structure's rotational stiffness in longitudinal direction for three different piles. An illustration of the application of the limit state equation is provided in the next section.

The Halifax County Bridge is analyzed to determine if the joint closure serviceability limit state. This bridge consists of 9 spans where the interior girder spans are supported by a continuous cap beam with 8 piles. The supporting square piles are 18 inch (45.7cm)

in width and are 40 feet (12.2m) to 50 feet (15.2m) long. The interior bents connection with the superstructure in 2 spans was achieved using Type I elastomeric bearing pads.

In this case, some changes are implemented in order to adapt the measured values from the full scale testing for use in this case study. Data from the full scale testing on the 20 inch (50.8cm) square pile with Type V and Type VI bearing pads are used. The rotational stiffness determined from full scale testing on the square pile will be multiplied by a factor of 15 to simulate the torsional stiffness of the entire bent connection of the Halifax county bridge. Additional simulations will be run assuming 1/10, 1/2, 2, and10 times the original torsional stiffness used in the case study. The analyses are run assuming the original joint gap between the spans is 0.5inches (1.27cm). If it is determined that there will be a component of the bridge that will fail before the joint closes, the required original joint gap will be calculated that ensures that the joint closure is the limiting failure mode.

Analyses on interior piles bents showed that the pile bent could not tolerate a horizontal load (transverse direction) greater than 44 kips (195kN) with a maximum displacement of 0.6 inches (1.5cm). Figure 2 shows the response curve of the lateral load verse transverse displacement of the pile bent. From Figure 2, the pile group stiffness (K2) term is defined as a horizontal capacity of 44 kips (195 kN). The abutment stiffness variable (K1) was estimated from Maroney (1995).

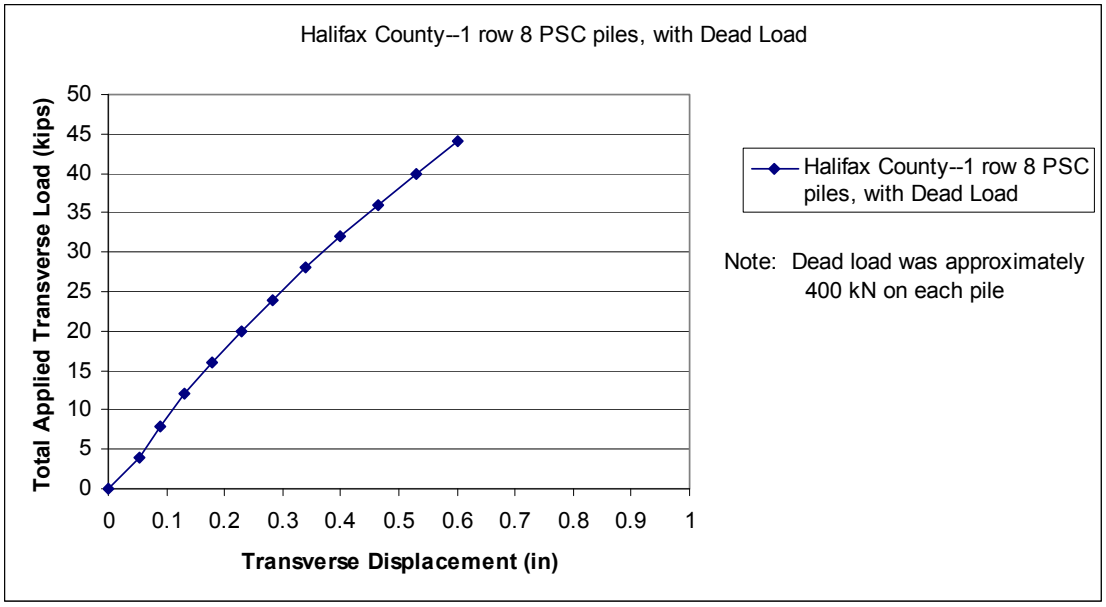

Figure 113. Halifax County Bridge Bent Response to Lateral Load

Table 31 shows the input variables used based on some known details of the Halifax county bridge, as well as information presented in Maroney (1995) and Figure 113,. It should be noted that it was assumed for this analysis that the thermal expansion component was not significant.

Table 31. Input variables for Halifax County bridge section

E (Young's Modulus of concrete)	550609	Ksf	26314593	kN/m^2
I (moment of inertia of superstructure)	6253	ft^4	53.97	m^4
L (length of outer spans)	40	Ft	12.2	m
L2 (length of interior span)	35	Ft	10.7	m
W (width of span)	35	ft	10.7	m
t (thickness of deck)	1.75	ft	0.5	m
K1	2579	k/ft	123269	kN/m^2
K2	884	k/ft	42267	kN/m^2
$\alpha\Delta T$ (thermal expansion component)	0			

The rotational stiffness values used in the analyses were taken form the testing results of the 3% ALR loading case with load level P1 on bearing pad type V, at the 0.75inch (19.1 mm) top displacement. This value was closest to the maximum capacity of 0.6inch (1.52cm) of the pile group presented in Figure 113. The results from the application of equations 1, 2, and 3 to define the limit state are presented in Table 32.

Table 32. Results from Joint Closure Investigation for Halifax County Bridge

Factors of Torsional Stiffness Assumed	Torsional Stiffness (**Kr**)		Thickness of expansion joint (**δj**)		Force Required to Close Gap (**Pmax**)		Total Transverse Lateral Displacement from Pmax (**δt**)		Total lateral force that will close the exp. Joint and displace the pile laterally (**FL**)	
	k-ft/rad	kN-m/rad	in	cm	kips	kN	in	Cm	kips	kN
Base Case	184349	249481	0.50	1.27	10.96	48.67	1.19	3.03	1066	4735
1/10	18435	24948	0.50	1.27	1.10	4.87	1.15	2.92	1016	4512
1/5	36870	49896	0.50	1.27	2.19	9.74	1.15	2.93	1022	4537
½	92174	124741	0.50	1.27	5.48	24.35	1.17	2.97	1039	4611
2	368697	498962	0.50	1.27	21.90	97.23	1.24	3.16	1122	4982
5	921743	1247406	0.50	1.27	54.57	242.31	1.39	3.54	1288	5719
10	1843487	2494812	0.50	1.27	108.57	482.04	1.64	4.18	1562	6937

Analyses results indicate that the force required to close a 0.5inch (1.27cm) expansion joint (**FL**) does not vary significantly given the range of the torsional stiffness values used in the analysis. These results also show that the force required to close the expansion joint is larger than the lateral load capacity of the interior pile bents, estimated as 44kips (195kN). If the torsional stiffness is assumed essentially equal to zero, the total lateral force that will close the expansion Joint was found equal to 1,011 kips (4488 kN). In this case, the pile bent has already experienced its lateral displacement limit of 0.6 inches (1.52cm) at 44kips(195kN) and represents the critical juncture in the limit state.

The most significant contributing factor to the force required to close the expansion joint is the abutment rotational stiffness as is evident by the nature of Equation 22. Data in Table 32 showed that the joint closure would not be the governing failure mode for a 0.5

inch (1.27cm) expansion joint. Alternatively, the required expansion joint thickness where closure of the joint is the critical limit state is determined. By limiting the required lateral force to close the expansion gap to 44 kips (195kN), the joint thickness for which joint closure represents the limit state is presented in Table 33.

Table 33. Results from determined required joint thickness for failure due to joint closure.

Factors of Torsional Stiffness Assumed	Torsional Stiffness		Thickness of expansion joint required for joint closure failure mode (**δj**)		Force Required to Close Gap (**Pmax**)		Total Transverse Lateral Displacement from Pmax (**δt**)		Total lateral force that will close the exp. Joint and move the pile laterally (**FL**)	
	k-ft/rad	kN-m/rad	in	cm	kips	kN	in	cm	kips	kN
Base Case	0.00	0.00	**0.0218**	0.0553	0.00	0.00	0.05	0.13	44	195
1/10	18435	24948	**0.0216**	0.055	0.05	0.21	0.05	0.13	44	195
1/5	36870	49896	**0.0215**	0.0547	0.09	0.42	0.05	0.13	44	195
½	92174	124741	**0.0212**	0.0538	0.23	1.03	0.05	0.13	44	195
2	368697	498962	**0.0196**	0.0498	0.86	3.81	0.05	0.12	44	195
5	921743	1247406	**0.0171**	0.0434	1.86	8.28	0.05	0.12	44	195
10	1843487	2494812	**0.0141**	0.0358	3.06	13.57	0.05	0.12	44	195

Given the values of the torsional stiffnesses sued in the analysis, the results in Table 4 show that the largest joint thickness for which closure is critical is 0.0218inches (0.0553cm). This value is not representative in the field and therefore it seems that the pile bents lateral capacity is governing limit state under the applied lateral load. This conclusion is only valid for the particular parameters idealized for the Halifax county bridge.

CHAPTER 7: RESISTANCE FACTORS FOR DRILLED SHAFTS

In Load Resistance Factor Design (LRFD), applied loads are multiplied by a factor and compared to ultimate resistances computed by methods commonly used in engineering practice. AASHTO (2006) has several load factors for bridge design, however the resistance factors for deep foundations have been more controversial, with a significant revision introduced between 2004 and 2006. In North Carolina, NCDOT developed regional resistance factors for driven piles based on static and dynamic pile load test data. Work presented herein aims at determining resistance factors for axial and lateral capacities of drilled shafts in North Carolina soils.

Axial load test reports, including subsurface conditions and drilled shafts dimensions, were provided by NCDOT to use for developing resistance factors. Ten lateral load and twenty axial load tests were analyzed. Based on each site's geotechnical conditions and site geometry, T-z, Q-z (for axial capacity) and P-y curves (for lateral capacity) were developed. Simulations of the load tests were performed using the MultiPier program. Resistance factors were estimated using probability and reliability analyses.

Modeling of the Axial Load Tests

Axial Skin Friction: T-z curves

MultiPier uses an asymptotic shaft resistance model to estimate the load transfer to the soil and the displacement of the shaft. The axial soil-shaft interaction models for drilled and cast in-place shafts that are available in MultiPier are summarized in Table 34 and described more fully in BSI (2000).

Table 34. MultiPier T-z curve models

Material	Developer	Used in this project
Drilled Shaft Sand	Wang and Reese (1993)	Used
Drilled Shaft Clay	Wang and Reese (1993)	Used
Drilled Shaft IGM (T-z)	Wang and Reese (1993)	Used
Drilled Shaft Limestone (McVay)	McVay (1989)	Used

The maximum frictional resistance of the drilled shaft in a clay model ranges from 0 to 0.4 ksf based on the effective vertical stress. In addition, the undrained shear strength is estimated on the basis of 20% of the effective vertical stress at the center of a given layer. The representative SPT N-values and the estimated undrained shear strength, S_u, of the clay layer for all axial load tests are presented in Table 35.

Table 35. Undrained shear strength of the drilled shaft clay model

Axial Load Tests	SPT N	Average σ'_v (ksf)	S_u range and (used) values (ksf)	Comments
DDP-1 & 2	10~40	0.7~2.6	0.1~0.5 (0.2)	Clay Layer
LT8650-1 ~ 5	2~13	0.3~1.4	0.1~0.3 (0.2)	Sandy Clay
LT8650-6 ~ 8	3~9	0.2~1.4	0.05~0.3 (0.1)	Sandy Clay
Bent-8	-	1.28	0.26 (0.2)	Muck Clay

The drilled shaft "sand" model is used for the 'silty sand' and 'sand and gravel layers' of Pier-19, Pier-34, Pier-48, LT8958-1, LT8958-2, and LT8402 axial load tests. The unit weight of each layer is estimated based on N-values. The unit weights used in the models are presented in Appendix B.

In order to simulate frictional resistance in weathered or weak rock layers, three different models are used. First, the Limestone (McVay) model, with NCDOT's empirical suggestion for drilled shaft rock socket skin friction values is used. In this case, the maximum frictional force is assumed to range from 4 to 6 ksf. The T-z curves for this model are presented in Figure 114 (a).

The maximum frictional force of the T-z model has also been obtained from empirical relations suggested by Horvath and Kenney (1979), as shown in Equation 23. This correlation uses the unconfined compressive strength of the rock, and is applied for LT 8958-1 and 8958-2 with Rock Quality Designation (RQD) and unconfined compressive strength, as shown in Table 36. The T-z curves for two axial load tests are presented in Figure 114 (b).

Equation 23 $$f_s(\text{psi}) = 2.5\sqrt{q_u(\text{psi})}$$

Where,

f_s =ultimate side resistance in units of lb/in^2

q_u =unconfined compressive strength of the rock in units of lb/in^2.

Table 36. Maximum frictional resistance of Horvath and Kenney (1979)

Axial Load Tests	RQD	q_u , psi (kPa)	f_{smax} in ksf (kPa)	Comments
LT8958-1	75	2589 (17850)	877 (42,000)	Isolated Clay Layer
LT8958-2	95	2974 (20500)	940 (45,000)	Sandy Clay

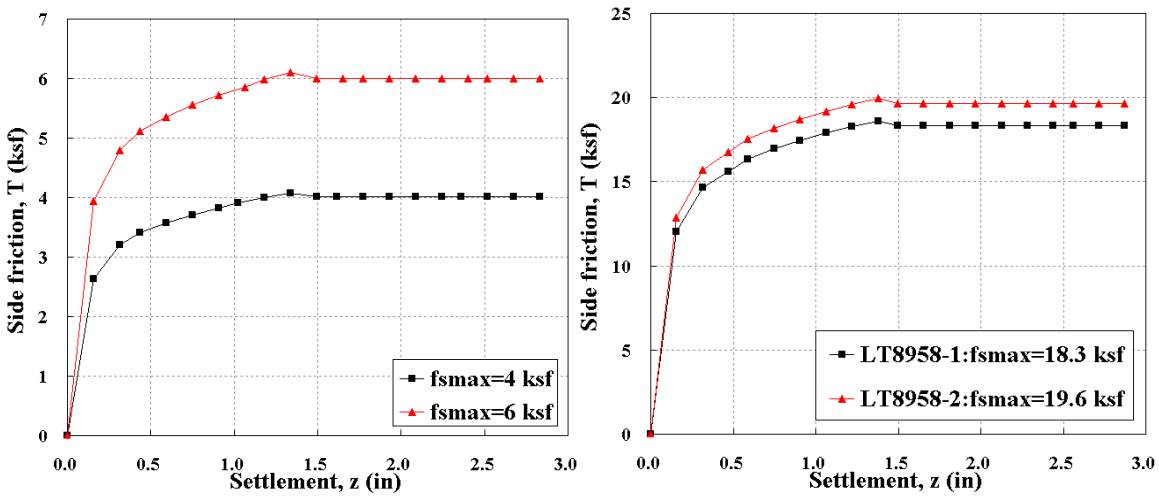

(a) NCDOT's empirical suggestion (b) Horvath and Kenney's equation

Figure 114. T-z curves for Limestone (McVay) model

Finally, the Intermediate Geo-Material (IGM) model is also used in addition to NCDOT's and Horvath and Kenney (1979)'s criteria. The model is applied to simulate subsurface conditions for LT8958-1, LT8958-2, and LT8402. The details of input parameters and T-z curves are presented in

Table 37 and Figure 115, respectively. In case LT8402 (see

Table 37), the unconfined compressive strength and split tensile strength (T_0) are estimated as 17,405 psi (120 MPa) and 0.29 ksi (2000 kPa), respectively, for shale based on Goodman (1997).

Table 37. Input properties for IGM (Intermediate Geo-Material) model

Axial Load Tests	γ_t in pcf (kN/m^3)	q_u in psi (MPa)	E_m in ksi (MPa)	E_m/E_i	T_0 in ksi (MPa)
LT8958-1	120.9 (19)	2,589 (17.9)	145 (1000)	0.9	0.363 (2.5)
LT8958-2	127.3 (20)	2,974 (20.5)	145 (1000)	0.9	0.363 (2.5)
LT8402	140.0 (22)	10,900 (75.2)	145 (1000)	0.2	0.290 (2.0)

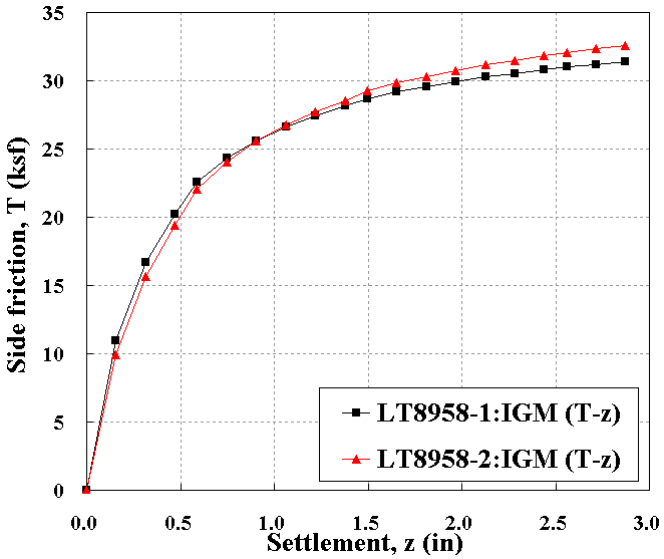

Figure 115. T-z curves for IGM (Intermediate Geo-Material) model

End Bearing: Q-z Curves

The Limestone model for end bearing resistance was used for most of the axial load test cases. For LT8958-1 and LT8958-2 cases, the IGM model for obtaining the Q-z curves is presented in Figure 116.

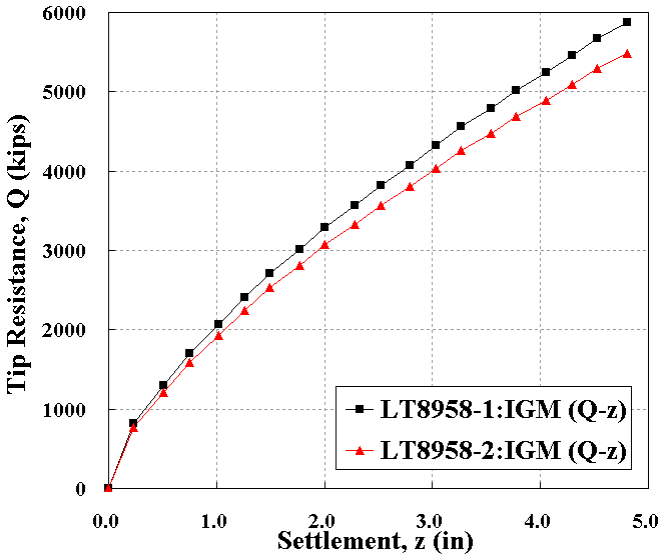

Figure 116. Q-z curves for IGM model

Soil Models for Lateral Load Tests

Stiff clay

The stiff clay model proposed by Reese, et al. (1975) has been used for simulating laterally loaded drilled shafts that are embedded in weathered rock. The model is presented in Equation 24. For all stiff clay profiles, undrained shear strength is estimated as 200 kPa, and the major principal strain at 50% of the maximum stress level, ε_{50}, is 0.004.

Equation 24 $$\frac{P}{P_{ur}} = \left(\frac{y}{16 y_{50}} \right)^{0.25}$$

P-y Curves of Reese's Weak Rock Model

Reese (1997)'s Weak rock model was developed based on data from two load tests, and is still considered 'interim' due to the limited data used in its development. The ultimate lateral resistance is estimated based on the compressive strength of the embedded rock and geometrical conditions, as shown in Equation 25 and Equation 26.

Equation 25 $$p_{ur} = \alpha_r q_{ur} b \left(1 + \frac{1.4 x_r}{b} \right)$$

Equation 26 $$p_{ur} = 5.2 \alpha_r q_{ur} b$$

where,

q_{ur} = compressive strength of the rock (usually the lower-bound as a function of depth)

α_r=strength reduction factor

B=width, or diameter of the pile

x_r=depth below the rock surface.

More details on this method were presented in the NCDOT report by Gabr et al. (2002). Also in the same report, the geotechnical properties and the P-y curves were presented for ten lateral load tests. Figure 117 shows the profiles of ultimate resistance using Reese's

interim model for the ten load cases used in this report. In Figure 117 (a), Nash/Caldwell/Wilson refers to cases from Nash, Caldwell, and Wilson County test sites. Since the ultimate resistance values of the I-40 and I-85 test shafts were estimated from several layers of weathered rock, the profile of the ultimate resistance has an irregular shape with depth, as shown in Figure 117 (b).

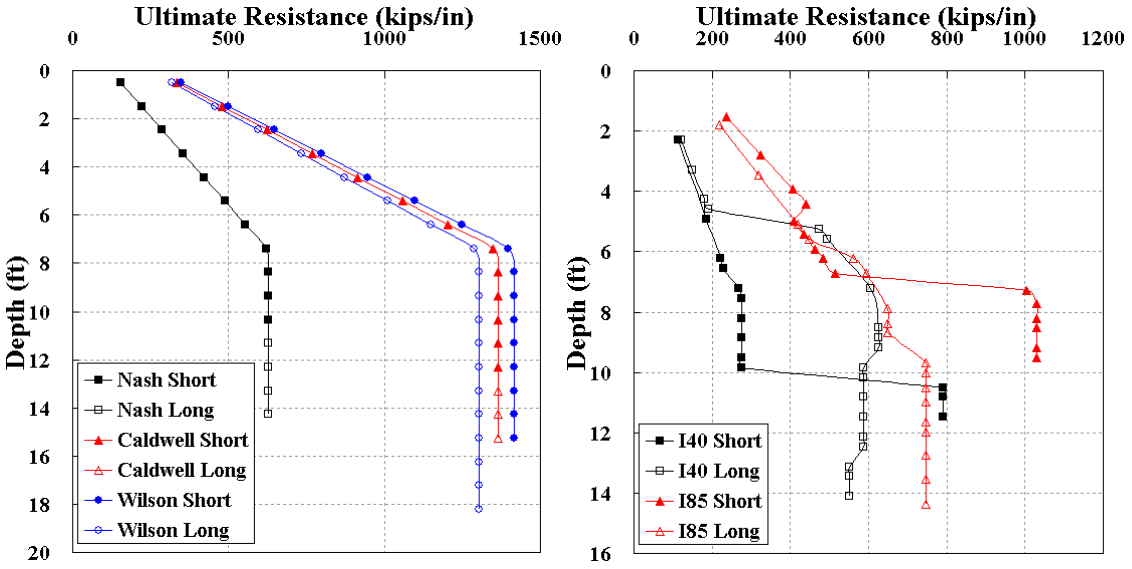

(a) Nash/Caldwell/Wilson (b) I-40/I-85

Figure 117. Ultimate resistance for Reese's Weak Rock model

Using Reese's model, P-y curves for the 10 lateral load tests were generated and are presented in

Figure **118** (a) to (j). Four representative curves are presented in

Figure **118** for each case as illustration of their shape and magnitude.

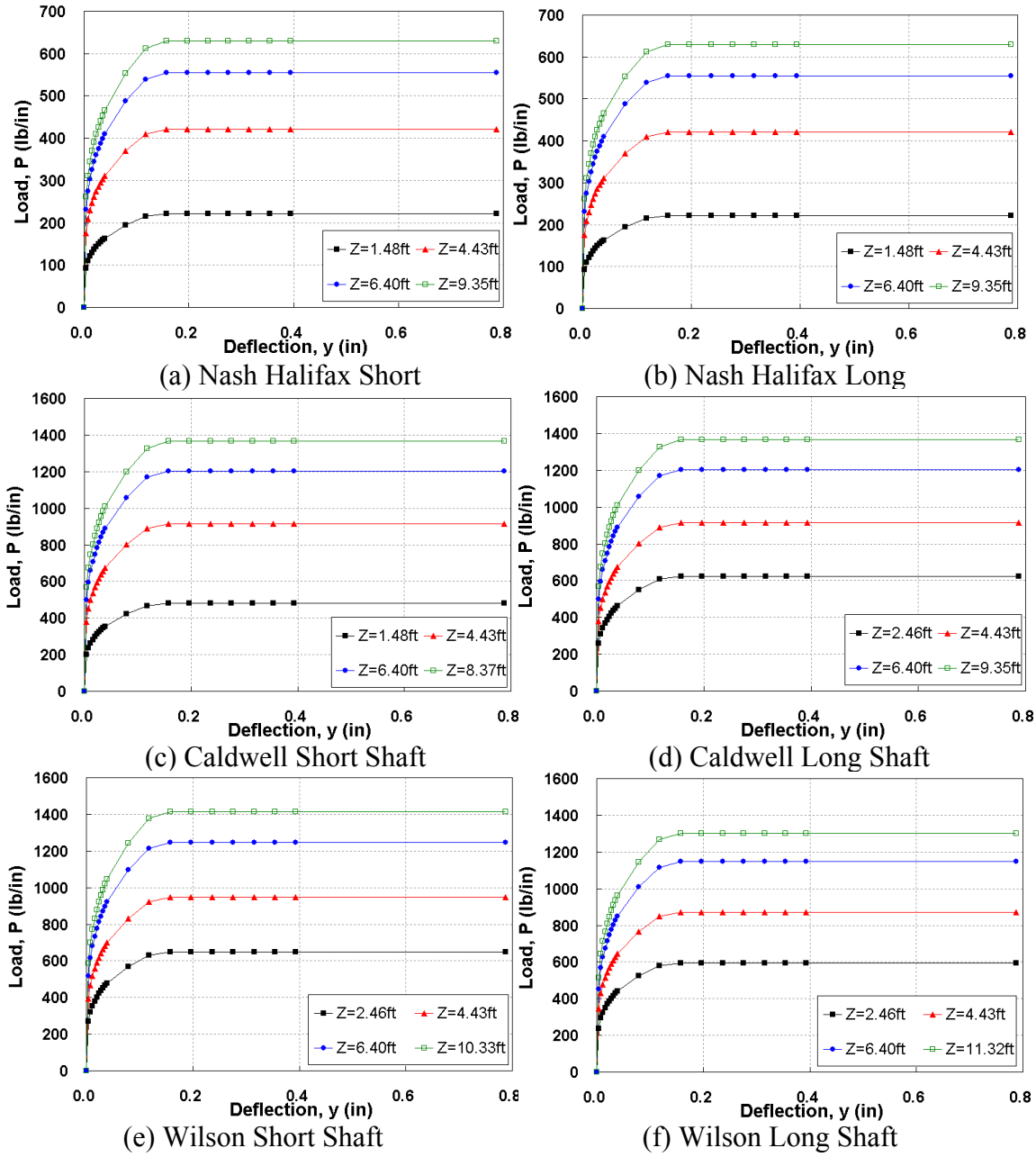

Figure 118. P-y curves for Reese's Weak Rock model

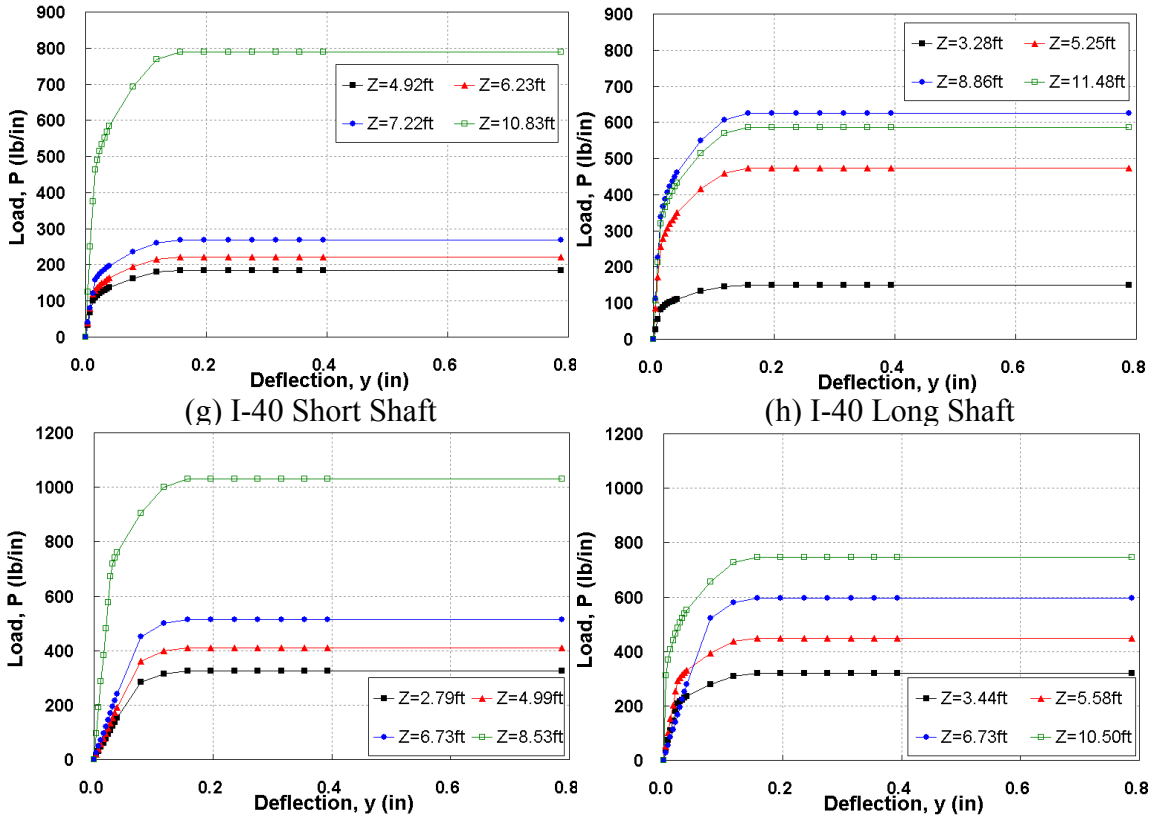

(g) I-40 Short Shaft (h) I-40 Long Shaft

(i) I-85 Short Shaft (j) I-85 Long Shaft

Figure 118. P-y curves for Reese's Weak Rock model (continued)

Geologic Model

The Geologic model is based on the model of Cho (2002), and uses properties such as the Geologic Strength Index (GSI), unconfined compressive strength, and rock mass parameters (m_i, m_s). This model was validated using test results from the laterally drilled shafts embedded in weathered rock as reported by Gabr et al. (2002).

As shown in Equation 27, one hypothesis proposed by Cho (2002) was that a hyperbolic function could adequately model P-y curves for weathered rock. The hyperbolic function is generated using two properties: lateral subgrade reaction and the lateral ultimate resistance.

Equation 27 $$P(y) = \frac{y}{a + by}$$

where,

$a = \frac{1}{k_h}$, k_h =initial tangent modulus (subgrade reaction)

$b = \frac{1}{p_{ult}}$, p_{ult} =ultimate resistance.

Table 38 and

Table 39 show the material properties of Nash/Caldwell/Wilson and I-40/I-85 test cases. These properties are used to generate the P-y curves based on the Geologic model. These properties were reported by Gabr et al (2002).

Table 38. Inputs for P-y curve of Geologic model (Nash, Caldwell, and Wilson)

Location	Nash		Caldwell		Wilson	
Type	Short	Long	Short	Long	Short	Long
Layers	1	1	1	1	1	1
L (ft)	11.0	15.0	13.1	15.7	15.9	18.7
γ' (pcf)	80	93	108	108	109	107
σ_{ci} (ksi)	2.8	4.0	4.5	8.8	9.1	8.4
GSI	15	20	25	30	40	25
m_i	9	19	33	33	9	9
m_b	0.432	1.091	2.266	2.709	1.056	0.618
S	0.00008	0.00014	0.00024	0.00042	0.00127	0.00024
A	0.5	0.5	0.5	0.5	0.5	0.5
E_s (ksi)	85	136	191	356	645	261
k_{ho} (psi/in)	22	35	48	91	164	66
K_R	0.00903	0.00163	0.00198	0.00051	0.00027	0.00035
T_0 (ft)	6.9	7.5	6.7	6.4	5.7	7.1
I_T	48.33	87.92	82.93	121.33	142.95	134.03

Table 39. Inputs for P-y curves of Geologic model (I-40 and I-85)

Location	I-40							I-85						
Type	Short Shaft			Long Shaft				Short Shaft			Long Shaft			
Layers	3			4				3			4			
Layer No.	1	2	3	1	2	3	4	1	2	3	1	2	3	4
L (ft)	5.9	3.3	1.6	3.9	4.6	3.3	2.0	3.9	2.3	2.5	3.9	4.6	3.3	2.0
γ' (pcf)	159	159	159	159	159	95.5.	95.5.	95.5.	95.5	95.5	95.5	95.5	95.5	95.5
σ_{ci} (ksi)	1.6	1.8	5.1	1.8	4.0	3.8	3.5	4.2	3.6	6.6	3.6	4.2	4.8	4.8
GSI	77	61	63	41	79	63	61	59	59	59	38	38	38	59
m_i	9	9	19	9	14	14	14	9	9	9	9	9	9	9
m_b	3.96	2.24	5.07	1.09	6.61	3.73	3.48	2.08	2.08	2.08	0.98	0.98	0.98	2.08
S	0.078	0.013	0.016	0.001	0.097	0.016	0.013	0.011	0.011	0.011	0.001	0.001	0.001	0.011
a	0.5	0.5	0.5	0.5	0.5	0.5	0.5	0.5	0.5	0.5	0.5	0.5	0.5	0.5
E_s (ksi)	2307	954	1811	302	4045	1560	1350	1313	1213	1642	363	389	418	1399
k_{ho} (psi/in)	586	242	460	77	1027	396	343	334	308	417	92	99	106	355
$E_{s(avg)}$ (ksi)	1691			1814				1389			642			
K_R	0.00048			0.00017				0.00139			0.00048			
T_0 (ft)	4.4			3.5				5.3			4.4			
I_T	123.20			200.61				92.13			163.22			

The GSI values were as suggested by Hoek and Brown (1997) based on RMR (Rock Mass Rating) value. The elastic modulus for a rock mass, E_s, was obtained from Equation 28 and from rock dilatometer testing.

Equation 28 $$E_s\ (GPa) = \sqrt{\frac{\sigma_{ci}}{100}}\,10^{\frac{GSI-10}{40}}$$

where,

σ_{ci} = compressive strength of intact rock (MPa).

The flexibility factor (K_R) was introduced based on the suggestion of Poulos and Davis (1980).

Equation 29 $$K_R = \frac{E_p I_p}{E_s L^4}$$

where,

E_p = Young's modulus of drilled shaft

I_p=moment inertia of drilled shaft

L=the length of drilled shaft

The point of rotation, normalized as a function of shaft-length (T_0/L), was estimated using the Equation 30 (Gabr et al 2002).

Equation 30 $$\frac{T_0}{L} = 1 + 0.18 \log K_R \quad (K_R \le 1)$$

An empirical multiplier (I_T) below point of rotation can be obtained from Equation 31

Equation 31 $$I_T = -28 - 383 \log(\frac{T_0}{L}) \qquad I_T \ge 1$$

Figure 119 (a through j) shows the P-y curves obtained using the procedure proposed by Gabr et al (2002). The variability in the shape and magnitude of the P-y curves with depth is attributed to the layered profiles and the associated properties as outlined in Table 38 and

Table 39.

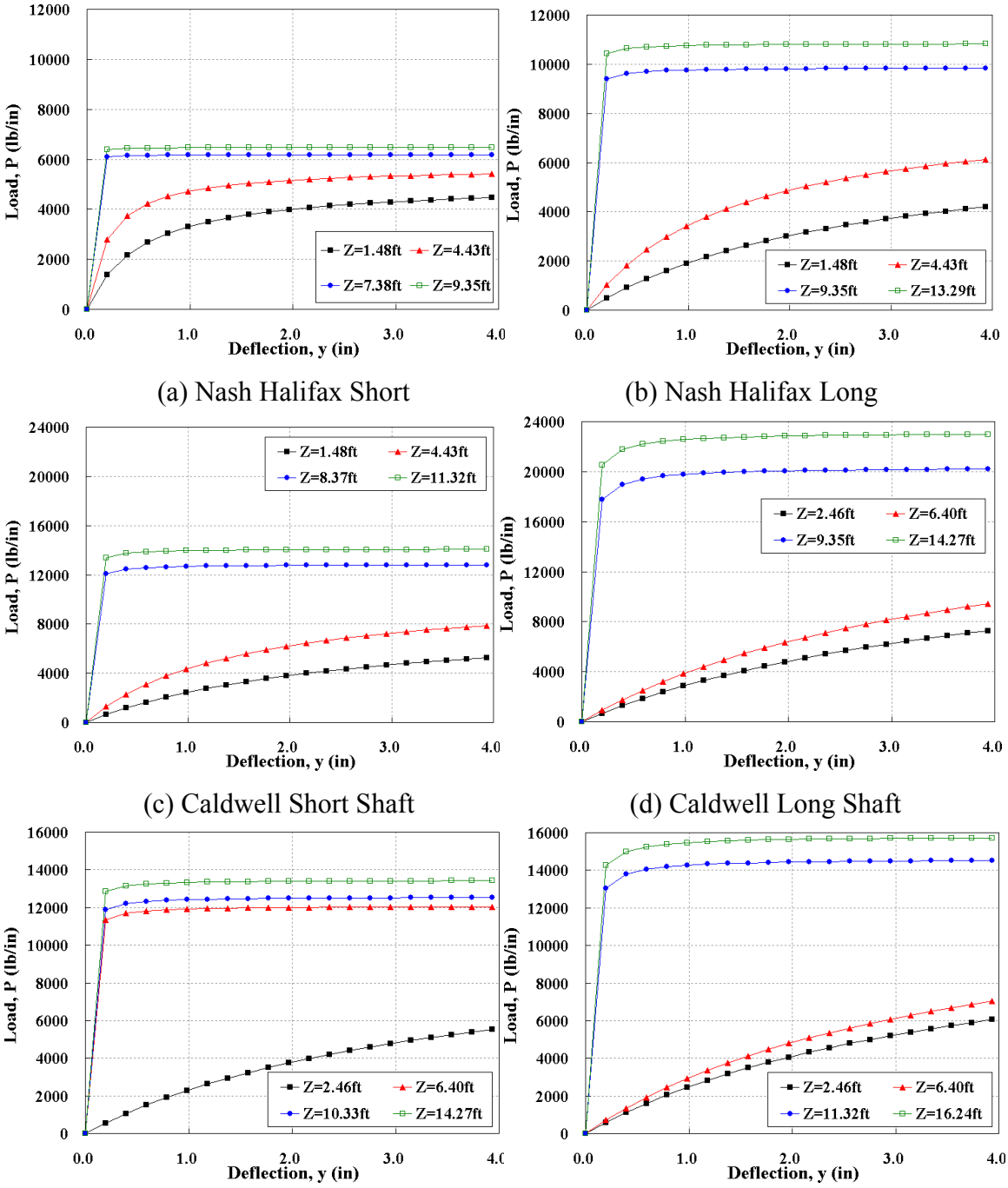

(a) Nash Halifax Short

(b) Nash Halifax Long

(c) Caldwell Short Shaft

(d) Caldwell Long Shaft

(e) Wilson Short Shaft

(f) Wilson Long Shaft

Figure 119. P-y curves for Geologic model

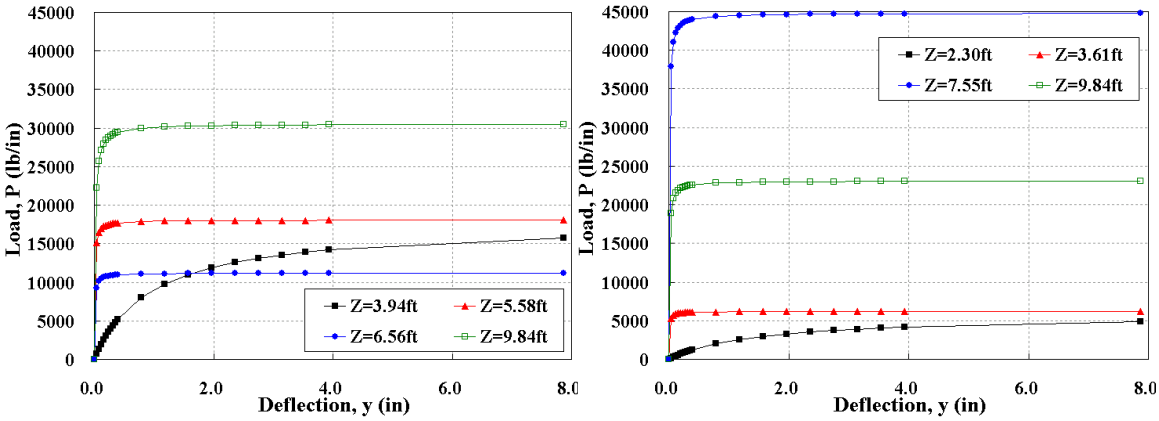

(g) I-40 Short Shaft (h) I-40 Long Shaft

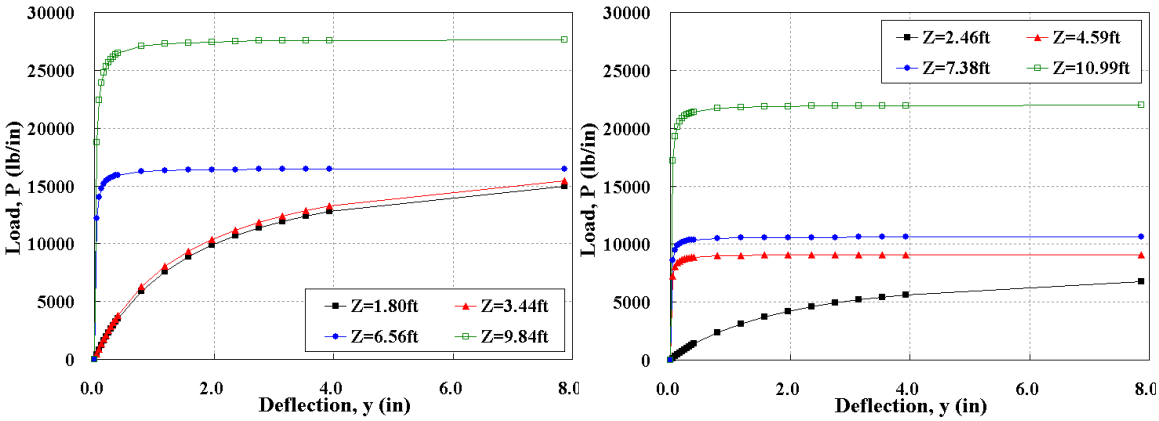

(i) I-85 Short Shaft (j) I-85 Long Shaft

Figure 119. P-y curves for Geologic model (continued)

Axial Pile Load Tests

The development of resistance factors for axial capacity is based on data from twenty load tests. The axial load tests were performed (by others for the project owner) using Osterberg and Statnamic methods. For the Statnamic tests, equivalent static load and settlement (vertical displacement at the top of the drilled shaft) plots were analyzed by the SUP (Segmental Unloading Point) method developed by Lewis and Mullins (1997). The length of the drilled shafts varied from 15 (4.57m) to 150 feet (45.7m) and their diameters ranged from 2.5 to 8.5 feet (0.76 to 2.59m), as shown in Table 40. The "LT-8650" series designated tests were performed using Osterber load cells for the Cooper River Bridge project. Description of each testing series is presented in the following sections.

Table 40. Dimension and structural design for the drilled shaft analyzed

Tests	L (ft)	Dia.(ft)	Reinforced bar			Shear rebar	
			Dia. (in)	No.	Dia. Cage (in)	Dia. (in)	Spacing (ft)
Bent-8	86.3	3.9	1.3	20	35.4	0.6	0.4
DDP-1	78.9	3.9	1.3	20	35.4	0.6	0.4
DDP-2	79.5	3.9	1.3	20	35.4	0.6	0.4
DP-1	17.0	2.5	1.4	10	23.6	0.6	0.4
DP-2	17.0	2.5	1.4	10	23.6	0.6	0.4
Pier-19	108.2	4.1	2.4	12	35.4	0.8	0.7
Pier-34	102.4	4.1	2.0	12	35.4	0.8	0.7
Pier-48	102.5	4.1	2.0	12	35.4	0.8	0.7
TS-1	13.2	3.0	1.0	6	31.5	0.5	1.0
TS-2	31.8	3.0	1.0	6	31.5	0.5	1.0
LT8650-1	161.6	8.5	2.3	36	84.0	0.7	0.2
LT8650-2	162.7	8.5	2.3	36	84.0	0.7	0.2
LT8650-3	114.6	8.5	2.3	36	84.0	0.7	0.2
LT8650-5	76.5	8.5	2.3	36	84.0	0.7	0.2
LT8650-6	150.3	8.5	2.3	36	84.0	0.7	0.2
LT8650-7	114.8	8.5	2.3	36	84.0	0.7	0.2
LT8650-8	110.2	8.5	2.3	36	84.0	0.7	0.2
LT8958-1	44.3	4.0	1.0	12	42.0	0.5	0.2
LT8958-2	52.3	4.0	1.0	12	42.0	0.5	0.2
LT8402	41.7	3.0	1.0	12	31.5	0.5	0.2

Cape Fear River Bridge: Demonstration Drilled Pier -1 & 2 (DDP-1 & 2)

Axial Statnamic load tests of Demonstration Drilled Pier 1 (DDP-1) and Demonstration Drilled Pier 2 (DDP-2) were performed as a part of the new Cape Fear River Bridge construction project. These tests were performed to estimate the effect of polymer and bentonite drilling fluid on the capacity of the shafts. DDP-1 was constructed using polymer drilling fluid, and DDP-2 was constructed using bentonite drilling fluid. The tests were performed on August 28 to 29, 2001 with a 3597 kips (16 MN) Statnamic device. Schematic of test set up is presented in Figure 120.

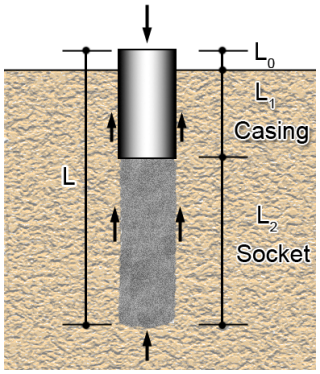

Figure 120. Length of drilled shaft

As shown in Table 40, DDP-1 and DDP-2 were constructed with an outer 48 inch (1220 mm) diameter, 0.5 inch (13 mm) wall. The total shaft length was 78.9 feet (24.1 m) consisting of 0.8 feet (0.24 m) of an exposed part (L_0), 54.1 feet (16.5 m) of casing part (L_1), and 24 feet (7.31 m) of socket part (L_2).

Based on boring log data, the soil profile consisted of fine to medium sand, silty fine sand, and a stiff silty sand layer. The stiff silty layer is located in the Peedee Formation which exists at a depth of 53.3 ft. (16.3 m) below the ground surface. It should be noted that SPT N-values greater than 100 blows per foot were recorded in the stiff silty layer. The idealized soil profile is shown in Figure 121. The groundwater table was located at top of the second layer, as shown in Figure 121 (b). For the DDP-1 and DDP-2 cases, the shafts were isolated from the subsurface soil down to 40 ft to negate the frictional resistance. So, for this portion, T-z model is generated using 0.1 ksf of undrained shear strength. The fourth layer of the model consisted of sand with a unit weight of 115 pcf (18.1kN/m^2).

The range of depth for each layer in the profiles where the axial load tests were simulated are presented in Appendix B. Since the construction method for DDP-1 and DDP-2 was different (using polymer versus bentonite) T-z curves for the shaft socket in weathered rock were determined using two different frictional resistances. The maximum shear resistance was taken as 6 ksf (0.287kN/m^2) for DDP-1, and 4 ksf (0.192kN/m^2) for DDP-2.

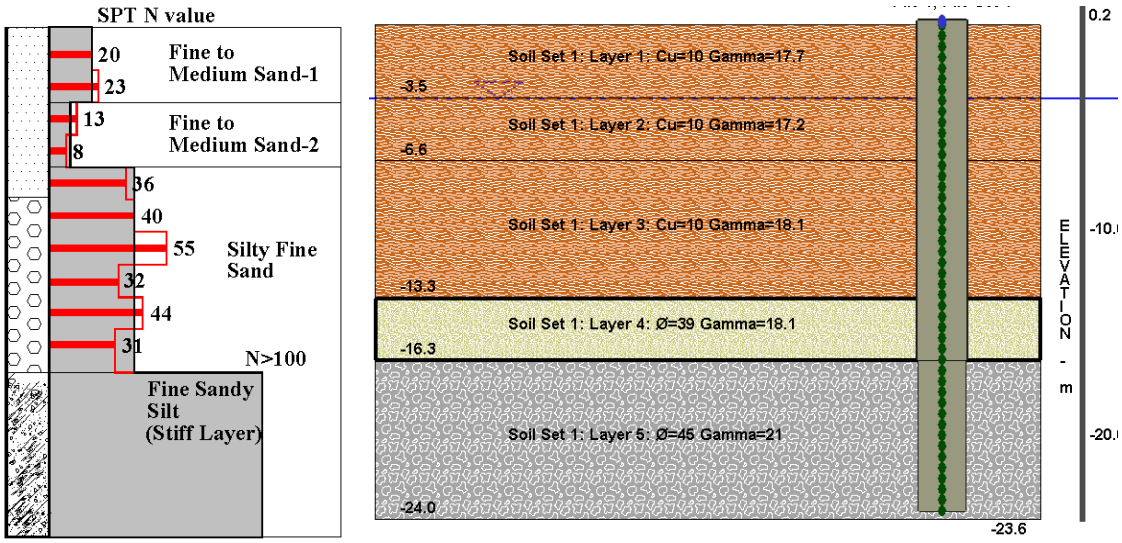

(a) Soil Profile & N value (b) Simulated Model

Figure 121. Soil Profile and Simulated Model by MultiPier for DDP-1 & 2

The maximum applied load was 3,100 kips (13,790 kN) at the second cycle for DDP-1, and 1,888 kips (8,400 kN) at the first cycle for DDP-2, as shown in Figure 122 and

Table 41.

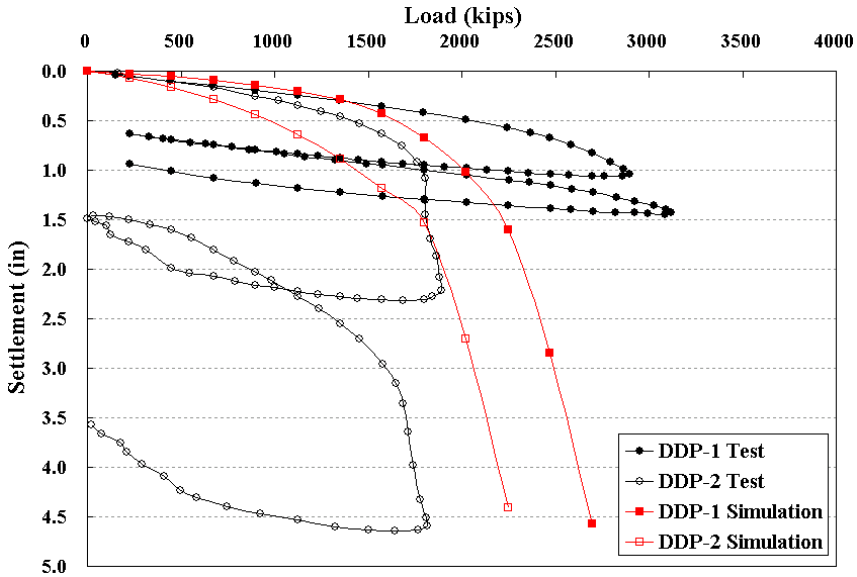

Figure 122. Results of axial load tests for DDP-1 & 2

Table 41. Test results of DDP-1 and DDP-2

Shaft	Cycle	Max. Static Load (kips)	Max. Displ.(in)
DDP-1	1	2893.3	1.07
	2	3100.1	1.45
DDP-2	1	1888.4	2.30
	2	1812.0	4.65

Drilled Pier-1 & 2 (DP-1 & 2)

DP-1 and 2 were tested on April 15 and 16, 2001, respectively at the Gregson Street Test Site. Both drilled shafts were constructed dry without the use of casing, in order to investigate the degree of degradation in Triassic Basin profiles by exposure to moisture. The drilled hole for DP-2 was soaked for 24 hours prior to concrete placement.

The profile consisted of residual soil, 2.7 feet (0.83 m) thick, overlaying a soft Triassic weathered rock layer which consisted of siltstone and claystone. The percentage of the sample recovery was 100 percent, and the RQD ranged from 44 to 96 percent. While for DP-1, an intermediate material model using RQD and general unconfined compressive strength could be applied to estimate the axial capacity, such model could not be applied for DP-2, because weathering by soaking altered the strength parameters.

DP-1 and 2 were 30 inch (760 mm) in diameter, and the total shaft length was 16.1 ft. (4.9 m) including a free length (L_0) of 0.9 ft. (0.28 m), 2.7 ft. (0.83 m) of soil, and 12.5 ft. (3.8 m) of weathered rock. The maximum applied load for DP-1 was 2,090 kips (9280kN), and 2,105 kips (9346kN) for DP-2, as shown in Table 42 and Figure 123.

Table 42. Results of DP-1 and DP-2

Shaft	Location	Max. Shear Resist. (psi)	Max. Tip Resist.(kips)	Max. Load (kips)	Max. Displ.(in)
DP-1	Upper Part	99.6	-	2,090	0.33
	Lowe Part	157.7	-		0.28
	End Bearing	-	232.45		0.28
DP-2	Upper Part	45.8	-	2,105	0.15
	Lowe Part	175.9	-		0.10
	End Bearing	-	562.25		0.09

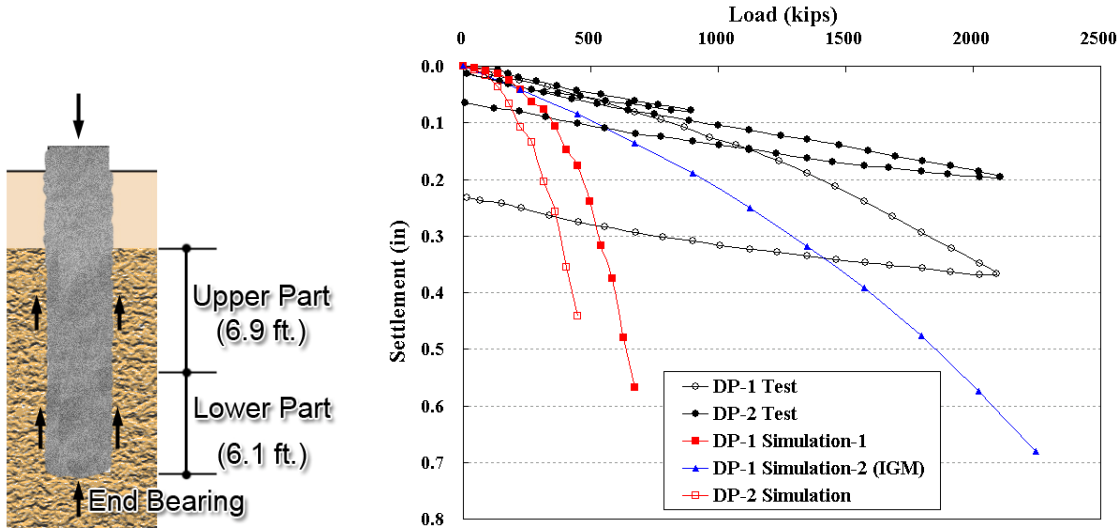

(a) Measuring Points (b) Load and Settlement Plot for DP-1 & 2

Figure 123. Results of DP-1 and DP-2

Neuse River Bridge: Pier – 19, Pier-34, and Pier-48

Axial Statnamic load tests for Pier-19, Pier-34, and Pier-48 were performed to measure the bearing capacity of drilled shafts in the Neuse River Bridge project (May 21 to 28, 1997.) The river bottom soils in which the test shafts were installed consisted of a layer of very loose or very soft silts, sands and organic material from an elevation of -5(-1.5m) to -11 feet(3.35m). The length of socket in weathered rock ranged from 26 to 42 feet. The weathered rock consisted of siltstone and limestone, as shown in App. 5-A, v to vii.

Pier-19, Pier-34, and Pier-48 were constructed with an outer diameter of 49 inches (1250 mm), with 0.6 inch (15 mm) thick steel casing. The total shaft length was 108.2 ft. (33 m), 102.4 ft. (31.2 m), and 102.5 ft. (31.3 m), respectively. Table 43 and Figure 124 show the magnitude of the shaft resistance at maximum displacement obtained during testing and the measured load-displacement relationships, respectively.

Table 43. Results of Pier-19, Pier-34, and Pier-48

Shaft	Max. Shear Resist. (ksf)	Tip Resist.(ksf)	Max Load (kips)	Max. Displ.(in)
Pier-19	5.62	150.7	3057.4	0.35
Pier-34	5.74	39.9	2585.3	0.26
Pier-48	6.50	38.8	2787.6	0.32

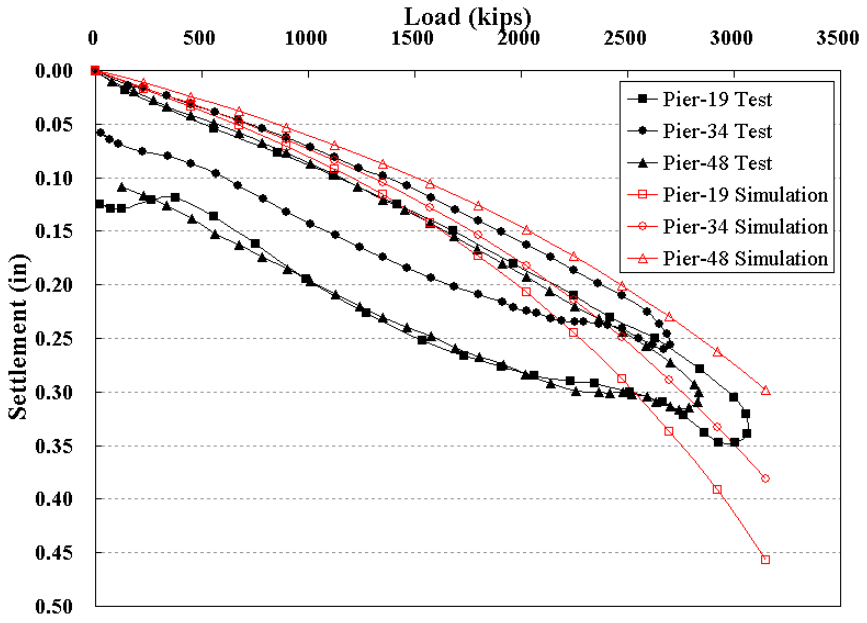

Figure 124. Results of Pier-19, Pier-34, and Pier-48

TS-1 and TS-2

Testing on drilled shafts TS-1 and TS-2 were performed for measuring side shear resistance and end bearing on January 6th 2003 by NCDOT. Both shafts were constructed with a temporary oversized upper isolation casing and a short upper permanent casing, 36 inches (91.4cm) in diameter. TS-1 was 13.2 feet (4.02m) and TS-2 was 31.8 feet (9.69m) as shown in Table 40. A permanent casing with a 36 inch (91.4cm) outer diameter and 1/2 inch (1.27cm) wall thickness was installed to a depth of 7.5 feet (2.29cm) for TS-1 and 8.75 feet (2.67cm) for TS-2. For TS-2 especially, Styrofoam was placed at the toe of the shaft for negating end bearing resistance (i.e. measuring mostly the skin friction.)

The top soil at the site consisted of embankment fill and coarse to fine sandy clay (A-6) with a depth of 6 (1.83m) to 7 feet(2.13m). This soil layer is underlain by weathered metamorphic granite rock. The N-values were over 100 in the weathered rock layer and the groundwater table was present at about 18(5.49m) to 20 feet (6.1m), as shown in Appendix B.

As shown in Table 44 and Figure 125, the maximum axial static load capacity of the drilled shaft was 2946 kips (13080kN) for TS-1 and 3639 kips(1109kN) for the first cycle of TS-2. Also shown in Figure 125 are the computed responses based on the site and shaft parameters. The displacement at the maximum static load was 3.53 inch (8.97cm) for TS-1, and 0.41 inch (1.04 cm) for the first cycle of TS-2. As shown in Figure 125, the static capacity of TS-2 is larger than that of TS-1. This may be due to the difference in mobilized frictional resistance due to the embedded length of each shaft in the weathered rock. The load test report explained this difference in frictional resistance as:

> "Even with the soft toe, the skin friction capacity was not fully mobilized. However, we believe the measured side shear resistance was about 90 percent of the yield value based on the amount of displacement achieved in the rock. Measured unit side shear values for TS-2 were 15.5 ksf in the upper 12 feet of the rock socket and 17.5 ksf in the lower 12 feet of the rock socket."

Table 44. Test Results of TS-1 and TS-2 Loading

Shaft	Cycle	Shear Resist. (ksf)	End Bearing (ksf)	Max. Capacity (kips)	Max. Displ.(in)
TS-1	1	13.50	332.0	2946.0	3.53
TS-2	1	15.50	17.5	3639.0	0.41
	2	13.90	16.4	3321.0	0.46

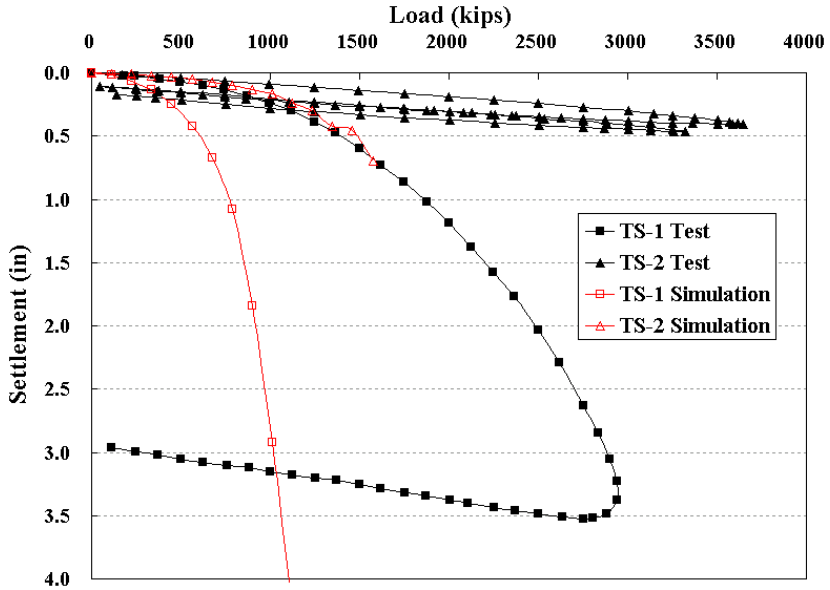

Figure 125. Results of TS-1 and TS-2

Cape Fear River Bridge: Bent-8

A Statnamic load test was performed in order to determine the bearing capacity of Bent-8 as part of the Cape Fear River Bridge construction project. The test was performed on April 11th 2003. The test shaft was constructed using a casing with a 47 inch (119.4 cm) outer diameter and wall thickness of 0.5 inches (1.27 cm). The total shaft length was 86.3 feet (26.3 m) of which 4.3 feet (1.31 m) of casing extended above the surface. Of the total length of the shaft, 32.6 feet (9.94 m) was socketed in weathered rock, and 49.4 feet (15.1 m) of the shaft embedded in the residual soil layer.

Soils from the ground surface to a depth of 7.6 feet (2.32 m) were noted as muck, and from a depth of 7.6feet (2.32 m) to 40 feet (12.2 m) were characterized as loose alluvial fine to coarse sand with traces of organic material and gravel. The underlying material below a depth of 40 feet (12.2 m) is described as the PeeDee formation. The PeeDee material is composed of green-gray, micaceous, fine sand. The maximum static capacity of the B-8 test shaft was 1,827 kips (8112 kN) at 0.39 inches (0.99 cm) of displacement, as shown in Figure 126.

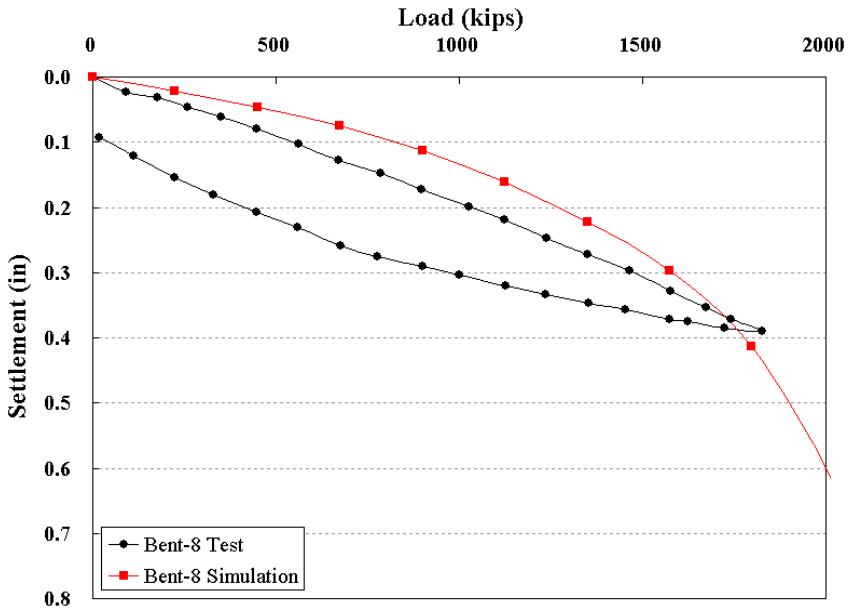

Figure 126. Results of Bent-8

Cooper River Bridge: LT8650-1, 2, 3, and 5

The load test (LT8650) series of drilled shafts from Cooper River Bridge project were performed using Osterberg load cells. LT-8650-1, 2, 3, and 5 were carried out on test shafts designated as MP-1, 2, 3, and 6, respectively between August and October, 2000.

For LT8650-1 and LT8650-2, three Osterberg cells with 2000 kip (8880 kN) capacities was placed at the bottom of the shaft, and two other Osterberg cells were placed at 46 feet (14.02 m) up from the bottom of the shaft. For LT8650-3, three Osterberg cells with 2000 kips (8880 kN) were only placed at the bottom of the shaft. For LT8650-5, two Osterberg cell with 3600 kips (15984kN) capacity were installed. The first cell was located at the bottom of the shaft, and the second was 5 feet higher than the first cell, as shown in Appendix B.

The lengths of LT8650-1 and LT8650-2 were approximately 160 feet (49 m), and the lengths of LT8650-3 and 5 were 110 feet (33.5 m) and 76.5 feet (23.3 m), respectively. The outer diameter of permanent casing was 102 inch (2.591 m) and had a thickness of 1 inch (2.54 cm). A rock socket with 96 inch (2.438 m) diameter was installed at depth of 53.8 feet (16.4 m), 67.2 feet (20.5 m), 66 feet (20.1 m), and 53.5 feet (16.3 m) for LT8650-1, 2, 3, and 5, respectively.

Based on boring log data, the soil profile consisted of a sandy clay to clayey sand layer that is approximately 38 feet (11.6 m) underlain by the Cooper Group Marl formation. The groundwater table was located at 5 feet (1.5 m) in depth. The equivalent static load and settlement curves are presented in Table 45 and Figure 127. The maximum equivalent static load in Table 45 was obtained after adjustments were made for elastic compression.

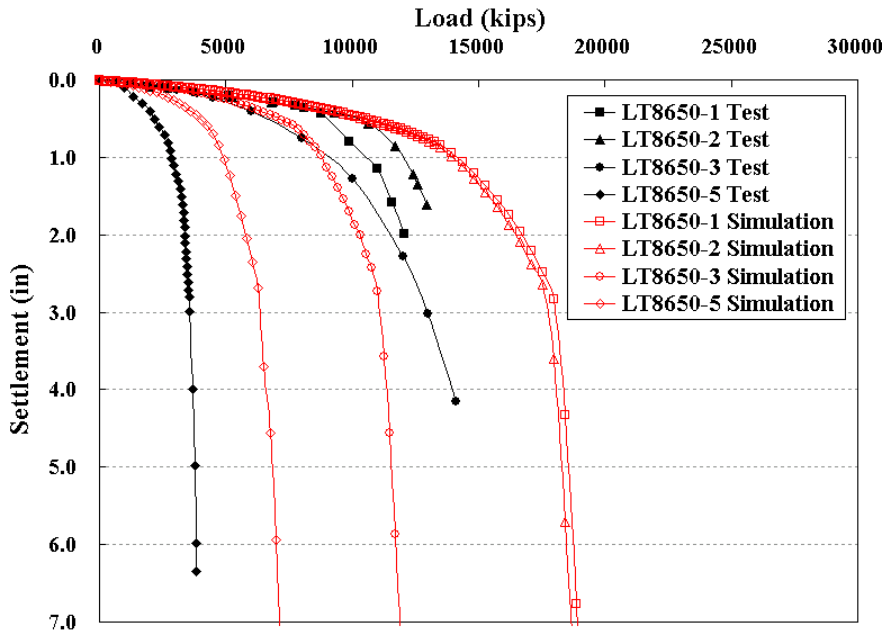

Figure 127. Results of LT8650-1 to LT8650-5

Table 45. Results of LT8650-1 to LT8650-5

Shaft	Avg. Shear Resist. (ksf)	Max. End Bearing (ksf)	Max. Capacity (kips)	Max. Displ.(in)
LT8650-1	3.88	74.9	12080.6	1.99
LT8650-2	4.05	68.3	12963.5	1.61
LT8650-3	3.52	54.4	14109.3	4.15
LT8650-5	-	-	3844.8	6.34

LT8650-6, 7, and 8

LT-8650-6, 7, and 8 were performed on shafts C-1, 2, and 3, respectively in September to October, 2000. For LT8650-6, three Osterberg cells with 3600 kip (15984kN) capacities were placed at the bottom of the shaft, and three Osterberg cells with 2000 kip (8880kN) capacities were placed 40 feet (12.2 m) higher from the first cells. For LT8650-7, and 3, Osterberg cells with a 2000 kip (8880kN) capacity were placed at the bottom of the shaft and then 40 feet (12.2 m) from the first cells, as shown in Appendix B.

The length of LT8650-6 and 7 was approximately 157 feet (48 m), and the length of LT8650-8 was about 111 feet (34 m). The outer diameter of the permanent casing was

102 inch (2.591 m) with a wall thickness of 1 inch (2.54 cm). Rock sockets (96 inch (2.438 m) in diameters) were placed at depth of 54.1 feet (16.5 m), 50.8 feet (15.5 m), and 62.3 feet (19 m) for LT8650-6, 7, and 8, respectively. The soil profile consisted of a sandy clay to clayey sand layer that is approximately 63 feet (19.2 m) thick underlain by Cooper Group Marl formation. The groundwater table was determined to be at a depth of 4 feet (1.2 m).

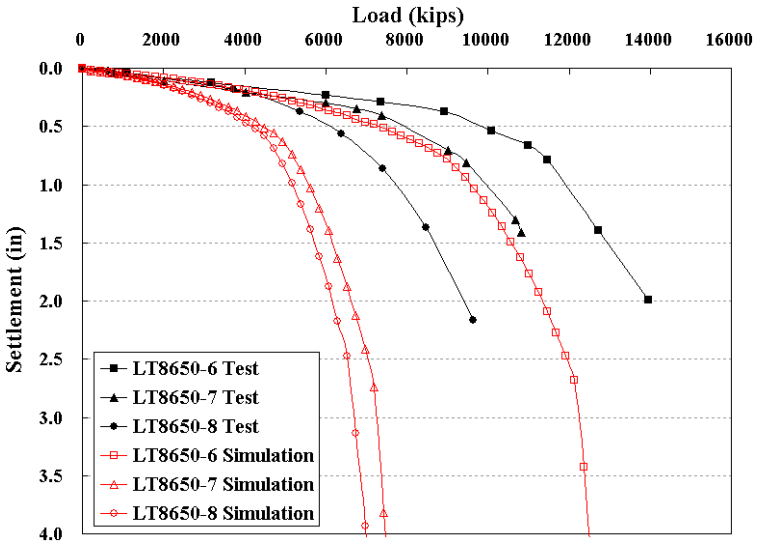

Figure 128. Results of LT8650-6 to LT8650-8

Table 46. Results of LT8650-6 to LT8650-8

Shaft	Max. Shear Resist. (ksf)	Max. End Bearing (ksf)	Max. Capacity (kips)	Max. Displ.(in)
LT8650-6	5.83	74.7	13969.1	1.99
LT8650-7	7.37	79.6	10834.3	1.41
LT8650-8	3.78	43.5	9648.0	2.16

The equivalent static load and settlement curves are presented in

Table 46 and in Figure 128. The maximum equivalent static load in

Table 46 was obtained after adjusting for elastic compression.

I-25, Trinidad, Colorado: LT8958-1 and 2

LT8958-1 and LT8958-2 were performed on drilled shaft that were a part of I-25 Trinidad project located in Trinidad, Colorado. The length of the LT8958-1 was 41 feet (12.5 m), and LT8958-2 was 48 feet (14.6 m). The diameter of each shaft was 48 inches.

The subsurface soil consisted of 8 to 10 foot (2.44 to 3.05m) layer of man-made fill overlying natural sand and silt, as well as natural sand and gravel. The soil layer was underlain by Pierre Shale bedrock at depth of approximately 30 feet. Figure 129 shows the load and settlement curves for LT8958-1 and LT8958-2. The maximum bearing capacity was estimated as 7422 kips (32954kN) at 1.0 inch (2.54cm) of displacement for LT8958-1, and the capacity for LT8958-2 was 8513 kips (37798kN) at 1.45 inch (3.68cm) of displacement, as shown in Figure 129.

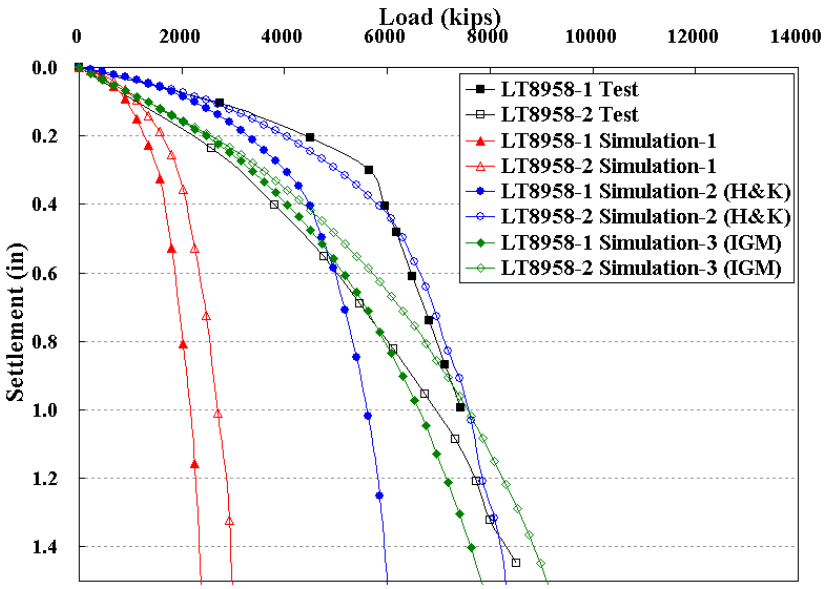

Figure 129. Results of LT8958-1 and LT8958-2

Highway 82: LT8402

LT8402 test was performed using Osterberg load cells on shafts that were a part of the Highway-82 project. The diameter of the test shaft was 36 inches. The length of the rock socket was about 30 feet (9 m), and total shaft length was 40 feet (12.1 m). The

subsurface soil consisted of a 6 foot (1.8 m) layer of silty sandy/gravel, and some clay zone with fractured Shale boulders. The soil layer was underlain by weathered shale which had an RQD of 0 to 67 %. The maximum bearing capacity of the test shaft was 12,000 kips (53280kN) at 2.2 inch (5.588kN) of settlement, as shown in Figure 130.

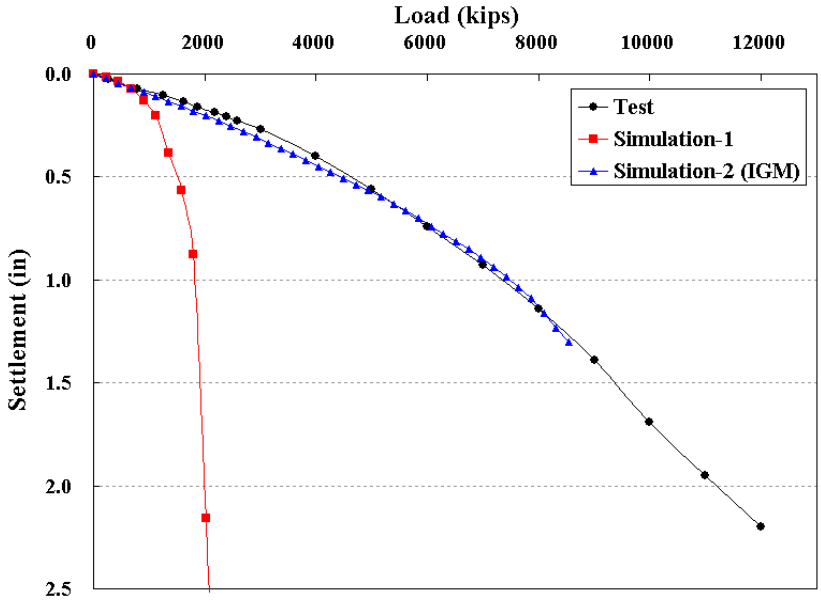

Figure 130. Results of LT8402

Lateral Load Tests

NCDOT and North Carolina State University performed ten lateral load tests on drilled shafts (Gabr et al., 2002) in accordance with ASTM D3966-90. The goal was to develop a P-y curve model for drilled shafts embedded in weathered rock. The results of these 10 cases are used for the development of resistance factors.

Table 47 summarizes the length of the drilled shafts used in these tests; the length of the shafts installed in weathered rock ranged from 10 to 20 feet (3 to 6 m). The diameter of shafts were 2.5 feet (0.76 m) for all cases.. All shafts were reinforced with 12 #10 steel bars and shear reinforcement to form a 1.6 ft diameter cage. Since the 2002 research was aimed at estimating the behavior of a drilled shaft embedded in weathered rock, the top soil was excavated.

A brief description of each test case is provided, followed by figures comparing the measured lateral load-deflection curves to those predicted by MultiPier using the P-y approaches described earlier in this chapter. Because each case is installed in weathered rock only, the same P-y model is used for the entire weathered rock mass. The data also provide a comparison of the back figured load-displacement curves to those developed using the stiff clay, Reese (1997) rock criteria, and geological model by Cho (2002).

Table 47. Basic information about lateral load test

Tests	Embedded Length (ft)
Nash County-Long	16.0
Nash County -Short	12.0
Caldwell County -Long	16.7
Caldwell County -Short	14.1
Wilson County -Long	19.7
Wilson County -Short	16.9
I-40 (Durham County)-Long	14.8
I-40 (Durham County)-Short	11.8
I85 (Durham County)-Long	14.7
I85(Durham County)-Short	9.7

Nash Halifax County Case

The base rock of this site consisted of a metamorphic mudstone, siltstone, and sandstone of the Eastern Slate Belt along the easterly edge of the Piedmont Physiographic Province. In spite of the presence of metamorphosed rock, the foliation of rock is poorly developed, and the rock is mostly sound, but some natural fractures are present. The recovery rate of the hard rock core was over 95% and the RQD for the lower 15 feet (4.57 m) exceeded 75%.

Two drilled shafts were constructed, 25 feet (7.62 m) apart. The short shaft was embedded approximately 11 feet (3.35 m), and the long shaft was embedded 15 feet (4.57 m). Both shafts were constructed with approximately 2 feet (0.61 m) of its length

extending above the ground to facilitate the attachment of the lateral load frame. The lateral load-displacement data are presented in Figure 131.

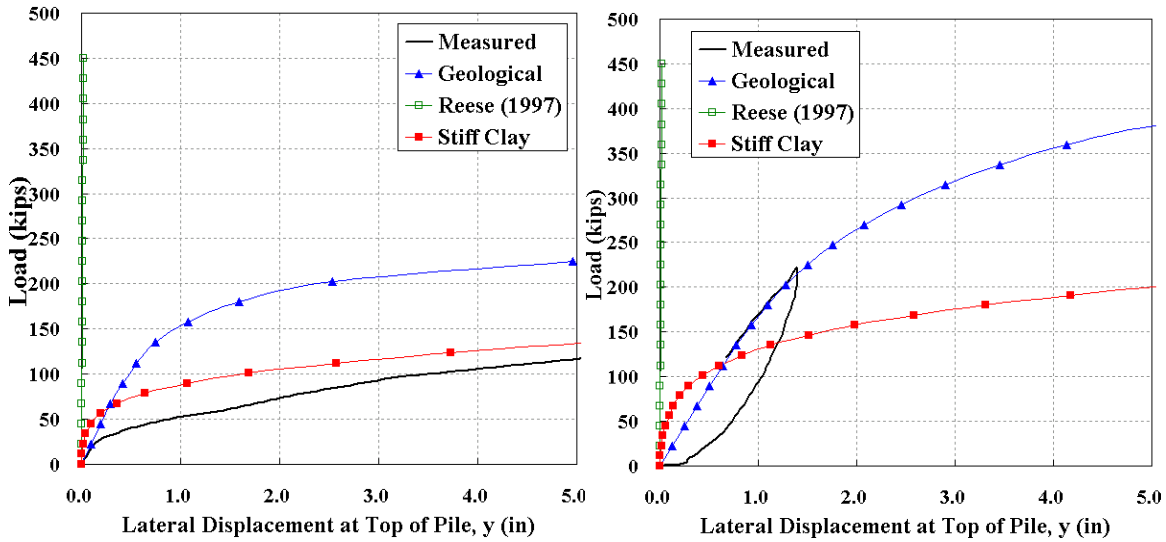

(a) Short shaft (b) Long shaft

Figure 131. Results of Nash Test Shafts

Caldwell County Case

The Caldwell County region is underlain by a Cenozoic age biotite gneiss and schist rock unit of the Inner Piedmont Belt which is characterized by a fine-to-coarse grain and composed of biotite, feldspar, and quartz (Cho, 2002). The lengths of the short and long shafts were 14.1 feet (4.2 m), and 16.7 feet (5.1 m), respectively. Both shafts were constructed 25 feet (7.62 meter) apart. The results for both shafts are presented in Figure 132.

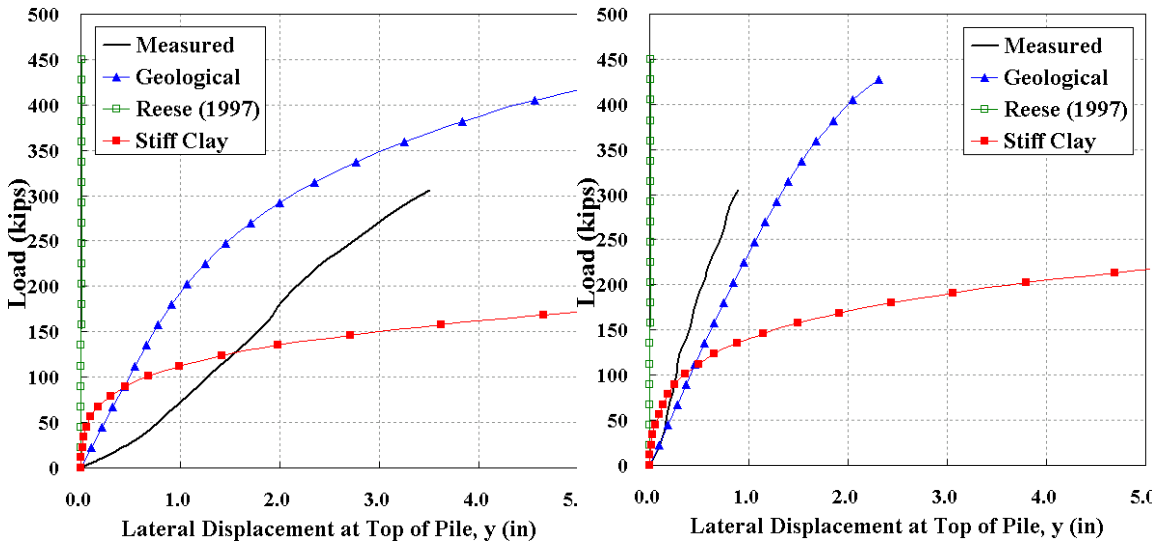

(a) Short shaft (b) Long shaft

Figure 132. Results of Caldwell Test Shafts

Wilson County Case

The subsurface profile consisted of tan brown fine to coarse sand, soft and hard weathered crystalline rock, and alluvial material spread of a variable extent at all bent locations. Based on boring data, the rock mass of both test sites is unlikely the same (Cho. 2002).

Two drilled shafts were constructed in the same manner as described for the previous cases. The depth of embedment was approximately 16 feet (4.85 m) and 18.7 feet (5.71 meter) for the short and long shafts respectively. The ground water table was found to be almost at the ground surface, which necessitated the use of steel casings to prevent the hole from collapsing during construction (Cho, 2002).

The long shaft response indicated yield under a load of 348 kips (1548 kN), and the short shaft did not reach the yield point. The reason that the long shaft yielded before the short shaft is mainly due to the different geological conditions. Figure 133 shows the measured and estimated lateral load-deflection curves.

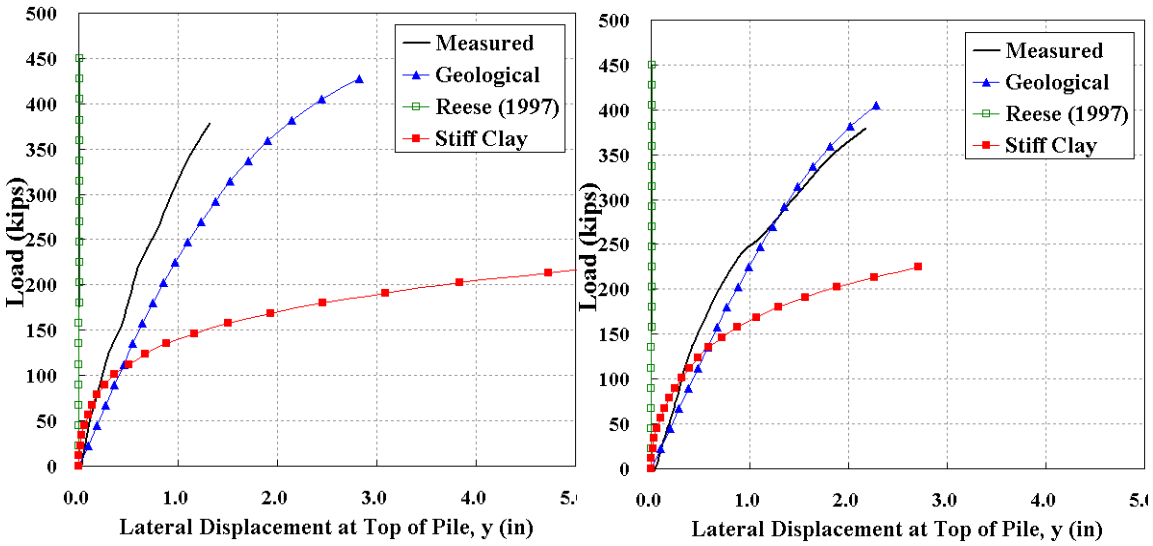

(a) Short shaft (b) Long shaft

Figure 133. Results of Wilson Test Shafts

I-40 Case

The I-40 test site was located at the northwest corner of the intersection of I-40 West and North Carolina Highway 55 in Durham County, North Carolina (Nixon, 2002). The test site was within the Durham Triassic Basin (DTB), which is in the deep river basin of North Carolina. According to Nixon (2002), the geological features in DTB area are as follows:

> "The DTB is primarily comprised of sedimentary rocks including red conglomerate, arkosic sandstone, siltstone, claystone and mudstone. The residual soils at the test site were predominately dark brown to dark red-brown silty clays with mica. The transition to weathered rock was encountered approximately 3 m below the ground surface."

The embedded rock mass has RQD values of 72 to 100%. The subsurface profile of the test site is shown in Appendix B. The test shaft was constructed in the same manner as the other cases. The embedded length for short shaft embedded was 11 feet (3.356 m) and for the long shaft 13.3 feet (4.057 m). The maximum lateral loads for the long and short shaft were 340 kips (1512 kN) and 379 kips (1685 kN), respectively. The lateral displacements at these loads were 0.63 inch (0.016 m) and 0.51 inch (0.013 m), as shown in Figure 134.

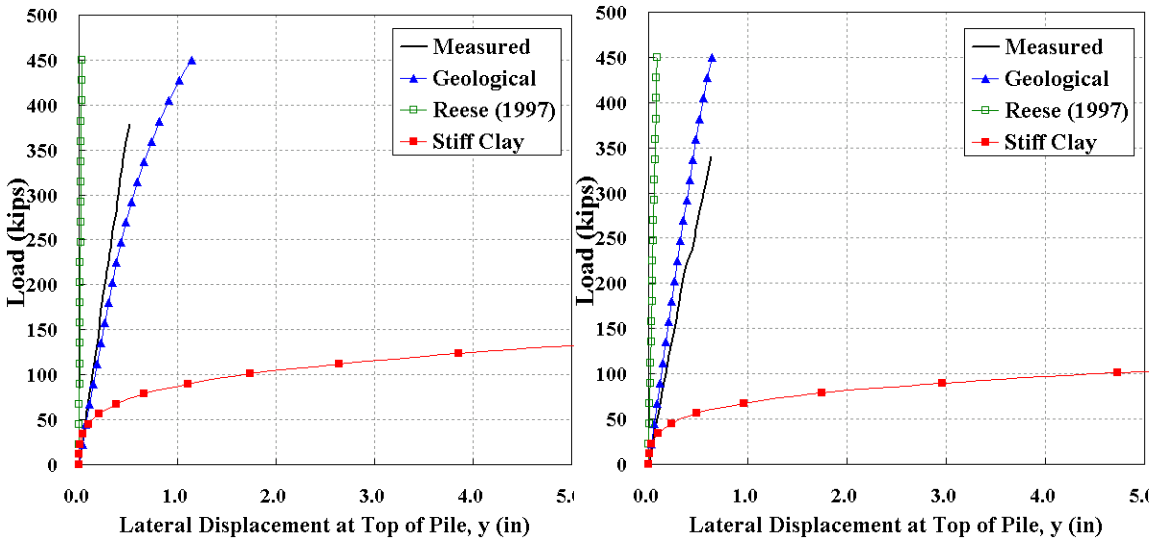

(a) Short shaft (b) Long shaft

Figure 134. Results for I-40 Test Shafts

I-85 Case

The I-85 test site was located within the exit ramp area of the Interstate 85 (I-85) North and Gregson Street interchange, in central Durham County (Nixon, 2002). The weathered rock layer was found at a depth of 4.9 feet (1.5 m) where the residual soil was excavated. This site was also in DTB region, and shares geological traits with the I-40 test site. RQD values ranged from 44 to 96%. A subsurface profile of the test site can be found in Appendix B.

The maximum load applied during testing was 300 kips (1334 kN) at which the short shaft exhibited yield behavior with 1.9 inch (0.048 m) lateral displacement. The maximum displacement obtained during the test for the long shaft was 0.68 inch (0.017 m), as shown in Figure 135.

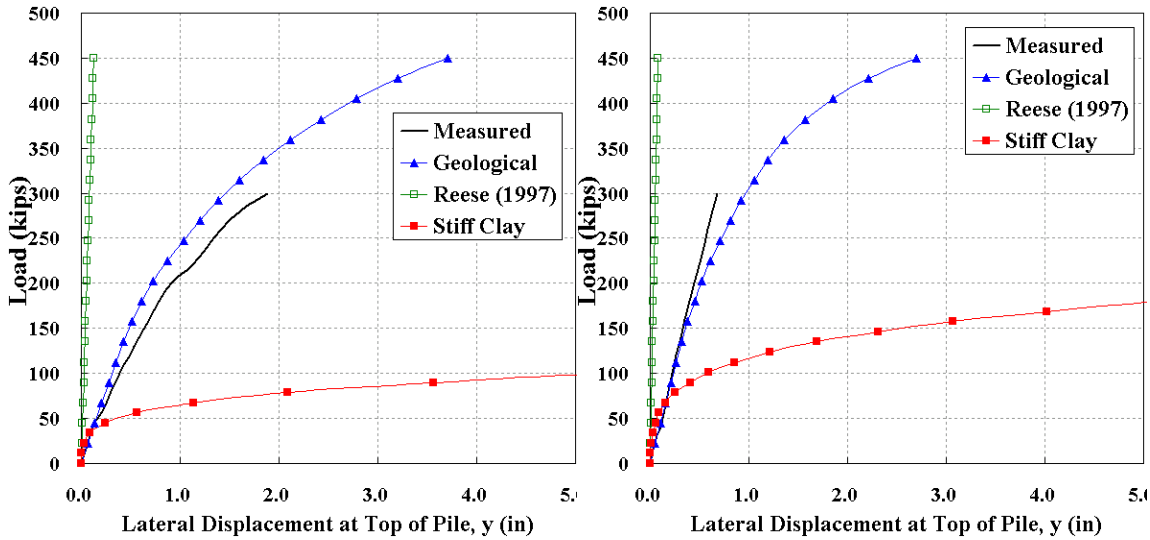

(a) Short shaft (b) Long shaft

Figure 135. Results of I-85 Test Shafts

Axial Load Tests: Failure Load Characterization

Once load-settlement curves were obtained from analytical simulations and load test data, it is necessary to systematically determine an ultimate load capacity based on established criteria. For the behavior of each shaft, determining the failure capacity from the load and settlement curve is not straightforward, because such relationships is non-linear and did not necessarily show plunging failures. Several methods have been developed for estimating the failure or yield load.

Methods of Determining Ultimate Axial Load

Table 48 summarizes several approaches published in literature for obtaining the failure capacity from the load-settlement curves. The methods can be categorized as follows:

- Graphical methods: for example, Chin, Brinch-Hansen, Mazurkiewics, Vander Veen.
- Failure capacity from a tangential line with a proposed slope: for example, Fuller and Hoy, Butler and Hoy, California, and Ohio DOT method.
- Criteria based on quantitative settlement: for example, specifications of particular countries (Holland, Japan, United Kingdom, and Singpore), De Beer, FHWA, AASHTO, Boston code, and DIN.
- Davisson's method: a summation of a quantitative settlement and the structural deformation related to elastic compression.

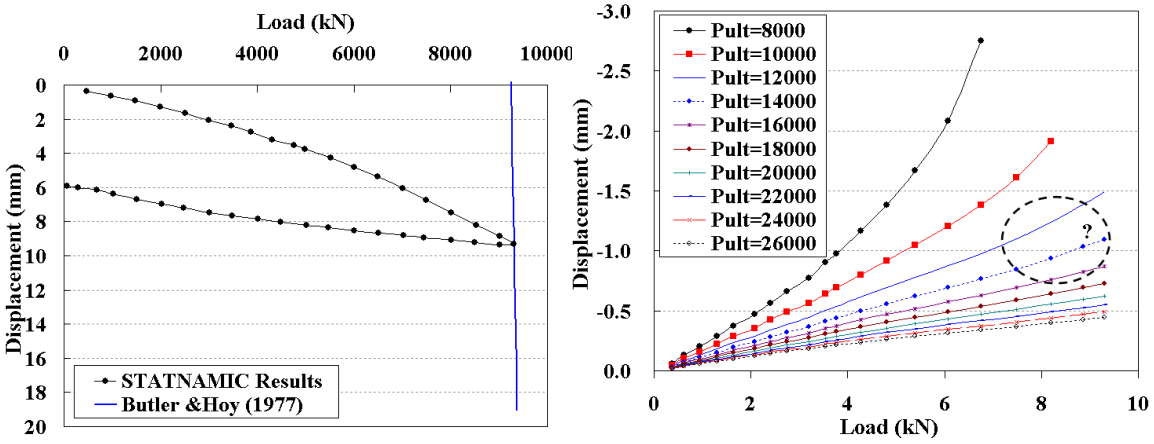

(a) Butler & Hoy (1977) (b) Vander Veen (1953)

Figure 136. Difficulties to determine the ultimate loads

Table 48. Various methods for estimating the failure capacity (USACE, 1991)

1. Limiting Total Butt Settlement
   a. 1.0 in. (Holland)
   b. 10% of tip diameter (United Kingdom)
   c. Elastic settlement + D/30 (Canada)
2. Limiting Plastic Settlement
   a. 0.25 in. (AASHO, N.Y. State, Louisiana)
   b. 0.5 in. (Boston) [complete relaxation of pile assumed]
3. Limiting Ratio: Plastic/Elastic Settlement 1.5 (Christiani and Nielson of Denmark)
4. Limiting Ratio: Settlement/Unit Load
   a. Total 0.01 in./ton (California, Chicago)
   b. Incremental 0.03 in./ton (Ohio),
      0.05 in./ton (Raymond International)
5. Limiting Ratio: Plastic Settlement/Unit Load
   a. Total 0.01 in./ton (N.Y. City)
   b. Incremental 0.003 in./ton (Raymond International)
6. Load-Settlement Curve Interpretation
   a. Maximum curvature - plot log total settlement vs log load; choose point of maximum curvature
   b. Tangents - plot tangents to general slopes of upper and lower portion of curves; observe point of intersection
   c. Break point - observe point at which plastic settlement curve breaks sharply; observe point at which gross settlement curve breaks sharply (Los Angeles)
7. Plunge
   Find loading at which the pile "plunges," (i.e., the load increment could not be maintained after pile penetration was greater than 0.2 B).
8. Texas Quick Load
   Construct tangent to initial slope of the load vs. gross settlement curve; construct tangent to lower portion of the load vs. gross settlement curve at 0.05 in./ton slope; the intersection of the two tangent lines is the "ultimate bearing capacity."

Some graphical methods are excluded from consideration herein because there was not enough data to apply them. The secant method, the tangential line method with a proposed rate of the load and settlement, was not applicable for several load tests, as for example is shown in Figure 136 (a). Similarly, and as shown in Figure 136 (b), the Vander Veen method has several possible failure loads interpretations for the same test.

For some load tests considered in this study, the settlement does not reach the suggested level to define failure. Therefore, the Chin method and Davisson's method are used herein for determining the failure capacity for the axial load tests as these two methods are the most appropriate for the data collected in this study.

Failure Load by Davisson's Method

Davisson's method is one of the most common methods used to estimate a failure load. This method considers the structural compression, and quantitative settlement, as shown in Equation 32 and Figure 137.

Equation 32 $$\delta = 0.15\,\text{inch} + D/120 + \frac{PL}{AE}$$

Where,

D=foundation diameter

P=applied load

L=foundation depth

A=foundation cross section area

E=foundation modulus of elasticity.

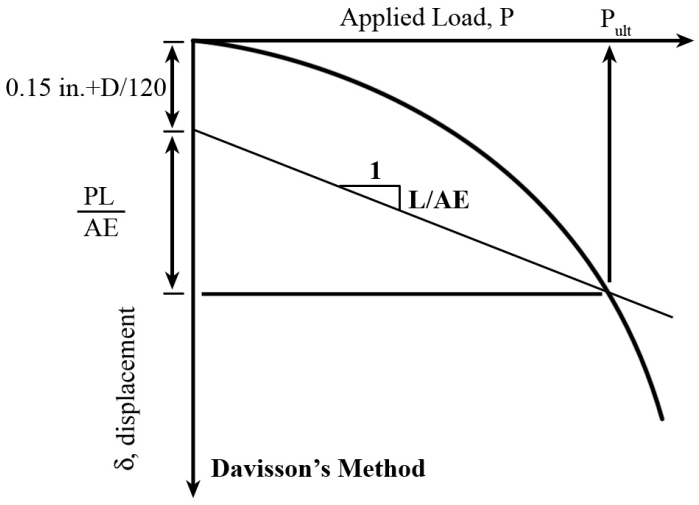

Figure 137. Davisson's method for estimating ultimate axial capacity

Figure 138 (a) show example of application of Davisson's method to DDP-1 and Figure 139 (b) shows for LT8650-1. The method is applied to data from Statnamic and Osterberg tests, respectively.

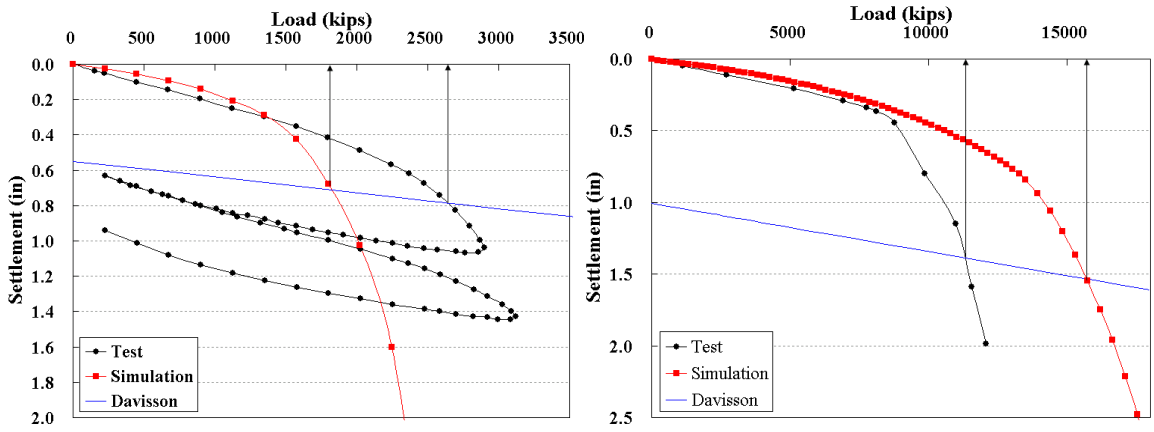

(a) DDP-1 (b) LT8650-1

Figure 138. Ultimate loadsestimated by Davisson's method for DDP-1 and LT8650-1

Even though Davisson's method is established in literature for estimating a failure load, a prediction cannot be carried out for cases when the Davisson failure line does not intersect the load test curve. Figure 139, showing Statnamic load test data for Pier-19, presents such a case. For this load-settlement curve, both the simulation and field data have about 0.3 inch (0.76cm) maximum settlement at the maximum applied loading, but Davisson's method specified 0.57 inches (1.45cm) of elastic compression which is more than the measured data.

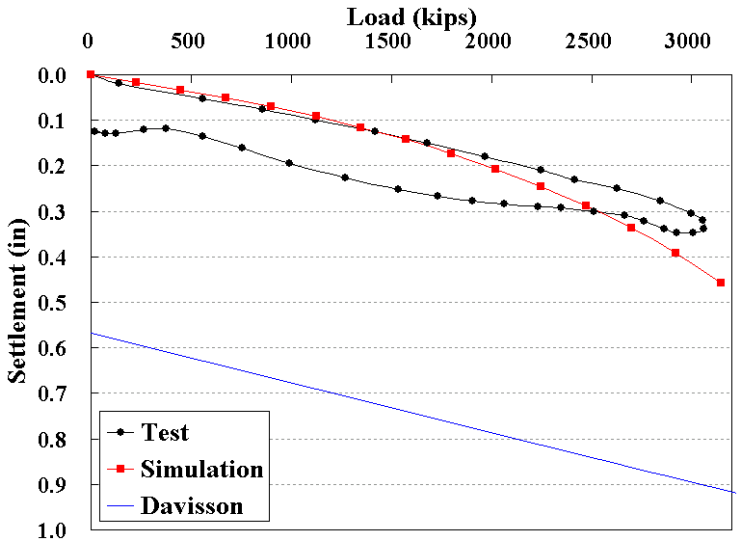

Figure 139. Inapplicable case of Davisson's method (Pier-19)

The "capacity" values of Bent-8, DP-1, DP-2, Pier-19, 34, 48, and TS-2 from Statnamic tests were not analyzed for this reason. The rest of the results are presented in Table 49.

Table 49. Results of Ultimate Loads by Davisson's method

Tests	Measured (kips)	Predicted Load (kips)
DDP-1	2631	2299
DDP-2	1619	1577
TS-1	1377	582
LT8650-1	11283	15687
LT8650-2	12698	15436
LT8650-3	9834	9146
LT8650-5	2906	5042
LT8650-6	12726	10255
LT8650-7	10534	5758
LT8650-8	8062	5334
LT8958-1	7538	1917
LT8958-2	6961	2457
LT8402	8451	1599

Ultimate Axial Load by Chin's Method

Chin's method (1970) assumes that the shape of the load and settlement curve is hyperbolic. As shown in Figure 140, the plot of settlement (δ) versus the ratio of settlement/load, δ/P, has a linear relationship after initial non-linear portion which normally represents the elastic behavior of the pile. The slope of the linear portion of the transformed curve indicates a reciprocal value of the ultimate pile capacity, as presented in Equation 33.

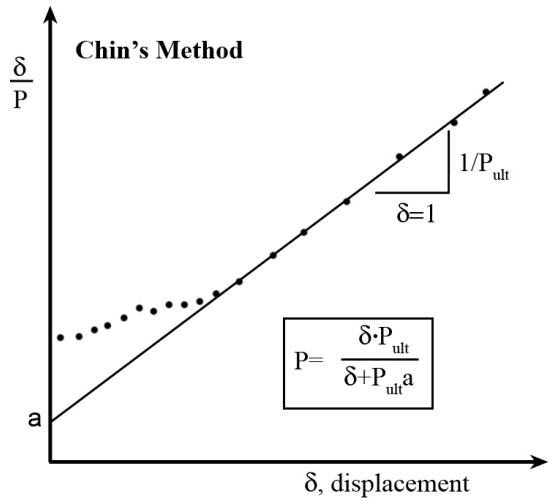

Figure 140. Chin's method

Equation 33 $$\frac{\delta}{P} = a + b \cdot \delta = a + \left(\frac{1}{P_{ult}} \right) \cdot \delta$$

Two applications of Chin's method are shown in Figure 141 (a) and (b). The ultimate loads for the axial load tests are estimated, as shown in Table 50. Figure 142 compares the ultimate loads from load test data and those computed using both the Chin and Davisson methods.

Table 50. Results of Ultimate Loads by Chin's method

Tests	Measured (kips)	Computed Load (kips)
Bent-8 (B8)	9801	2934
DDP-1 (DDP1)	4051	3574
DDP-2 (DDP2)	1990	2692
DP-1 (DP1)	4976	923
DP-2 (DP2)	7076	548
Pier-19 (P19)	5925	5757
Pier-34 (P34)	8925	6371
Pier-48 (P48)	11,484	6868
TS-1 (TS1)	3265	1400
TS-2 (TS2)	9826	1991
LT8650-1 (L1)	14,128	20,247
LT8650-2 (L2)	14,846	20,012
LT8650-3 (L3)	16,578	12,732
LT8650-5 (L5)	4115	7884
LT8650-6 (L6)	15,916	14,014
LT8650-7 (L7)	13,432	8809
LT8650-8 (L8)	11,584	8467
LT8958-1 (LT1)	9147	2910
LT8958-2 (LT2)	16,039	3611
LT8402 (LT3)	19,539	2237

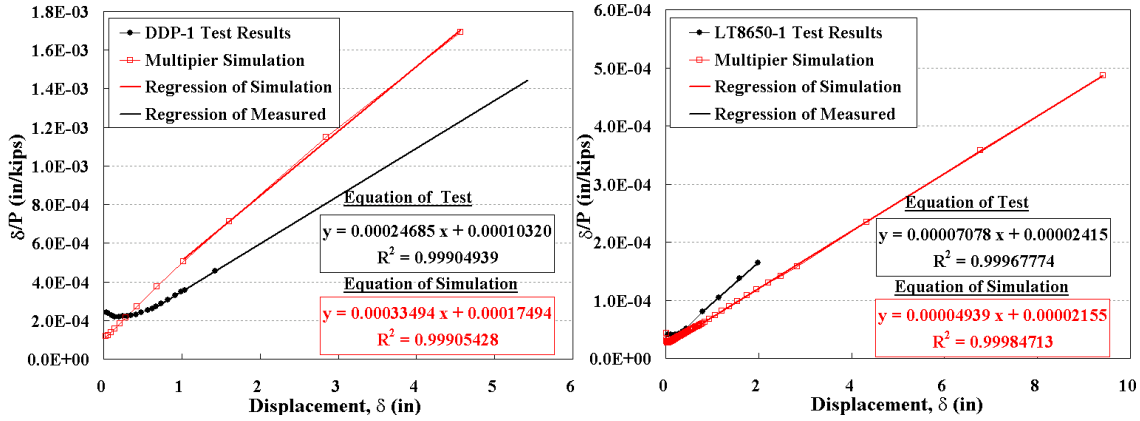

(a) DDP-1 (b) LT8650-1

Figure 141. Ultimate loads estimated by Chin's method for DDP-1 and LT8650-1

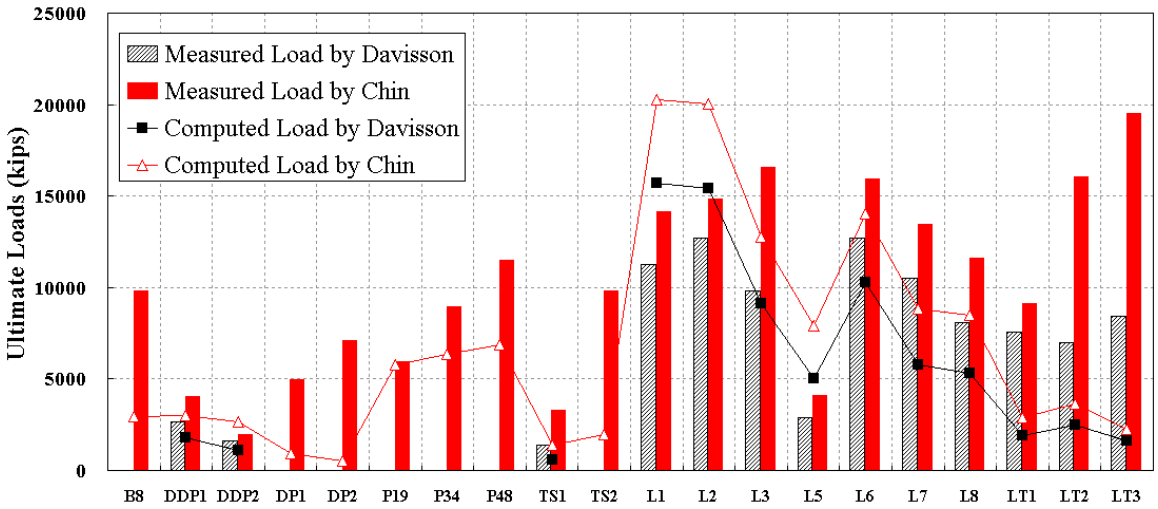

Figure 142. Comparison of Davisson's and Chin's method for measured and computed loads

Lateral Load Tests

The results of the simulation by MultiPier using three different P-y curve models are presented in Appendix B. As shown in Appendix B, the Geological model closely estimates the lateral load-deflection curve compared with the results from other methods. It should be mentioned however that the geological method was developed specifically for weathered rock in North Carolina.

In order to estimate the failure load for the laterally loaded drilled shaft, a 1 inch (2.54 cm) and 0.5 inch (1.27 cm) deflection criteria are proposed by the project team. The former is based on the general NCDOT's experience. In some cases, however, it is not possible to determine the failure load, since the lateral displacement did not reach the 1 inch (2.54 cm) limit, as shown in Figure 143.

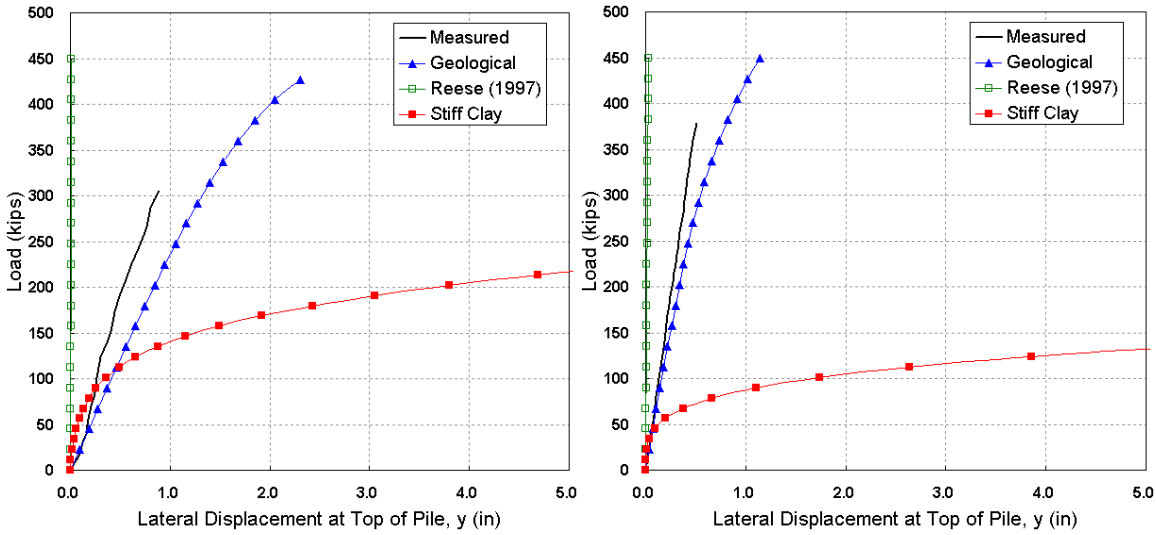

(a) Caldwell Long Shaft Case (b) I-40 Short Shaft Case

Figure 143. Inapplicable cases of 1 inch criteria for lateral load tests

The 0.5 inch (1.27 cm) deflection limit is applicable for all cases. The load magnitudes corresponding to 0.5 inches are presented, as shown in Figure 145. The design loads corresponding to the pre-defined deflection criterion of 0.5 inch (1.27cm) are presented in Table 51. Figure 145 shows an example of estimating the design loads for the case of the Nash County drilled shafts. As shown in Figure 145, lateral response based on Reese's model does reach the 0.5 inches (1.27cm) criterion, and therefore the design loads for Reese's model were not obtained.

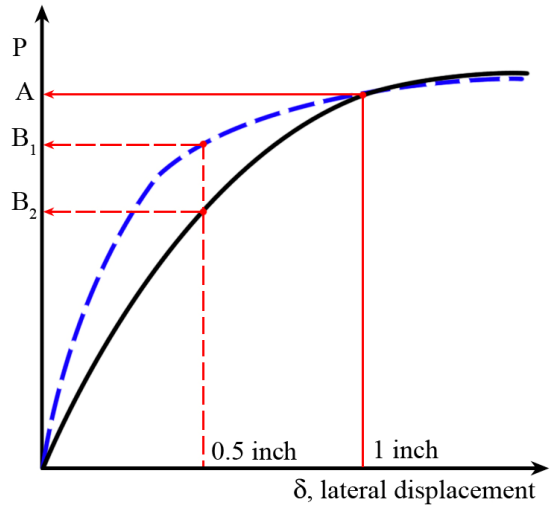

Figure 144. Case of incorrect prediction for 0.5 inch criteria with the same load at 1 inch criteria

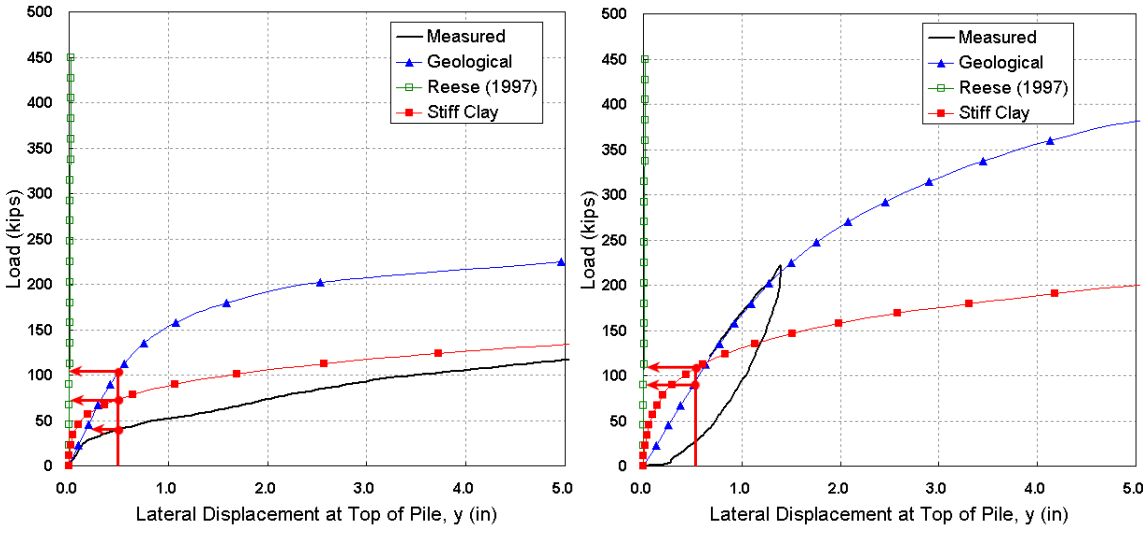

(a) Nash Halifax Short Shaft (b) Nash Halifax Long Shaft

Figure 145. Determination of Design Load using 0.5 inch criteria

Table 51. Measured and computed design loads at a 0.5 inch deflection for each lateral load test

Tests	Measured (kips)	Predicted Load (kips)	
		Geological	Stiff Clay
Nash Short	40.2	103.7	73.1
Nash Long	86.5	88.6	105.3
Caldwell Short	27.8	103.6	92.5
Caldwell Long	190.5	121.8	112.7
Wilson Short	182.6	123.2	112.4
Wilson Long	155.5	118.0	126.6
I40 Short	371.9	279.4	72.3
I40 Long	271.4	372.2	56.6
I85 Short	121.2	154.3	54.1
I85 Long	222.1	194.0	95.7

Reliability Analysis

Reliability analyses using the model simulations and field data are applied to develop resistance factors. A limit state function is defined by two random variables; that is, the load (Q) and the resistance (R). It is assumed that failure of a deep foundation occurs when g(R, Q) <0. The probability of failure, P_f, can be expressed by the integral of the joint probability density function as shown in Equation 34 (Haldar, et al., 2000; Kim, 2002).

Equation 34
$$P_f = \iint_{g<0} f_{R,Q}(r,q)\,dr\,dq$$

Alternative simplified methods are used for evaluating P_f. These are First Order Reliability Methods (FORM) and Second Order Reliability Methods (SORM). The FORM can further be based on Mean Value First Order Second Moment (MVFOSM) or Advanced First Order Second Moment (AFOSM) method. The reliability approach for developing the resistance factors for this project is based on both methods, and the resistance factors are obtained from the AFOSM. The detail procedures for AFOSM are presented in Appendix B.

Load Statistics

Load statistics are obtained from the combination of dead load (Q_D) and live load (Q_L) for bridge design. According to Kim (2002), the load factors used in the reliability analysis are 1.25 for dead load and 1.75 for live load. The bias factor for load statistics is defined as the ratio of the observed actual load over the nominal load. The results of statistical analysis of highway dead and live loads are presented in Table 52 (After Nowak, 1992).

According to Withiam, et al. (1998), the mean and the coefficient of variation of bias factor for dead load are 1.08 and 0.13, respectively, and for live load are 1.15 and 0.18, respectively. A lognormal distribution is assumed for the bias factor of both dead and live loads.

Table 52. Statistics of Bridge Load Component (After Nowak, 1992)

Load Component	Bias Factor Mean	Bias Factor COV
Dead Load	**1.08**	**0.13**
- Factory Made	1.03	0.08
- Cast-In-Place	1.05	0.10
- Asphalt Wearing Surface	1.00	0.25
Live Load	**1.15** (1.10-1.20)	**0.18**

Resistance Statistics: Axial Capacity

The bias factor for the resistance statistics is defined as the ratio of the measured pile capacity over the predicted pile capacity. Table 53 shows the measured and predicted ultimate loads. Computed bias factors are also presented. Cases LT8958-1 and LT8958-2 have loads computed by the Horvath and Kenney (1979), termed H&K, and Intermediate Geo-Material (IGM) models. Computations for LT8402 also include estimation using the IGM model because the material properties were available. For LT 8958-1, LT 8958-2, and LT 8402, the results from the two other models are included for their improved bias factor results, since computations by the Geologic model are considerably different from the measured loads.

Table 53. Predicted load and bias factor by Davisson's method

Tests	Measured (kips)	Computed Load (kips)			Bias Factor, λ		
		WR model	H & K	IGM	WR model	H & K	IGM
DDP-1	2630.8	1815.6	-	-	1.449	-	-
DDP-2	1619.3	1122.9	-	-	1.442	-	-
TS-1	1376.7	581.8	-	-	2.366	-	-
LT8650-1	11282.5	15686.9	-	-	0.719	-	-
LT8650-2	12698.0	15435.6	-	-	0.823	-	-
LT8650-3	9833.9	9145.9	-	-	1.075	-	-
LT8650-5	2905.9	5041.6	-	-	0.576	-	-
LT8650-6	12726.0	10254.8	-	-	1.241	-	-
LT8650-7	10533.5	5757.5	-	-	1.830	-	-
LT8650-8	8061.6	5333.6	-	-	1.511	-	-
LT8958-1	7537.7	1917.4	5475.6	6554.1	3.931	1.377	1.150
LT8958-2	6961.0	2457.3	7669.3	7785.1	2.833	0.908	0.894
LT8402	8451.1	1598.9	8354.0	-	5.286	1.012	-

Table 54 shows the measured and predicted ultimate loads estimated by Chin's method, and bias factors. The H&K and IGM model predictions are also included for cases when the material properties required for these models were available. For cases LT8958-1, LT8958-2, and LT8402, the Geologic model yielded results that were approximately 3 to 5 times less than the measured data, while computations using the Horvath and Kenney (1979) model are closer to the measured data.

Table 54. Predicted load and bias factor by Chin's method

Tests	Measured (kips)	Predicted Load (kips)			Bias Factor, λ		
		WR model	H & K	IGM	WR model	H & K	IGM
Bent-8	9801.0	2933.5	-	-	3.341	-	-
DDP-1	4051.0	2985.5	-	-	1.357	-	-
DDP-2	1990.2	2660.1	-	-	0.748	-	-
DP-1	4975.6	922.5	-	5322.8	5.393	-	0.935
DP-2	7075.6	547.6	-	-	12.921	-	-
Pier-19	5924.9	5757.1	-	-	1.029	-	-
Pier-34	8925.4	6370.6	-	-	1.401	-	-
Pier-48	11483.7	6868.1	-	-	1.672	-	-
TS-1	3265.4	1399.7	-	-	2.333	-	-
TS-2	9826.1	1991.4	-	-	4.934	-	-
LT8650-1	14128.3	20247.0	-	-	0.698	-	-
LT8650-2	14845.6	20012.0	-	-	0.742	-	-
LT8650-3	16578.2	12732.4	-	-	1.302	-	-
LT8650-5	4115.2	7883.9	-	-	0.522	-	-
LT8650-6	15916.0	14013.5	-	-	1.136	-	-
LT8650-7	13431.8	8809.0	-	-	1.525	-	-
LT8650-8	11583.5	8466.7	-	-	1.368	-	-
LT8958-1	9146.6	2910.4	6791.2	12926.6	3.143	1.347	0.708
LT8958-2	16038.5	3611.2	9342.3	15487.1	4.441	1.717	1.036
LT8402	19538.9	2237.1	-	18622.0	8.734	-	1.049

As shown in Figure 146, the estimated capacities using Davisson's method yield better results in terms of measured and predicted load-settlement curves as compared to Chin's method. It is generally known that Chin's method tends to yield upper bounds of failure loads, and therefore the overall higher computed loads compared to Davisson's approach.

For performance of reliability analysis, the use of Chin's method may be problematic. The prediction by Chin's method is obtained from the shape of the plastic area of the load- settlement curve, while Davisson's method estimates the load at the specific settlement including the elastic deformation. The case of DDP-2 is used to illustrate this

point. The computed load by Davissson's method (1,123 kips) is smaller than the measured value of 1,619 kips. On the other hand, the computed load by Chin's method (2,660 kips) is nearly 1000 kips larger than the measured value. In this case, the bias factor is 1.44 for Davisson's method and 0.75 for Chin's method, reflecting the Davisson methods penchant for underprediction and the Chin method's tendency toward overprediction.

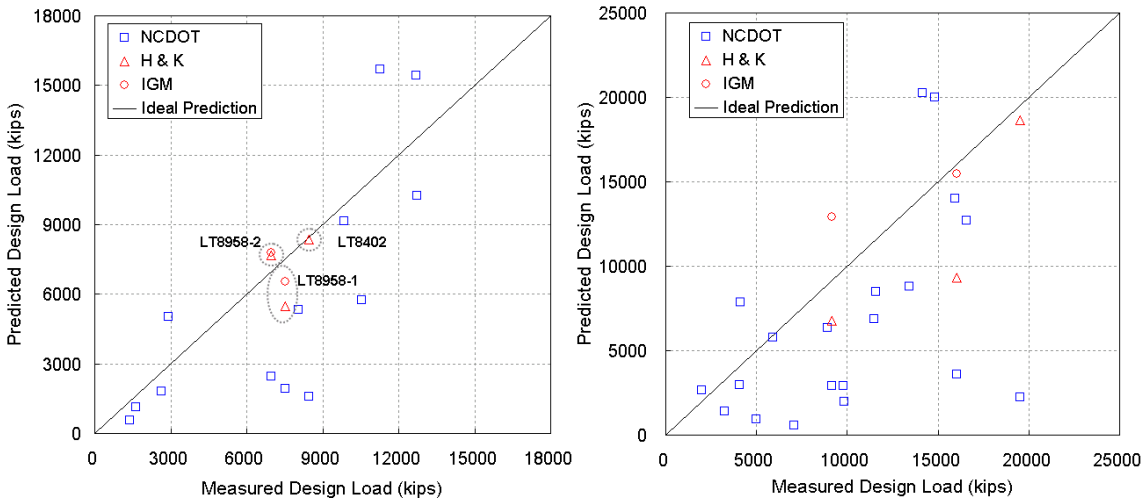

(a) Davisson's method (b) Chin's method

Figure 146. Dispersive graphs of the measured and predicted load

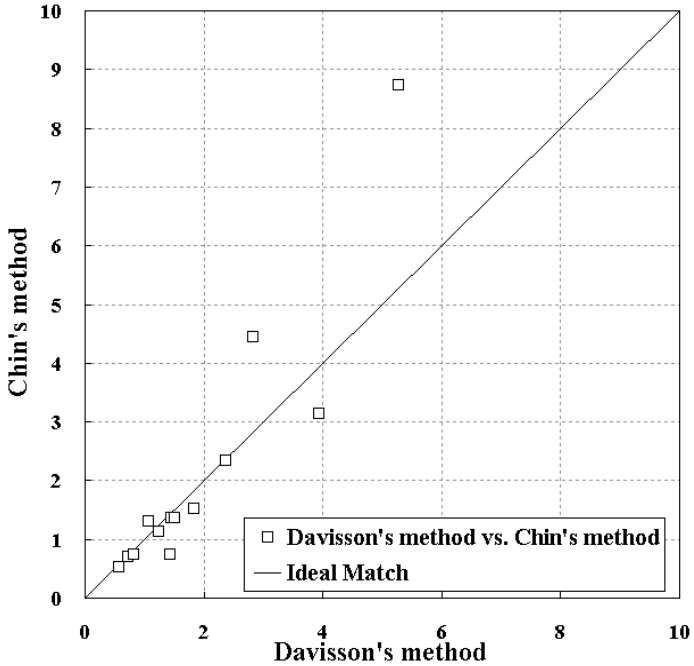

Figure 147. Comparison of Bias factor for Davisson's and Chin's method

Since Chin's method is affected by the shape of the plastic area, some bias factors reach a value of 9, which is too high to consider in the reliability analysis, as shown in Figure 147.

Two factors are taken into account: 1) the determination method for ultimate loads (i.e. Davisson's and Chin's methods and 2) the two different T-z models including those using AASHTO recommended methods, and the IGM model. The results for four analyses cases (Davisson's or Chin's methods with either T-z model development approaches) are presented in Table 55. There was sufficient information to apply the IGM model for some cases such as LT8958-1, LT8958-2, and LT8402. Those cases were not predictable using AASHTO, because they were embedded in rock layers with 70 to 90% of RQD.

Table 55. Cases for the reliability analysis

λ / Tests	Davisson's method		Chin's method	
	AASHTO	IGM	AASHTO	IGM
Bent-8	-	-	3.341	-
DDP-1	1.449	1.449	1.357	1.357
DDP-2	1.442	1.442	0.748	0.748
DP-1	-	-	5.393	**0.935**
DP-2	-	-	12.921	-
Pier-19	-	-	1.029	1.029
Pier-34	-	-	1.401	1.401
Pier-48	-	-	1.672	1.672
TS-1	2.366	2.366	2.333	2.333
TS-2			4.934	-
LT8650-1	0.719	0.719	0.698	0.698
LT8650-2	0.823	0.823	0.742	0.742
LT8650-3	1.075	1.075	1.302	1.302
LT8650-5	0.576	0.576	0.522	0.522
LT8650-6	1.241	1.241	1.136	1.136
LT8650-7	1.830	1.830	1.525	1.525
LT8650-8	1.511	1.511	1.368	1.368
LT8958-1	3.931	**1.150**	3.143	**0.708**
LT8958-2	2.833	**0.894**	4.441	**1.036**
LT8402	5.286	**1.012**	8.734	**1.049**

Table 55 presents the bias factors for the four cases. The bold bias factors are cases by IGM model. The basic statistics of the four cases are presented in Table 56. The values using NCDOT practice for generation of T-z curves along with the use of Chin's method (case 4) yielded the highest bias factors. On the other hand, the use IGM model provided relatively close match as shown in Table 56.

Table 56. Statistics of cases for Davisson's and Chin's method

Item	Davisson's method		Chin's method	
	AASHTO	IGM	AASHTO	IGM
Average	1.929	1.238	2.937	1.151
SD	1.374	0.489	3.138	0.447
COV	0.712	0.395	1.068	0.388

Resistance Factors for Axial Loading

The reliability analysis was performed on the four cases mentioned earlier.

Table 57 shows the reliability indices computed two methods: AFOSM and MVFOSM. The reliability index (β) is defined as the ratio of the mean of the limit state function (g) and the standard deviation of the function (ζ_g). The reliability index provides an indication of the probability of failure. Figure 148 Figure 149 compare the reliability indices versus FS of 2, 2.5, and 3. It seems that the use of the combined AASHTO-IGM approach provides higher reliability indices compared to the methods based on current AASHTO specifications.

As expected, AFOSM yields higher reliability indices than MVFOSM except for values corresponding to FS=2.0 for the AASHTO method. Three points, which are β=2.0, 2.5, and 3.0, are considered as the reliability indices for obtaining the resistance factor, as these values correspond to FS=2.5 or FS=3.0, as shown in Figure 148 and Figure 149.

Table 57. Summary of reliability analyses for axial load tests

FS	AFOSM				MVFOSM			
	AASHTO	IGM	AASHTO	IGM	AASHTO	IGM	AASHTO	IGM
2.0	1.32	2.21	0.97	2.23	1.58	1.72	1.46	1.54
2.5	2.02	3.39	1.48	3.43	1.91	2.23	1.71	2.05
3.0	2.74	4.60	2.01	4.65	2.17	2.64	1.91	2.47

The resistance factors for reliability indices of 0 to 8 are presented in Figure 150. Since the bias factors are dispersive when the AASHTO method was used, the resistance factors corresponding to reliability index above 3 could not be obtained, as shown in Figure 150. Resistance factors are summarized in Table 58. Based on Davisson's method, it can be estimated that the resistance factor of drilled shaft under axial loading condition is 0.38 for reliability index of 2.5. In addition, if results are combined, a resistance factor of 0.57 is obtained for the same reliability index, as shown in Table 58.

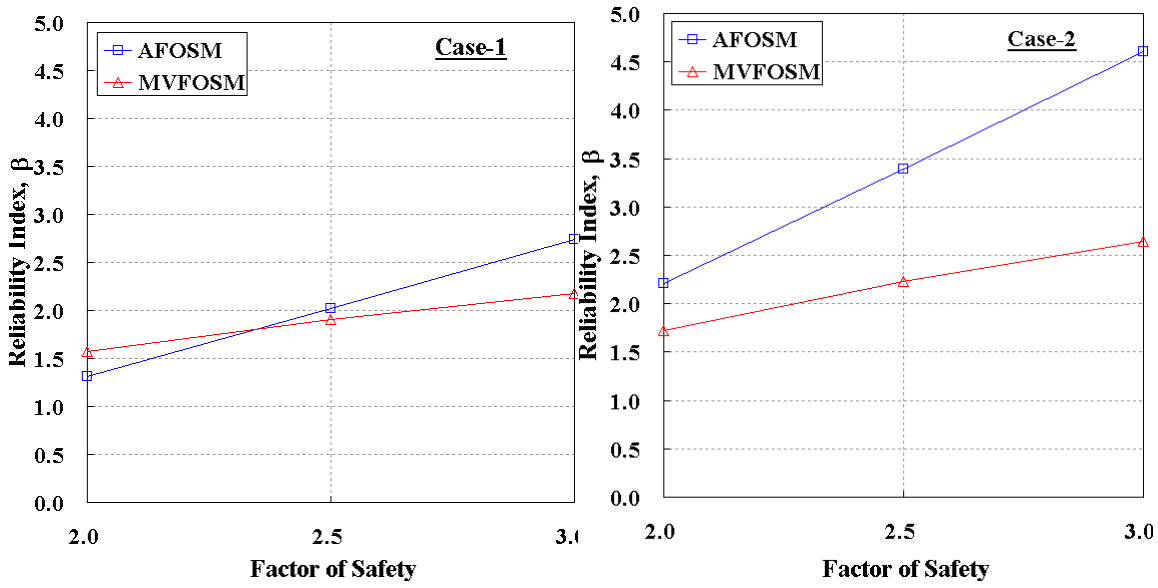

(a) AASHTO (b) IGM

Figure 148. Reliability index by Davisson's method for FS=2.0 to 3.0

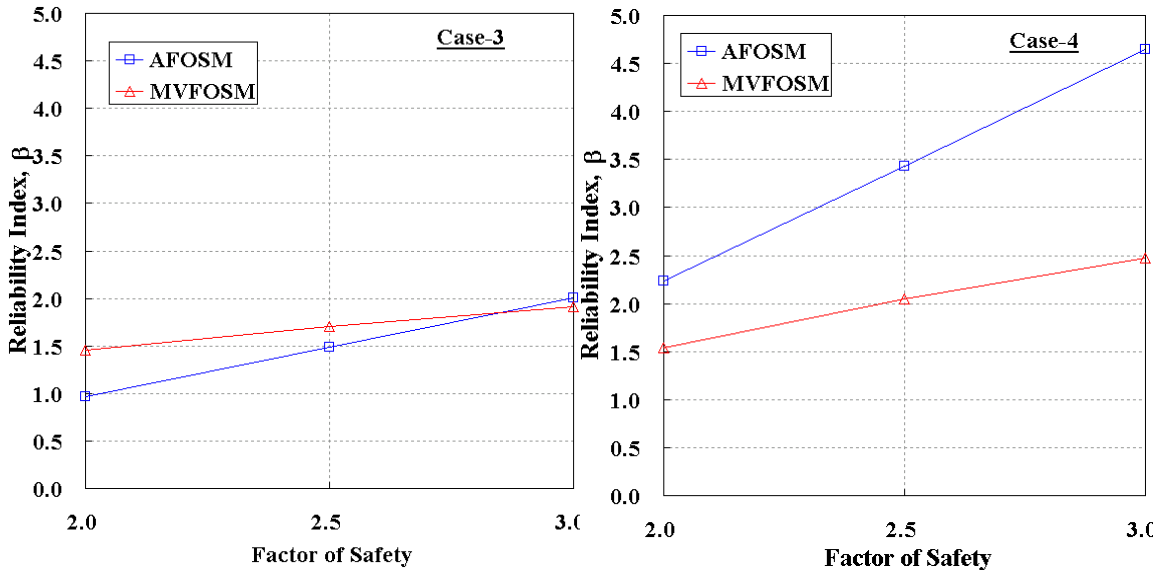

(a) AASHTO (b) IGM

Figure 149. Reliability index by Chin's method for FS=2.0 to 3.0

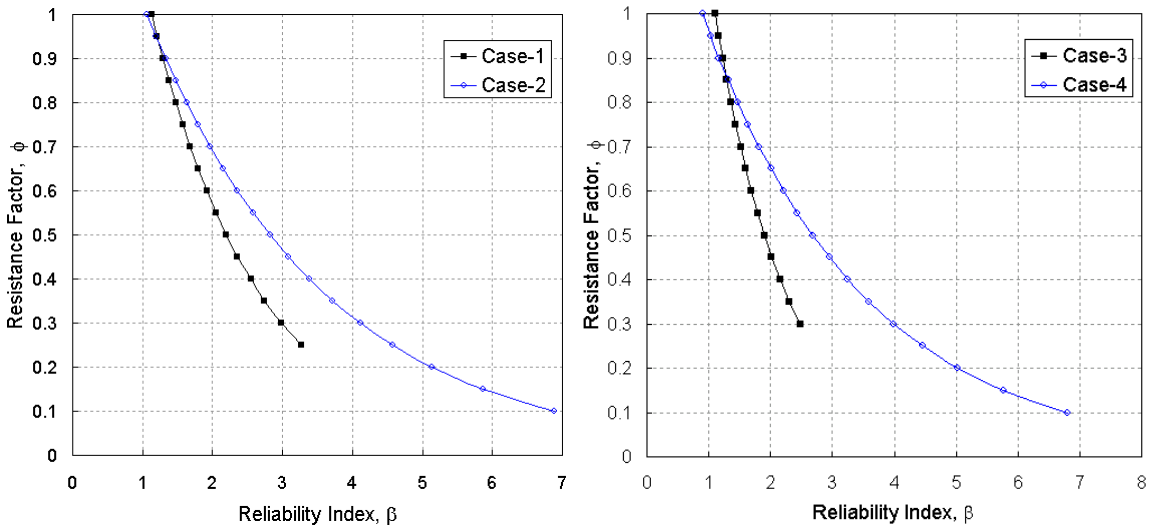

(a) Davisson's method (b) Chin's method

Figure 150. Resistance factor plot vs. reliability index for two criteria

Table 58. Resistance factors for each case

Item	Davisson's method						Chin's method			
	AASHTO			IGM			AASHTO	IGM		
	β=2.0	β=2.5	β=3.0	β=2.0	β=2.5	β=3.0	β=2	β=2.0	β=2.5	β=3.0
ϕ	0.57	0.38	0.3	0.69	0.57	0.47	0.46	0.65	0.54	0.44

Resistance Statistics: Lateral Loading

Table 59 shows the bias factors using the geologic and Stiff Clay models based on the ten lateral load tests studied in this project. Except for the Nash and the Caldwell short shaft cases, bias factors for other cases, based on the Stiff Clay model, have a value higher than unity. The average, standard deviation, and COV (Coefficient of Variation) are presented in Table 60. While the average of bias factor for geologic model is about 1.0, the computed responses using the Stiff Clay model are approximately half of the measurements. The standard deviation using the Stiff Clay model is about 1.7, with dispersive fit as shown in Figure 151.

Table 59. Bias factors of lateral load tests

Tests	Bias Factor, λ	
	Geological	Stiff Clay
Nash Short	0.388	0.550
Nash Long	0.976	0.821
Caldwell Short	0.268	0.301
Caldwell Long	1.564	1.690
Wilson Short	1.482	1.625
Wilson Long	1.318	1.228
I40 Short	1.331	5.144
I40 Long	0.729	4.795
I85 Short	0.785	2.240
I85 Long	1.145	2.321

Table 60. Statistics for the NCDOT practice and Stiff Clay model

Item	NCDOT practice	Stiff Clay
Average	0.999	2.072
SD	0.449	1.667
COV	0.449	0.805

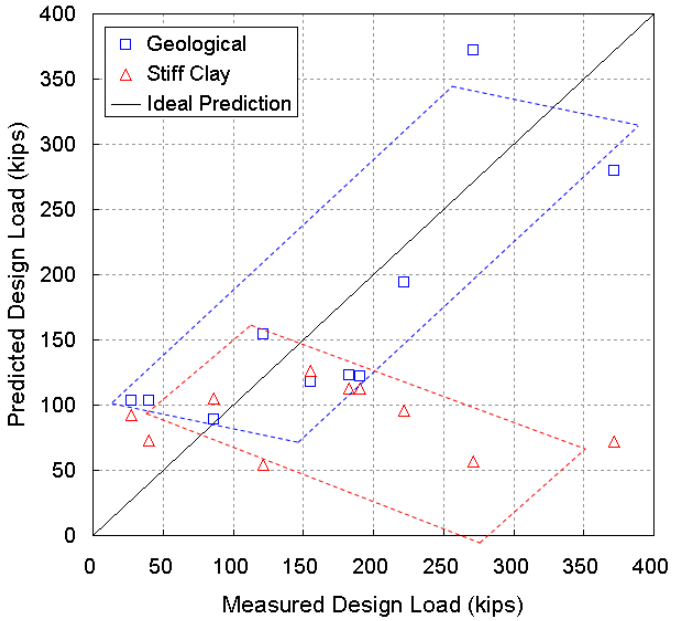

Figure 151. Dispersive plot of lateral load tests

Resistance Factors for Lateral Loading

A reliability analysis was performed using the computed results from the geologic and Stiff Clay models. Table 61 shows the reliability indices computed for the two models, and Figure 152 compares the reliability indices versus FS of 2, 2.5, and 3. For the Stiff Clay model, since the simulated loads were underestimated, the reliability indices were lower than those obtained based on the geologic model approach. A reliability index of 3 at FS=2.5 is obtained using the geologic model, but the value for the Stiff Clay model is only 1.83 at FS=2.5, which means the Stiff Clay model is not reliable to apply. For attaining a reliability index of over 2.5, a factor of safety of 2.5 is used in conjunction with the geologic model, while a factor of safety of 3.0 is used in conjunction with the Stiff Clay.

Table 61. Summary of reliability analyses for axial load tests

FS	AFOSM		MVFOSM	
	NCDOT practice	Stiff Clay	NCDOT practice	Stiff Clay
2.0	1.96	0.50	1.08	1.48
2.5	2.97	1.83	1.55	1.78
3.0	4.09	2.48	1.92	2.03

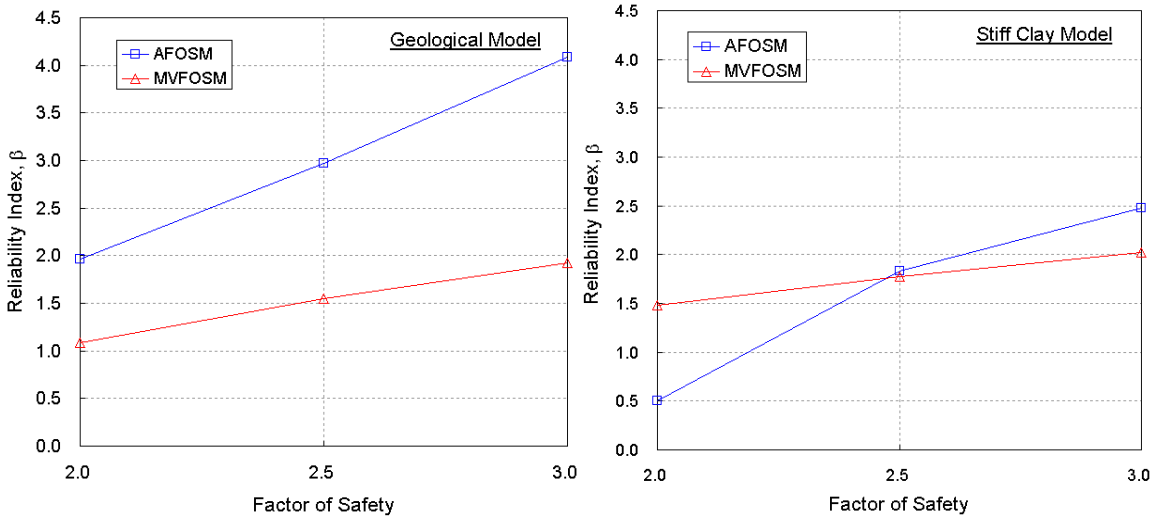

(a) Geological model (b) Stiff clay model

Figure 152. Reliability indices by two models for FS=2.0 to 3.0

Based on the data in Figure 153 and reliability indices, resistance factors are obtained, as shown in Table 62. A resistance factor of 0.4 is estimated at a target reliability index of 2.5. The reader is reminded that these values correspond to shaft top lateral deflection of 0.5 inches.

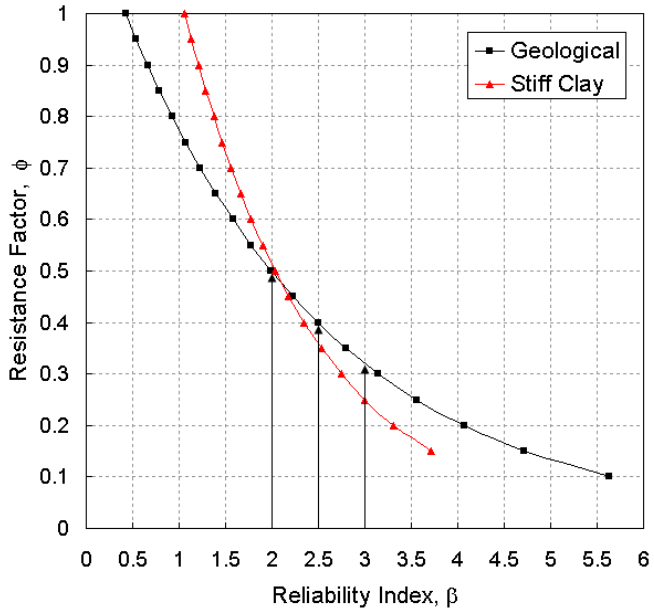

Figure 153. Resistance factors of geological and stiff clay

Table 62. Resistance factors for lateral loading condition (on the basis of 0.5 inches lateral deflection)

Resistance Factor	NCDOT practice			Stiff Clay		
	β=2.0	β=2.5	β=3.0	β=2.0	β=2.5	β=3.0
ϕ	0.50	**0.40**	0.32	0.51	0.36	**0.25**

Comparison with AASHTO and NCHRP507

Resistance factors are compared with the recommendations of NCHRP507 which forms the basis for LRFD in AASHTO's Deep Foundation Specifications. The NCHRP project was initiated to provide "(1) recommended revisions to the driven pile and drilled shaft portions of section 10 of the AASHTO LRFD Bridge Design Specifications (AASHTO, 2001) and (2) a detailed procedure for calibrating deep foundation resistance factors." (NCHRP 507, 2004). Table 63 shows the factors for axial capacity suggested by NCHRP507 based on several construction methods. Table 63 shows the results from NCHRP 507 reliability analyses, and provides comparison with those estimated in this project.

Table 63. Comparison of axial capacity resistance factors with NCHRP 507

Design Method		Construction Method	No. of Cases	Mean	COV	Resistance Factors for a given reliability index β		
						2	2.5	3
FHWA		Mixed	44	1.19	0.30	0.82	0.69	0.58
		Casing	21	1.04	0.29	0.73	0.62	0.52
		Dry	12	1.32	0.28	0.94	0.80	0.68
		Slurry	10	1.29	0.27	0.94	0.80	0.69
R&W		Mixed	44	1.09	0.35	0.68	0.57	0.47
		Casing	21	1.01	0.42	0.55	0.45	0.36
		Dry	12	1.20	0.32	0.79	0.67	0.56
		Slurry	10	1.16	0.25	0.88	0.76	0.65
NCDOT	Davisson's	Mixed	20	1.93	0.71	0.57	**0.38**	0.30
	Chin's		20	1.24	0.40	0.46	-	-
NCDOT + IGM	Davisson's		20	2.94	1.07	0.69	**0.57**	0.47
	Chin's		20	1.15	0.39	0.65	0.54	0.44

In Table 63, FHWA means the prediction by Reese and O'Neill (1988), R&W are predictions based on the models of Reese and Wright (1977), and IGM by the Intermediate Geo-Material as presented by O'Neill and Reese (1999).

The resistance factors estimated herein are not categorized by the construction method because most cases were constructed by wet (slurry) and mixed (casing and slurry) methods. In order to compare the resistance factors, results for the mixed cases reported in NCHRP 507 are selected. As shown in Figure 154, the resistance factors by FHWA are the highest while those developed based on R&W and the mixed method are in the mid range. Resistance factors based on NCDOT practice are at the low end of the range. It should be noted, however, that resistance factors from FHWA and R&W methods were for drilled shafts that were not necessarily installed in weathered rock profiles.

The resistance factor for axial capacity based on data in this report is 0.38 using AASHTO capacity calculations, and 0.57 for the mixed case of AASHTO and IGM model. A resistance factor of 0.57 is similar to that of Reese and Wright (1977), as shown in Figure 154. The case of lateral loading is addressed in AASHTO by specifying a resistance factor of 1. The approach followed in this study is to develop resistance factor based on deformation level and thus no comparison in presented for the lateral loading cases.

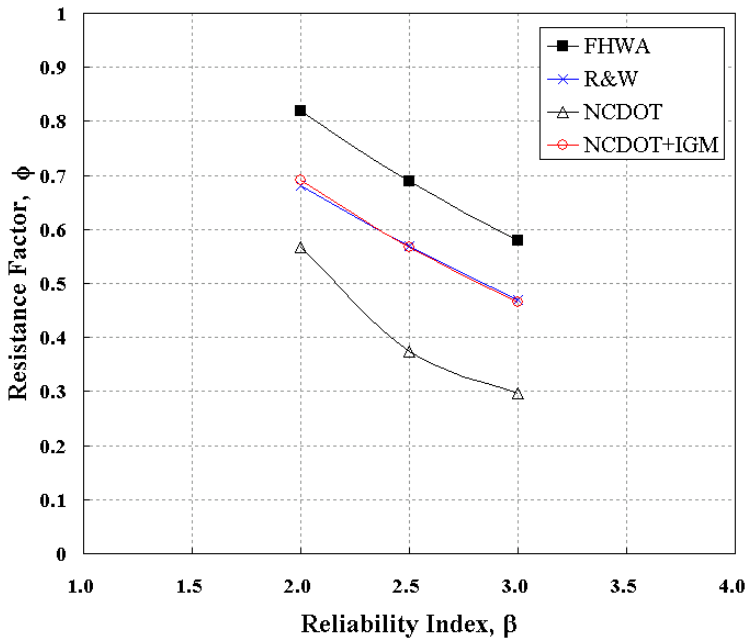

Figure 154. Comparison plot of resistance factor versus reliability index

Application Examples

In order to explain the Load and Resistance Factor Design (LRFD) procedure for axial and lateral loadings, two examples with axial and lateral load cases, respectively, are presented and results are compared to those using the Allowable Strength Design (ASD) procedure. The data for axial and lateral loading condition are obtained from the LT8650-1 and I-40 long shafts, respectively.

Example 1: Axial load case

Circular drilled shafts that are 102 inches in diameter are designed to support the Cooper River Bridge. Each drilled shaft consists of two different sections; one is concrete filled steel casing with 102 inch outer diameter, and second is a rock socket with 96 inch diameter embedded in Cooper Group Marl Formation (which is similar to a weathered rock layer). The ratio of dead load and live load (Q_D/Q_L) is assumed to be 1.5, and unfactored design load is given as 4000 kips per drilled shaft.

In ASD, the required ultimate pile capacity is 10,000 kips at FS=2.5, and the required length of the drilled shaft is 112 feet, as shown in Figure 155. It is assumed that the

resistance factor is 0.47 at a factor of safety of 2.5 and the target reliability index=3.0 for NCDOT practice. A value of 6 ksf is used for skin friction.

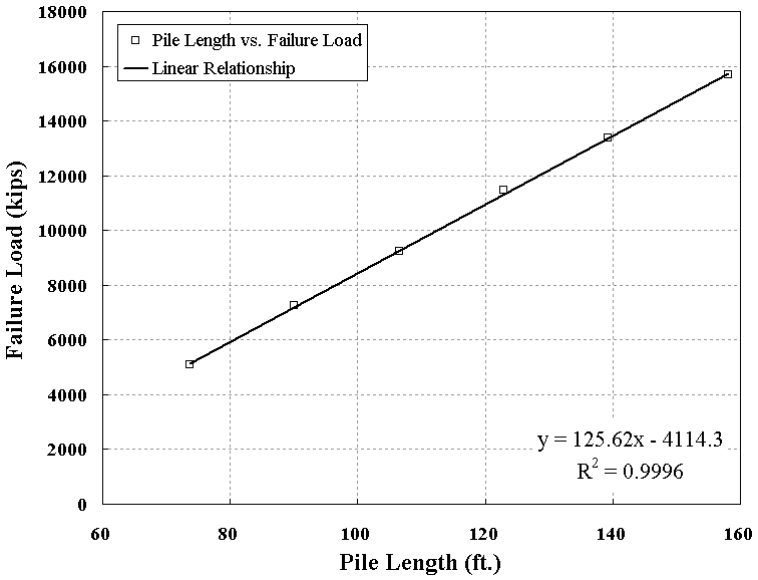

Figure 155. Predicted failure loads vs. pile length for LT8650-1 case

According to load factors for dead load and live load from AASHTO (2006), the resistance of the drilled shaft can be expressed by Equation 35:

Equation 35 $$\phi R = 0.47R = \sum \gamma_i Q_i = 1.25Q_D + 1.75Q_L$$

Equation 35can be rewritten as Equation 36:

Equation 36 $$0.47R = 1.25 \cdot (0.6Q) + 1.75 \cdot (0.4Q) = 1.45Q$$

From the Equation 36, the resistance (R) of LRFD is 12,340 kips (=4000 kips × 1.45 / 0.47), which is correspond to FS=3.08. However from the MultiPier analyses, the required length to satisfy a 0.5 inch lateral displacement criterion is 131 feet.

Example 2: Lateral load case

Circular drilled shafts 2.5 feet in diameter are designed to support the pier of the bridge for the north-west corner of the intersection of I-40 West and North Carolina Highway 55 in Durham. The drilled shaft, with steel casing, was embedded in weathered rock layer with 72% to 100% of RQD.

Similar to the axial loading case, the ratio of dead load and live load (Q_D/Q_L) is assumed to 1.5, and unfactored design load is given as 150 kips per shaft. In ASD, the required ultimate pile capacity is 375 kips at FS=2.5, and the required length of the drilled shaft is 13.3 feet, as shown in Figure 156.

It is assumed that the resistance factor is 0.4 at the factor of safety=2.5 and the target reliability index=2.5 for the Geologic model. According to load factors for dead load and live load from AASHTO (2006), the resistance of the drilled shaft can be expressed by Equation 37.

Equation 37 $$\phi R = 0.4R = \sum \gamma_i Q_i = 1.25Q_D + 1.75Q_L$$

Equation 37 can be rewritten as Equation 38:

Equation 38 $$0.4R = 1.25 \cdot (0.6Q) + 1.75 \cdot (0.4Q) = 1.45Q$$

From the Equation 38, the resistance (R) of LRFD is 544 kips (=150 kips × 1.45 / 0.4), which is correspond to FS=3.63. However, from the MultiPier analyses, the required length for to satisfy a 0.5 inch displacement criterion is 26.2 feet, which is 12.9 feet longer than ASD.

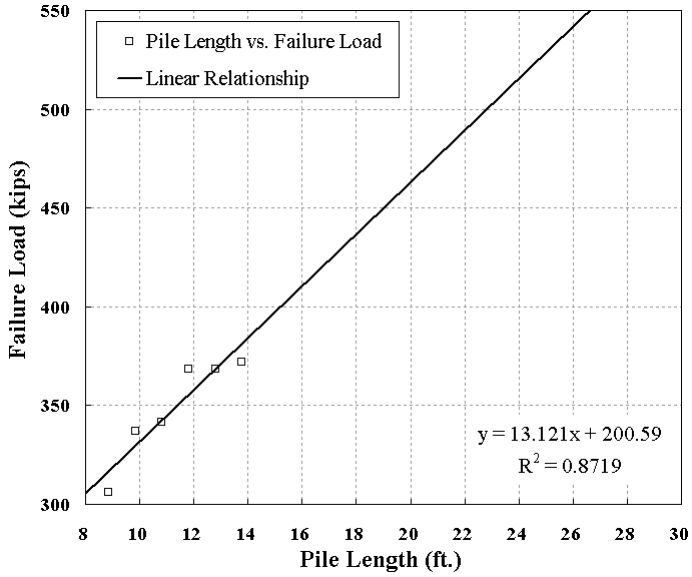

Figure 156. Predicted failure loads vs. pile length for I-40 case

In summary, twenty axial and ten lateral load tests are analyzed and simulated using T-z, Q-z, or P-y curve approaches. By applying a reliability analysis to the results, resistance factors are developed and proposed for use by NCDOT.

The Limestone (McVay) model, used by NCDOT in practice, is employed to simulate the response measured from axial load tests. For some cases with high RQD and unconfined compressive strength of rock mass layer, Horvath and Kenney, and Intermediate Geo-Material models are considered for the cases. The geologic model and the Stiff Clay model are considered for the simulation of lateral load-deflection response

Analyses results yielded a resistance factor of 0.38 for the axial loading condition. If sufficient geotechnical information is available, and IGM model is used for the analysis, the resistance factor can be increased to 0.57, a value close to that recommended using R&W model in NCHRP 507. For the determination of a failure load from axial load-settlement relationship, Davisson's method is recommended, because the capacity prediction by this method resulted in relatively less scatter as well as consistent underestimation of the measured shaft capacity. Values obtained using Chin's method tended to overestimate the shaft capacity.

For the simulations of lateral load tests, the Geologic model yielded good estimates of capacity corresponding to 0.5 inch displacement. The mean of the bias factors is nearly 1.0. The Stiff Clay model, which was not developed for weathered rock profiles, provided results that underestimated the measured response. Reese's rock model, using rock property values recommended in literature, was too stiff to provide a capacity estimation at 0.5 inches of lateral displacement.

The resistance factor of lateral loading condition is 0.4 for the Geologic model, and 0.36 for Stiff Clay model at 2.5 of target reliability (and for a 0.5 inch lateral displacement). If a target reliability index =2 is used for the design, the resistance factor is increased to 0.5.

CHAPTER 8: SUMMARY AND CONCLUSIONS

The geotechnical and structural design of bridge bents generally does not consider the superstructure-substructure interaction, with the superstructure idealized as a series of static loads and moments applied to the bearing locations on the bridge bent. The research work presented in this report aims at understanding and optimizing the design process of drilled shafts bents for safety and functionality. The work included the examination of the design process for drilled shaft bents and the approach used to estimate the shaft length and designate a corresponding point of fixity. Potential areas of conservatism in the current practice are studied through modeling and experimental studies. Modeling included analysis of three existing bridge case studies to characterize the impact of the current assumptions on sizing the various components of the bridge bent. In addition, resistance factors are developed for drilled shafts, based on load test data from the state's geologic regions, for compatibility with LRFD implementation. The load factors for axial and lateral resistance of drilled shafts are developed in preparation for the transition to LRFD approach albeit on the basis of a limited number of field tests performed in soils similar to those found in the North Carolina. The results nonetheless provide a framework for future updating of the resistance factors as more field data are available.

The experimental program included testing bearing pads in compression and shear to define their index properties. The bearing pads are then tested in a prototype bridge set up to measure their performance under simulated loading. Prototype experimental program included 42 tests on three different foundation configurations: (1) Pre-stressed square concrete pile; (2) Circular tube concrete pile; and (3) H-pile. Each foundation element is tested with two different elastomeric bearing pads. These are Type V bearing pads commonly used for a steel superstructure, and Type VI pads commonly used for a concrete superstructure. Two AASHTO Type II girders that are 30 ft (9.14 m) long were used as a part of the prototype system. The girders were made continuous with a diaphragm following the NCDOT specifications. The test section included the assembly of a deck, girder, diaphragm, sole plate-anchor bolt, bearing pads, and bent cap-pile

components. Loading was displacement controlled and was monitored using 55 separate sensors for strain, deformation, load, and pressure measurements.

Each concrete pile was subjected to three different levels of axial load ratio (ALR). The H-Pile was not loaded axially due to the insensitivity of steel stiffness to axial loads. In addition, for each ALR, the axial load on the bearing pads was varied to three levels. Lateral load was applied to the test setup until the yield displacement of the pile, and in some cases until the inelastic range of displacement. The results provided the magnitude of the super-sub structure connection rotational stiffness which was then used in modeling to determine the impact of rotational stiffness on the response of the laterally loaded shafts and the k-factor used in buckling analyses.

Based on the results obtained in this research, the following conclusions are advanced:

i. Modeling of three bridge structures were performed within the framework of MultiPier and SAP 2000. The results demonstrated that MultiPier model results can be reproduced in the 3-D SAP program. Analyses results indicated the feasibility of optimized design through reducing the number, or size, of the shafts while maintaining the same load cases. For example, in the Wake County bridge cases, seven 54 inch diameter drilled shafts were originally used as the foundation support system. Analyses results indicated the possibility of optimized design by reducing the size of the shafts to 30 inches while maintaining demand capacity ratios of less than 0.5 .Lateral displacements in the transverse direction exceeded 2.5 inches. Further reduction of the shaft diameter was not possible, as the analysis would not converge. If the superstructural elements (including the bearing pad connection) could tolerate lateral displacements of this magnitude while maintaining functionality and safety, and no further extreme events are expected, then this would appear to be a valid design outcome.

ii. The equivalent point of fixity model proposed in Robinson et al. (2006) was used for the analysis of shafts supporting the bridges in the three case studies. The results from the point of fixity model yielded responses that are comparable to those obtained from both the SAP and MultiPier analyses, provided that the most critical lateral load case is used to evaluate the parameters for the equivalent model. The equivalent frame model yielded similar moments, axial loads and shear loads in the most critical case. The use of the equivalent point of fixity model is recommended, as it should lead to more optimal and possibly reduced sizing of the structural elements.

iii. In all three case studies, it was shown that some savings in material and installation costs can be realized by using the nonlinear analysis. Thus, compared to the approach traditionally used by NCDOT for defining the point of fixity, there is some room for cost and material savings by using the equivalent model proposed by Robinson et al. (2006).

iv. Results from index testing on the bearing pads indicated that Type VI bearing pad have a higher shear modulus than the Type V pad. Type V and VI pads used in testing have a hardness magnitude of 50 and 60, respectively, with hardness serving as an indicator of a higher shear modulus.

v. The compressive modulus for the Type V is estimated equal to approximately 3000 psi versus 6000 psi for the Type VI. According to Yura et al (1995), the hardness of the material and the shape factor influence the bearing pad compressive behavior. The compressive stiffness increased with the increase in hardness values.

vi. Observations from the performance testing indicated the first yielding of the longitudinal steel bars in the square and circular piles occurred at approximately 3 in (76 mm) top deflection (at the point of load application.) The theoretically-estimated first yield displacement was 1 inch (25.4 mm)

with the assumption of a fixed base column. The anchor bolt-bearing pad connection therefore provided some rotational stiffness that did not allow the square and circular pile columns to behave as pure cantilevers.

vii. In the case of the circular pile it was observed that a deflection of 3.26 inches (83 mm) at the point of load application produced yielding of the longitudinal steel at a strain of 0.002. When the pile was loaded to ductility 1.5 (4.89 inches displacement) the testing was terminated because bending was noted around the weak axis of the sole plate. It was observed that the weakest link for this connection was the sole plate that is located at the top of the bearing pad, although this may have been exacerbated by a slightly longer weld length connecting the sole plate to the girder.. The force produced by the bending of the sole plates caused a gap between the embedded plate and the girder because of the pulling action. However, the force experienced during this test was not enough to pull out the embedded plate from the girder. The bending of sole plates caused crushing of the concrete around the diaphragm area.

viii. Results from performance testing also indicated an increase in the rotational stiffness of the connection corresponding to an increase in the test pile and bearing pad stiffness (as induced by applying higher axial loads.) For the conditions simulated in this testing program, the largest contributors to the total displacement response of the tested system were cap beam rotation (approximately 60%), followed by the pile lateral deformation (approximately 25%).

ix. The shear strain limit criteria established in the AASHTO LRFD Bridge Design Specifications call for shear modulus calculated between 0 to 50% or between -50% and 50% shear strain. For Type V bearing pad (50 hardness) the measured shear modulus ranged between 101 to 109.7 psi (0.70-0.76 MPa) using the 0-50% shear modulus definition. For the Type VI bearing pad (60 hardness) the values ranged between 133.7 to 176.3 psi (0.92-1.22 MPa).

Although the compounds in the neoprene material vary among manufacturers, values obtained in this study are comparable to those found in the literature.

x. The results from the full scale testing show the capacity of sole plate-anchor bolt and bearing pads system for transferring the applied moments. Given the test components strength and stiffness parameters, the maximum moment in the pile cap for all of piles tested was between 150 (218.5) and 225(327.8) k-ft (kN/cm). The maximum cap rotation was approximately 0.5 degrees for all loading cases except for the H-pile tests on the Type V bearing pad. In this case, the maximum pile cap rotation was more than double that experienced in the other cases.

xi. Observations of the system components during testing indicated that the steel sole plates located at the top of the bearing pads were bent during load application, which led to crushing of the concrete at the diaphragm area. Under the applied lateral loads, the sole plates bending action led to pull out of the embedded plate on the girder. The embedded plate has four studs of 178 mm (7 in) in length, which provided enough strength against the pulling force produced by the bending of the sole plates.

xii. In the case of the H-pile testing (which was tested last after the square and circular cross sections) a top deflection of 6.23 inches (158 mm) at a horizontal load of ~18 kips was needed to reach the first yielding. After completion of the elastic cycles, cracks developed between the H-Pile and the pile cap. These cracks became more pronounced as the second loading protocol began. Testing continued to the completion of a ductility of 1.5 where the top deflection at the point of load application reached 9.34 inches (237 mm). The prying action of the embedded part of the HP pile caused large damage in the cap beam.

xiii. Beyond yield of pile reinforcement, the following items limited the capacity of the system: (1) bending of each sole plate about its weak axis, which led to gaps opening between the embedded plate and the girder. (2) During H-Pile testing at high displacements, significant prying and cracking of the cap beam were observed. The superstructure and pile cap otherwise showed very few signs of significant distress

Regarding the H-Pile prying issue, H-Piles are often designed as a pinned connections between pile and pile cap. Regardless of this assumption, the system did show significant moment transfer. It is possible to more fully take advantage of this moment capacity through deeper embedment of the H-Pile and more careful detailing of the rebar tie-in will be needed. If additional lateral displacements are expected to be tolerated, this connection needs to be improved.

xiv. The general trend observed during testing is an increase in the rotational stiffness with increasing confining stress (as induced by axial load on the pads) for the square concrete pile. The secant rotational stiffness for the square pile under the P3 load level of approximately 45 kips was 550 k-ft/deg for type V bearing pad and 660 k-ft/deg for type VI at 1 inch lateral displacement (at the point of load application.) At the same displacement level, and using the circular pile, the secant rotational stiffness was approximately 325 k-ft/deg for the system with both type V and VI bearing pads. In comparison, the secant rotational stiffness for the H-pile was approximately 150 k-ft/deg for the system with both type V and VI bearing pads. The square pile is stiffer than both the circular and HP piles. Such higher stiffness is contributing more to the ductility of the connection.

xv. The magnitude of rotational stiffness can be affected by several factors. These include the elastic modulus for the bearing pads, the load applied to the

bearing pad, the bending of the sole plate, and cracking and failure of the bent cap around the anchor bolt. It should be noted that POT and TFE bearing pads are not included in this investigation as NCDOT does not use a diaphragm to connect adjacent girders with these types of bearings.

xvi. In the longitudinal direction, without a diaphragm and continuity of the deck, such connections will not transfer moment, and a K factor for buckling analysis of 2.1 is deemed appropriate. However, when a diaphragm and bearing pad is present, it has been shown that, using the method for estimating k in Robinson et al. (2006) with the equivalent length from a fixed head analysis, the k value can be reduced if a rotational spring simulating the sub to super structure connection is modeled at the top of the pile in the single lateral pile analysis. As the rotational stiffness increases, the K factor will decrease from 2.1 down toward the value for a fixed head.

xvii. NCDOT currently assumes a K value of 1.4, which indicates the fixity of the connection. It should be noted that, in the transverse direction, such an assumption seems to be valid, and no investigation is focused on the behavior in the transverse direction.

xviii. It can also be concluded that a conservative estimate of yield displacement, that can be used as a design limit state, can be easily calculated with Equation 18 and Equation 19 for free head and fixed head response respectively. The yield displacement is directly proportional to the square of the equivalent length and inversely proportional to the diameter of the section. For the seven bridges studied (three in this report and four in the previous), the yield displacement calculated by equations and by pushover analyses are higher than the one inch design limit generally used by the NCDOT.

xix. The resistance factors for laterally and axially loaded drilled shaft are developed based on limited test data from sites in North Carolina. The

Resistance factors for drilled shafts subjected to axial loads are calibrated to Statnamic and Osterberg load test results and summarized in Table 64. Based on Davisson's approach, the estimated resistance factor for the axial loading condition is estimated as 0.38 at a reliability index of 2.5 and using the AASHTO analysis methods. If the simulated capacities were obtained from the combination of AASHTO methods in the soil and IGM methods in rock, then the results show a resistance factor of 0.57 for the same reliability index. The resistance factors for axial compressive resistance of drilled shafts outlined in AASHTO (2006) range from 0.40 to 0.60 with a limit of 0.70 depending on the method used to estimate the capacity. In AASHTO, the basis for estimating the resistance factors is capacities from static load tests in compression which are dependent on the number and variability of the sites in which the shafts were installed and do not necessarily reflect geology in North Carolina

Table 64. Resistance factors for drilled shafts under axial loading

Item	Davisson's method						Chin's method			
	AASHTO			IGM			AASHTO	IGM		
	β=2.0	β=2.5	β=3.0	β=2.0	β=2.5	β=3.0	β=2	β=2.0	β=2.5	β=3.0
ϕ	0.57	0.38	0.3	0.69	0.57	0.47	0.46	0.65	0.54	0.44

xx. The resistance factors under lateral loading based on 0.5 inches of lateral deflection at the top of the shaft (at the ground level) is estimated as 0.4 at a reliability index of 2.5. Lateral resistance factors were calculated at 0.5 inches instead of 1.0 inches because very few of the provided load tests achieved 1 inch deflections. The values for other reliability index values are shown in Table 65. In the AASHTO LRFD specifications, drilled shafts under horizontal loading have a recommended resistance factor of 1.0 with the connotation that these values are dependent on a specified deformation criterion but no specifics were provided.

Table 65. Resistance factors for lateral loading condition (on the basis of 0.5 inches of shaft top lateral deflection)

Resistance Factor	NCDOT practice			Stiff Clay		
	β=2.0	β=2.5	β=3.0	β=2.0	β=2.5	β=3.0
ϕ	0.50	0.40	0.32	0.51	0.36	0.25

xxi. Currently, NCDOT practice utilizes a performance level of one inch lateral displacement at the bent cap to assess shaft length. Robinson et al (2006) suggested a serviceability limit state of the superstructure characterized by expansion joint closure due to lateral loading in the transverse direction. Analyses on interior bents showed that shaft bents analyzed in this study could not tolerate a horizontal load (transverse direction) greater than those required to close the expansion joint. Accordingly, the lateral deformation of the shaft bents, not the closure of the expansion joints, represented the critical juncture in the serviceability limit state for the bridge that was modeled**.**

Work in the report provides a better understanding of the performance of bents supported by drilled shafts under AASHTO loading conditions. Such understanding serves as a tool that provides NCDOT engineers with the flexibility of specifying the level of conservatism to be built into a specific bridge bent design. An improved set of design guidelines and recommendations regarding bearing pad rotational stiffness, shaft/pile top boundary conditions, and resistance factors are presented along with characterizing the impact of the current practice and various design assumptions on sizing components of bridge bents.

REFERENCES

American Association of State Highway and Transportation Officials (AASHTO). (2004). AASHTO LRFD Bridge Design Specifications, Customary U.S. Units, Third Edition, Washington, D.C.

AASHTO (2006). AASHTO LRFD Bridge Design Specifications, Customary U.S. Units, 2006 Interim edition, Washington, D.C.

Abendroth, R. E., Klaiber, F. W., and Shafer, M. W. 1995. ‘‘Diaphragm effectiveness in prestressed-concrete girder bridges,’’ *Journal of Structural Engineering (ASCE)*, V. 121, No.9, September, 1362–1369.

American Institute of Steel Constructors (AISC). 2001. “LRFD Manual of Steel Construction.” 3rd Edition,2001. p. 16.1-189.

Bridge Software Institute (BSI). (2004). MultiPier Manual, Version 4. University of Florida, USA. http://bsi-web.ce.ufl.edu/

Chin, F. K. (1970), “Estimation of Ultimate Load of Piles from Tests Not Carried to Failure,” *Proceedings of the Second Southeast Asian Conference on Soil Engineering*. Singapore, pp. 81-90.

Cho, K.H. (2002) “P-y Curves for Laterally Loaded Drilled Shafts Embedded in Soft Weathered Rock,” Ph. D. Thesis, North Carolina State University, Raleigh, North Carolina.

Computers and Structures, Inc. (2004). SAP Manual. Berkeley, California, USA.

Eamon, C. and Nowak, A.,“Effect of secondary elements on bridge structural system reliability considering moment capacity”, Structural Safety ,V. 26, February, 2004, pp. 29–47.

Ensoft, Inc. (2004). LPILE Manual. Austin, Texas, USA

Esmaeily, A. (2000). “USC-RC software.” Available at http://www.usc.edu/dept/civil_eng/structural_lab/software.html

Gabr, M.A. Borden, R.H., Cho, K.H., Clark, S.C. and Nixon, J.B. (2002) “P-y Curves for Laterally Loaded Drilled Shafts Embedded in Weathered Rock.” Federal Highway Administration, Report No. FHWA/NC/2002-008. 289 pages. http://www.ncdot.org/doh/preconstruct/tpb/research/download/2002-13FinalReport.pdf

Gambhir, M.L. (2004). “Stability analysis and design of structures.” Springer, New York.

Georgia Department of Transportation (revised, 1994). "Analysis and Design of Multiple Column Piers for Bridges E75700," Georgia Pier Program Manual Version 4.2. Revised by the North Carolina Department of Transportation. 132 pages.

Goodman, R.E. (1989). "Introduction to Rock Mechanics, second edition," John Wiley & Sons.

Green, T., Yazdani, N., and Spainhour, L.,"Contribution of intermediate diaphragms in enhancing precast bridge girder performance", *Journal of performance of constructed facilities (ASCE),* V. 18, No. 3, August, 2004, pp. 142-146.

Hoek, E. and Brown, E.T. (1997). "Practical estimates of rock mass strength," *Intnl. J. Rock Mech. & Mining Sci. & Geomechanics Abstracts.* Vol. 34, No. 8, pp. 1165-1186.

Horvath, R.G., and Kenney, T.C. (1979). "Shaft Resistance of Rock-Socketed Drilled Piers," *Proceedings*, Symposium on Deep Foundations, ASCE, Atlanta, pp. 182-214.

Kim, K. J. (2002). "Development of resistance factors for axial capacity of driven piles in North Carolina." Doctor of Philosophy Dissertation, North Carolina State University.

LEAP Software, 2006. RC-Pier User's Manual.

McVay,M. C., M., Niraula, L. (2004) "Development of Modified T-Z Curves for Large Diameter Piles/Drilled Shafts in Limestone for FB-Pier," Report Number 4910-4504-878-12, National Technical Information Service, Springfield, VA.

Moulton, L.K. (1986). "Tolerable Movement Criteria for Highway Bridges." Report to the Federal Highway Administration (FHWA-TS-85-228). 93 pages

Mullins, G.; Lewis, C.; and Justason, M. (2002) "Advancements in statnamic data regression techniques" *Geotechnical Special Publication*, ASCE, n 116 II, 915-930

Muscarella J.V. and Yura J.A. "An experimental study on elastomeric bridge bearings with design recommendations". FHWA/TX-98/1304-3. Austin, Texas. October, 1995.

NCDOT (2004, 2005). Bid Averages.
http://www.ncdot.org/doh/preconstruct/ps/contracts/bidaverages/avgdefault.html

Nixon (2002) "Verification of the Weathered Rock Model for P-y Curves," Master's Thesis, North Carolina State University. Raleigh, North Carolina.

O'Neill, M.W., Townsend, F. C., Hassan, K. M., Buller, A., and Chan, P. S., "Load Transfer for Drilled Shafts in Intermediate Geomaterials," Report No. FHWA-RD-95-172, November 1996.

O'Neill, M. W., and Reese, L. C. (1999). "Drilled shafts: Construction procedures and design methods." *Publication No. FHWA-IF-99-025*, U.S. Dept. of Transportation, Federal Highway Administration, Washington, D.C., 535.

Osterberg, J. (1999). "What has been learned about drilled shafts from the Osterberg Load Test." *Proceedings of the Deep Foundations Institute Annual Meeting*. http://www.loadtest2005.net/papers/Learned.pdf

Rahman, M. S., Gabr, M. A., Sarica, R.Z., and Hossain, M. S. (2002). "Load and Resistance Factor Design (LRFD) for Analysis/Design of Piles Axial Capacity." Report No. FHWA/NC/2005-08, Federal Highway Administration, 247 pages. http://www.ncdot.org/doh/preconstruct/tpb/research/download/2002-14FinalReport.pdf

Reese, L. C., Cox, W. R. and Koop, F. D "Analysis of Laterally Loaded Piles in Sand," Paper No. OTC 2080, Proceedings, Fifth Annual Offshore Technology Conference, Houston, Texas, 1974 (GESA Report No. D-75-9).
Reese, L.C., and Welch, R.C. (1975). "Lateral Loading of Deep Foundations in Stiff Clay," Journal of the Geotechnical Engineering Division, ASCE, V 101, N 7, Jul, 1975, pp. 633-649.

Robinson, B.; Rausche, F.; Likins, G; and Ealy, C. (2002). "Dynamic load testing of drilled shafts at National Geotechnical Experimentation Sites." *Geotechnical Special Publication*, ASCE, n 116, 851-867.

Robinson, B., Suarez, V., Robalino, P., Kowalsky, M. and Gabr, M., "Pile Bent Design Criteria." *NCDOT Research Project 2005-19*. Report no. FHWA/NC/2006-14. June, 2006.

Wang, S. T., and Reese, L. C. (1993) "COM624P-Laterally loaded pile analysis for the microcomputer, ver. 2.0" FHWA-SA-91-048, Springfield, VA.

Yazdani, N., Scott, E., and Chun, C.,"Effect of bearing pads on precast prestressed concrete bridges", *Journal of Bridge Engineering (ASCE)*, V. 5, No.3,August, 2000, pp. 224-232.

Yoon, D.Y., Yoo, C.H., and Lee, S.C., "On the behavior of sole plates in steel girders", *Thin-Walled Structures*, V. 42, No.1, January, 2004, pp. 59-77.

Yura J.A, Kumar, A., Yakut A., Topkaya C., Becker E., and Collingwood J. "Elastomeric bridge bearings: recommended test methods". NCHRP Report 449. 2001.